

SMALL BODIES, SMALL STARS: THE FATE OF COMETS

by

Dang Cao Pham

A thesis submitted in conformity with the requirements
for the degree of Doctor of Philosophy

David A. Dunlap Department of Astronomy and Astrophysics
University of Toronto

Small Bodies, Small Stars: The Fate of Comets

Dang Cao Pham
Doctor of Philosophy

David A. Dunlap Department of Astronomy and Astrophysics
University of Toronto
2025

Abstract

Elements heavier than Helium are expected to sink quickly on white dwarf atmospheres, yet are observed on 25-50 per cent of white dwarfs, indicating that these stars are accreting material from their planetary systems. First, the scenario of an Oort cloud polluting white dwarfs is studied. The dynamics of Oort cloud comets around white dwarfs with the effects of Galactic tide and a massive companion, either stellar or planetary, is characterised through numerical and analytic methods. A fast, direct N-body simulation including these dynamical effects is developed, which can simulate a large number of comets to resolve the rate of comets entering a white dwarf's Roche limit over one gigayear. Through simulations, pollution rates by Oort cloud objects onto white dwarfs with and without planetary companions are found to broadly produce observed pollution rates. Second, an upgrade to the adaptive timestep criterion of IAS15, a numerical integrator, is presented to improve N-body simulation efficiency. Third, the impact rate between interstellar objects and neutron stars is considered to explain another phenomenon — fast radio bursts. Various observational predictions of this radiation emission are discussed. Fourth, the evolution of cometary volatiles as a Sun-like star evolves post-main sequence is studied. The volatile budget in Solar system long-period comet reservoirs are simulated, along with debris discs at various distances for exoplanetary systems. A coupled stellar-dynamical-thermal-mass evolution model is developed to resolve comets on the most eccentric orbits around a highly luminous star. We find that debris discs at different distances retain volatiles and hyper-volatiles at varying fractions, depending on distance and object sizes, though all show signs of volatile depletion. This finding supports observations that many white dwarfs are polluted with rocky materials. This thesis seeks to explain phenomena around compact objects and consider how observations can probe small bodies across the Universe.

Tặng ba mẹ và em

To my parents and sister

Acknowledgements

I acknowledge the immense privileges which made it possible to pursue a PhD in astronomy and astrophysics, and that this effort was not done in isolation.

The only certainty I have in this thesis is that it could not have been done without my advisor, Hanno Rein, who has shown me how to do science with care and creativity. I have grown a lot as a scientist thanks to your patience with my research, your encouragements of my divergent scientific interests, and your constant push for my growing independence. I will strive to emulate your high standard of rigour and vast scientific breadth for the rest of my career. Beyond science, I have also learned many things from you, from pedagogy as a teaching assistant for your classes to wood sanding for my hurdy gurdy. In addition, your interests outside of science have shown me that it is possible to truly have a good life, freely pursuing one's passions. Perhaps that will be the even higher standard.

I would like to thank my other academic advisors: Scott Tremaine, Norm Murray, Yanqin Wu, and Lisa Kaltenegger. I am grateful to Scott and Norm for being on my thesis committee; your questions and creativity have greatly improved my research. In addition, your advice, from the beginning of my thesis to my postdoctoral applications, has been crucial to my career. I would like to thank Yanqin Wu, who although is not on my committee, has always been interested in my research and offered many advices greatly improving my works. I am especially grateful to Lisa Kaltenegger, who generously accepted me to pursue undergraduate research, and continued to offer constant support and collaboration throughout my PhD.

I have been fortunate to collaborate and work with amazing scientists, all of whom have made research a lot more interesting: Abigail Crites, Dongwoo Chung, Martin Schlecker, David Chernoff, Rosanne Di Stefano, Matthew J. Hopkins, Aster Taylor, Joy Li, David Ruppert, David S. Spiegel, and Sam Hadden. I am grateful for the white dwarfs and dynamics scientific communities, who have been so welcoming at conferences and beyond, especially Nadia Zakamska, Smadar Naoz, Konstantin Batygin, Santiago Torres, Chris O'Connor, Siyi Xu, Yubo Su, and Tiger Lu. I am also grateful to the professors in the Toronto astronomy department who have taught, supported, and advocated for me in many capacities: Chris Matzner, Renée Hložek, Ting Li, Maria Drout, Marta Bryan, Adam Hincks, and Josh Speagle. I would like to thank my high school teacher, Herman Keith, who helped me begin my physics education. I am grateful to Margaret Meaney, whose support began by helping with logistics of moving to Canada in the middle of the pandemic.

To my cohort, Steffani Grondin, Sam Berek, Ayush Pandhi, Yuyang Chen, and Bolin Fan, we have grown a lot since our weekly pandemic Zoom meetings and I have had a lot of fun hanging out with all of you! Many thanks to other graduate students for making my PhD a lot more enjoyable: Michael Poon, Mark Dodici, Jacob Meadus, Henry Leung, Steffani Grondin, Mairead Heiger, Sam Berek, Garrett Brown, Victor Chan, Taylor Kutra, Emily Deibert, Shivan Khullar, Joshua Bromley, Simran Nerval, Eesha Das Gupta and all others

whom I physically cannot fit into the margins of this thesis. A special acknowledgement to Eesha Das Gupta and Shivan Khullar for visa commiseration in perpetually “interesting” times. In addition, I appreciate the occupants of AB 203 (Mark Dodici and Michael Poon) who are willing to regularly discuss with me about any science topics. To Garrett Brown, our weekly, hours-long science discussions have been greatly insightful. Thank you to Henry Leung, Michael Poon, and Jacob Meadus for weekly hangouts, Riichi mahjong, and board games. I am especially grateful to Michael Poon for greatly improving my PhD through robust discussions on science, reimbursements, life, career, and most importantly, food.

Some of the happiest memories I have had was made at Cornell, and I am grateful to all who have made that possible. I cannot possibly list everyone, but it would be a huge remiss to not mention Alex Mule, Chase Funkhouser, Polina Ermoshkina, Warrick Ma, Zach Whipps, Riley Jacob, Shawn Hikosaka, Sam Stonebraker, Zach Murray, Erin Yandel, Murali Saravanan, Calvin Chen, and William Woodruff. Thank you Shawn for our monthly geopolitics discussions! A special acknowledgement to Alex, Zach, and Calvin, with whom I learned everything between mechanics and algebraic geometry.

I would like to thank friends outside of the university, who keep me sane and my life fun: Min Su, Gavin Miller, Rob Bedolfe, and Michael Rundle. Likewise, I would like to thank friends whom I have never met, but have known for almost a decade: Tommy Banks, Alex Ercolani, Andre, Joe, Elias, Dylan, Toby, Lindsay. A special acknowledgement is extended to my two oldest friends: Anh Nguyen and Vy Mai. Your company in the last fifteen years has been a source of joy, tea, and (in)stability. A debt is owed to Anh Nguyen, who has greatly improved many of my writings.

I would like to thank Út and chú Viên, who supported me through high school. I am extremely grateful to my sister, who has been a source of support and joy throughout my PhD. A special shoutout to my friend, Miso (cat), who endured much petting. At the beginning of it all, I would like to thank my grandmother, who kindled my interests in physics and astronomy. Most importantly, I am grateful to my father and mother, to whom a proper acknowledgement would take another thesis. Their unwavering support for me has been a source of motivation and joy, for which I cannot express more gratitude.

Contents

Abstract	ii
Acknowledgements	iv
Table of Contents	vi
List of Tables	viii
List of Figures	x
1 Introduction	1
1.1 Astrophysical Toolbox	2
1.1.1 Keplerian Orbits	2
1.1.2 Hamiltonian Dynamics	4
1.1.3 Numerical Simulations	7
1.2 Astronomical Phenomena	8
1.2.1 Stars and Stellar Remnants	8
1.2.2 Comets	10
1.3 This Thesis	15
2 Polluting White Dwarfs with Oort Cloud Comets	17
2.1 Introduction	18
2.1.1 Notations	20
2.2 Analytic Theory: Galactic Tide	21
2.2.1 Vertical Tide Model	21
2.2.2 Loss Cone Theory and Comet Injection Rate	22
2.2.3 Oort cloud Distribution Function	26
2.3 Analytic Theory: Companion Dynamics	27
2.3.1 Precession	27
2.3.2 Precession Barrier Efficiency	31
2.3.3 Scattering Timescale	33
2.3.4 Modified Loss Cone Theory	36

2.3.5	Timescales Comparison	39
2.4	Simulation Method	41
2.4.1	Integration Scheme	43
2.4.2	Boundary Condition	43
2.4.3	Initial Condition and Rejection Sampling	44
2.5	Numerical White Dwarf Pollution Rate	49
2.5.1	Galactic Tide Only	49
2.5.2	Efficiency of Companion-induced Precession and Scattering	50
2.5.3	Planetary-Mass Companion	51
2.5.4	White Dwarf – White Dwarf Binary	55
2.5.5	Pollution Over Time	58
2.6	Discussion	61
2.6.1	Robustness of the Oort cloud	62
2.6.2	Stellar Flybys	62
2.6.3	Surviving Stellar Evolution	63
2.6.4	Cometary Composition	64
2.6.5	Accretion Disc Delivery	65
2.6.6	Very Close Companions	65
2.6.7	Widely Separated Companions	66
2.7	Conclusion	67
3	Numerical Methods: Fast Integration and Adaptive Timestep	70
3.1	Introduction	71
3.2	The Fast Integration Method	74
3.2.1	Orbit and Force Calculations	74
3.2.2	Tests	76
3.2.3	Conclusion	82
3.3	A New Timestep Criterion for N-body Simulations	82
3.3.1	Other Timestep Criteria	84
3.3.2	Finite Floating Point Precision	85
3.3.3	New Timestepping Criterion	86
3.3.4	Tests	93
3.3.5	Conclusion	100
4	Fast Radio Bursts and Interstellar Objects	102
4.1	Introduction	103
4.2	Interstellar Objects – Neutron Stars Collision Rate	104
4.3	Emission Properties	106
4.4	Discussion	110
4.5	Conclusion	111

5 Post-Main Sequence Evolution of Cometary Volatiles	113
5.1 Introduction	114
5.2 Analytic Theory: Thermal and Ice Evolution	116
5.2.1 Thermal Evolution	117
5.2.2 Ice Evolution	123
5.3 Timescales	125
5.3.1 Cometary Timescales	125
5.3.2 Orbital Timescales	127
5.3.3 Stellar Timescales	129
5.4 Simulation Methods	132
5.4.1 N-body coupling and Inverse-square Law Timescale	132
5.4.2 Simulation Grid	133
5.4.3 Finite Difference	134
5.4.4 Approximating Sublimation and Gas Transport	136
5.4.5 Method of Lines, Timestep Limit, and Integrator Switching	141
5.4.6 A Long-term Evolution Simulation	142
5.5 Volatile Content: Kuiper Belt and Scattered Disc	146
5.5.1 Comets at Distances Less Than 1000 AU	147
5.5.2 Simulation Setup	147
5.5.3 Results	148
5.5.4 Water Retention	151
5.6 Discussion	153
5.7 Conclusion	154
6 Conclusion	156
6.1 Future Research Directions	158
Bibliography	161

List of Tables

2.1	Order of magnitude values of the dimensionless quantity α , which describes the ratio of densities between the Galaxy and the binary system (Equation 2.28).	28
2.2	Order of magnitude β values for comets with pericentre distance $q = 5a_p$. The dimensionless quantity β describes the comet's orbit relative to the companion orbit (Equation 2.29).	29
3.1	Comparison of integration walltime between the fast integration method and normal integration in seconds. The speed-up factor is the ratio of normal integration time over fast integration time. The last column compares the initial test particle's semi-major axis to the planet's. The 'Energy kicks' test case initialised test particles on parabolic orbits, so a/a_p cannot be defined. In that case, we show the initial test particle distance to that of the planet.	80
4.1	Planetesimal size distributions power-law exponents q and the resultant predicted interstellar object-neutron star collision energy distribution exponent γ , compared to the observed FRB energy distribution exponent.	109
5.1	List of symbols used and their associated SI units in this chapter.	118
5.2	List of constants in our simulation, their values, and the references to publications where these values are used and/or measured. We refer the reader to Table 5.1 for the definitions of these constants. The first half of this table are values inferred from comet properties through modelling. The second half of the table are for laboratory measured values. <i>References:</i> K75 (Klinger, 1975), K80 (Klinger, 1980), K81 (Klinger, 1981), ES83 (Ellsworth & Schubert, 1983), H06 (Huebner et al., 2006), G11 (Guilbert-Lepoutre et al., 2011), GB12 (Gundlach & Blum, 2012).	119
5.3	Parameters of long-lived radioactive isotopes. This selected list of relevant long-lived isotopes are from De Sanctis et al. (2001) with values from Carmichael (1984).	120

5.4 Constants A , B for the saturated vapour pressure (Equation 5.20) and molecule masses for H ₂ O, CO, and CO ₂ . Values of A , B are from Table 4 in Prialnik et al. (2004).	126
5.5 The orbital initial conditions and radii (top) for comets in our simulations and initial conditions common to all comets (bottom). No gas are trapped in amorphous ice (f_{CO} , f_{CO_2} zero). The dust-to-water, CO-to-water, and CO ₂ -to-water ratios are from typical values in the literature (e.g. Bockelée-Morvan et al., 2004; Huebner et al., 2006; Britt et al., 2006; Gkotsinas et al., 2024). The initial temperature is set to be 10 K.	148

List of Figures

1.1	An illustration of the orbital element angles in a Keplerian orbit (of interests are the longitude of ascending node Ω , argument of pericentre ω , and true anomaly ν or f). ω describes how the elliptical orbit points, Ω describes the rotation of such an orbit out of a plane, and ν (or f) describes the phase at which the particle is on during the orbit at some time. Original work by Lucas Snyder (username Lasunncty) at the English Wikipedia (CC BY-SA 3.0).	3
1.2	Images of comets 67P/Churyumov–Gerasimenko (top) and 1P/Halley (bottom), as visited by the spacecrafts Rosetta in 2014 and Giotta in 1986, respectively. Credit for top picture: ESA/MPAe Lindau (ESA Standard Licence). Credit for bottom picture: ESA/Rosetta/MPS for OSIRIS Team MPS/UPD/LAM/IAA/SSO/INTA/UPM/DASP/IDA (CC BY-SA 4.0).	11
1.3	ALMA’s observations of 20 protoplanetary discs. Credit: ALMA (ESO/NAOJ/NRAO), Andrews et al. (2018).	13
1.4	An illustration showing the locations of the Solar system planets, Kuiper Belt, and Oort Cloud. The Kuiper Belt is between 30-50 AU, while the Oort Cloud has semi-major axes between 3000 - 100 000 AU. Not shown here is the Scattered Disc, which is between these two populations. Credit: ESA (ESA Standard Licence).	14
2.1	Diagram illustrating the loss cone theory by Heisler & Tremaine (1986). The engulfment loss cone is in grey and comets engulfed are shown as crosses. The regime on the left of a_{crit} is the empty loss cone, on the right is the full loss cone. This figure closely follows Figure 1 in O’Connor et al. (2023).	23
2.2	Values of ζ over a grid of α and β (see Table 2.1 and 2.2 for typical values). Dashed lines are where $\zeta = 0.1, 1, 10$. In the top right corner, $\zeta \gg 1$ and Galactic tide is stronger than companion-induced precession, and vice-versa in the bottom left.	30

2.3 Efficiency of the precession barrier induced by a companion, measured from numerical simulations. Simulation values of M_p, M_*, a, a_p, q are chosen from grid values of (α, β) so that scattering does not matter. In other words, this efficiency is purely from the effects of the torque induced by a planetary companion, reducing the effectiveness of Galactic tide. The colour shows the efficiency of the planet's torque at inhibiting Galactic tide, where $N_{\text{companion}}$ is the number of comets that can enter a certain q in the existence of a companion and Galactic tide and N_{GT} is the same but there is only Galactic tide (no companion). Dashed lines show contours for $\zeta = 0.1, 1, 10$. Above the $\zeta = 10$ dashed line, the precession barrier efficiency is 0% and comets fully experience Galactic tide and can be excited to high eccentricity, migrating inward in pericentre q . Below the $\zeta = 10$ dashed line, we begin to see the precession barrier suppressing Galactic tide and the efficiency decreases. At the very bottom left point, Galactic tide is completely suppressed, and efficiency is $\sim 100\%$.	32
2.4 Numerical scattering timescales for coplanar (orange) and isotropic (blue) comets interacting with a stellar-mass (top) and planetary (bottom) companion. The analytic diffusive timescales are shown in both panels, but can only be used in the bottom panel where $M_p \ll M_*$. Blue and orange shaded areas are the range of measured numerical scattering timescales. In both cases, the high diffusive timescale flattens to the strong scattering regime (where comets are ejected within one pericentre passage with timescale $P_{\text{comet}}/2$) as the pericentre q decreases.	35
2.5 Diagram illustrating the modified loss cone theory by O'Connor et al. (2023). The engulfment loss cone is in grey, the ejection loss cone is in orange. Comets ejected are shown as plus signs and comets capable of engulfment are shown as crosses. This figure is created following closely Figure 12 in O'Connor et al. (2023).	36
2.6 Timescale comparison of Galactic tide, companion-induced precession and scattering. From the bottom panel up, these show various cases of increasing importance of companions. Timescales are measured from simulations of a Solar system-like Oort cloud ($n(a) \propto a^{-3.5}$, $a \in [3000, 10^5]$ au). The shaded area shows the 3σ spread of timescales for this particular distribution of comets.	40

2.7 A diagram to illustrate our hybrid integration scheme. The first stage is using secular Galactic tide equations of motion in (Equations 2.4, 2.5 and 2.6) to quickly integrate a comet. If a comet can be excited to $q = q_{\text{switch}} = 4a_p$, then its orbital elements are extracted to be integrated directly using REBOUND. The direct integration by REBOUND uses the full equations of motion and can include interactions with the white dwarf and its companion. A comet is extracted when its apocentre exceeds the white dwarf's Hill sphere ($Q > 0.8$ pc), when it's ejected due to interactions with a companion ($a < 0$) or when it is engulfed by the white dwarf ($d \leq 1R_\odot$, where d is the distance between the comet and the white dwarf). Integrations are stopped when the simulation time reaches $t = 1$ Gyr.	42
2.8 The broken powerlaw (Equation 2.42) and the resulting powerlaw sampling (Equation 2.20) with a powerlaw index $\gamma = 3.5$	45
2.9 The efficiency of performing rejection sampling on a broken powerlaw versus rejection sampling on a uniform distribution. We can see that using the broken powerlaw distribution to create powerlaw samples is much more effective. With the broken powerlaw rejection sampling, the number of usable samples at any particular γ is about half of the total simulated samples.	47
2.10 Accretion rate of comets into $q_{\text{crit}} = 1R_\odot$ over various Oort cloud structures γ , where $n(a) \propto a^{-\gamma}$. The mean simulation rate is shown in blue and the analytic expectation (Equation 2.18) is in red. This accretion is due solely to the effects of Galactic tide (no companion in this case). The equivalent mass accretion rate on the right is found by assuming an Oort cloud with $N_{\text{Oort}} = 10^{11}$ comets and $M_{\text{Oort}} = 2M_\oplus$. The blue shaded area shows the Poisson 1σ confidence interval of the solid blue line (mean rate).	48
2.11 Efficiency of a companion at suppressing Galactic tide and preventing comets from entering q . These are numerical results from simulations of incoming Solar system-like Oort cloud comets. The three cases here are the same as those in Figure 2.6. The values of α for each case are shown on the right side with their corresponding colours. At $q = 5a_p$, a typical value for β is $\sim 5 \times 10^7$	50
2.12 Accretion rate of comets into $q_{\text{crit}} = 1R_\odot$ over various Oort cloud structures γ , where $n(a) \propto a^{-\gamma}$. In this simulation, there is a $10M_{\text{Jup}}$ planetary companion at 10 au. The mean simulation rate is shown in blue and the analytic expectation is in red. The analytic rate in the case where there is no planet (Equation 2.18) is shown as a solid black line for comparison. The analytic prediction in the presence of a planet that can create a sufficiently strong ejection barrier (Equation 2.36) is shown as a red dashed line. The blue shaded area shows the Poisson 1σ confidence interval of the solid blue line (mean rate).	52

2.13 Distribution of accreted comets' initial semi-major axis at $\gamma = 2$. Histograms are counted per a_{initial} bin. The blue histogram shows distribution when there is Galactic tide only. The orange histogram shows the case with Galactic tide and a $10M_{\text{Jup}}$ planet. Vertical lines show $a_{\text{crit,ej}}$ (dashed) and a_{crit} (solid).	54
2.14 Accretion rate of comets into one star in a white dwarf – white dwarf binary over various Oort cloud structures γ . The binary is in a circular orbit and separated by 10 au. The pollution rate in g s^{-1} is shown on the right axis, assuming a Solar system Oort cloud.	56
2.15 Accretion rate over a 1 Gyr timescale from Oort clouds with $\gamma = 2.5$ and 3.5. There are no companions in this case. Accretion rates from simulations (red) is binned per Myr. Analytic rates are shown as horizontal blue lines. A moving average with a sliding window of 10 Myr is shown in grey. The accretion rate can be sustained over a 1 Gyr time period. An equivalent mass accretion rate on the right is found by assuming an Oort cloud with $N_{\text{Oort}} = 10^{11}$ comets and total cloud mass $M_{\text{Oort}} = 2M_{\oplus}$	59
2.16 Accretion rate over a 1 Gyr timescale from Oort clouds with $\gamma = 2.5$ and 3.5. There is a planetary-mass companion with $M_p = 10M_{\text{Jup}}$ at $a_p = 10$ au. Accretion rates from simulations (red) are binned per Myr. Analytic expectations are shown as horizontal blue lines. A moving average with a sliding window of 10 Myr is shown in grey. The accretion rate is slightly decreased over the 1 Gyr period, but no more than 0.5 dex.	60
3.1 A diagram illustrating our fast, properly time-adaptive integration method in REBOUND. There is only one particle in the simulation: the comet (red). The positions of the white dwarf and its companions (shown in grey) can be calculated analytically because they are in a 2-body system. After each simulation timestep, the forces are analytically computed and added to the acceleration of the comet particle. IAS15 is used as an adaptive timestep and is capable of resolving timesteps as: large timestep when the comet is far away (the timestep is a fraction of the comet's orbital period), and small timestep when the comet is close in (fraction of the companion's orbital period). This ensures that all close encounters are properly handled while still maintaining fast integration speed.	73

3.2 The semi-major axis (top), eccentricity (middle), and pericentre (bottom) evolution of a test particle with an initial semi-major axis at 50 000 AU and initial pericentre at 15 AU. There is a $10^{-3} M_\odot$ planet on a circular orbit at 10 AU and a $1M_\odot$ central star; there are also gravitational effects from vertical Galactic tide. The comet is started at its pericentre. The solid curve shows the results from our fast simulation method ($N = 1$ particle in the simulation), and the dashed curve shows the results from a normal REBOUND setup ($N = 3$ particles). The vertical dashed-dot line shows the initial orbital period of the comet. The fast integration method is done in 0.3 seconds walltime, whereas the usual integration method is done in 541.6 seconds.	77
3.3 $\sigma_x = \sqrt{\langle x^2 \rangle}$ is the root-mean-square change in $x = 1/a$ over one pericentre passage. The test particles start on a parabolic orbit with a pericentre q , with random longitudes of the ascending node (Ω) and periapsis (ω) drawn from a uniform distribution. The test particle's inclinations, I , are drawn from a uniform distribution in $\cos I$. Each test particle begins at a distance $200a_p$ relative to the barycentre. There are 10^4 incoming test particles, and the system has a planet at semi-major axis a_p having mass 10^{-3} that of the stellar mass. This setup is done with the fast integration method (dashed curve) and normal integration (solid curve). The results here can be directly compared with the isotropic curve in Figure 9.3 in Tremaine (2023). To produce this plot, the fast integration method takes 45.3 seconds walltime to run, while the usual integration method takes 1116.0 seconds.	79
3.4 The distribution of Kuiper Belt objects (treated as test particles) after 100 Jupiter orbital periods. The 10^4 test particles are initialised on semi-major axes are drawn uniformly between [30, 50] AU, eccentricity drawn uniformly between [0.01, 0.2], inclinations drawn from a Rayleigh distribution with mean inclination 10° , and all other angles drawn isotropically. The fast integration is done in 29.6 seconds walltime, and the normal integration is done in 155 seconds.	81
3.5 The timestep chosen by IAS15 for an Oort cloud comet encountering a planet. The dashed curve shows the timestep as originally proposed by Rein & Spiegel (2015), referred to as RS15. The solid curve is the new timestep proposed in Pham et al. (2024b) and this chapter, abbreviated as PRS23. On the top axis, we show the comet's distance, d , relative to the planet's semi-major axis, a_{planet} . To resolve the close encounter, RS15 chooses a prohibitively small timestep (~ 10 ms), which is much smaller than the pericentre timescale (dotted horizontal line, cf. Equation 3.21), effectively stalling the simulation.	83

3.6	The position y and its first 9 derivatives in the eccentric two body problem. The top panel shows the values at pericentre, the bottom panel at apocentre. We use dimensionless units in which $G = a = 1$	88
3.7	Timesteps as a function of eccentricity in an eccentric two body problem as determined by different timestepping criteria. The top panel shows the timesteps at pericentre, the bottom panel shows the timesteps at apocentre. Also shown is the pericentre timescale, defined such that it is 2π for circular orbits.	90
3.8	Same as Figure 3.7 but for hyperbolic orbits at pericentre. Because hyperbolic orbits do not have an orbital period, timesteps are shown in units of the pericentre passage timescale.	91
3.9	Relative energy error in simulations of the outer Solar System after 100 Jupiter orbits as a function of the accuracy control parameter ϵ . The blue curve shows the error in simulations using timesteps given by dt_{RS15} . The red curve shows the error in simulations using dt_{PRS23} . Also shown is the expected power law scaling for a 15th-order method.	95
3.10	Relative energy error in 24 simulations of the outer Solar system as a function of time using the default $\epsilon = 10^{-9}$. The red curves show the error in simulations using timesteps given by dt_{RS15} . The blue curves show the error in simulations using timesteps given by dt_{PRS23} . Shown in black is the scaling expecting if the simulations follow Brouwer's law.	96
3.11	Minimal timesteps used in a two body problem as a function of eccentricity e and offset from the coordinate origin \bar{y} . We work in units where $G = a = 1$. The top, middle, and bottom panels show the minimal timesteps in simulations using dt_{RS15} , dt_{A85} , and dt_{PRS23} respectively. The diagonal lines correspond to orbits around the Solar System planets whose pericentre touches the planet's surface. Simulations using dt_{PRS23} are able to accurately calculate timesteps for offsets 10^8 times larger than simulations using dt_{RS15}	97
3.12	Runtime and relative energy error in a simulation of a stellar cluster with 50 binaries. The red curves show simulations using our new dt_{PRS23} criterion which performs best in this test.	99
4.1	The CHIME Catalog 1 distribution of FRB boxcar pulse width. On the top axis, we show the equivalent planetesimal size, R , assuming tensile strength $s = 500$ Pa and density $\rho_0 = 3$ g cm $^{-3}$. Dashed vertical lines show the estimated sizes of two observed interstellar objects, 1I/'Oumuamua and 2I/Borisov. The apparent sudden cutoff in FRB pulse duration at 10 0 ms is due to CHIME's time resolution (0.983 ms, CHIME/FRB Collaboration et al., 2021).	108

5.1	The relevant timescales for the internal evolution of comets in our simulation: sublimation for CO, CO ₂ , H ₂ O crystalline ice (solid curves, τ_{subl}), gas transport to surface timescale (shaded area, τ_{gas}), crystallisation timescale (dashed dot curve, $\tau_{\text{crystallisation}}$), the bulk thermal timescale to transfer heat from the surface to a comet's centre ($\tau_{\text{thermal,bulk}}$), and the Courant-Friedrichs-Lowy timescale (τ_{CFL}). τ_{gas} strongly depends on the distance to transport and the temperature of the gas, resulting in the spread shown here. $\tau_{\text{thermal,bulk}}$ and τ_{CFL} are only shown as bars indicating their potential timescales because they are independent of temperature (they are dependent on either the size of the comet or the minimum grid cell size). For completeness, we also show the timescales of long-lived radioactive nuclides (τ_{rad} , cf. Table 5.3). This figure closely follows Figure 5.3 in Huebner et al. (2006).	128
5.2	The pericentre timescale (τ_{peri}) as a function of pericentre distance and semi-major axis. The contours outline the timescale order of magnitude value. As seen, τ_{peri} can be many orders less than the orbital period, especially for a very eccentric orbit like those from the Oort cloud (with semi-major axes between $3000 - 10^5$ AU).	130
5.3	The stellar mass loss timescale, τ_M , (top) and luminosity change timescale, τ_L , (bottom) for the last 400 Myr evolution of a $1M_\odot$ star before it becomes a white dwarf. The luminosity and mass of the star (orange curves with values corresponding to the right y-axis) are taken from the MESA Isochrones & Stellar Tracks (MIST, Dotter, 2016; Choi et al., 2016).	131
5.4	An example simulation of a 5 km Oort cloud comet with semi-major axis 20 000 AU and pericentre 3 AU. The central star is $1M_\odot$ and has a luminosity of $10^3 L_\odot$. On the left is the non-uniform, hyperbolic tangent grid used in this simulation. On the right is the temperature evolution in $\log_{10} T[\text{K}]$. The solid horizontal line shows the pericentre thermal depth ($\Delta r_{\text{thermal}}$), which is the length that heat is transported from the surface over one pericentre passage. The dashed vertical line shows the bulk thermal timescale ($\tau_{\text{thermal,bulk}}$), which is the timescale to transport heat from the surface to the centre. The streaks at the top show the increase heat from the surface from increasing stellar irradiation every time the comet approaches pericentre. As seen, the simulation is capable of properly resolving the rapidly changing surface boundary condition when this happens. After the pericentre, we can see that the heat is propagated inward.	135

5.5	The fraction of amorphous ice relative to all initial H_2O ices (top) and the same for crystalline ice (bottom) over time in a 5 km comet with semi-major axis of 30 AU, pericentre of 1 AU, around a $10^3 L_\odot$ star. The comet is initially cold (10 K uniformly throughout) and initially all H_2O are in the amorphous form. The top panel shows amorphous ice transitioning to crystalline ice. The bottom panel shows the crystallised ice layer and the ablated front near the surface where all H_2O are lost.	138
5.6	The fraction of CO_2 ice relative to initial CO_2 ice over time in a 5 km comet with semi-major axis of 30 AU, pericentre of 1 AU, around a $10^3 L_\odot$ star. The comet is initially cold (10 K uniformly throughout). The left panel shows approximation method 1 for gas sublimation-transport used in this work, the right panel shows the method by Schörghofer & Hsieh (2018) (method 2).	140
5.7	A summary of a long-term comet evolution coupled with stellar evolution. <i>Top:</i> Mass and luminosity changes during the last 400 Myr of stellar evolution for a Sun-like $1 M_\odot$ star. <i>Middle:</i> The orbital evolution of a comet around this star with an initial orbit at 400 AU and pericentre distance of 30 AU, typical of a Solar system Scattered Disc object. <i>Bottom:</i> The average internal temperature of the comet over time. As seen, the temperature is sufficiently high to sustain CO sublimation.	143
5.8	The temperature evolution over the last 400 Myr evolution of a 30 km radius comet with an initial semi-major axis of 400 AU and initial pericentre distance of 30 AU. We can observe that our numerical method properly resolves the heat transfer throughout the comet, even during the most luminous stellar evolution phases when the received stellar flux increases by 2.5 orders of magnitude over a timescale on the order of $10^2 - 10^3$ years (cf. top panel of Figure 5.9).	144
5.9	Four panels showing the evolution over the last 400 Myr of stellar evolution of amorphous H_2O ice (top left), crystalline H_2O ice (top right), CO_2 ice (bottom left), and CO ice (bottom right). All panels show the fraction of volatiles relative to their initial abundance. The comet has an initial semi-major axis of 400 AU and pericentre distance of 30 AU. Initially, all H_2O ices are in amorphous form.	145
5.10	The volatile content for CO (top) and for CO_2 (bottom) as a function of initial semi-major axis after 400 Myr of post-main sequence stellar evolution for a Sun-like star. The curves are for various comet sizes. Initially, all comets have a pericentre distance of 30 AU. This setup represents the current Solar system Kuiper Belt (shaded in grey) and Scattered Disc.	149

5.11 The volatile content for CO (top) and for CO ₂ (bottom) as a function of initial semi-major axis after 400 Myr of post-main sequence stellar evolution for a Sun-like star. The curves are for various comet sizes. Initially, all comets have circular orbits, representing comets in circular debris discs.	150
5.12 The volatile content for H ₂ O as a function of initial semi-major axis after 400 Myr of post-main sequence stellar evolution for a Sun-like star. The curves are for various comet sizes. Initially, all comets have circular orbits, representing comets in circular debris discs.	152

Chapter 1

Introduction

But, in the mean time, you defer too much to my ability in searching into this subject...If I have seen further it is only by standing on the shoulders of giants.

Isaac Newton, *Letter to Robert Hooke* (1676)

The study of planetary systems ushered in the beginning of modern astronomy and astrophysics. The field often faced challenging questions, often posed through vexing observations. These observations motivate the development of novel hypotheses and models to explain them. This began with the pioneering tabulations of the position of Solar system planets in *Astronomia Nova* ([Kepler, 1609](#)). Although these observations provided strong evidence for the heliocentric model, some questions naturally accompanied them: How to explain and predict the seemingly regular motion of the Solar system planets. In [Newton \(1687\)](#), the explanation for Keplerian orbital motion was proposed through two equations. First, in an inertial frame of reference, a massive body of mass m that experiences a force \vec{F} will have an acceleration:

$$\vec{a} = \frac{d^2\vec{r}}{dt^2} = \frac{\vec{F}}{m}. \quad (1.1)$$

Second is the law of gravitation, giving the expression of this force exerted by a point mass M at position \vec{r}_0 on a body with mass m at position \vec{r}_1 :

$$\vec{F} = G \frac{Mm}{|\vec{r}_1 - \vec{r}_0|^3} (\vec{r}_1 - \vec{r}_0) \quad (1.2)$$

where G is the gravitational constant. Solving these two equations with various techniques has yielded immense successes in the prediction of planetary motion both in the Solar system and beyond. The successful prediction and subsequent observational discovery of Neptune is a particularly triumphant achievement for Newtonian gravity. This was predicted as

observations of Uranus' orbit exhibit deviations from Newton's gravity prediction, implying that there was a missing planet ([Bouvard, 1821](#); [Le Verrier, 1846](#)).

However, by the nineteenth century, Newton's gravity formulations encountered a problem as its predictions for Mercury's orbit yield values contrary to the observations tabulated by [Le Verrier \(1843\)](#). This time, there were no missing planets and the deviations to Mercury's orbit cannot be explained. Resolving this observation requires the development of the theory of general relativity by [Einstein \(1915, 1916\)](#). Again, peculiarity in planetary observations pushed the development of theory. Although Newton's formulations have been superseded by Einstein's, they are still accurate to explain all current observations in planetary systems with the use of relativistic corrections. Therefore, it is sufficient for us to use Newtonian gravity in this thesis.

The next great observation for planetary systems came in the 1990s with the discovery of planets around other stars ([Wolszczan & Frail, 1992](#); [Mayor & Queloz, 1995](#)). These exoplanetary systems, defined as planetary systems outside of our Solar system, contain phenomena previously unimaginable, such as a planet the size of Jupiter orbiting its host star every four days. The study of novel observations from exoplanetary systems have provided theorists with many problems in the last three decades. Many of these problems remain open. These discoveries and problems begin the study of exoplanets — which is the youngest field of astrophysics while the study of Solar system planets is the oldest. This dichotomy presents a rich landscape for science, where many physics and mathematical tools from centuries of development await their theoretical predictions and applications on newly discovered exoplanetary systems.

1.1 Astrophysical Toolbox

1.1.1 Keplerian Orbits

The first of these physics and mathematical tools is the description of the Keplerian orbit. One way of parameterising an orbit is describing the moving bodies via Cartesian position and velocity ($x, y, z, \dot{x}, \dot{y}, \dot{z}$). However, this is cumbersome since all six of these variables change as an object moves. It would be better for computation (and intuition) if we can reduce the number of changing variables.

This can be done by describing the motion via the family of curves from conic sections. This formulation originates from physical observations, particularly those of [Kepler \(1609\)](#) where the author noted that the motions of planets are elliptical. In this paradigm, the orbit of a body subjected to the gravitational force of another point mass has four shapes: elliptical, parabola, hyperbola, and radial.

The radial orbit is simplest: A particle travels on a straight line directly towards or away from another particle. The elliptical orbit is a bound-orbit and can be described by six parameters: the semi-major axis (a), eccentricity (e), inclination (I), argument of

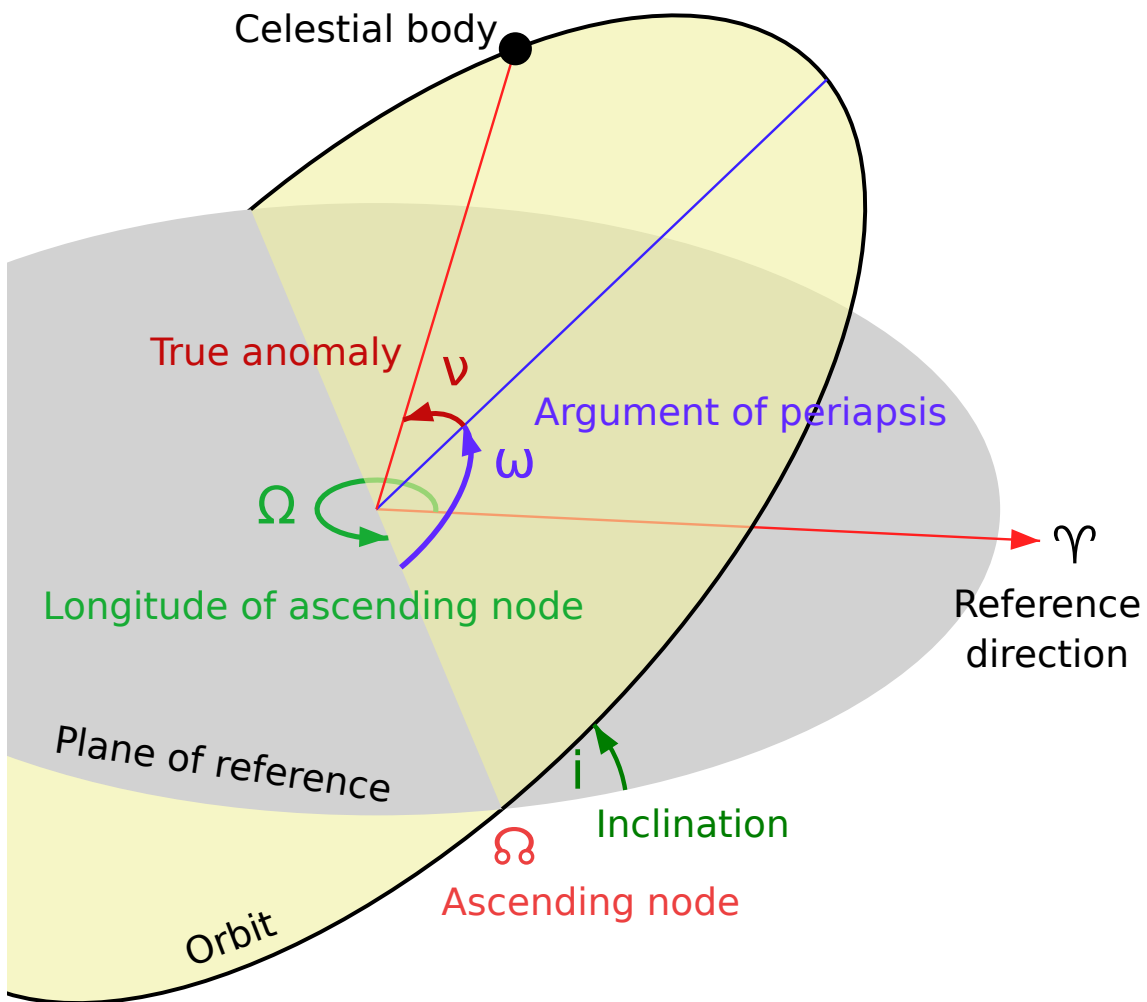


Figure 1.1: An illustration of the orbital element angles in a Keplerian orbit (of interests are the longitude of ascending node Ω , argument of pericentre ω , and true anomaly ν or f). ω describes how the elliptical orbit points, Ω describes the rotation of such an orbit out of a plane, and ν (or f) describes the phase at which the particle is on during the orbit at some time. Original work by Lucas Snyder (username Lasunncty) at the English Wikipedia (CC BY-SA 3.0).

pericentre (ω), longitude of the ascending node (Ω), and the true anomaly (ν or f , both are used in thesis). Figure 1.1 shows how these orbital elements define an ellipse. An elliptical orbit has values between $0 \leq e < 1$; at $e = 0$, the orbit is circular. The closest distance between the two bodies in a Keplerian orbit is called the pericentre distance (also called the perigee, perihelion, periapsis depending on the context) and the furthest distance is called the apocentre (apogee, apohelion, apoapsis). Over a Keplerian orbit, the parameters a, e, I, ω, Ω are constant while only the true anomaly f changes between $[0, 2\pi]$. We have now accomplished our goal of reducing six varying Cartesian elements to only one varying Keplerian element that can describe all bound orbits. The motion of asteroids, comets, planets or even another star in a planetary system can be described by these orbital elements for an elliptical orbit. In contrast, the parabolic and hyperbolic orbits are unbound. Some notable characteristics are their semi-major axes are either undefined (for parabolic orbit) or negative (for hyperbolic orbits), and their eccentricities have values $e \geq 1$. Objects on parabolic or hyperbolic orbits have at most one close approach to the other point mass, and then they travel to infinity unless there is a perturbation to their orbit caused by another body. These unbound orbits describe the motion of interstellar objects, such as 1I/'Oumuamua, which visited the Solar system in 2017 and then left.

1.1.2 Hamiltonian Dynamics

The second helpful physics tool is Hamiltonian dynamics (Hamilton, 1833). Although the Newtonian formulation of force-acceleration can be tremendously helpful to describe the Keplerian motion of one or two massive particles, it can become intractable when there are three or more particles. In fact, making advances to the N-body problem (where $N > 2$) has been the major problem since Newton. To analytically study the motion of more than two massive particles, it is more advantageous to use Hamiltonian dynamics. We refer the reader to textbooks, such as Tremaine (2023), for a deeper discussion on Hamiltonian dynamics. For our purpose, the Hamiltonian of a test particle around a body with mass M is:

$$H = H_K(\vec{r}, \dot{\vec{r}}) = \frac{1}{2}\dot{\vec{r}}^2 - \frac{GM}{|\vec{r}|} \quad (1.3)$$

where we used Cartesian elements to describe the Keplerian orbit. Then, one can apply Hamilton's equations to describe the Keplerian motion of the particle (e.g., see Tremaine, 2023):

$$\frac{d\vec{r}}{dt} = \frac{\partial H}{\partial \dot{\vec{r}}} \quad (1.4)$$

$$\frac{d\dot{\vec{r}}}{dt} = -\frac{\partial H}{\partial \vec{r}}. \quad (1.5)$$

If the particle is subjected to another potential, $\Phi(\vec{r}, t)$, from another mass (or masses), then the Hamiltonian can simply be modified to be

$$H(t, \vec{r}, \dot{\vec{r}}) = H_K(\vec{r}, \dot{\vec{r}}) + \Phi(\vec{r}, t) \quad (1.6)$$

and Hamilton's equations can be re-applied to find the new perturbed equations of motion. This simple formulation makes Hamiltonian dynamics a powerful tool. However, a caveat here is that not all variables can be used; only canonical variables can be used with Hamilton's equations. In this example, we can use the Cartesian elements $(\vec{r}, \dot{\vec{r}})$ because they are canonical. Unfortunately for us, the intuitive and helpful set of Keplerian orbital elements is not canonical.

Delaunay Elements

Now, we are back to find a set of variables that can describe orbits, but now they must be canonical like Cartesian elements, while also not quickly varying like Keplerian elements. Delaunay elements satisfy these requirements. They are a set of canonical variables and their relationships to Keplerian elements are:

$$\begin{aligned} \Lambda &= \sqrt{GMa} & l \\ L &= \sqrt{GMa(1 - e^2)} & \omega \\ L_z &= \sqrt{GMa(1 - e^2)} \cos I & \Omega \end{aligned} \quad (1.7)$$

where l is the mean anomaly. Like the true anomaly previously mentioned, the mean anomaly describes the phase during the orbit and also ranges between $[0, 2\pi]$. An intuitive understanding of why these variables are canonical conjugates of each other is as follows. If we only have a circular orbit, the only meaningful way to identify a point on a circle is through the pair (a, l) . The semi-major axis (equivalent to the circle's radius in this case) gives the distance while the mean anomaly gives the location on the circle. Thus, we have the variable Λ (which is proportional to a) being the conjugate variable to the angle l . Now, we increase the degree freedom by allowing the circle to become an ellipse. To describe the ellipse, we require the eccentricity to describe the “stretched” circle (cf. Figure 1.1). However, this stretched ellipse now also have a direction where the stretch is oriented. To describe the orientation of our ellipse, we now need ω . This describes the second pair of variables L and ω . Note that when we only have a circle, there is no preferred direction and ω would be ill-defined. Finally, if we allow our orbit to tilt up and down with an inclination I , we must further describe how that plane is oriented by the variable Ω . This completes our set of variables with the last pair (L_z, Ω) .

It can be shown through Newton's laws that the quantity $L = \sqrt{GMa(1 - e^2)}$ actually corresponds to the magnitude of the angular momentum of the orbit (e.g., see in [Tremaine](#),

2023). Likewise, L_z is the z component of the orbital angular momentum vector. Λ is sometimes called the circular angular momentum because it is the magnitude of the angular momentum if the orbit was circular. In fact, given a semi-major axis a , Λ is the maximum angular momentum that an orbit could have (as a potentially confusing corollary, the circular orbit has the most angular momentum). Because (Λ, L, L_z) have the same units as momentum and (l, ω, Ω) are all angles between $[0, 2\pi]$, these sets of variables are called action-angle variables.

Furthermore, the three variables (Λ, L, L_z) all correspond to conserved quantities. Λ is proportional to the orbital energy of a body ($E = -GM/2a$), which is conserved for the two-body problem. Likewise, the angular momentum L are conserved in the two-body problem. In the presence of perturbations to the central potential, these quantities can vary, leading to richer dynamical behavior. The conservation of L_z comes from the axisymmetry of the potential. That is, given a potential that is invariant (does not change) under a continuous rotation about the z axis, L_z is conserved by Noether's theorem. Since axisymmetry is more common than full spherical symmetry in celestial mechanics, it is common for Λ and L to be perturbed while L_z remains conserved. Finally, note that the total energy and total angular momentum of a closed N-body gravitational system can also be shown to be conserved, corresponding to continuous symmetry in time (potential is invariant under time translation) and rotation (invariant under rotation), respectively.

Perturbations to Orbits

Of course, the interesting dynamics arise when there are perturbations to the orbit. For example, perturbations from the background Milky Way Galaxy, from other planets, or from the fact that planets are not point-masses. Working in Hamiltonian dynamics allows us to identify the variables that change due to these perturbations and variables that are conserved. The procedure is typically as follows: Write the Hamiltonian for the system with perturbations, identify the angles in the Hamiltonian, if an angle exists in the Hamiltonian, then the corresponding conjugate momenta is not conserved. For example, if we have a Hamiltonian of the form $H = H(\omega, L, L_z)$, then Λ, L_z are conserved while L will change. This can be seen by applying Hamilton's equations to the Hamiltonian. Furthermore, because Λ, L_z are conserved but L is not, the semi-major axis a is conserved, while the eccentricity and inclination are exchanged. This is the behaviour underlying some well-known dynamics phenomena like the von Zeipel-Lidov-Kozai effect (von Zeipel, 1910; Lidov, 1962; Kozai, 1962).

If the perturbations to the Delaunay actions are slow, then we call these secular evolutions. Here, slow means the change occurs over many orbits. When perturbations are secular, we are interested in studying how the shapes of orbits change over a long time. Because we are no longer interested in exact positions, we can average out the quickly changing variable l to simplify the equations of motion. Averaging over l is called orbit-averaging

and takes the form:

$$\langle X \rangle = \int_0^{2\pi} \frac{dl}{2\pi} X = (1 - e^2)^{3/2} \int_0^{2\pi} \frac{df}{2\pi} \frac{X}{(1 + e \cos f)^2} \quad (1.8)$$

for some quantity X that we would like to average over an orbit. In the second equality, we show the orbit-averaging over true anomaly instead of over mean anomaly. We refer the reader to [Tremaine \(2023\)](#) for some other commonly-used orbit-averaging results.

1.1.3 Numerical Simulations

The third tool to understand the evolution of orbits is the computer. Although computers are recent, computation has long been used to predict the motion of planetary bodies. For example, [Halley \(1705\)](#) used Newton's laws to find the gravitational perturbations of Jupiter and Saturn on the orbits of comets. At the centre of this endeavour has been to solve the differential equations comprising of Newton's laws when there are many massive bodies. To do this, numerical integration is employed to estimate the value of the resulting definite integral. The goal is to calculate the new position and velocities of bodies after some timestep dt : The smaller the timestep, the better the integral estimate. Many strategies (integrators) have been developed to perform this integration more efficiently and with better error (e.g., [Euler, 1768](#); [Runge, 1895](#); [Kutta, 1901](#); [Hairer & Wanner, 1999](#); [Hairer et al., 2006](#)).

An important class of integrator is the symplectic integrator. The goal of symplectic integrators is to find numerical solutions to Hamilton's equations, such that under time evolution the canonical coordinates are volume-preserving in phase space. Preserving canonical coordinates' phase-space volume is preferred because the trajectory flow in Hamiltonian systems are constrained. Specifically, the Liouville theorem proves that phase-space volumes are conserved by Hamiltonian flow. Integrators that are not symplectic may not follow Hamiltonian trajectories as well as those specifically built to do so. A consequence of this is that energy is conserved by symplectic integrators in each timestep (and by Noether's theorem, we also have time-reversibility). Since most systems in our interests can be written as a Hamiltonian, symplecticity is desirable. Some well-known examples of symplectic integrators are the leapfrog integrator, which can be traced to [Newton \(1687\)](#), and the Wisdom-Holman integrator ([Wisdom & Holman, 1991, 1992](#)).

With the advent of computers, early works jumped to use these machines to numerically solve the Solar system's N-body problem (e.g. [Eckert, 1951](#); [Cohen & Hubbard, 1965](#); [Cohen et al., 1973](#); [Newhall et al., 1983](#)) culminating in project LONGSTOP ([Roy et al., 1988](#)). With computer simulations, there have been continued interests in minimising error to ensure simulation accuracy through developing and improving integrators (e.g., [Rein & Tamayo, 2015](#); [Rein & Spiegel, 2015](#)). There are two main sources of errors: truncation and round-off. Truncation error arises because we no longer have a continuous Hamiltonian

system in time, but rather discretised jumps in timestep dt . Round-off error arises because computers do not have infinite precision and their number representation cannot represent real numbers. Round-off error is inevitable and naturally accumulates over each integration timestep. Truncation error can be minimised by choosing a small timestep dt . Thus, choosing the correct timestep dt to advance the dynamical state of simulations is also an important area of study. Choosing an overly large timestep causes numerical inaccuracy, while choosing an overly small timestep introduces significant computational cost. A rule of thumb is that the timestep dt must be a small fraction of the particle's orbital period:

$$\tau_{\text{period}} = 2\pi \sqrt{\frac{a^3}{GM}}. \quad (1.9)$$

However, this is no longer appropriate if there are any close-encounters between particles, such as when comets approach close to the Earth.

1.2 Astronomical Phenomena

The astrophysics introduced so far have wide-ranging applications to explain the observations spanning many domains in astronomy. In this section, we discuss the two extreme ends of objects in the Universe: the largest and densest objects (stars and their remnants) and the smallest and least dense objects (comets).

1.2.1 Stars and Stellar Remnants

Perhaps one of the first intriguing astronomical observations for humanity is our closest star, the Sun. Stars can have wide-ranging masses, spanning four orders of magnitude. The smallest stars are red dwarfs, with masses as low as $0.08M_\odot$ [mass of the Sun]. The largest stars can have masses on the order of $100M_\odot$. All stars are supported by fusion to provide pressure counteracting gravity, this is called hydrostatic equilibrium. The internal structure of stars can be quite diverse, strongly depending on their mass. The amount of mass a star has largely controls the interplay between temperature and fusion, radiation and gas pressures, all of which affects how luminous a star can be and the length of its main-sequence lifetime. Likewise, the various fates of stars are largely dependent on their mass¹.

Neutron Stars

For example, extremely massive stars ($\gtrsim 30M_\odot$) can directly collapse in black holes. Other massive stars (masses between $10\text{-}20 M_\odot$) eventually becomes neutron stars. At the end of

¹Note that the mass estimates here can be quite different if there is binary evolution (i.e. there is another companion star), for example, see [Belczynski & Taam \(2008\)](#). This is not uncommon since in fact most (massive) stars are in a binary and even higher-order systems ([Moe & Di Stefano, 2017](#)).

these stars' evolution, they experience a supernova, ejecting the majority of their mass. Left behind is a stellar remnant called a neutron star. Neutron stars are supported by neutron degeneracy pressure — a quantum mechanical effect — and no longer have fusion. They are extremely dense, having a radius ~ 10 km and a mass of $\sim 1.4M_{\odot}$. There is much on-going research into the equations of state for neutron stars, such as structure (Lattimer & Prakash, 2004; Fraga et al., 2016) and their associated phenomenology. Neutron stars have been attributed to several astronomical phenomena, such as pulsars (cf. Bell Burnell, 2017) and potentially even fast radio bursts (Thompson et al., 2002). A pulsar is a rotating neutron star with a strong magnetic field which emits strong beams of electromagnetic radiation. Observed from Earth, these beams can emit regular “pulses” on periods as fast as milliseconds. It was the timing of these pulsar that led to the first discovered exoplanetary system in Wolszczan & Frail (1992). Another phenomenon is fast radio bursts, which is a class of radio transient event first detected by Lorimer et al. (2007). These events typically occur in the gigahertz frequency band and usually occurs on millisecond-timescales. The radiation emission mechanism(s) of fast radio bursts remains an active field of subject, but most current consensus place neutron stars at the centre of all these processes (cf. Thompson et al., 2002; Platts et al., 2019). In particular, recent efforts by Nimmo et al. (2025) using scintillometry have constrained that the emission process for fast radio bursts is likely to have originated from within the magnetosphere of a central compact object, such as a neutron star.

White Dwarfs

In contrast, stars like the Sun will eventually expand into a red giant with radius potentially reaching as far as the Earth. Then, the Sun will then subsequently undergo a Helium flash, when the luminosity released is 5000 times its current luminosity, and evolve through the asymptotic giant branch, when the luminosity again reaches high values. Towards the end of this process, the star loses 40% of its mass by shedding away its outer layers of gas. Left behind where the giant star was will be an object the size of the Earth, but still has about 60% the mass of the Sun. This object is called a white dwarf, which is the end state of most stars in the Universe. White dwarfs are dense, supported by electron degeneracy pressure and have no nuclear fusion, slowly radiating their heat away (and consequently, decreases in temperature over time). They have a very strong surface gravity and is expected to have a thin atmosphere containing only Hydrogen and Helium, with all heavier elements rapidly sinking into the core.

Interestingly, observations found that 25-50% of white dwarf atmosphere spectra show signs of elements heavier than Helium (van Maanen, 1917; Zuckerman et al., 2003; Koester et al., 2014; Wilson et al., 2019; Blouin & Xu, 2022)². Because of the fast sinking timescale,

²One of the first discovered white dwarfs (van Maanen, 1917) was actually a polluted one, showing Fe, Ca, Mg in its atmosphere. However, because of these metal lines, the author classified the star as an F-star.

these source of these “pollutants” must have recently been or is currently being delivered to the white dwarf. It is generally agreed that bodies from the surrounding evolved planetary system are supplying materials to white dwarfs. Since this pollution is systemic and they show the composition of the parent polluting body, studying polluted white dwarfs allow us to use them as cosmic spectrometers to study the composition of planetary bodies outside the Solar system (Putirka & Xu, 2021; Xu & Bonsor, 2021). Some open questions remain: Where do polluting bodies come from and how are they delivered into white dwarfs?

1.2.2 Comets

General Properties

We now turn our attention to the smallest and least dense³ objects in a planetary system. Comets are small bodies (also referred to as planetesimals), with radii between 1-100 km, having low density on the order of $\sim 0.5 \text{ g cm}^{-3}$. They are aggregates of dust, H₂O ices, CO ice, CO₂ ice, and many other volatile species (Bockelée-Morvan et al., 2004; Huebner et al., 2006). Even amino acids have been found in comets (Elsila et al., 2009). These properties of comets have been found either through observations from Earth or through spacecrafts sent to probe comets, such as the recent mission by Rosetta to visit comet 67P/Churyumov–Gerasimenko. Figure 1.2 shows the images of two comets as taken by visiting spacecrafts. In the same Figure, we observe that comets have highly irregular shapes. This is because they are not massive enough for self-gravity to make them spherical.

Comets can be quite difficult to detect when they are far away (Inno et al., 2025). This is because they have a low albedo (they do not reflect a lot of light), and they reflect light from the Sun weakly where their brightness scales as $\propto r^{-4}$ as viewed from Earth. This is because light from the Sun decreases in flux by a factor r^{-2} to reach the comet, and decreases by another factor of r^{-2} to reach back to the Earth. However, when they approach close to the Sun during a pericentre passage for an eccentric orbit, the solid volatile ices rapidly sublimate and outgas, creating coma tails (see bottom panel of Figure 1.2). These coma tails have been readily observed from Earth since ancient times, and are continued to be scientifically studied to analyse the composition of comets.

In the Solar system, there are a few populations of comets, traditionally classified as (Tremaine, 2003): Jupiter-family comets (those with period < 20 years), Halley-type comets ($20 \text{ years} < \text{period} < 200 \text{ years}$), and long-period comets (period > 200 years). Long-period comets can be further classified into three populations: the Kuiper Belt (semi-major axis between 30-50 AU, mostly circular orbits), the Scattered Disc (semi-major axis between 50-3000 AU, highly eccentric orbits with pericentre distance at 30-40 AU), and the Oort Cloud (semi-major axis between 3000-100 000 AU). Figure 1.4 illustrates the Kuiper Belt and Oort Cloud in context of the Solar system planets. There is another population of

³The typical density of a comet ($\sim 0.5 \text{ g m}^{-3}$) would allow it to float on water (density of water being $\sim 1 \text{ g m}^{-3}$).

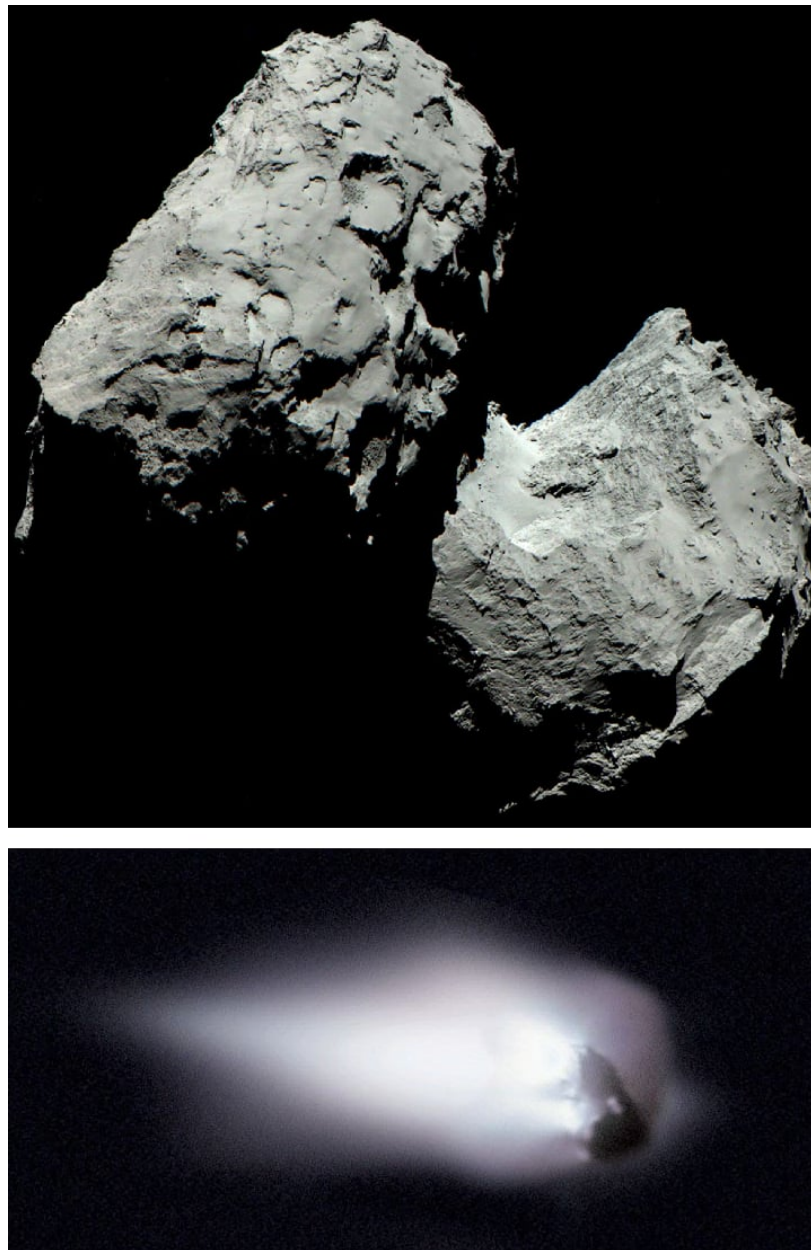


Figure 1.2: Images of comets 67P/Churyumov–Gerasimenko (top) and 1P/Halley (bottom), as visited by the spacecrafts Rosetta in 2014 and Giotta in 1986, respectively. Credit for top picture: ESA/MPAe Lindau (ESA Standard Licence). Credit for bottom picture: ESA/Rosetta/MPS for OSIRIS Team MPS/UPD/LAM/IAA/SSO/INTA/UPM/DASP/IDA (CC BY-SA 4.0).

comets: those that are unbound from planetary systems. These are interstellar objects, which are comets and asteroids that have been ejected from planetary systems during their early formation when they interact with giant planets. So far, three interstellar objects have been detected as they visit the Solar system. Studying the origin, kinematics, composition of interstellar objects is a new field of research.

The Formation of Comets

We now discuss the formation of comets and their various reservoirs. A planetary system is formed through protoplanetary discs, many of which have been observed by telescopes like ALMA (e.g., [Andrews et al., 2018](#)). These discs are composed of gas, dust, and volatiles like H₂O, CO₂, CO and many other molecules. Observations of protoplanetary discs by ALMA are shown in Figure 1.3 (from Figure 3 in [Andrews et al., 2018](#)). In this Figure, we can observe that at the centre of a protoplanetary disc is the newly formed protostar. At distances close to the protostar, the disc temperatures are high and the volatiles we mentioned are sublimated. Further out, a distance can be identified as the “ice line” ([Sasselov & Lecar, 2000](#)), which is the location at which the temperature is low enough for water ice to stably exist (the sublimation temperature for water ice is 180 K). By calculating the temperature due to solar flux at various distances, estimates put ice line of the Solar system’s protoplanetary disc at about a few AUs ([Sasselov & Lecar, 2000](#)). As they are composed of many species of volatiles, comets are believed to have formed beyond the ice line. Comets are formed as dust (with volatile ices on them) grains from the protoplanetary disc clump together ([Armitage, 2007](#)), forming the aggregate of materials that we know as comets today. As mentioned, these aggregates can have wide range of sizes, with radii from 1 up to 100 km.

The formation location of comets put them in the neighbourhood where planets are also forming. Planets often migrate in protoplanetary discs through interactions with the gas disc ([Armitage, 2007; Rein, 2011](#)). This movement often causes planets to interact gravitationally with comets. Note that planets can also migrate after the protoplanetary disc has dispersed its gas through dynamical instabilities from planet-planet interactions (e.g., [Obertas et al., 2017](#)). One dynamical scenario is the so-called Nice model ([Morbidelli et al., 2005; Tsiganis et al., 2005; Gomes et al., 2005](#)), where Uranus and Neptune migrated and switched places with each other in the early Solar system. Comets play several roles in the Nice model. First, those that remain are the ones that avoided the trajectory of these moving giant planets. This would form the Kuiper Belt (see [Morbidelli & Nesvorný, 2020](#), for a review on the Kuiper Belt), which is a population of comets (and even some minor planets) at distances of 30 - 50 AU, which is right outside the orbit of Neptune. This can be seen in the illustration in Figure 1.4. Second, those that have interacted with the planets but are still bound to the Solar system form the Scattered Disc and the Oort cloud. The Scattered Disc population have much higher semi-major axes as mentioned, but have

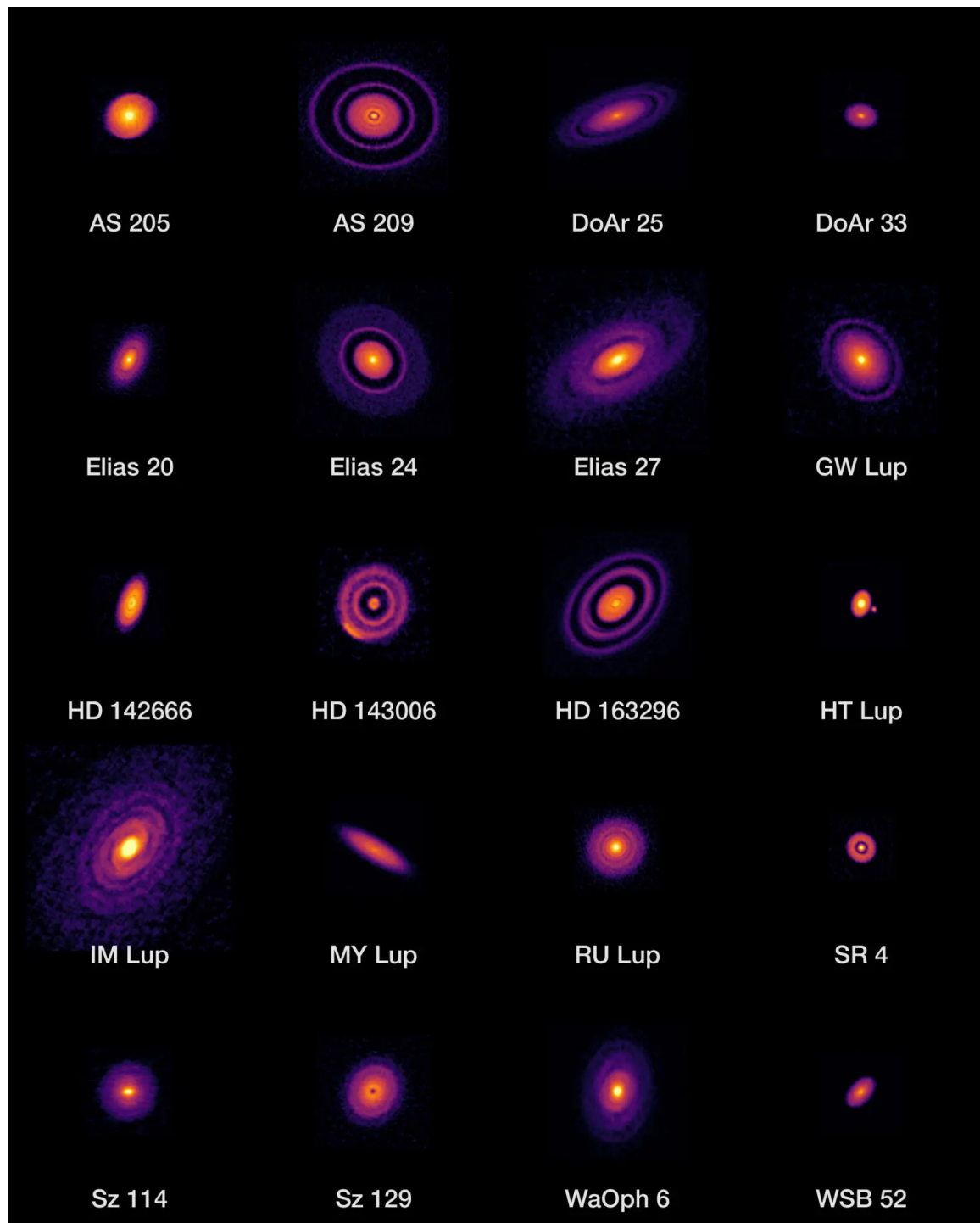


Figure 1.3: ALMA's observations of 20 protoplanetary discs. Credit: ALMA (ESO/NAOJ/NRAO), [Andrews et al. \(2018\)](#).

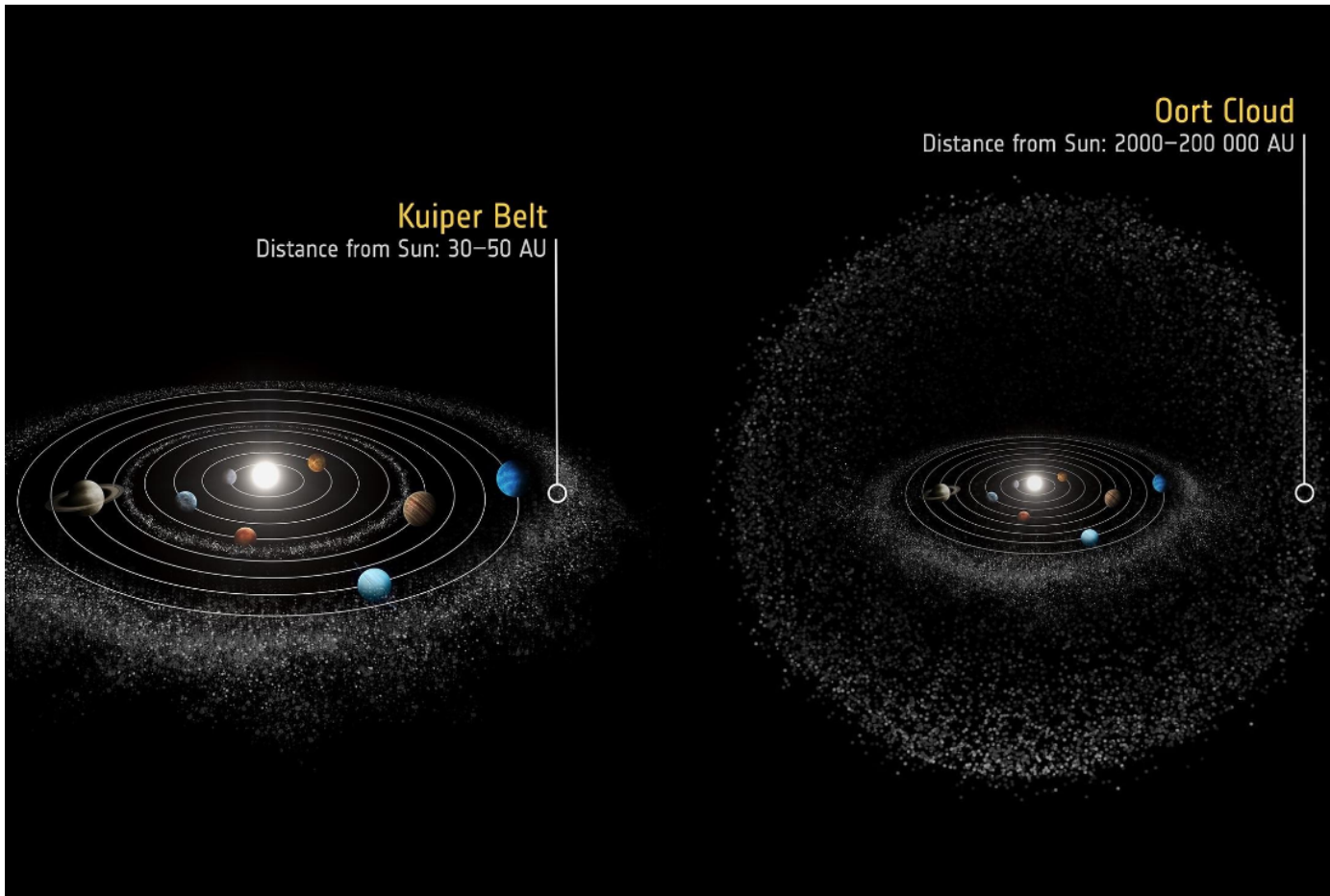


Figure 1.4: An illustration showing the locations of the Solar system planets, Kuiper Belt, and Oort Cloud. The Kuiper Belt is between 30-50 AU, while the Oort Cloud has semi-major axes between 3000 - 100 000 AU. Not shown here is the Scattered Disc, which is between these two populations. Credit: ESA (ESA Standard Licence).

a low pericentre distance at 30-40 AU (e.g., [Vokrouhlický et al., 2019](#)). This is because Keplerian orbits are closed, and thus the Scattered Disc comets keep return to where they were kicked, preserving their low pericentre distance. Note that these are Scattered Disc comets with pericentres beyond Neptune because those with pericentres near Neptune would be ejected after multiple encounters. The Oort cloud is the most distant reservoir of comets. Oort cloud objects do not all have highly eccentric orbits like those in the Scattered Disc. This is because they are at such great distances that the gravitational influences from the Milky Way (called the Galactic tide) becomes important. This becomes a cosmic tug-of-war between the Sun and the Galaxy, the consequence being that a comet cloud is formed ([Heisler & Tremaine, 1986](#)). From simulations by [Duncan et al. \(1987\)](#), Oort cloud comets are believed to be isotropically distributed (there are comets in every direction pointing away from the Sun), and is “thermalised” (they have all values of eccentricities ranging from 0 to 1). Third, many comets are ejected from the Solar system when they interacted with the migrating planets ([McGlynn & Chapman, 1989](#)). This would have populated the interstellar objects where the Sun was formed (['Oumuamua ISSI Team et al., 2019](#)). Fourth, some of these scattered comets have highly eccentric or hyperbolic orbits and can enter the inner Solar system to collide with Earth. Since comets are rich in H₂O and other volatiles (which are depleted in the protoplanetary disc at Earth’s distance), one popular idea for Earth’s large water content is that they came from early comet collisions (e.g., [Gomes et al., 2005](#)). Finally, since planet migration is not unique to the Solar system ([Rein, 2012](#)), it is not unreasonable to expect various populations of comets as a natural byproduct of planet formation in most exoplanetary systems. These debris discs are expected to ubiquitous and bountiful reservoirs of materials ([Sefilian et al., 2021, 2023](#)).

1.3 This Thesis

The current field of exoplanets have many open problems, ranging from understanding planet formation, orbital dynamics and evolution, atmospheres, detection techniques, geochemistry, to astrobiology. These planetary systems and their peculiarity renew questions that have long troubled humanity: How did we get here and are we alone? That being said, these questions are not the subject of this thesis. Rather, this thesis will contribute to the question of what will happen to planetary systems in the far future through analytic theories and development of numerical methods.

In Chapter 2, the hypothesis that Oort cloud comets can be delivered from tens of thousands AU to pollute white dwarfs is investigated. The dynamics of Oort cloud objects as they experience the Galactic tide and companion dynamics are characterised through analytical and numerical means. Then, through simulations, we find that Oort clouds like the one in the Solar system will have enough materials for pollution and can deliver those materials into white dwarfs at a constant rate over billions of years. The results are

discussed in context of volatiles-poor and volatiles-rich polluted white dwarf observations, and the retention of Oort cloud objects after the post-main sequence stellar evolution.

In Chapter 3, we present the new numerical integration scheme that allows the fast integration of a massive number of Oort cloud objects. This integration method is tested in a variety of settings and we found that it allows simulation speed up between 5-1800 times, depending on the case. Then, we find a new criterion for estimating the timestep dt in N-body simulations. This criterion is adaptive, and can change the timestep as a particle has a close-encounter or is travelling far away. We find that our criterion is less susceptible to floating-point error and improves the performance of N-body simulations in a variety of contexts.

In Chapter 4, we turn our attention a more distant source of small bodies — interstellar objects — to collide with a much smaller stellar core — neutron stars. Instead of producing pollution signals on neutron stars, we propose that collisions of small bodies like comets with neutron stars would create an energy outburst. This mechanism could potentially be a progenitor to fast radio bursts. In this chapter, we calculate the cosmic collision rate of interstellar objects and neutron stars and compare that with fast radio burst rates over cosmic time. We also compare the size distribution of small bodies to energy distribution of fast radio bursts. Finally, we discuss the fast radio bursts event morphology and where they should be found if our hypothesis holds.

In Chapter 5, we return to white dwarf pollution, but now focusing on the volatile content on comets during the post-main sequence stellar evolution stage. First, we develop a numerical code capable of tracking volatiles evolution for highly eccentric comets around a highly luminous post-main sequence star. Our numerical code couples stellar, gravitational, thermal, and mass evolution. Then, we use this code to study how the Kuiper Belt, Scattered Disc, and circular debris discs at varying distance would retain or lose volatile content over the last 400 Myr of intense stellar evolution. We discuss our results in context of the future Solar white dwarf pollution and for proposed debris disc reservoirs in the literature.

Chapter 6 summarises the findings of this thesis. Finally, we discuss the interesting prospects for future research on the long-term evolution of comets in the Solar system and beyond.

Chapter 2

Polluting White Dwarfs with Oort Cloud Comets

The motions of the comets are exceedingly regular, and are governed by the same laws with the motions of the planets...for comets are carried with very eccentric motions through all parts of the heavens indifferently...

Isaac Newton, *Scholium Generale in Principia* (1687)
translated by Motte

The following text, as well as its associated figures and tables, was published in the Monthly Notices of the Royal Astronomical Society, Volume 530, Issue 3, pp. 2526-2547 as Pham & Rein (2024). Hanno Rein is the co-author in this publication.

Abstract

Observations point to old white dwarfs accreting metals at a relatively constant rate over 8 Gyrs. Exo-Oort clouds around white dwarfs have been proposed as potential reservoirs of materials, with Galactic tide as a mechanism to deliver distant comets to the white dwarf's Roche limit. In this work, we characterise the dynamics of comets around a white dwarf with a companion having semi-major axes on the orders of 10 - 100 au. We develop simulation techniques capable of integrating a large number (10^8) of objects over a 1 Gyr timescale. Our simulations include Galactic tide and are capable of resolving close-interactions with a massive companion. Through simulations, we study the accretion rate of exo-Oort cloud comets into a white dwarf's Roche limit. We also characterise the dynamics of precession and scattering induced on a comet by a massive companion. We find that (i) white dwarf pollution by an exo-Oort cloud can be sustained over a Gyr timescale, (ii) an exo-Oort

cloud with structure like our own Solar system's is capable of delivering materials into an isolated white dwarf with pollution rate $\sim 10^8 \text{ g s}^{-1}$, (iii) adding a planetary-mass companion reduces the pollution rate to $\sim 10^7 \text{ g s}^{-1}$, and (iv) if the companion is stellar-mass, with $M_p \gtrsim 0.1M_\odot$, the pollution rate reduces to $\sim 3 \times 10^5 \text{ g s}^{-1}$ due to a combination of precession induced on a comet by the companion, a strong scattering barrier, and a low-likelihood of direct collisions of comets with the companion.

2.1 Introduction

Between 25 to 50 per cent of white dwarf atmospheres observed are polluted with heavy metals (e.g., [Zuckerman et al., 2003, 2010](#); [Koester et al., 2014](#); [Wilson et al., 2019](#)). It is generally believed that the heavy metals of polluted white dwarfs come from its evolved planetary system, such as exomoons, exoplanets or exo-asteroid belts, through a variety of mechanisms which induce destabilisation in these sources (e.g., [Debes & Sigurdsson, 2002](#); [Debes et al., 2012](#); [Mustill et al., 2014](#); [Smallwood et al., 2018](#); [Maldonado et al., 2020](#); [Trierweiler et al., 2022](#); [O'Connor et al., 2022](#)). The bodies must be delivered to the white dwarf Roche radius at $\sim 1R_\odot$ to be tidally disrupted for pollution (e.g., [Veras & Heng, 2020](#)).

Observations of old polluted white dwarfs (those with cooling age older than 1 Gyr) found accretion rates ranging five orders of magnitude between 5×10^5 to 10^{10} g s^{-1} ; the mean pollution rate is around 10^7 g s^{-1} with about a 1 dex spread (e.g., [Blouin & Xu, 2022](#); [Johnson et al., 2022](#); [Cunningham et al., 2022](#)). The current minimum detection limit is about a few 10^5 g s^{-1} ([Koester et al., 2014](#)). [Blouin & Xu \(2022\)](#) also find that the white dwarf accretion rate decreases by no more than one order of magnitude over 8 Gyr. Thus, their observational findings require a reservoir and mechanism that can deliver materials in the white dwarf's Roche radius over such long timescales.

The chemical composition of accreted materials can be analysed to study the original reservoir of the accreted bodies. Until now, a few dozen white dwarfs have been followed up spectroscopically to measure their element abundances ([Jura & Young, 2014](#)). The majority of polluted white dwarfs exhibit compositions resembling the bulk Earth. This suggests that the sources of materials polluted white dwarfs must be rocky in nature ([Jura, 2006](#); [Jura & Xu, 2012](#); [Xu et al., 2017](#); [Doyle et al., 2019](#); [Trierweiler et al., 2023](#)). There are observations of polluted white dwarf atmospheres with volatiles, although they are more rare ([Farihi et al., 2013](#); [Klein et al., 2021](#); [Doyle et al., 2021](#)). At present, there is one observation of a polluted white dwarf with an icy body composition ([Xu et al., 2017](#)). Because the majority of observations point to rocky materials as a source, the Oort cloud has often been ruled out as a reservoir for white dwarf pollution.

The Oort cloud is a byproduct of Solar system formation, where planetesimals are either ejected or kicked into high semi-major axes via interactions with a giant planet

(Vokrouhlický et al., 2019; Kaib & Volk, 2022). For objects kicked into higher semi-major axes, they can be circularised by Galactic tide or stellar flybys (Duncan et al., 1987; Hahn & Malhotra, 1999; Higuchi & Kokubo, 2015; Vokrouhlický et al., 2019). These objects form the Solar system’s Oort cloud, which is a structure containing $10^{11} – 10^{12}$ objects with a total mass of $\sim 2M_{\oplus}$ with semi-major axes ranging between 3 000 au to 100 000 au (e.g., Weissman, 1983; Boe et al., 2019).

Since the Solar system’s Oort cloud is a byproduct of interactions of planetesimals with planets, it is not unreasonable to expect Oort clouds to exist around other main-sequence and even white dwarf planetary systems. As a result, several studies have investigated if the Oort cloud is a suitable reservoir for pollution. They often employ a mix of numerical and analytic methods to study the pollution rate of Oort cloud comets. Mechanisms considered consist of Galactic tidal effects, stellar flybys, white dwarf natal kicks and stellar mass loss during post-main-sequence evolution (Alcock et al., 1986; Parriott & Alcock, 1998; Veras et al., 2014; Stone et al., 2015; Caiazzo & Heyl, 2017). In the literature of simulations of comets in to a $1R_{\odot}$ tidal radius around white dwarfs, we are not aware of any that can resolve the pollution rate over time due to being resolution limited in the number of simulated comets. Most recently, O’Connor et al. (2023) perform an extensive analytic and numerical study on the effects of Galactic tide, planetary perturbations, white dwarf natal kicks and stellar mass loss on the pollution rate of white dwarfs with exo-Oort clouds as a source of materials. They find that combining these effects together points to an accretion rate of a few 10^5 g s^{-1} , which is just at or slightly below the detection limit. They argue that this is potentially why we do not observe many volatiles-rich polluted white dwarf atmospheres.

In this thesis, we contribute to this existing line of investigation by answering the following question through numerical simulations: Can an Oort cloud similar to the one we have in the present-day Solar system pollute a white dwarf over a Gyr timescale? We also investigate this question in cases where the white dwarf has a planetary-mass or a stellar-mass companion. Since we currently have no knowledge of extrasolar Oort clouds, we simply assume throughout this work that other Oort clouds have the total number of objects and total mass like the current Solar system Oort cloud. We also study how various Oort cloud powerlaw density profiles affect pollution. All of our results can be easily scaled to another Oort cloud with different masses, number of objects, and density profiles.

We start by presenting the analytic theory of white dwarf pollution through Galactic tide and white dwarf companion (planet or star). Specifically, in Section 2.2, we summarise the analytic vertical Galactic tide model (Heisler & Tremaine, 1986), the loss cone theory, leading to the expected analytic pollution rate as predicted by O’Connor et al. (2023). In Section 2.3, we study additional dynamics comets experience when there is a companion. Specifically, we analyse the dynamics of Galactic tide together with precession and scattering induced by a companion. We also summarise the loss cone shielding model proposed by

O’Connor et al. (2023) leading to a prediction of the white dwarf pollution rate in the presence of a companion in that framework.

In Section 2.4, we describe our simulation methodology which is capable of integrating a large number of comets (10^8 comets) over a long time (1 Gyr), initial conditions, and boundary conditions.

In Section 2.5, we present pollution rate over various Oort cloud structures, in the presence of Galactic tide only. Then, we present the pollution rate in the presence of a stellar companion, and in the presence of a planetary companion. Finally, we show the pollution rate over a 1 Gyr timescale. In Section 2.5, we also compare and discuss our results with analytic expectations from O’Connor et al. (2023).

In Section 2.6, we discuss the advantages and major concerns of using an Oort cloud as a potential reservoir for white dwarf pollution, such as if an Oort cloud can survive post-main-sequence evolution and that the majority of observed white dwarfs are volatiles-poor. We also discuss our results in contexts of observations of close-in binaries and wide binaries. In Section 2.7, we summarise our findings.

2.1.1 Notations

In this chapter, we denote M_* as the white dwarf mass. We denote the orbital elements of a comet as: a for the semi-major axis, e for eccentricity, I for inclination, ω for argument of pericentre, Ω for longitude of ascending node, and l for mean anomaly. Orbital elements ω and I are measured relative to the Galactic plane. Some other quantities used to describe the comet orbits are: q for the pericentre distance, Q for the apocentre distance, and P for the orbital period. The comet is assumed to be a mass-less test particle. Orbital elements with the subscript p denote that they are the orbital elements for the white dwarf companion (e.g., M_p is the companion mass). We also regularly use the following set of Delaunay action-angle variables (quantities Λ , L , L_z are actions in units of specific angular momentum, and l, ω, Ω are angles):

$$\begin{aligned} \Lambda &= \sqrt{GM_*a} & l \\ L &= \Lambda\sqrt{1-e^2} & \omega \\ L_z &= L \cos I & \Omega \end{aligned} \tag{2.1}$$

Λ is referred to as the circular angular momentum, L as the angular momentum, and L_z as the z component of the angular momentum.

We use the terms ‘exo-Oort cloud’ and ‘Oort cloud’ interchangeably. An exo-Oort cloud is presumed to start at the inner semi-major axis edge, a_1 , ends at a_2 , follows a powerlaw number density profile $n(a) \propto a^{-\gamma}$, has N_{Oort} comets and a total cloud mass M_{Oort} .

When referring to our own Solar system’s Oort cloud, we state ‘Solar system Oort cloud’ explicitly. In the Solar system, estimates for N_{Oort} typically range between $10^{11} - 10^{12}$

comets (e.g., [Francis, 2005](#); [Boe et al., 2019](#)). We assume $N_{\text{Oort}} = 10^{11}$ in this chapter. It is estimated that $M_{\text{Oort}} \sim 2M_{\oplus}$ for the Solar system Oort cloud, which we will use as our fiducial value. In addition, numerical simulations show that the Solar system Oort cloud has a powerlaw exponent $\gamma = 3.5$ (e.g., [Duncan et al., 1987](#); [Higuchi & Kokubo, 2015](#); [Vokrouhlický et al., 2019](#)). Note that the total mass of the Solar system Oort cloud is also quite uncertain from simulations and observations of incoming long-period comets (e.g., [Weissman, 1983](#); [Boe et al., 2019](#)).

2.2 Analytic Theory: Galactic Tide

2.2.1 Vertical Tide Model

[Heisler & Tremaine \(1986\)](#) study how the Galactic tide affects Oort cloud comets through an analytic model. There are three main assumptions used in their model. First, the star-comet system moves in a circular orbit around the Galaxy.

Second, the most important component of the Galactic tidal force is in the z direction. z is defined as the direction orthogonal to the Galactic midplane, with the midplane defined at $z = 0$. Note that because of the way z is defined in our coordinate system, the inclination I and argument of pericentre ω are measured relative to the $x - y$ plane parallel to the Galactic midplane, instead of the usual measurement relative to the ecliptic (cf. [Heisler & Tremaine, 1986](#); [Tremaine, 2023](#)). All I and ω used throughout this chapter follow this convention. In the Solar system, the second assumption is valid since Galactic tidal terms in the x and y components are about one order of magnitude lower than the z term. Since observations of polluted white dwarfs are typically within the Solar neighbourhood, the second assumption is likewise not unreasonable to apply in nearby white dwarf planetary systems.

Third, the Galactic tidal potential experienced by the comet is approximated as the potential inside a homogeneous slab with constant density ρ_0 . The parameter ρ_0 is the averaged background density of gas and stars in the Galaxy. As a star system orbits around the Galaxy, it oscillates up and down the Galactic midplane. As a result, ρ_0 also varies over time. Following previous works (e.g., [Heisler & Tremaine, 1986](#); [O'Connor et al., 2023](#); [Tremaine, 2023](#)), we adopt an averaged fiducial value of $\rho_0 = 0.1M_{\odot} \text{ pc}^{-3}$ ([Holmberg & Flynn, 2000](#); [McKee et al., 2015](#)).

The Galactic potential with these assumptions can be written as ([Heisler & Tremaine, 1986](#)):

$$\Phi_{\text{GT}} = 2\pi G\rho_0 z^2. \quad (2.2)$$

This potential can be averaged over the orbit of the comet and then written in Delaunay elements as:

$$\langle \Phi_{\text{GT}} \rangle = \frac{\pi\rho}{GM_*^2} \left(\frac{\Lambda}{L} \right)^2 (L^2 - L_z^2)(L^2 + 5(\Lambda^2 - L^2) \sin^2 \omega) \quad (2.3)$$

from which we find the secular (orbit-averaged) equations of motion by applying Hamilton's equations:

$$\left\langle \frac{dL}{dt} \right\rangle_{\text{GT}} = -\frac{5\pi G\rho}{(GM_*)^2} \left(\frac{\Lambda}{L}\right)^2 (L^2 - L_z^2)(\Lambda^2 - L^2) \sin(2\omega) \quad (2.4)$$

$$\left\langle \frac{d\omega}{dt} \right\rangle_{\text{GT}} = \frac{2\pi G\rho}{(GM_*)^2} \left(\frac{\Lambda}{L}\right)^2 \left[\left(\frac{L_z^2}{L} (L^2 + 5(\Lambda^2 - L^2) \sin^2 \omega) \right) + (L^2 - L_z^2)(L - 5L \sin^2 \omega) \right] \quad (2.5)$$

$$\left\langle \frac{d\Omega}{dt} \right\rangle_{\text{GT}} = \frac{2\pi G\rho}{(GM_*)^2} \left(\frac{\Lambda}{L}\right)^2 L_z (L^2(5 \sin^2 \omega - 1) - 5\Lambda^2 \sin^2 \omega). \quad (2.6)$$

\dot{L}_{GT} and $\dot{\omega}_{\text{GT}}$ are coupled differential equations. The phase space evolution described by these coupled equations is studied in detail in [Heisler & Tremaine \(1986\)](#); [Tremaine \(2023\)](#). Briefly, they show that through these equations of motion, the comet can oscillate in the (L, ω) phase space due to Galactic tide. There are two conserved Delaunay elements. Λ is conserved because the mean anomaly is not in $\langle \Phi_{\text{GT}} \rangle$ due to orbit averaging. Thus, the comet's semi-major axis is conserved under the secular Galactic tidal effect. Similarly, L_z is conserved because Ω is not in $\langle \Phi_{\text{GT}} \rangle$. Since L_z is conserved but L is not conserved, this implies that the Galactic tide can excite the comet to very high eccentricity by exchanging eccentricity with inclination. This inclination-eccentricity exchange is periodic and is analogous to the von Zeipel-Lidov-Kozai mechanism ([von Zeipel, 1910](#); [Lidov, 1962](#); [Kozai, 1962](#)), where the Galaxy itself acts as the third body.

2.2.2 Loss Cone Theory and Comet Injection Rate

[Heisler & Tremaine \(1986\)](#) study the injection rate of Oort cloud comets into the Solar system. To do so, they use the Galactic tide equations of motion, together with the loss cone theory framework as proposed by [Lightman & Shapiro \(1977\)](#). Without perturbations from a planetary companion, this can be used to estimate the rate of Oort cloud comets capable of being excited to any arbitrarily small pericentre distance.

First, we describe Oort cloud comets by a distribution function f , defined as the number of comets per volume of phase space:

$$dN_{\text{Oort}} = f(\Lambda, L, L_z, \omega, \Omega, l) d\Lambda dL dL_z d\omega d\Omega dl. \quad (2.7)$$

Following previous works ([Heisler & Tremaine, 1986](#); [Wiegert & Tremaine, 1999](#); [O'Connor et al., 2023](#)), the distribution function is integrated over angles, assuming a spherical distribution of comets. This is motivated by observations in long-term Solar system Oort cloud simulations that the Oort cloud is spherically symmetric (e.g., [Duncan et al., 1987](#);

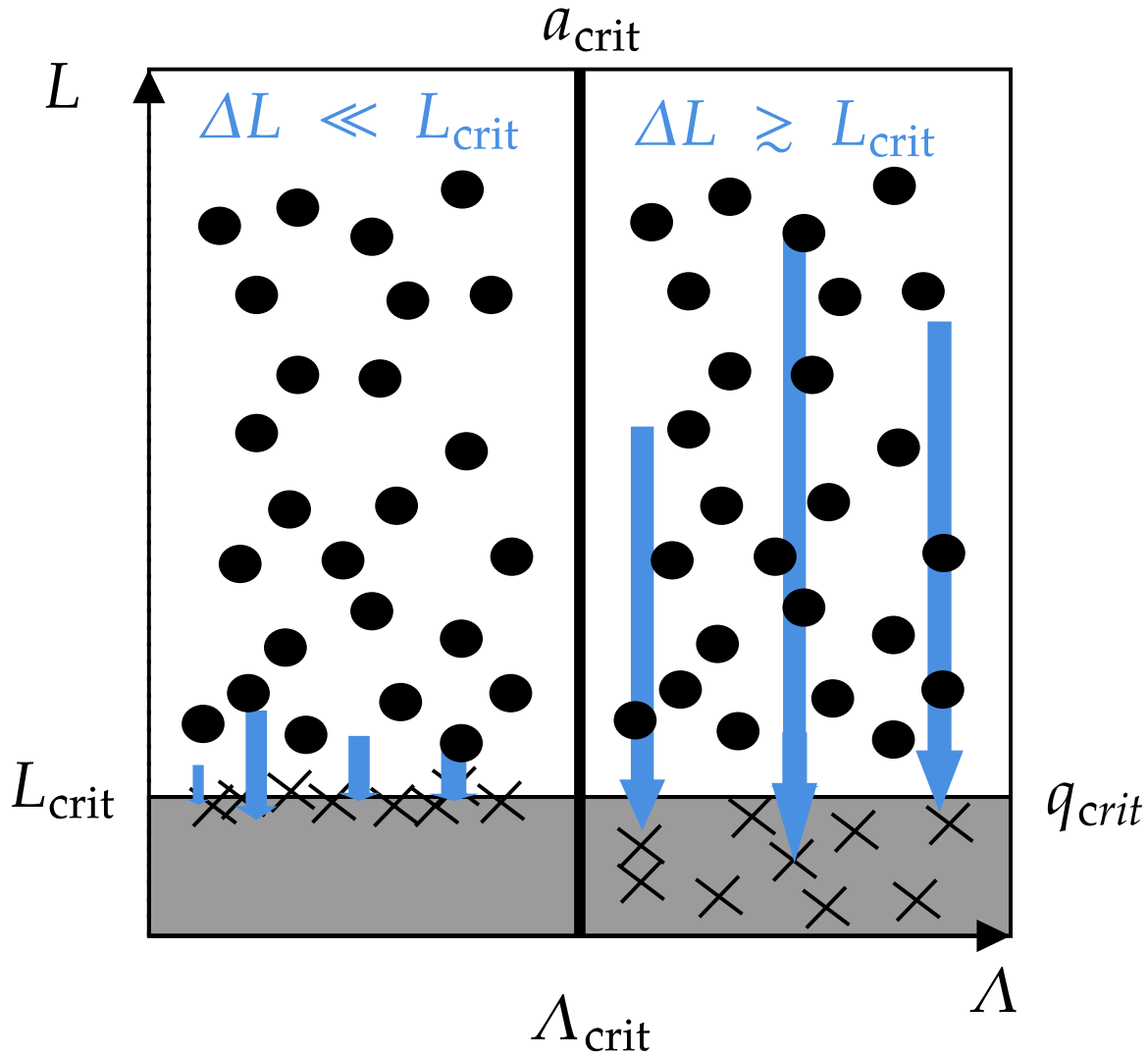


Figure 2.1: Diagram illustrating the loss cone theory by [Heisler & Tremaine \(1986\)](#). The engulfment loss cone is in grey and comets engulfed are shown as crosses. The regime on the left of a_{crit} is the empty loss cone, on the right is the full loss cone. This figure closely follows Figure 1 in [O'Connor et al. \(2023\)](#).

Vokrouhlický et al., 2019).

$$\begin{aligned} dN_{\text{Oort}} &= f(\Lambda, L) dL d\Lambda \int_{-L}^L dL_z \int_0^{2\pi} d\omega \int_0^{2\pi} d\Omega \int_0^{2\pi} dl \\ &= (2\pi)^3 f(\Lambda, L) \cdot 2L dL d\Lambda \end{aligned} \quad (2.8)$$

where $\int dN_{\text{Oort}} = N_{\text{Oort}}$ with N_{Oort} as the total number of comets in the Oort cloud. With this description of the Oort cloud, we can proceed to find the pollution rate.

In the white dwarf pollution case, we are interested in the rate of comets that can be excited to $q = q_{\text{crit}} = 1R_{\odot}$, the fiducial Roche limit of a white dwarf that we adopt. At this distance, we assume that a comet will be tidally disrupted by the white dwarf.

For comets with high eccentricity, $e \lesssim 1$, the angular momentum can be related to the pericentre distance q as:

$$L \approx (2GM_*q)^{1/2}. \quad (2.9)$$

Through this, we define a critical angular momentum once a comet has achieved a certain critical pericentre distance q_{crit} :

$$L_{\text{crit}} \equiv (2GM_*q_{\text{crit}})^{1/2}. \quad (2.10)$$

The loss cone is defined as the phase space region where $L \leq L_{\text{crit}}$. This is the tidally-disrupted loss cone. Once a comet enters this loss cone, we assume it is removed from the Oort cloud (because it is tidally disrupted).

Comets can be injected into the loss cone in two regimes: the filled and empty loss cones, depending on their semi-major axis a (or equivalently, Λ). Intuitively the dependency on a is because these two regimes depend on how strong the Galactic tide can affect a comet. In one case the Galactic tide induces small changes in angular momentum ΔL over multiple orbits, slowly migrating a comet inward in q over many orbits. This is the empty loss cone case. In the other case, the Galactic tide is sufficiently strong to induce a large ΔL and the comet is capable of reaching the loss cone within one orbit. This is the filled loss cone case. Figure 2.1 (following Figure 1 in O'Connor et al., 2023) is a diagram illustrating these two regimes.

First, we consider the empty loss cone case, which happens when:

$$\Delta L \leq L_{\text{crit}} \quad (2.11)$$

where the angular momentum change induced by the Galactic tide over one orbit can be estimated by:

$$\Delta L \sim |dL/dt| \times P. \quad (2.12)$$

It has been shown by Heisler & Tremaine (1986) that the comet injection rate in the empty

loss cone regime, Γ_e (dimension of number of comets per unit Λ per unit time) is:

$$\Gamma_e(\Lambda) d\Lambda = \frac{160\pi^3 G\rho_0}{3} \frac{L_{\text{crit}}\Lambda^4}{(GM_*)^2} f(\Lambda, L_{\text{crit}}) d\Lambda \quad (2.13)$$

where $L_{\text{crit}} \ll \Lambda$ (highly eccentric orbit). Γ_e is found by using Equation 2.4 and calculating the rate at which comets are pushed into the loss cone boundary at L_{crit} .

Next, we consider the filled loss cone case when:

$$\Delta L \geq L_{\text{crit}}. \quad (2.14)$$

In this case, the injection rate for the filled loss cone, Γ_f (same dimension as Γ_e) is:

$$\Gamma_f(\Lambda) d\Lambda = 4\pi^2 (GM_*)^2 \frac{L_{\text{crit}}^2}{\Lambda^3} f(\Lambda, L_{\text{crit}}) d\Lambda \quad (2.15)$$

where Γ_f is found by dividing the number of comets inside the loss cone by the comets' orbital period (because these comets are lost within one orbit). Note that the subscript f here denotes ‘full’, not the distribution function f .

The loss cone is empty at small a and full at large a . The transition between the two cases can be found by equating the two rates, $\Gamma_e = \Gamma_f$, yielding:

$$\begin{aligned} a_{\text{crit}} &= \left(\frac{3}{20\sqrt{2}\pi} \frac{M_*}{\rho_0} q_{\text{crit}}^{1/2} \right)^{2/7} \\ &\approx 10\ 500 \text{ au} \cdot \left(\frac{M_*}{0.6M_\odot} \right)^{2/7} \left(\frac{\rho_0}{0.1M_\odot \text{ pc}^{-3}} \right)^{-2/7} \left(\frac{q_{\text{crit}}}{1R_\odot} \right)^{1/7}. \end{aligned} \quad (2.16)$$

When $a < a_{\text{crit}}$, a comet is in the empty loss cone regime. When $a \geq a_{\text{crit}}$, it is in the full loss cone regime. In Delaunay variables, these conditions are equivalent to $\Lambda < \Lambda_{\text{crit}}$ and $\Lambda \geq \Lambda_{\text{crit}}$ with

$$\Lambda_{\text{crit}} \equiv (GM_* a_{\text{crit}})^{1/2}. \quad (2.17)$$

The total injection rate (number of comets entering a certain q_{crit} per unit time) can be found by adding up the two injection rates, integrated over Λ :

$$\Gamma_{\text{total}} = \int_{\Lambda_1}^{\Lambda_{\text{crit}}} \Gamma_e(\Lambda) d\Lambda + \int_{\Lambda_{\text{crit}}}^{\Lambda_2} \Gamma_f(\Lambda) d\Lambda \quad (2.18)$$

where $\Lambda_1 = (GM_* a_1)^{1/2}$ and $\Lambda_2 = (GM_* a_2)^{1/2}$, with a_1 the inner semi-major axis edge of the Oort cloud and a_2 the outer edge.

Finally, since $\Gamma_e \propto a^2 f(a)$, the injection rate per unit Λ increases from a_1 to a_{crit} . On the other hand, $\Gamma_f \propto a^{-3/2} f(a)$, the injection rate per unit Λ decreases from a_{crit} to a_2 . At a_{crit} , $\Gamma_e = \Gamma_f$. Since the injection rate increases until a_{crit} and then decreases, the majority of the total injection rate is contributed from the region around a_{crit} .

2.2.3 Oort cloud Distribution Function

Now, we find the explicit form of the distribution function f . First, for a dynamically relaxed distribution, the distribution is ‘thermal’ and the distribution in e^2 is uniform (Jeans, 1919; Ambartsumian, 1937). This ‘thermal’ distribution of Oort cloud comets is seen after long-term simulations of Solar system Oort cloud (cf. Figure 7 in Vokrouhlický et al., 2019). In this case, $f = f(\Lambda)$ is independent of L . We can further simplify by integrating over $L = \sqrt{GM_*a(1-e^2)}$ which is now uniform between $[0, (GM_*a)^{1/2}] = [0, \Lambda]$:

$$dN_{\text{Oort}} = (2\pi)^3 f(\Lambda) d\Lambda \int_0^\Lambda 2L dL = (2\pi)^3 f(\Lambda) \Lambda^2 d\Lambda. \quad (2.19)$$

By definition, for a spherically distributed shell with width $[a, a + da]$, we also have:

$$dN_{\text{Oort}} \equiv n(a) dV = n(a) \cdot 4\pi a^2 da \quad (2.20)$$

where $n(a)$ is the number density profile of comets.

Before finding $f(\Lambda)$ through these equations, we first choose $n(a)$. Long-term simulations of the Solar system Oort cloud find that our own Oort cloud generally follows a powerlaw density profile (e.g., Duncan et al., 1987; Higuchi & Kokubo, 2015; Vokrouhlický et al., 2019):

$$n(a) \propto a^{-\gamma} \quad (2.21)$$

where $a \in [a_1, a_2]$, with a_1 and a_2 as the inner and outer semi-major axis edge of an Oort cloud. Following O’Connor et al. (2023), we consider $2 \leq \gamma \leq 4$ in this chapter, with $\gamma = 3.5$ as a fiducial value for a Solar system-like Oort cloud.

With a description of $n(a)$, we can find the distribution function $f(\Lambda)$ by equating the two relations for dN (O’Connor et al., 2023):

$$f = f(\Lambda) = \begin{cases} CN_{\text{Oort}}(\Lambda/\Lambda_1)^{3-2\gamma} & , \Lambda_1 \leq \Lambda \leq \Lambda_2 \\ 0 & , \text{otherwise} \end{cases} \quad (2.22)$$

where Λ_1 and Λ_2 are the circular angular momenta associated with a_1 and a_2 . C is the normalisation constant:

$$C = \frac{8\pi}{(2\pi)^3} \cdot \begin{cases} (\gamma - 3) (4\pi\Lambda_1^3 (1 - (\Lambda_1/\Lambda_2)^{2\gamma-6})^{-1} & , \gamma \neq 3 \\ (8\pi^3\Lambda_1^3 \ln(\Lambda_2/\Lambda_1))^{-1} & , \gamma = 3 \end{cases}. \quad (2.23)$$

Equipped with the distribution function $f(\Lambda)$, it is possible to find the total comet injection rate Γ_{total} (dimension of number of comets per unit time) by substituting $f(\Lambda)$ and integrating Equation 2.18. With Γ_{total} , we can also predict the pollution rate (i.e. in

g s^{-1}) into a white dwarf:

$$\dot{M}_Z = \Gamma_{\text{total}} \cdot \frac{M_{\text{Oort}}}{N_{\text{Oort}}}. \quad (2.24)$$

2.3 Analytic Theory: Companion Dynamics

In this section, we refer to a companion in a binary system with the white dwarf as planetary if it has mass $M \leq 10^{-2} M_{\odot} = 10 M_{\text{Jup}}$, or stellar if it has mass $M \geq 10^{-1} M_{\odot}$.

In section 2.3.1, we analyse the effects of companion-induced precession on a comet with semi-major axis a and pericentre q from a companion with mass M_p on a circular orbit at semi-major axis a_p . Companion-induced precession is compared against Galactic tide-induced precession. In section 2.3.2, we study the efficiency of precession at preventing comets' migration due to Galactic tide through simulations.

2.3.1 Precession

Galactic tidal effects can be suppressed by angular momentum change induced by a companion, which is also accompanied by an apsidal precession. We compare the apsidal precession rates, $\dot{\omega}$, induced by Galactic tide and companion to study when each effect is dominant. In our case, we consider the regime where $q \geq a_p$ — no orbit crossings occur and the companion must be interior to the comet.

With secular forcing by a companion, a comet experiences apsidal precession (at the quadrupole order) at a rate (Farago & Laskar, 2010)¹:

$$\langle \dot{\omega}_p \rangle = \frac{M_p M_*}{(M_* + M_p)^2} \cdot \left(\frac{a_p}{a} \right)^{7/2} \cdot \frac{3n_p}{8(1 - e^2)^2} \cdot (5 \cos^2 \Delta I - 1) \quad (2.25)$$

where n_p is the companion's mean motion and ΔI is the mutual inclination between the comet and companion. This is a secular interaction, integrated over orbital motions of both companion and comet. There are higher order terms to $\dot{\omega}_p$ (the next non-zero term occurs at the hexadecapole order, see Palacián & Yanguas, 2006; Vinson & Chiang, 2018), which become important as $q \rightarrow a_p$. However, for our analysis in this section, the quadrupolar term is sufficient to give an estimate. When we require numerical results for $\dot{\omega}_p$ (Figure 2.6), $\dot{\omega}_p$ is measured numerically and is not limited by this approximation.

Galactic tide likewise induces apsidal precession (Equation 2.5). Companion-induced precession begins to dominate that of Galactic tide when these rates are comparable:

$$\zeta \equiv \left| \frac{\langle \dot{\omega}_{\text{GT}} \rangle}{\langle \dot{\omega}_p \rangle} \right| \sim 1. \quad (2.26)$$

¹Gauß was first to notice that this apsidal precession rate is equivalent to that of a test particle induced by the quadrupole moment of a homogeneous ring with mass $M_* M_p / (M_* + M_p)$ and radius a_p (cf. Touma et al. (2009) and references therein).

Table 2.1: Order of magnitude values of the dimensionless quantity α , which describes the ratio of densities between the Galaxy and the binary system (Equation 2.28).

α	$M_p [M_\odot]$	$M_* [M_\odot]$	$M_{\text{reduced}} [M_\odot]$	$a_p [\text{au}]$
10^{-14}	0.6	0.6	0.3	10
10^{-13}	10^{-1}	0.6	10^{-1}	10
10^{-12}	10^{-2}	0.6	10^{-2}	10
10^{-10}	0.6	0.6	0.3	200
10^{-9}	10^{-1}	0.6	10^{-1}	200
10^{-8}	10^{-2}	0.6	10^{-2}	200

Precession in the argument of pericentre ($\Delta\omega$) accompanies angular momentum change (ΔL). That is, the companion also induces a change in angular momentum, suppressing the angular momentum change from Galactic tide and inhibiting further migration in pericentre q .

Expanding ζ to first order in q/a (the high eccentricity limit, $e \sim 1$) and taking the order of magnitude terms, we find:

$$\zeta \sim \frac{32\pi\sqrt{2}}{3} \cdot \alpha \cdot \beta \simeq 50 \cdot \alpha \cdot \beta \quad (2.27)$$

where we defined two dimensionless quantities α and β .

α is the ratio of densities between the Galaxy and the binary system:

$$\begin{aligned} \alpha &\equiv \frac{\rho_0}{M_{\text{reduced}}/a_p^3} \\ &\approx 10^{-9} \cdot \left(\frac{\rho_0}{0.1 M_\odot \text{ pc}^{-3}} \right) \left(\frac{M_{\text{reduced}}}{10^{-2} M_\odot} \right)^{-1} \left(\frac{a_p}{100 \text{ au}} \right)^3 \end{aligned} \quad (2.28)$$

where $M_{\text{reduced}} = M_* M_p / (M_* + M_p)$ is the reduced mass. As α becomes smaller, $\rho_0 \ll M_{\text{reduced}}/a_p^3$, we expect the effects of the binary to be stronger than that of Galactic tide.

β compares the orbit of a comet to the companion's orbit:

$$\begin{aligned} \beta &\equiv \left(\frac{q}{a_p} \right)^{3/2} \left(\frac{a}{a_p} \right)^{7/2} = (1 - e)^{3/2} \cdot \left(\frac{a}{a_p} \right)^5 \\ &\approx 10^7 \cdot \left(\frac{q}{a_p} \right)^{3/2} \left(\frac{a}{10^4 \text{ au}} \right)^{7/2} \left(\frac{a_p}{100 \text{ au}} \right)^{-7/2}. \end{aligned} \quad (2.29)$$

Higher β means that the comet experiences less torque from the companion. β is mostly dominated by a/a_p . When a comet has a large orbit compared to the companion ($a \gg a_p$), it spends most of its orbital time far from the companion and thus, receives less torque. β is large in this case. There is also a dependence on q (or equivalently, on the eccentricity

Table 2.2: Order of magnitude β values for comets with pericentre distance $q = 5a_p$. The dimensionless quantity β describes the comet's orbit relative to the companion orbit (Equation 2.29).

β	a_p [au]	q [au]	a [au]
10^{11}	10	50	10^4
10^8	100	500	10^4
10^7	200	1000	10^4

e). As a comet migrates inward due to Galactic tide, the orbit becomes more eccentric, e increases, q decreases and thus β also decreases.

Typical values of α and β are shown in Tables 2.1 and 2.2. In table 2.1, typical scenarios are evaluated: white dwarf – white dwarf binary, white dwarf – M dwarf, and white dwarf – large giant planet. Table 2.2 shows cases where the comet pericentre is at $q = 5a_p$. This is chosen because here, scattering is generally weaker compared to both precession and Galactic tide (see Figure 2.6). A comet semi-major axis of 10^4 au is chosen because this is typical for incoming comets. In both tables, we give sample values for a close-in companion at $a_p = 10$ au and a wider companion at $a_p = 100 - 200$ au.

Figure 2.2 shows ζ on a grid of α and β . The dashed lines show the contours where $\zeta = 0.1, 1, 10$. Near and below $\zeta = 1$, we expect companion-induced precession to be stronger than Galactic tide; that is, precession can overcome Galactic tide and suppress inward migration. We confirm the analytic values of ζ through simulations measuring the torque a comet experiences due to only Galactic tide and only companion-induced precession.

For close companions at $a_p = 10$ au, we have $\beta > 10^{11}$. In this case, to have precession dominates tide by making $\zeta \lesssim 1$, we require $\alpha < 10^{-13}$, which can be supplied by a stellar-mass companion with mass $M_p \geq 0.1M_\odot$ as shown in Table 2.1. However, a planetary-mass companion does not provide sufficient torque to overcome the Galactic tide. For more distant companions at $a_p = 100 - 200$ au, the same conclusions can be reached through their values of ζ . Therefore, a stellar-mass companion ($M_p \geq 0.1M_\odot$) is required to produce a precession barrier, which reduces the efficiency of Galactic tide delivering comets from an exo-Oort cloud.

Limitations

We note that there are four limitations when using ζ :

1. $\dot{\omega}_p$ as shown in Equation 2.25 is only valid for $q \geq a_p$; that is, a comet must be strictly exterior to companion.
2. We only use the quadrupole term for $\dot{\omega}_p$. As q approaches a_p , contributions from higher order terms become important. Thus, ζ should not be used when $q \approx a_p$.

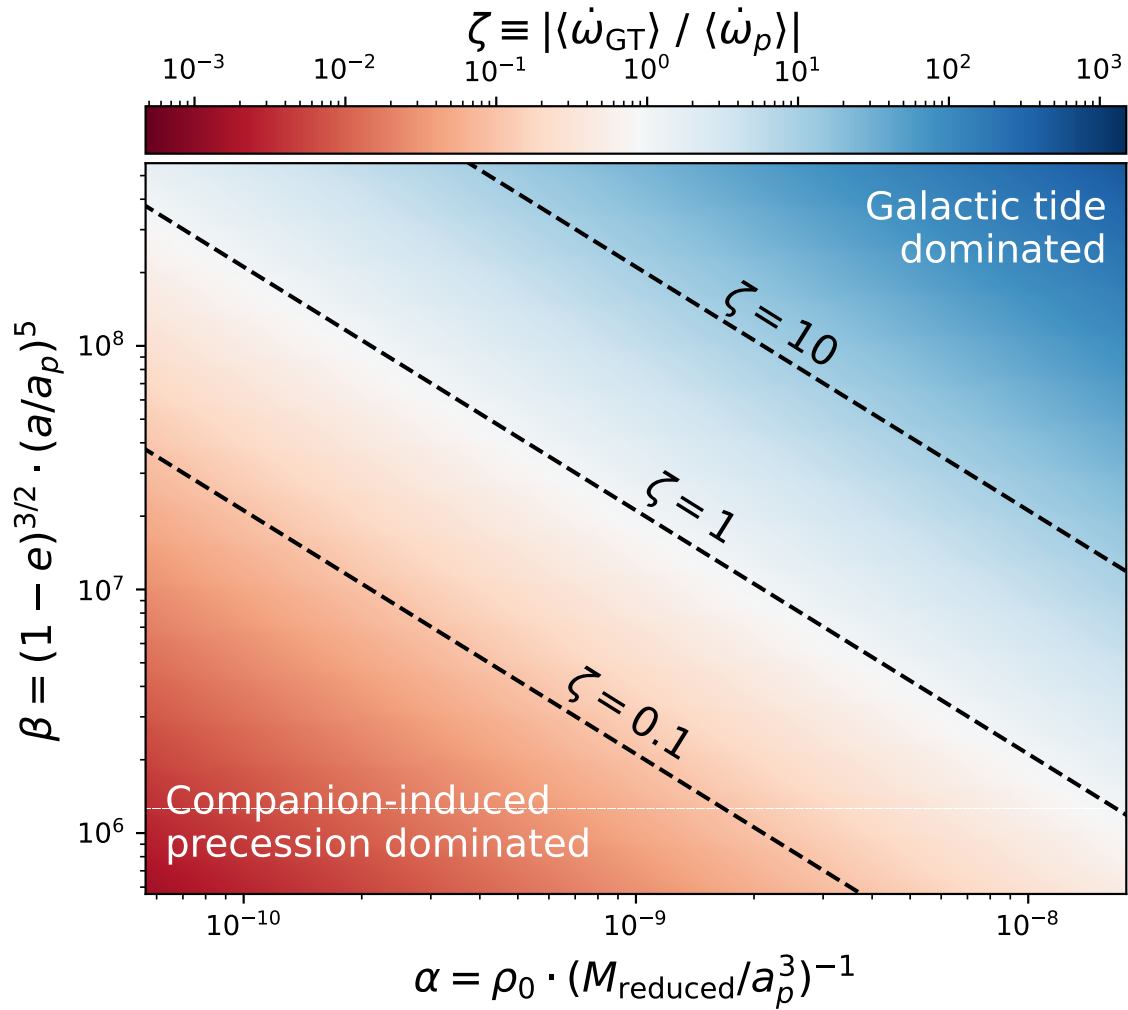


Figure 2.2: Values of ζ over a grid of α and β (see Table 2.1 and 2.2 for typical values). Dashed lines are where $\zeta = 0.1, 1, 10$. In the top right corner, $\zeta \gg 1$ and Galactic tide is stronger than companion-induced precession, and vice-versa in the bottom left.

3. We ignore angular dependencies in I, ω, Ω . However, as we will see in Figure 2.3 where results are over angles, ζ without angular dependencies is still able to give an order of magnitude estimate of the strength between precession and Galactic tide.
4. We expand ζ in the limit $q \ll a$. In other words, ζ is not a good approximation for very circular orbits ($q \approx a$), or for very close-in comets encountering very widely-separated companions (a is small, but a_p is large, so q is comparable to a). For the first case, when $q \approx a$, the comet is on a circular orbit and mostly affected by Galactic tide and not by the companion. For the second case, we must limit our analyses to companions with $a_p \ll a$. The closest Oort cloud comets in our model have $a \approx 3000$ au, so at most, we should only consider $a_p \leq 300$ au for ζ analysis.

2.3.2 Precession Barrier Efficiency

Figure 2.3 presents the efficiency of the precession barrier at overcoming Galactic tidal effects over a grid of α and β . The efficiency in this figure is defined as:

$$\text{Efficiency} = 1 - (N_{\text{companion}}/N_{\text{GT}}) \quad (2.30)$$

where N_{GT} is the number of comets that can enter a certain pericentre q with only Galactic tide. $N_{\text{companion}}$ is the same number, but there are Galactic tide and a companion. As defined, the efficiency measures the effectiveness of a companion in suppressing tidal effects. A companion can do this either by inducing a precession barrier or by inducing a scattering barrier. In this subsection, we only consider the efficiency of the precession barrier.

We found N_{GT} and $N_{\text{companion}}$ numerically. For each set of (α, β) , two simulations are run: with and without a companion. In both simulations, Galactic tide is included. This is evaluated on a grid of α and β , which depends on M_p, M_*, a, a_p, e . These values are chosen so that the effect of scattering is always weaker than that of Galactic tide and companion-induced precession. Other Keplerian orbital elements for a comet (I, ω, Ω) are drawn randomly assuming comets are isotropically distributed.

We compare the efficiency over a grid of (α, β) to the analytic values of ζ in Figure 2.3. Above the $\zeta = 10$ contour, companion-induced precession does not suppress any comets experiencing Galactic tide. Here, 100% of comets can come into q due to Galactic tide. As ζ decreases, the precession barrier becomes stronger and eventually at the bottom left corner, all comets are suppressed from Galactic tide, preventing inward migration in q . At $\zeta \sim 1$, when Galactic tide is on the order of companion-induced precession, about half of the comets are suppressed from entering. Below $\zeta = 0.1$, the barrier efficiency is 100% and all comets are suppressed from Galactic tide.

These efficiency behaviours found from simulations match well with what we expected from ζ over many orders of magnitude: when $\zeta \lesssim 1$ companion-induced precession suppresses Galactic tide. We find that ζ is a useful indicator of where companion-induced

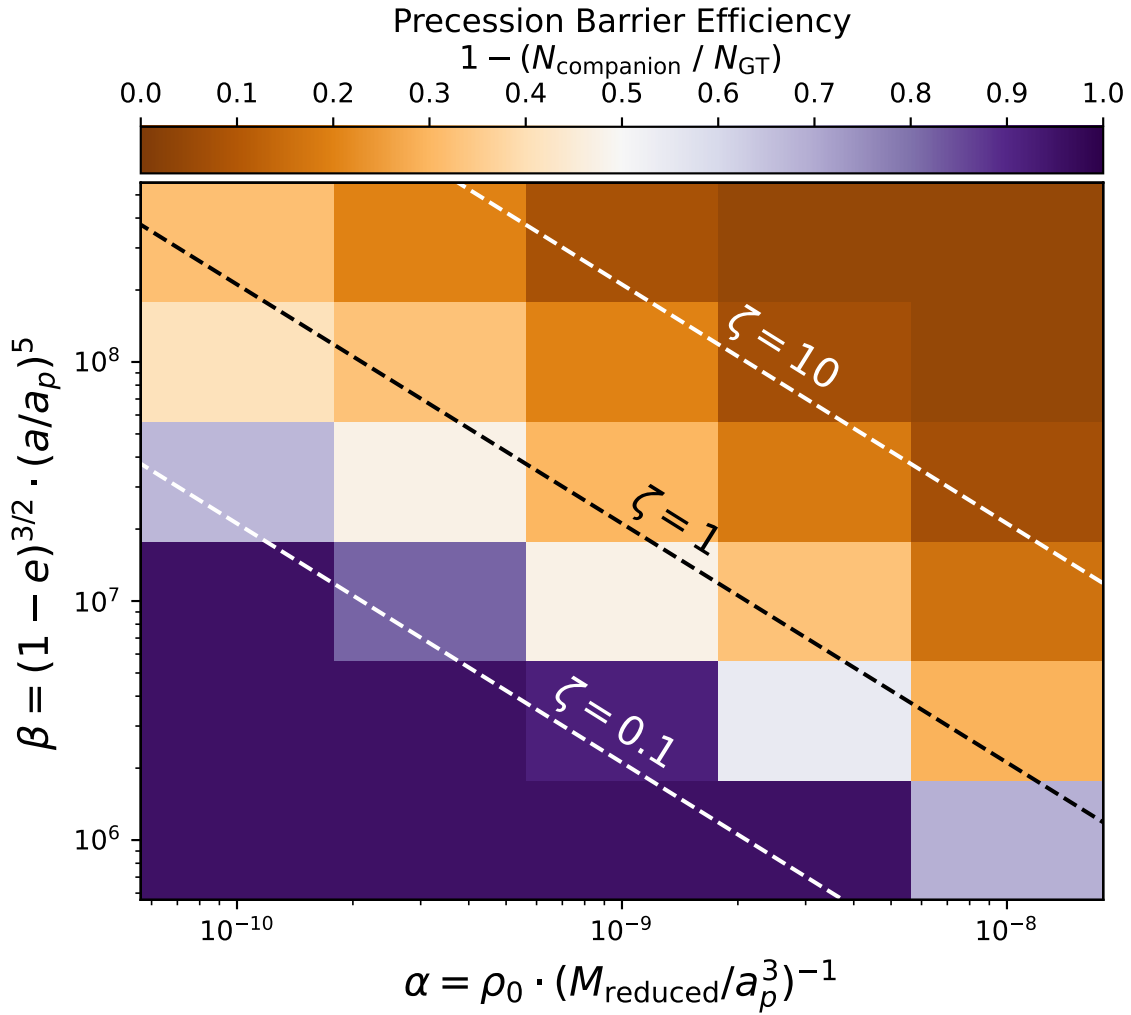


Figure 2.3: Efficiency of the precession barrier induced by a companion, measured from numerical simulations. Simulation values of M_p, M_*, a, a_p, q are chosen from grid values of (α, β) so that scattering does not matter. In other words, this efficiency is purely from the effects of the torque induced by a planetary companion, reducing the effectiveness of Galactic tide. The colour shows the efficiency of the planet's torque at inhibiting Galactic tide, where $N_{\text{companion}}$ is the number of comets that can enter a certain q in the existence of a companion and Galactic tide and N_{GT} is the same but there is only Galactic tide (no companion). Dashed lines show contours for $\zeta = 0.1, 1, 10$. Above the $\zeta = 10$ dashed line, the precession barrier efficiency is 0% and comets fully experience Galactic tide and can be excited to high eccentricity, migrating inward in pericentre q . Below the $\zeta = 10$ dashed line, we begin to see the precession barrier suppressing Galactic tide and the efficiency decreases. At the very bottom left point, Galactic tide is completely suppressed, and efficiency is $\sim 100\%$.

precession is important relative to Galactic tide. Specifically, the contour $\zeta \approx 10$ is a good indicator separating regimes of where Galactic tide dominates and where precession dominates. When ζ decreases, precession begins to dominate Galactic tide, and becomes increasingly more effective as $\zeta \ll 1$ where the efficiency tends to 100%.

2.3.3 Scattering Timescale

Comets not only experience a torque in ΔL causing precession but also experience a kick in energy causing a change in semi-major axis. There are two regimes where comets experience semi-major axis kicks from a massive companion: strong and diffusive scattering. In the strong scattering regime, $q \gtrsim a_p$, comets are ejected from the system within one pericentre passage. Here, the scattering timescale is approximately $T_{\text{scattering}} \approx P_{\text{comet}}/2$; comets are kicked during their incoming pericentre passages.

In the diffusive regime, $q > a_p$, comets experience small random semi-major axis kicks during multiple pericentre passages. These kicks vary in strength due to the phase difference between the comet and the companion during the encounters. [Hadden & Tremaine \(2024\)](#) investigate comet-companion interactions through an analytic mapping approach. Using the results they found, we can write the characteristic timescale on which small diffusive kicks in semi-major axis will lead to an order unity change in binding energy (or equivalently, order unity change in semi-major axis). Specifically, Equation 25 in [Hadden & Tremaine \(2024\)](#) is re-written as the timescale on which the comet experiences a strong scattering event due to diffusive kicks in semi-major axis:

$$T_{\text{scattering}} \approx 1.5 \times 10^4 \text{ yr} \cdot \left(\frac{M_p}{10^{-2} M_\odot} \right)^{-2} \left(\frac{M_*}{0.6 M_\odot} \right)^{3/2} \cdot \left(\frac{a}{10^4 \text{ au}} \right)^{3/2} \exp \left(7.4 \cdot \frac{q}{a_p} \right). \quad (2.31)$$

There are three main assumptions to using the results found by [Hadden & Tremaine \(2024\)](#) diffusive timescale for Oort cloud comets. First, the incoming comet is assumed to be coplanar to the companion – white dwarf orbital plane. This is not true for Oort cloud comets, which are isotropically distributed. Second, $M_p \ll M_*$, the companion’s mass is much smaller than the central star’s mass. Hence, we cannot use this timescale to estimate the scattering timescale in the stellar-mass companion case. Third, they assume the comet is on a parabolic orbit ($e = 1$). While this is not exactly true in our case, Oort cloud comets have highly eccentric orbits when they interact with companions. Hence, we further assume that we can use the $e = 1$ diffusive timescale as written here, for comets with $e \lesssim 1$. Finally, since we assume $e \lesssim 1$, this timescale is only applicable in cases where $q \ll a$ and $a_p \ll a$ (the companion is much closer in than the comet).

Next, we compare analytic expectations of $T_{\text{scattering}}$ to numerical simulations. We simulate two cases: a stellar-mass companion with $M_p = 0.6 M_\odot$ and planetary-mass companion

with $M_p = 10^{-2} M_\odot$. In both cases, the companions are on a circular orbit at $a_p = 200$ au around a central white dwarf with mass $M_* = 0.6 M_\odot$ and the companion's initial phase is randomised. At each pericentre q , where $q \in [1, 6]a_p$, 200 comets are initialised with $a = 15\,000$ au (typical semi-major axis of incoming comets to interact with companions at $a_p = 200$ au). The comets' initial position is set at apocentre. Comets' angles are initialised either coplanar or isotropically. Simulations are stopped when comets experience a kick $\Delta a/a_0 > 0.3$ relative to the initial semi-major axis a_0 , or until the simulation time reaches 10^{11} years and we call this time the numerical scattering timescale. The numerical condition, $\Delta a/a_0 > 0.3$, is somewhat arbitrary but we found that this is a good indicator for when comets experience order unity changes in binding energy (strong scattering).

Figure 2.4 compares numerical scattering timescales with analytic expectations. In both panels, numerical timescales for coplanar and isotropic comets are shown. The solid-coloured lines are the mean scattering timescales and the shaded areas are the timescale ranges from 200 comets. The top panel shows the timescales for a stellar-mass companion and the bottom panel for a planetary-mass companion. First, there are clearly two scattering regimes. Comets sufficiently far away experience long scattering timescales according to the diffusive timescale. As the pericentre decreases, the timescale eventually converges to the strong scattering regime where comets are ejected within one pericentre passage. Second, in the bottom panel, we find the timescale for coplanar comets interacting with a planet matches well within an order of magnitude with the analytic expectations. The slopes between numerical and analytic match well in the diffusive regimes. The analytic $T_{\text{scattering}}$ is consistently off by a factor of a few. We attribute this to the arbitrary $\Delta a/a_0 > 0.3$ numerical scattering condition. Third, isotropic comets have a higher scattering timescale. In addition, as the pericentre increases, coplanar and isotropic timescales converge. This behaviour is expected since isotropic comets experience weaker kicks than coplanar comets. But at high pericentre distances, their kick strengths are both small. Fourth, in the top panel, we find the analytic expectation no longer gives a reliable scattering timescale. This is because the condition $M_p \ll M_*$ is strongly violated. Here, we observe that coplanar comets quickly become strongly scattered at $q \approx 6a_p$, while isotropic comets transition slower. Note that in an investigation of a test particle on an initially circular orbit around a binary, Holman & Wiegert (1999) found a stability limit around $4a_p$ for equal mass binaries. Their result is different from ours because their test particles are on circular orbits while ours are highly eccentric. Hence, their test particles can experience effects from mean motion resonances, as discussed in detail in Holman & Wiegert (1999). That being said, their result and ours are reminiscent of each other.

Once a comet reaches a pericentre within the strong scattering regime, it cannot survive multiple encounters. Thus, when there is a scattering barrier strong enough to create a strong scattering regime, comets in the empty loss cone are prevented from slowly migrating inward. However, this does not mean there are no comets entering smaller q . Comets in

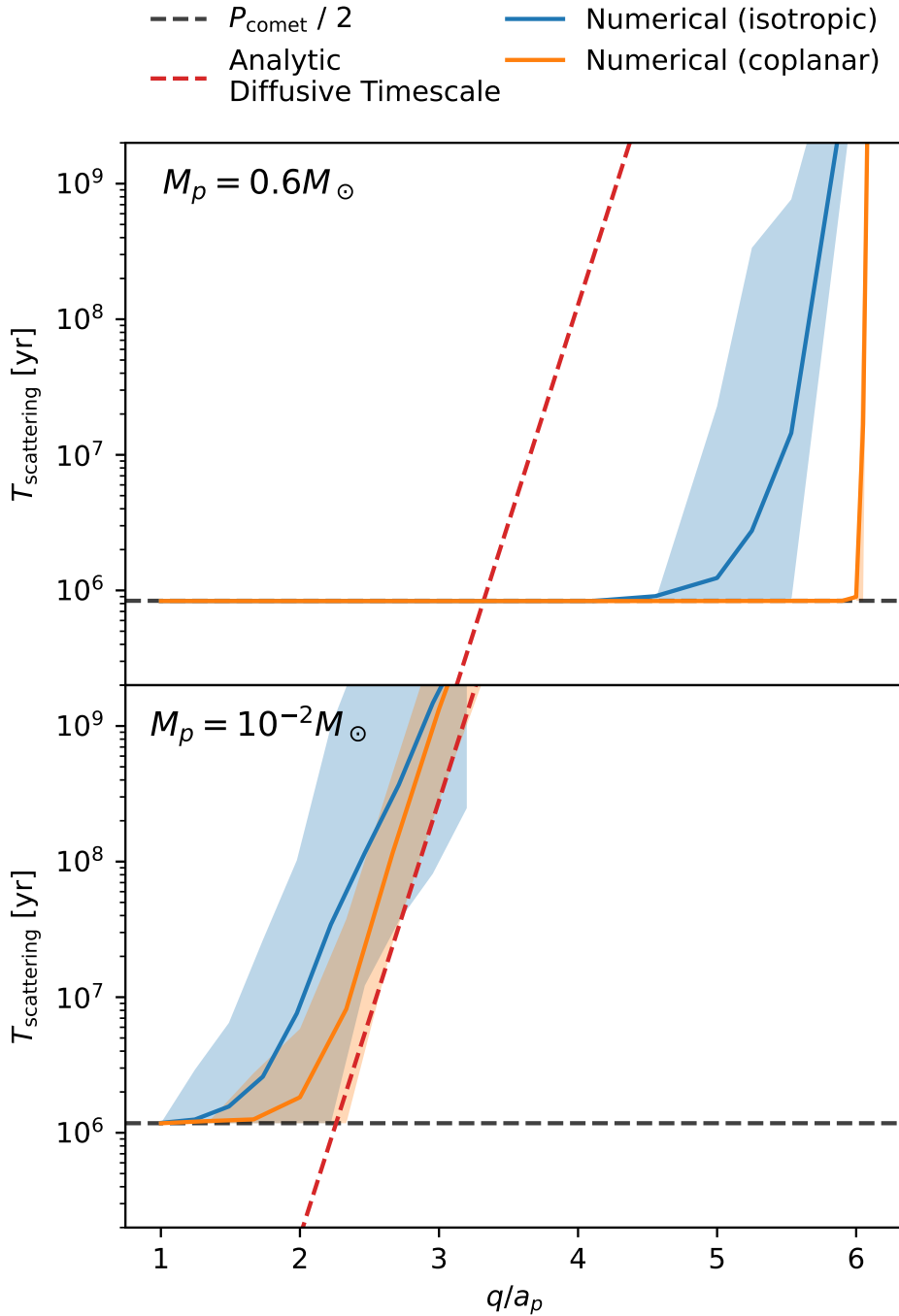


Figure 2.4: Numerical scattering timescales for coplanar (orange) and isotropic (blue) comets interacting with a stellar-mass (top) and planetary (bottom) companion. The analytic diffusive timescales are shown in both panels, but can only be used in the bottom panel where $M_p \ll M_*$. Blue and orange shaded areas are the range of measured numerical scattering timescales. In both cases, the high diffusive timescale flattens to the strong scattering regime (where comets are ejected within one pericentre passage with timescale $P_{\text{comet}}/2$) as the pericentre q decreases.

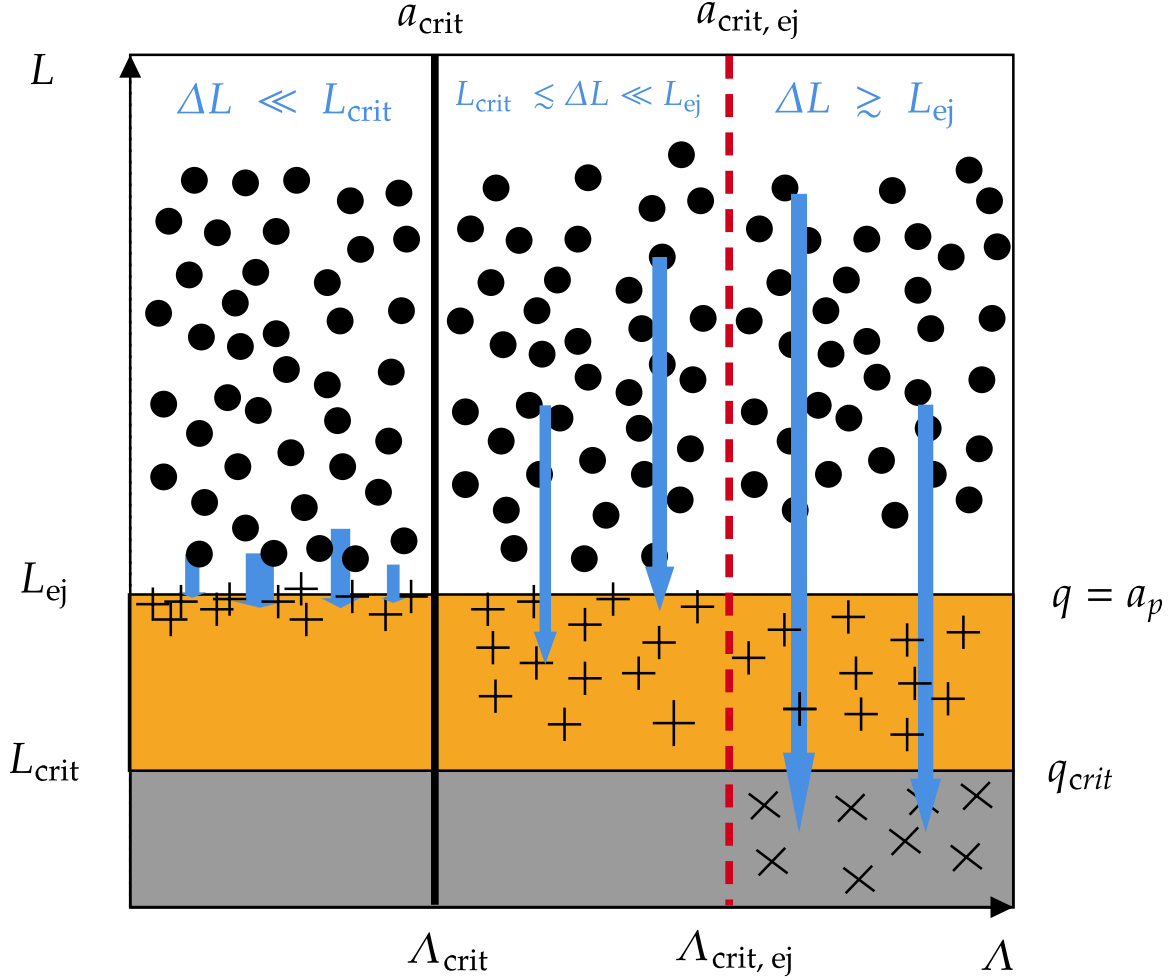


Figure 2.5: Diagram illustrating the modified loss cone theory by O'Connor et al. (2023). The engulfment loss cone is in grey, the ejection loss cone is in orange. Comets ejected are shown as plus signs and comets capable of engulfment are shown as crosses. This figure is created following closely Figure 12 in O'Connor et al. (2023).

the full loss cone regime can still migrate within one orbital period to be engulfed by the white dwarf because they only interact with the companion once. This is the motivation for the modified loss cone theory in section 2.3.4.

2.3.4 Modified Loss Cone Theory

O'Connor et al. (2023) estimate the reduction of pollution rate in the presence of a planetary companion by modifying the loss cone theory. We summarise their theory below and illustrate the modified loss cone theory in Figure 2.5. We also discuss the limitations of this modified loss cone framework. A similar effect is proposed by Teboul et al. (2024) for dense star clusters with a central black hole called “loss cone shielding”.

An ‘ejection loss cone’ is defined as the region where comets are shielded from further

migrating inward due to repeated encounters with the planet. During multiple strong encounters, the comet experiences changes in semi-major axis which can eventually eject the comet. The location of the ejection loss cone is defined at:

$$L_{\text{ej}} = \sqrt{2GM_{\text{total}}a_p} \quad (2.32)$$

nesting on top of the tidal-disruption loss cone at

$$L_{\text{crit}} = \sqrt{2GM_{\text{total}}q_{\text{crit}}}. \quad (2.33)$$

where $M_{\text{total}} = M_* + M_p$ is the total mass of the white dwarf star and the planetary companion. In the case where the planet is far away from the tidal radius, $a_p \gg q_{\text{crit}}$, we have $L_{\text{ej}} \gg L_{\text{crit}}$. The two loss cones overlap, but the ejection loss cone covers a much larger region of phase space than the tidal loss cone.

As a comet experiences a change in angular momentum ΔL due to Galactic tide, it drifts inward encountering these loss cones. A comet with relatively small a experiences a small $\Delta L \ll L_{\text{ej}}$, and drifts slowly to the edge of the ejection loss cone; the ejection loss cone is empty. Vice versa, a comet with larger a experiences a much greater $\Delta L \gtrsim L_{\text{ej}}$, and jumps through the ejection loss cone in one orbital period; the ejection loss cone is filled. In addition, if a comet experiences a sufficiently large change in angular momentum, $\Delta L \gtrsim L_{\text{crit}}$, it can jump through both loss cones and can be tidally disrupted and pollute a white dwarf. These regimes are illustrated in Figure 2.5 (following Figure 12 in O'Connor et al., 2023). The comet avoids ejection since it reaches the engulfment loss cone in one orbital period. The transition semi-major axis between the two ΔL regimes is:

$$\begin{aligned} a_{\text{crit,ej}} &\sim a_{\text{crit}} \cdot \left(\frac{a_p}{q_{\text{crit}}} \right)^{1/7} \\ &\approx 32\,000 \text{ au} \cdot \left(\frac{a_p}{10 \text{ au}} \right)^{1/7} \left(\frac{q_{\text{crit}}}{1R_{\odot}} \right)^{-1/7} \end{aligned} \quad (2.34)$$

where in the last expression we used values of $a_{\text{crit}} = 10\,500 \text{ au}$ (Equation 2.16), $q_{\text{crit}} = 1R_{\odot}$ and $a_p = 10 \text{ au}$. This transition semi-major axis corresponds to a critical circular momentum

$$\Lambda_{\text{crit,ej}} = \sqrt{GM_{\text{total}}a_{\text{crit,ej}}}. \quad (2.35)$$

Under this framework, only comets with $a > a_{\text{crit,ej}}$ can experience a sufficiently large $\Delta L \gtrsim L_{\text{ej}}$ to pollute a white dwarf. In addition, comets that can pollute white dwarfs are in the filled loss cone regime because $a_{\text{crit,ej}} > a_{\text{crit}}$. Therefore, the pollution rate is estimated as the filled loss cone rate integrated over semi-major axes ranging between $a_{\text{crit,ej}} \leq a \leq a_2$, or equivalently over Λ :

$$\Gamma_{\text{total,planet}} = \int_{\Lambda_{\text{crit,ej}}}^{\Lambda_2} \Gamma_f(\Lambda) d\Lambda. \quad (2.36)$$

O'Connor et al. (2023) further simplify this expression to find:

$$\frac{\Gamma_{\text{total,planet}}}{\Gamma_{\text{total,GT}}} \sim \left(\frac{q_{\text{crit}}}{a_p} \right)^{(2\gamma-1)/14}. \quad (2.37)$$

Taking a fiducial value of $\gamma = 3.5$ (for a Solar system Oort cloud), the factor on the right-hand side is approximately 0.05 for $q_{\text{crit}} = 1R_\odot$ and $a_p = 10$ au. With this, we analytically expect the existence of a planetary companion to reduce the white dwarf pollution rate by about 1.5 orders of magnitude for $\gamma = 3.5$.

Limitations

First, comets with $\Delta L \ll L_{\text{ej}}$ drift slowly to the edge of the ejection loss cone and then are assumed to be fully ejected when they enter into the ejection loss cone. However, comet-planet interactions can be weak and not sufficiently strong to eject comets. For example, we expect a comet to experience a much weaker kick in semi-major axis by a much smaller mass planet. A planet the size of the Earth and a planet with $10M_{\text{Jup}}$ will create loss cone barriers with very different efficiency. Another example is if a comet is very inclined relative to the planet's orbital plane, the kick will also be much weaker. Therefore, not every comet with $a < a_{\text{crit,ej}}$ will be ejected. In the small planet mass limit, we expect $\Gamma_{\text{total,planet}} = \Gamma_{\text{total,GT}}$ since the planetary ejection barrier is not effective at all. In the large planet mass limit, the planet creates a 100% effective scattering barrier, *reducing* pollution rate as described by Equation 2.37. O'Connor et al. (2023) recognised that planet mass should affect ejection efficiency, yet Equation 2.37 does not have a mass dependence. To identify which planet could create a sufficiently strong ejection barrier, the authors propose a quantity²:

$$\lambda = \left(\frac{M_p}{M_{\text{Jup}}} \right) \left(\frac{M_\odot}{M_*} \right) \left(\frac{a}{10^4 \text{au}} \right) \left(\frac{10 \text{au}}{a_p} \right). \quad (2.38)$$

If $\lambda \ll 1$, the ejection barrier is weak and the comet receives negligible kicks and can safely migrate inward through multiple orbits. If $\lambda > 1$, then the ejection barrier becomes important. Using λ , a $10M_{\text{Jup}}$ planet at $a_p = 10$ au should be able to create a sufficiently strong ejection barrier. We will test the ejection barrier strength of a planet with this configuration later.

Second, this theory cannot account for additional dynamics that can be induced by a planetary-mass companion. For example, a comet can be captured into smaller orbits and experience more complicated dynamics which can also facilitate delivery into white dwarfs, such as von Zeipel-Kozai-Lidov or inverse Kozai (Farago & Laskar, 2010; Vinson & Chiang, 2018).

Third, as discussed earlier, another important additional dynamical effect is that a

²Note that λ is originally called Λ in O'Connor et al. (2023). We already used Λ in this thesis for the circular angular momentum.

comet experiences small random kicks in semi-major axis, Δa , through multiple diffusive encounters. This causes the semi-major axis to change over time which also changes how a comet experiences Galactic tide ΔL over time. Since ΔL due to Galactic tide is strongly dependent on a comet's semi-major axis, these random walks in a induced by a planet can potentially cause a comet to experience vastly different Galactic tidal effects over time. Therefore, assuming a white dwarf pollution rate through integrating the total full loss cone rate Γ_f ranging between a fixed range of semi-major axes for all comets over all time (Equation 2.36) might not be a suitable estimate.

Consider an example where a comet begins with an initial semi-major axis $a < a_{\text{crit,ej}}$. Through Galactic tide, the comet migrates inward in pericentre distance q . At some point later in time when the comet achieves a $q \gtrsim a_p$, the comet begins to experience random kicks in semi-major axis every pericentre passage through interactions with the planet. Due to multiple small Δa kicks, the comet is migrated to $a \gtrsim a_{\text{crit,ej}}$. In this example, we initially count this comet to be in the empty ejection loss cone and thus, cannot pollute comets. But random interactions with a planet bring the comet to a larger a , where Galactic tide induces a stronger ΔL allowing the comet to bypass the ejection loss cone and pollute the white dwarf. In this example, having a larger planet might actually *increase* pollution rate because larger planets can induce stronger random walks in a at a larger range pericentre range.

In the Solar system, this mechanism for Oort cloud comets to bypass the Jupiter-Saturn ejection barrier is shown in [Kaib & Quinn \(2009\)](#). In this case, weak perturbations by Uranus and Neptune are attributed to inducing small kicks in a , bringing comets into a stronger ΔL regime capable of bypassing the ejection barrier. As shown in Figure 2.4, one single planet can likewise induce small perturbations on comets. Thus, the comets in our case can similarly bypass the ejection barrier through these small kicks in a .

Finally, there is a small chance of a comet becoming unbound through a strong kick, but can still pollute a white dwarf on its last inbound passage.

2.3.5 Timescales Comparison

To analyse the importance of the companion's scattering and precession versus Galactic tide, we investigate the timescales on which these effects are important.

These timescales are measured from simulations of 10^5 comets from a Solar system-like Oort cloud: $n(a) \propto a^{-3.5}$ from 3000 to 10^5 au. Here, we directly simulate all comets with an additional Galactic tidal force at every timestep — no secular integration of Galactic tide as done in Section 2.4.1. This is to ensure that we accurately capture all companion-comet interactions at all q . In addition, we measure independently the contribution of Galactic tide and companion at a given pericentre q .

First, we simulate 10^5 comets around a centre-of-mass point mass (the total mass of a white dwarf and its companion) with Galactic tide. This simulation is run until comets'

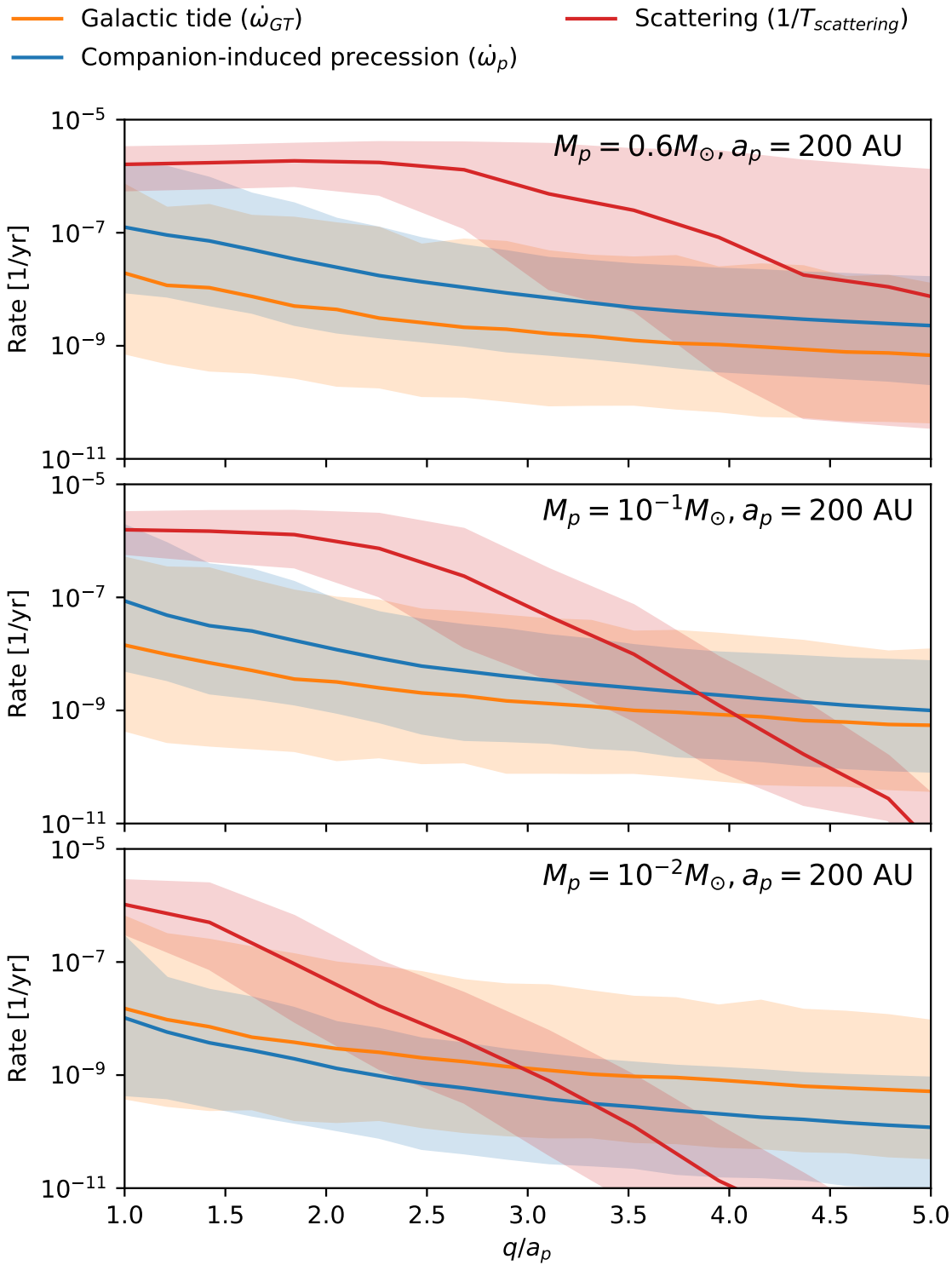


Figure 2.6: Timescale comparison of Galactic tide, companion-induced precession and scattering. From the bottom panel up, these show various cases of increasing importance of companions. Timescales are measured from simulations of a Solar system-like Oort cloud ($n(a) \propto a^{-3.5}$, $a \in [3000, 10^5] \text{ au}$). The shaded area shows the 3σ spread of timescales for this particular distribution of comets.

pericentres reach a certain q . The orbital elements of incoming comets with pericentre q are then saved. Next, we measure the Galactic tidal torque over one orbit at this q , giving us $\dot{\omega}_{\text{GT}} \approx \Delta\omega/P_{\text{comet}}$. Second, we run another simulation on these saved comets, but now there is a companion and the Galactic tide is turned off. In this simulation, we measure the companion-induced precession change on the comet over one orbit, giving us $\dot{\omega}_p \approx \Delta\omega/P_{\text{comet}}$. Third, these comets are again run in a third simulation with a companion and no Galactic tide to measure the scattering timescale. The difference between the second and third simulations is in the third simulation comets are simulated longer. In the third simulation, comets are integrated until they experience a scattering event, $\Delta a/a > 0.3$, or until the simulation time reaches 10^{12} years. Recording the times when comets experience a scattering event gives us $T_{\text{scattering}}$. These simulations are run for every q between $q = a_p$ to $q = 5a_p$ and for companions with masses $M_p = 10^{-2}, 0.1, 0.6M_\odot$ (corresponding to a white dwarf, M dwarf, and the upper limit of a planetary-mass companion, $10^{-2}M_\odot = 10M_{\text{Jup}}$).

We compare the rates (inverse timescales) of these effects in Figure 2.6. The shaded area is the 3σ spread, showing the range of most comets' timescales. These three cases show the increasing importance of companion-induced precession and scattering. As expected, increasing the companion mass increases the strength of scattering. With a $10^{-2}M_\odot$ planet companion, scattering begins to dominate at $q \approx 3a_p$, whereas this is increased to $q \approx 3.5a_p$ for a $0.1M_\odot$ stellar companion. For the white dwarf – white dwarf binary case, scattering seems to dominate at all q considered here. Note that the scattering timescale flattens out as $q \rightarrow a_p$. This is similar to the scattering behaviour we analysed earlier: comets are ejected within one orbital period in this regime, $T_{\text{scattering}} \approx P_{\text{comet}}/2$. Similar to scattering, precession's strength becomes stronger relative to Galactic tide as companion mass increases. Finally, Figure 2.6 shows that in all cases, as $q \simeq a_p$, the dominant effect is companion-induced scattering.

2.4 Simulation Method

The previous sections provide us with some understanding of what dynamical effects we should expect in this kind of system. We now turn to numerical simulations to study the long-term (1 Gyr) dynamics of Oort cloud comets under the influence of Galactic tide and a companion. There are two main components in our integration scheme: first is a secular integration of the Galactic tide equations of motion. If a comet can be excited to a certain $q = q_{\text{switch}}$, its orbital elements are extracted and the comet is then integrated directly with REBOUND (Rein & Liu, 2012) when $q \leq q_{\text{switch}}$. When comets violate their boundary conditions (section 2.4.2) they are removed. Figure 2.7 illustrates the components of our integration.

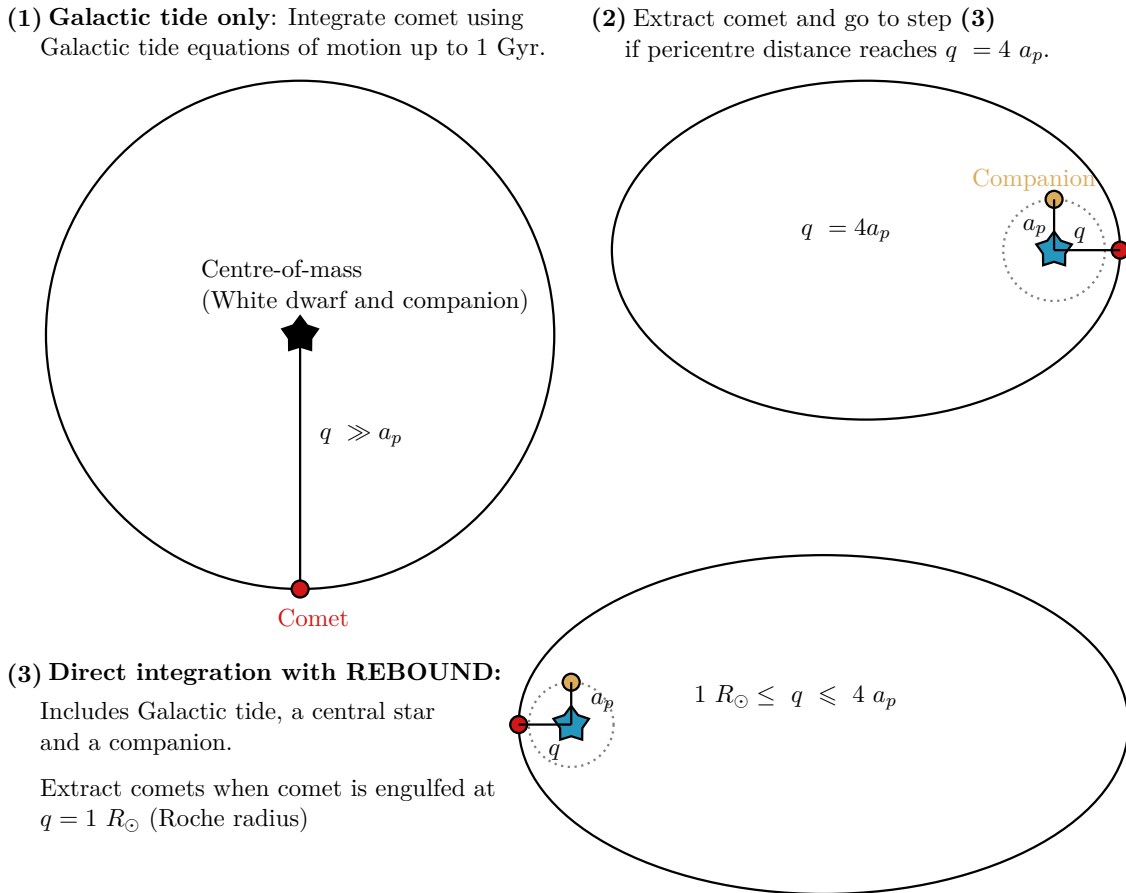


Figure 2.7: A diagram to illustrate our hybrid integration scheme. The first stage is using secular Galactic tide equations of motion in (Equations 2.4, 2.5 and 2.6) to quickly integrate a comet. If a comet can be excited to $q = q_{\text{switch}} = 4a_p$, then its orbital elements are extracted to be integrated directly using REBOUND. The direct integration by REBOUND uses the full equations of motion and can include interactions with the white dwarf and its companion. A comet is extracted when its apocentre exceeds the white dwarf's Hill sphere ($Q > 0.8$ pc), when it's ejected due to interactions with a companion ($a < 0$) or when it is engulfed by the white dwarf ($d \leq 1R_\odot$, where d is the distance between the comet and the white dwarf). Integrations are stopped when the simulation time reaches $t = 1$ Gyr.

2.4.1 Integration Scheme

The majority of Oort cloud comets at most times do not have sufficiently high eccentricity to interact with the central white dwarf or its close companion.

In this regime, the motion of a comet is largely governed by its orbit around the white dwarf and companion centre of mass and tidal effects from the Galaxy. In this case, we can use the orbit-averaged equations of motion (Equations 2.4, 2.5 and 2.6) to quickly evolve comets. We use the fourth-order Runge-Kutta to evolve these coupled differential equations with an adaptive timestep scheme as implemented in `scipy` (Virtanen et al., 2020). We find that the Runge-Kutta adaptive timestep scheme reproduces well the evolution in (L, ω) as seen in Heisler & Tremaine (1986).

If a comet can reach a certain critical q_{switch} , it is removed from the secular integration and integrated with `REBOUND` to allow for full interactions with the white dwarf and its companion. When switched over to integrating with `REBOUND`, we develop a fast simulation method where only one particle is simulated to further speed up the simulation. This fast `REBOUND` integration method is described in detail in the following chapter of this thesis.

One caveat of using these orbit-averaged equations of motion is that they are not appropriate when $\Delta L \gg L_{\text{crit}}$. This is in the filled loss cone regime. In this case, within one orbital period, a comet experiences a significant change in its angular momentum and is considered lost. Thus, orbit-averaging is no longer appropriate. This is also resolved by switching over to `REBOUND` where we integrate with the full (not orbit-averaged) equations of motion.

When a comet achieves a pericentre distance $q_{\text{switch}} \approx 4a_p$, interactions with a planetary-mass companion become important. We show this earlier in Figure 2.6 and its discussion. At q_{switch} , a comet is extracted from secular equations of motion integration and simulated in `REBOUND`. In `REBOUND`, we simulate full interactions between the comet and white dwarf – companion system, and we use the full (not orbit-averaged) equations of motion for vertical Galactic tide. The companion is set on a circular orbit at a semi-major axis a_p with $I_p = 0$.

When there is no planet, we still extract comets from the secular integration when the comets reach $q_{\text{switch}} = 10$ au. This choice is somewhat arbitrary, but it ensures that $q_{\text{switch}} \gg q_{\text{crit}} = 1R_\odot$. This is to make sure that engulfment into the white dwarf is integrated with the full (not orbit-averaged) equations of motion through `REBOUND`, so that all Galactic tidal dynamics are properly captured. As discussed, the secular equations of motion fail in the regime where ΔL is sufficiently strong to inject the comet into the loss cone in one orbital period.

2.4.2 Boundary Condition

During the `REBOUND` part of our simulation, we enforce the following boundary conditions:

1. comets with apocentre exceeding the Hill sphere of a $0.6M_\odot$ star ($Q > 0.8$ pc) and

- are outbound away from the white dwarf,
2. comets are ejected ($a < 0$) and are outbound away from the white dwarf,
 3. comets are engulfed ($d \leq 1R_{\odot}$, where d is the distance from a comet to the white dwarf)

Only boundary condition (3) contributes to white dwarf pollution. Boundary conditions (1) and (2) remove comets because these comets are ejected from the Oort cloud reservoir. These three boundary conditions are checked at every simulation timestep. In addition, the simulation is stopped when the simulation time reaches $t = 1$ Gyr.

The Hill sphere of a white dwarf is scaled down from the Solar system's Hill sphere at ~ 1 pc (e.g., [Higuchi & Kokubo, 2015](#)). For a $0.6 M_{\odot}$ white dwarf, the Hill radius is at 0.8 pc ([O'Connor et al., 2023](#)). In addition, boundary conditions (1) and (3)

$$\begin{aligned} q &= a(1 - e) \leq 1R_{\odot} \\ Q &= a(1 + e) \leq 0.8 \text{ pc} \end{aligned} \tag{2.39}$$

imply that there is a maximum semi-major axis:

$$a_2 \approx 85\,000 \text{ au}. \tag{2.40}$$

This is the outer semi-major axis edge of the Oort cloud. Comets beyond a_2 cannot be excited to high eccentricity since they will be removed for exceeding the apocentre limit. The lowest pericentre comets at this semi-major axis without exceeding the white dwarf Hill sphere is $q \sim 5\,000$ au. In addition, this upper semi-major axis limit can also be found by scaling down the Solar system's Oort cloud outer semi-major axis edge at $a_2 = 10^5$ au, for a $M_* = 0.6M_{\odot}$ central star.

2.4.3 Initial Condition and Rejection Sampling

The initial conditions of Oort cloud comets are generated based on a spherical cloud distribution. Comets' argument of pericentre ω and longitude of the ascending node Ω are drawn randomly from $\mathcal{U}[0, 2\pi]$ where \mathcal{U} is the uniform distribution. Comets' inclination are drawn according to $\cos I \sim \mathcal{U}[0, 1]$. The sign of the comet's $\cos I$ is not important since we set the planet at $I_p = 0$.

Next, the semi-major axis is drawn such that Oort cloud comets follow a powerlaw density profile $n(a) \propto a^{-\gamma}$:

$$dN(a) \propto a^{-\gamma} a^2 da \tag{2.41}$$

with $a \in [a_1, a_2]$. $a_1 = 3\,000$ au is the inner semi-major axis edge, set based on the Solar system's Oort cloud simulations (e.g., [Duncan et al., 1987](#); [Vokrouhlický et al., 2019](#)). $a_2 = 85\,000$ au is the outer semi-major axis edge, as found in the previous subsection.

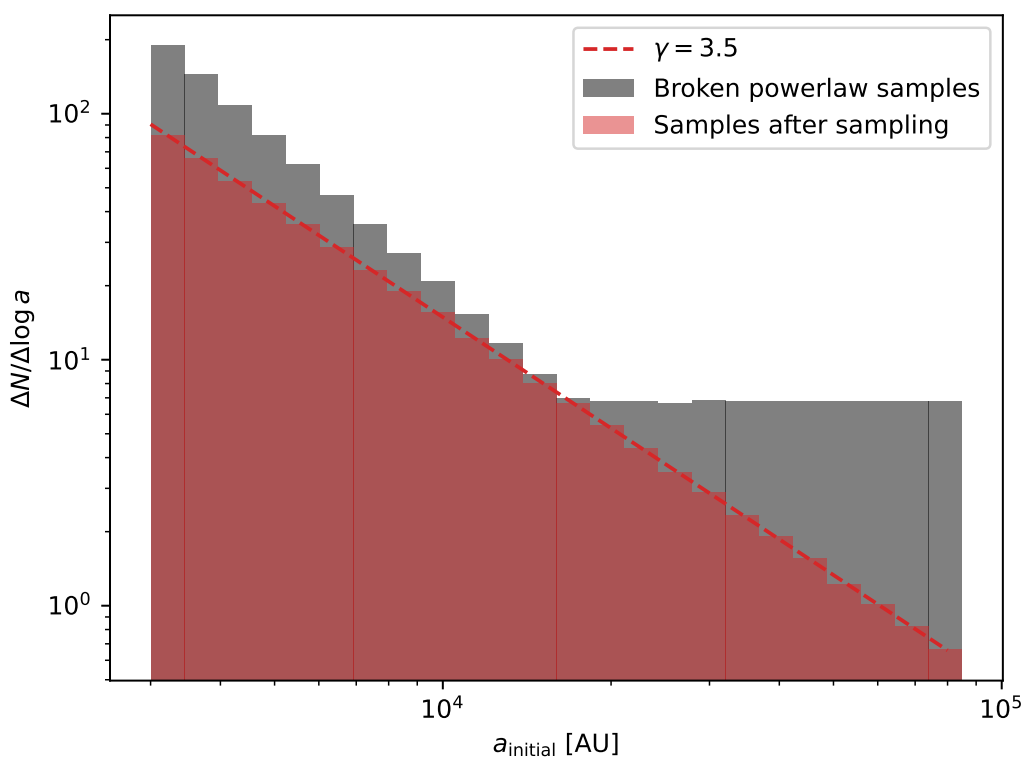


Figure 2.8: The broken powerlaw (Equation 2.42) and the resulting powerlaw sampling (Equation 2.20) with a powerlaw index $\gamma = 3.5$.

The distribution of comet semi-major axis follows a density profile described by a power-law relationship $n(a) \propto a^{-\gamma}$. In this context, we wish to study all semi-major axes described by $2 \leq \gamma \leq 4$. We could draw samples of a at fixed γ , run simulation, and repeat this process over a grid γ . However, this procedure increases the computation costs significantly. For example, creating Figure 2.10 would require running 20 simulations at different γ . To efficiently simulate all γ without re-running simulations many times, we use a rejection sampling scheme to draw samples for the semi-major axis distribution.

Comets' semi-major axes are initialised on a broken powerlaw distribution (cf. Equation 2.20):

$$dN(a) \propto \begin{cases} a^{-\gamma_{\max}} \cdot a^2 da, & a_1 \leq a \leq a_{\text{turnover}} \\ a^{-\gamma_{\min}} \cdot a^2 da, & a_{\text{turnover}} \leq a \leq a_2 \end{cases} \quad (2.42)$$

where $\gamma_{\min} = 2$ is the minimum γ that we can sample and $\gamma_{\max} = 4$ is the maximum. $a_{\text{turnover}} = 17\,000$ au is the broken powerlaw turnover point. a_{turnover} is determined heuristically to maximise the efficiency of rejection sampling.

Figure 2.8 shows the broken powerlaw and an example of the semi-major axis distribution after rejection sampling to create a $\gamma = 3.5$ powerlaw distribution.

We simulate $N_{\text{comets}}^{\text{sim}}$ comets with semi-major axes drawn from this broken powerlaw distribution. Their initial and final positions are recorded. Using rejection sampling, we select comets after running the simulations to construct results for any particular γ we are interested in.

In Figure 2.9, the efficiency of rejection sampling from the broken powerlaw at various γ is shown. We also compare that with rejection sampling from a uniform distribution instead. As shown, the broken powerlaw is much more efficient for rejection sampling into a powerlaw distribution than a uniform distribution. We find that using the broken powerlaw as proposed gives a 50% efficiency. That is, to construct results at any particular γ , the number of comets representative in that results is $N_{\text{comets}}^{\text{eff}} \sim 0.5 N_{\text{comets}}^{\text{sim}}$. As a consequence, we need to simulate twice the number of comets we would like to see for any particular result. However, this is still less than 20 simulations (or one simulation per value of γ).

After having a drawn by rejection sampling, we draw the squared eccentricity, e^2 , from:

$$e^2 \sim \mathcal{U}[0, 1 - 2q_{\text{initial,min}}/a] \quad (2.43)$$

for a distribution uniformly filling the energy phase space (Heisler, 1990), appropriate for a dynamically relaxed Oort cloud as seen after long-term simulations of Solar system Oort cloud formation (e.g., Higuchi & Kokubo, 2015; Vokrouhlický et al., 2019). Note that we impose an upper e (or equivalently, a minimum initial pericentre $q_{\text{initial,min}}$). $q_{\text{initial,min}}$ set sufficiently far that a comet's interaction with a companion or the white dwarf is negligible initially. This is to ensure that all comets – companion – white dwarf interactions are induced by Galactic tide, rather than by random initial condition. Specifically, in the case

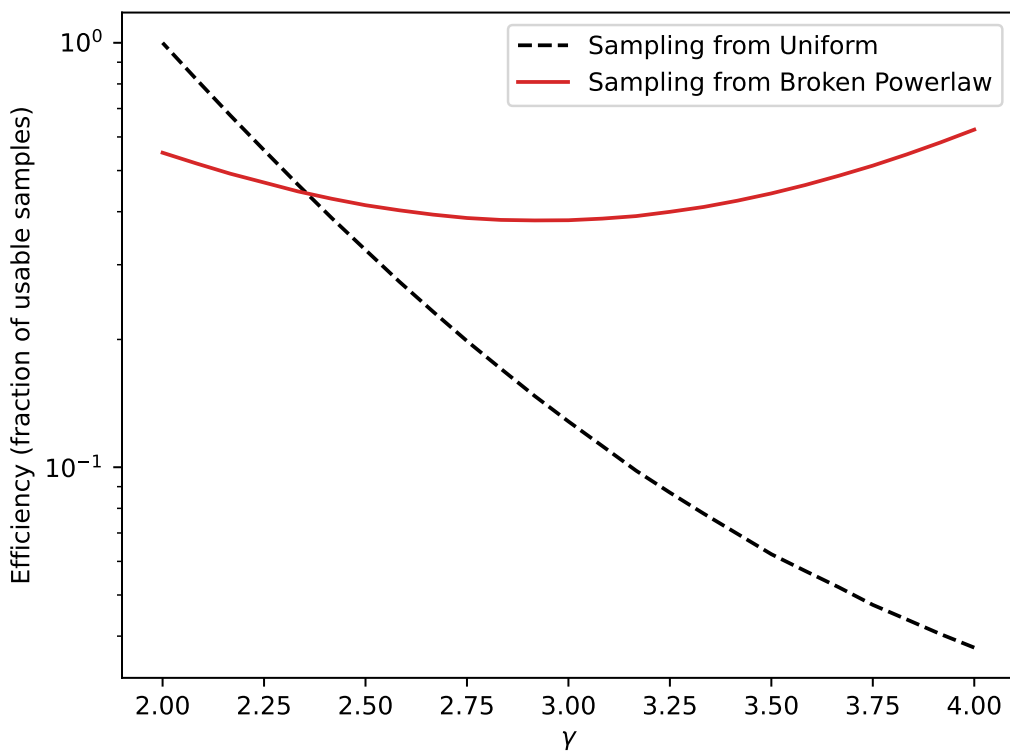


Figure 2.9: The efficiency of performing rejection sampling on a broken powerlaw versus rejection sampling on a uniform distribution. We can see that using the broken powerlaw distribution to create powerlaw samples is much more effective. With the broken powerlaw rejection sampling, the number of usable samples at any particular γ is about half of the total simulated samples.

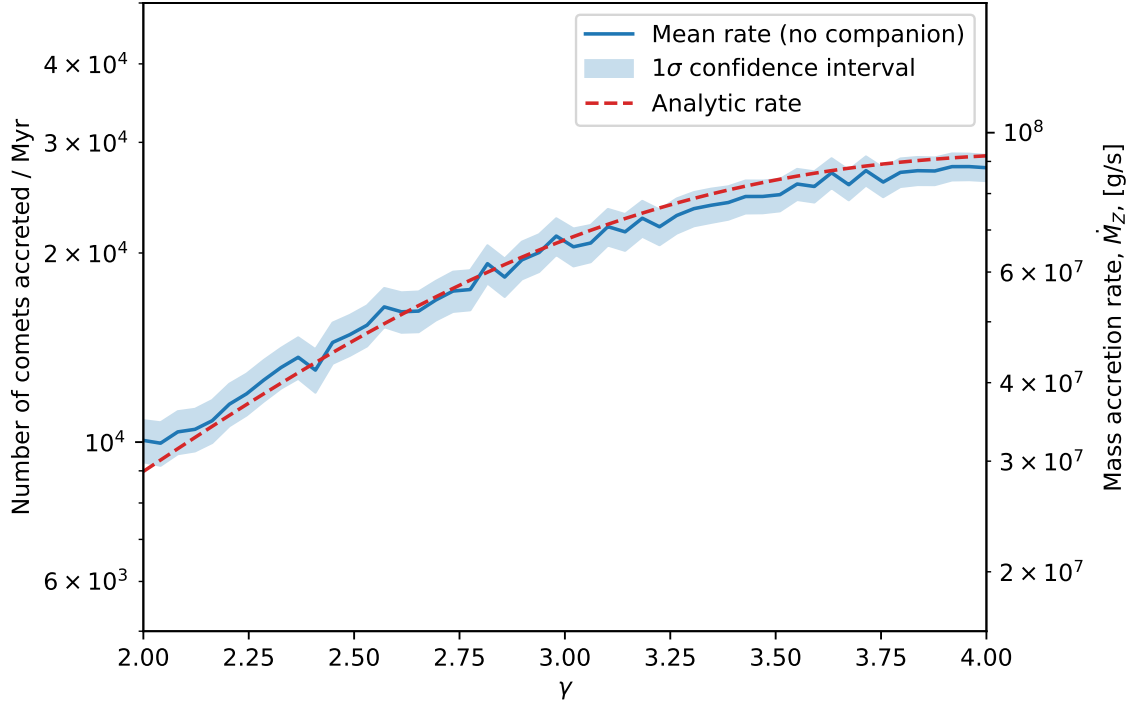


Figure 2.10: Accretion rate of comets into $q_{\text{crit}} = 1R_{\odot}$ over various Oort cloud structures γ , where $n(a) \propto a^{-\gamma}$. The mean simulation rate is shown in blue and the analytic expectation (Equation 2.18) is in red. This accretion is due solely to the effects of Galactic tide (no companion in this case). The equivalent mass accretion rate on the right is found by assuming an Oort cloud with $N_{\text{Oort}} = 10^{11}$ comets and $M_{\text{Oort}} = 2M_{\oplus}$. The blue shaded area shows the Poisson 1σ confidence interval of the solid blue line (mean rate).

where a companion exists, we set

$$q_{\text{initial,min}} = 6a_p. \quad (2.44)$$

In the case where there is only Galactic tide and a central white dwarf, it is somewhat more arbitrary:

$$q_{\text{initial,min}} = 15 \text{ au}. \quad (2.45)$$

This is to ensure that $q_{\text{initial,min}} \gg q_{\text{crit}} = 1R_{\odot}$. This ensures all comets will be initially integrated using the secular equation of motion and then switched over to be integrated by REBOUND until white dwarf engulfment, ejection, or reaching 1 Gyr.

2.5 Numerical White Dwarf Pollution Rate

2.5.1 Galactic Tide Only

We perform numerical simulations to explore the pollution rate of comets into a white dwarf’s Roche limit ($1R_{\odot}$) over various Oort cloud powerlaw structures (γ). Initial conditions and sampling are done according to Section 2.4.3, allowing us to sample a variety of powerlaw exponents γ . Here, we simulate with $N_{\text{comets}}^{\text{sim}} = 4 \times 10^7$ comets. Because there are no companions in this case, comets are allowed to freely migrate inward in pericentre distance due to Galactic tide.

First, we compare the simulation rate of comet accretion with analytic prediction over various Oort cloud structures. The rates are shown in Figure 2.10; the solid blue line represents simulation rates and the red-dashed line shows analytic expectations (Equation 2.18). γ on the x-axis is the Oort cloud powerlaw exponent value; the number density of Oort cloud objects scale as $n(a) \propto a^{-\gamma}$. The rate on the left is the number of accreted comets per Myr. On the right axis is the rate in g s^{-1} , assuming a fiducial Solar system Oort cloud mass and number of comets with $N_{\text{Oort}} = 10^{11}$ comets and a total cloud mass of $M_{\text{Oort}} = 2M_{\oplus}$. To get this rate, we count the total number of comets accreted, N_{accreted} , after the warm-up phase which is about 400 Myr (subsection 2.5.5). Dividing N_{accreted} by the remaining 600 Myr of simulations yields the number of comets accreted over time as shown on the left-hand side of Figure 2.10.

First, we find that simulated rates match well with the analytic expectations from O’Connor et al. (2023) based on the framework by Heisler & Tremaine (1986).

Second, the average pollution rate of comets into white dwarfs due solely to Galactic tide is $\dot{M}_Z \approx 5 \times 10^7 - 10^8 \text{ g s}^{-1}$, depending on γ . Over the course of 1 Gyr, these rates correspond to the delivery $\sim 5 \times 10^{-4} M_{\oplus}$ of materials. Thus, in the case of Galactic tide alone where the only comet removal mechanism is engulfment by the white dwarf, the Oort cloud reservoir is minimally depleted.

Finally, the 1σ blue shaded area is found by assuming that comet engulfment is a Poisson process: comet accretion into a white dwarf is a discrete event and comets arrive independently. Since we can count the total number of comets accreted, N_{accreted} , the Poisson process assumption allows us to estimate the standard deviation to be $\sigma = \sqrt{N_{\text{accreted}}}$. Recall that N_{accreted} is the total number of accreted comets counted over 600 Myr. Thus, $\sqrt{N_{\text{accreted}}}$ is the uncertainty of comets entering $1R_{\odot}$ due to our limited number of comets in our simulation (10^7 comets) over a 600 Myr timescale. In addition, we simulate a sufficiently large number of comets such that N_{accreted} is not a small integer and the 1σ interval can be meaningfully interpreted. Finally, $\sqrt{N_{\text{accreted}}}$ is based on the total number of comets in our simulation ($\sim 10^7$ comets). If our simulation contained 10^{11} comets like a full Oort cloud, the blue area would be smaller by 2 orders of magnitude. In summary, the blue shaded interval is the uncertainty of the total number of accreted comets, N_{accreted} , from

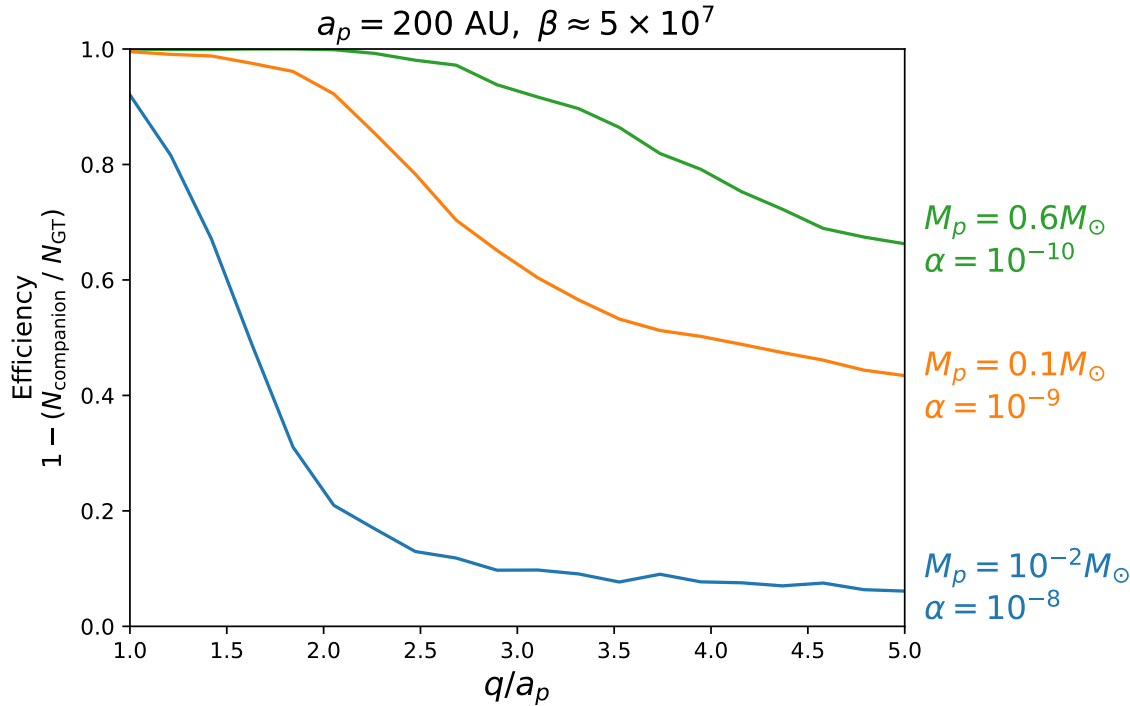


Figure 2.11: Efficiency of a companion at suppressing Galactic tide and preventing comets from entering q . These are numerical results from simulations of incoming Solar system-like Oort cloud comets. The three cases here are the same as those in Figure 2.6. The values of α for each case are shown on the right side with their corresponding colours. At $q = 5a_p$, a typical value for β is $\sim 5 \times 10^7$.

our simulation containing $\sim 10^7$ comets, over a 600 Myr timescale.

2.5.2 Efficiency of Companion-induced Precession and Scattering

We now add a companion to our simulation. We investigate the effects of different companion masses on a Solar system-like Oort cloud. Figure 2.11 shows the efficiency (Equation 2.30) over different q with varying companion mass: $M_p = 0.6, 10^{-1}, 10^{-2} M_\odot$. In contrast to Figure 2.3 previously, we now measure over a range of q . Hence, this efficiency can include the effects of both the precession and scattering barriers produced by a companion. Especially as $q \rightarrow a_p$, both precession and scattering barriers can become very important in increasing the efficiency. Efficiency is 0% when Galactic tide is the only dominant effect. Vice-versa, the efficiency is 100% when precession and scattering barriers induced by a companion can suppress all Galactic tidal effects.

First, we use the formulations of ζ to predict if the precession barrier is stronger than the Galactic tide at $q = 5a_p$. We choose to focus at $q = 5a_p$ because scattering is not important there for $M_p = 10^{-2}$ and $0.1 M_\odot$ (cf. timescales in Figure 2.6). This can also be done at

other q provided those q are within the limitations of our formulations, and scattering is not important. The three companion cases in Figure 2.11 correspond to $\alpha = 10^{-10}, 10^{-9}, 10^{-8}$. From simulations, typical incoming comets into a pericentre $q = 5a_p = 1\,000$ au have semi-major axes $a \sim 15\,000$ au, giving a $\beta \approx 5 \times 10^7$. For $\alpha = 10^{-8}$, $\zeta = 25 \gg 1$ so we expect the tide to be dominant. For $\alpha = 10^{-9}$, $\zeta \approx 1$ so we expect companion-induced angular momentum change to be important and suppress some comets' Galactic tidal torque. For $\alpha = 10^{-10}$, the precession-barrier is dominant over Galactic tide. Figure 2.6 at $q = 5a_p$ confirms these expectations.

Second, we can predict the efficiency of the precession barrier in reducing comet engulfment by using Figure 2.3 with values of (α, β) . At $\beta \approx 5 \times 10^7$, Figure 2.3 predicts about a 0% efficiency for $\alpha = 10^{-8}$. At $\alpha = 10^{-9}$, it is expected to be around 40% efficient. At $\alpha = 10^{-10}$, we expect about a 60% efficiency. We confirm these predictions with Figure 2.11 at $q = 5a_p$.

Third, scattering becomes important at $q = 3 - 5a_p$ as seen in the timescale analysis in Figure 2.6. In Figure 2.11, this corresponds to the fast increase in efficiency at that q range. In both cases, a stellar-mass companion increases the efficiency by almost 100% by $q = 1a_p$ due to strong precession and scattering barriers.

Fourth, combining precession and scattering effects, we predict that white dwarfs with a stellar-mass companion are unlikely to be able to be polluted by an Oort cloud exterior to the companion. The actual rate of white dwarf pollution rate in the presence of a stellar-mass companion is discussed later in Section 2.5.4. This is because the white dwarf – star binary case is special due to the centre-of-mass of the system being far from the white dwarf itself. Thus, to pollute a white dwarf in the presence of a stellar companion, we need to also consider the efficiency of direct collisions between incoming comets and the white dwarf itself. In contrast, with a planet companion, the centre-of-mass is close to the central white dwarf and all comets migrated to $q \sim 1R_\odot$ will be engulfed by the white dwarf.

Finally, for a planetary-mass ($M_p \leq 10M_{\text{Jup}}$) companion, planet-induced precession does not play a strong role. At $q = 5a_p$, the efficiency is still roughly 0%. Thus, effects from the planet at the q distance is not important. There is a quick increase in efficiency beginning at $q \approx 2a_p$ due to scattering. However, this increase is not as strong as the cases with stellar-mass companions to completely prevent further pollution. We will further analyse the pollution rate in the presence of a planetary-mass companion in the next subsection.

2.5.3 Planetary-Mass Companion

As discussed in Section 2.3.4, additional effects due to having a planetary companion are complicated: Having a planet can decrease the pollution rate due to the ejection loss cone, but can also potentially increase the pollution rate since comets can diffuse to higher semi-major axes to experience stronger Galactic tide. We study the effects of having a planet through numerical simulations and compare them with analytic expectations from Section

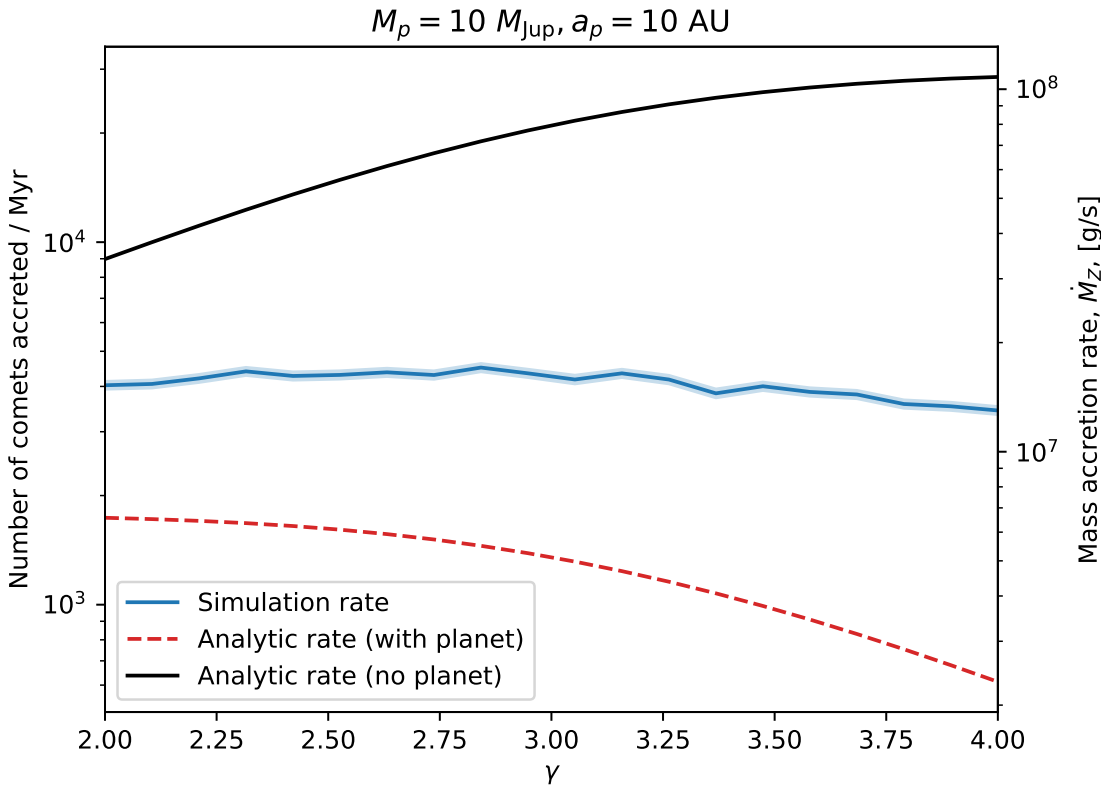


Figure 2.12: Accretion rate of comets into $q_{\text{crit}} = 1R_{\odot}$ over various Oort cloud structures γ , where $n(a) \propto a^{-\gamma}$. In this simulation, there is a $10M_{\text{Jup}}$ planetary companion at 10 au. The mean simulation rate is shown in blue and the analytic expectation is in red. The analytic rate in the case where there is no planet (Equation 2.18) is shown as a solid black line for comparison. The analytic prediction in the presence of a planet that can create a sufficiently strong ejection barrier (Equation 2.36) is shown as a red dashed line. The blue shaded area shows the Poisson 1σ confidence interval of the solid blue line (mean rate).

2.3.4. The simulation here uses the same methodology as discussed in Section 2.4 with $N_{\text{comets}}^{\text{sim}} = 10^8$ comets.

In Figure 2.12, we present the simulated white dwarf pollution rate at various γ in the presence of a $M_p = 10M_{\text{Jup}} = 10^{-2}M_{\odot}$ planet at $a_p = 10$ au. These planet mass and semi-major axis values are chosen because this configuration gives a value of $\lambda \approx 10$ (Equation 2.38), which is predicted to create a strong ejection barrier. In this figure, we find that having a planet decreases the pollution rate into $q_{\text{crit}} = 1R_{\odot}$ by about 1 order of magnitude. Assuming a Solar system Oort cloud with $N_{\text{Oort}} = 10^{11}$ comets and a total cloud mass of $M_{\text{Oort}} = 2M_{\oplus}$, the white dwarf pollution rate in this case is $\dot{M}_Z^{\text{(planet)}} \sim 10^7 \text{ g s}^{-1}$. We further observe that the simulation rate does not match analytic expectations. As seen in the plot, the simulation rate is about 2–5 times higher than the predicted analytic rate. Furthermore, the simulation rate matches better to analytic expectation at low γ than at high γ .

First, we discuss the behaviour of the analytic expectation. We notice that the analytic rate decreases as γ increases. This can be understood intuitively through analysing where comets are distributed relative to $a_{\text{crit,ej}}$. In the $\gamma = 4$ limit, comets are more centrally distributed. Thus, more comets have $a < a_{\text{crit,ej}}$. Recall that these are the comets that experience small $\Delta L < L_{\text{ej}}$ due to Galactic tide and migrate slowly in q until they are ejected through encounters with the planet. Therefore, since most comets are centrally distributed, they have $a < a_{\text{crit,ej}}$ and we analytically expect most comets to be ejected, reducing the pollution rate. On the other hand, in the $\gamma = 2$ limit, comets are less centrally distributed, some still have $a < a_{\text{crit,ej}}$ but not as many as in the case of $\gamma = 4$. Therefore, we have more comets with $a > a_{\text{crit,ej}}$. These comets are capable of experiencing a strong $\Delta L \gtrsim L_{\text{crit}}$, drifting through the ejection loss cone in one orbit, polluting the white dwarf. In other words, comet ejection is more effective at $\gamma = 4$ than at $\gamma = 2$ because there are more comets available to be ejected.

Second, we discuss why simulation rate matches with theory better at $\gamma = 2$ than at $\gamma = 4$. With the same intuition where comets are distributed, we further consider that the ejection loss cone is not 100% effective. If the barrier is 100% effective, expect all comets with $a < a_{\text{crit,ej}}$ to be all ejected. However, because the ejection loss cone is not 100% effective, some comets are capable of drifting through the ejection loss cone and eventually pollute the white dwarf. Since there are more comets at $\gamma = 4$ with $a < a_{\text{crit,ej}}$ than at $\gamma = 2$, the assumption of having a 100% effective ejection loss cone leads us to overestimate the reduction of pollution rate more at $\gamma = 4$ than at $\gamma = 2$.

Next, we analyse the distribution of accreted comets' initial semi-major axes, a_{initial} in Figure 2.13. The initial semi-major axis is shown on the x-axis because comets experience kicks in a over time.

First, in the regime where $a_{\text{initial}} < a_{\text{crit,ej}}$, the planet significantly reduces pollution rate as predicted. However, we still see comets with $a_{\text{initial}} < a_{\text{crit,ej}}$ polluting the white dwarf.

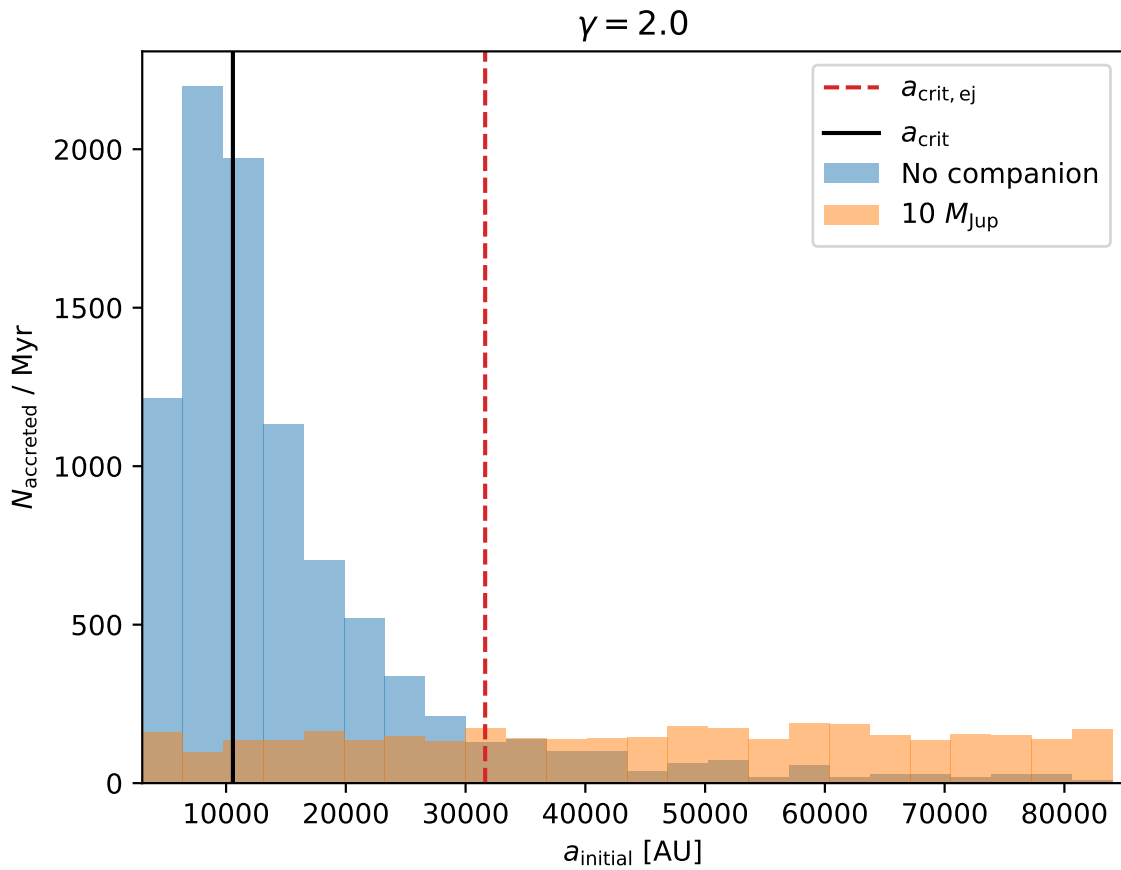


Figure 2.13: Distribution of accreted comets' initial semi-major axis at $\gamma = 2$. Histograms are counted per a_{initial} bin. The blue histogram shows distribution when there is Galactic tide only. The orange histogram shows the case with Galactic tide and a $10 M_{\text{Jup}}$ planet. Vertical lines show $a_{\text{crit}, \text{ej}}$ (dashed) and a_{crit} (solid).

We find that the ejection loss cone barrier is not 100% effective. Therefore, the assumption in Equation 2.36 that the pollution rate does not have any contribution with comets from $a < a_{\text{crit},\text{ej}}$ gives an underestimate of the pollution rate.

Second, in the regime where $a_{\text{initial}} \leq a_{\text{crit},\text{ej}}$, the number of comets capable of polluting the white dwarf increases steadily. As $a_{\text{initial}} \rightarrow a_{\text{crit},\text{ej}}$, comets need a smaller kick in Δa to deliver them over into the $a \geq a_{\text{crit},\text{ej}}$ regime where Galactic tide can induce a strong enough ΔL to drift them through the ejection loss cone. On the other hand, in the $a_{\text{initial}} \ll a_{\text{crit},\text{ej}}$, comets will need to experience multiple interactions with the planet that increase their semi-major axis, but not strong enough to eject them.

Third, as a increases beyond $a_{\text{crit},\text{ej}}$, the pollution rate is higher than in the case of no planet. There are several mechanisms to explain this. First, these comets can be kicked into higher a , allowing stronger ΔL to migrate further in, as described in Section 2.3.4. Second, these comets have lower energy (because of large a) and can be kicked into much smaller orbits. At that point, they can be excited to high eccentricity and pollute the white dwarf with effects like von Zeipel-Kozai-Lidov or inverse Kozai. Third, they have lower energy and are also easier to be ejected. However, in their last inbound passage, they have pericentre distances sufficiently low to pollute the white dwarf. None of these additional dynamics would be possible without perturbations to the comet. Without additional perturbations like a planet, a comet at $a = 50\,000$ au for example, will stay there and if it cannot reach q_{crit} during a Galactic tide cycle, will never be able to do so. Hence, when we assume in Equation 2.36 that the pollution rate strictly follows Γ_f based on a fixed distribution of a_{initial} , a lot of these additional dynamics are ignored giving an incorrect rate in that regime. As we have seen, the contribution in region $a > a_{\text{crit},\text{ej}}$ is higher than expected in Equation 2.36 leading to another source of underestimation of pollution rate.

In summary, we find that the existence of a planetary-mass companion significantly reduces the pollution rate for comets with initial semi-major axes $a_{\text{initial}} \leq a_{\text{crit},\text{ej}}$ as predicted by O'Connor et al. (2023). However, we find that this reduction is not 100% effective, that comets experience rich dynamics, and that beyond $a_{\text{initial}} > a_{\text{crit},\text{ej}}$ the pollution rate does not simply follow the full loss cone rate Γ_f . That being said, when comparing the overall rates in Figure 2.12, the analytic predictions by O'Connor et al. (2023) still yield a good order of magnitude estimate for the pollution rate, although it can be off by a factor of 2-5 times. We find that the white dwarf pollution rate in the presence of a planetary companion is reduced by one magnitude to $\dot{M}_Z^{(\text{planet})} \sim 10^7$ g s⁻¹, assuming a Solar system Oort cloud.

2.5.4 White Dwarf – White Dwarf Binary

An interesting question is how a white dwarf – white dwarf binary would be polluted by an Oort cloud reservoir. The formation of planetary systems around binary stars have been studied in Ledda et al. (2023); Columba et al. (2023), their dynamical evolution is analysed in Kostov et al. (2016), and these systems have exciting detection prospects across the

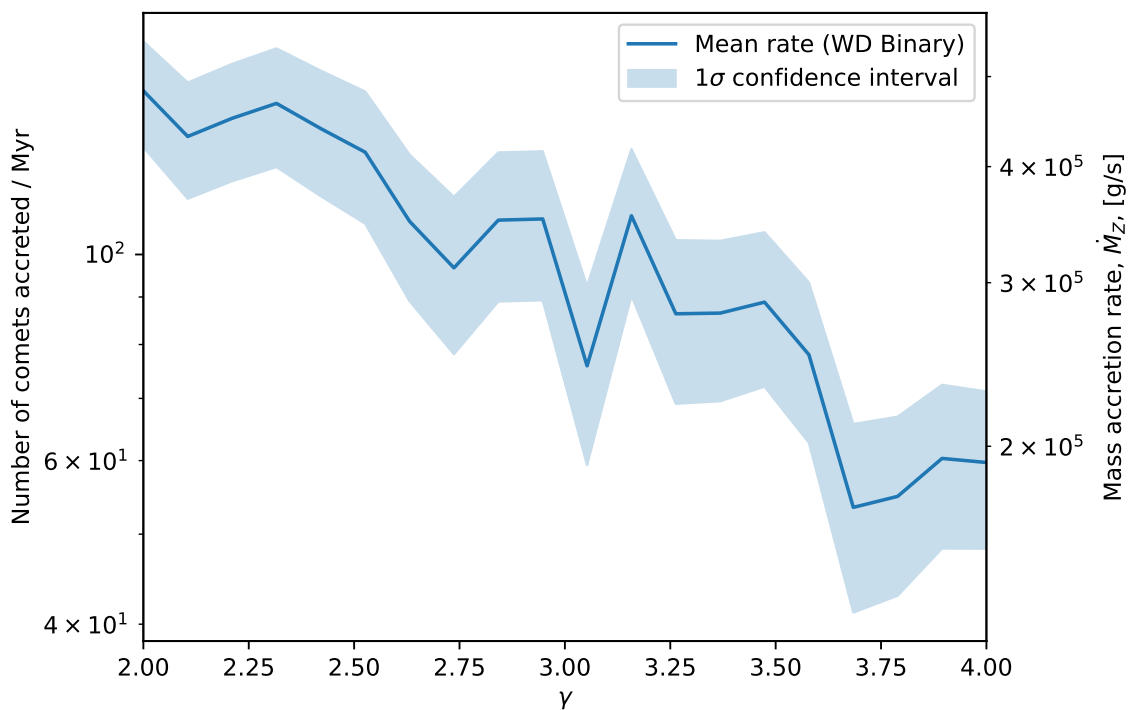


Figure 2.14: Accretion rate of comets into one star in a white dwarf – white dwarf binary over various Oort cloud structures γ . The binary is in a circular orbit and separated by 10 au. The pollution rate in g s^{-1} is shown on the right axis, assuming a Solar system Oort cloud.

Galaxy and beyond using gravitational waves astronomy as demonstrated in Korol et al. (2017); Tamanini & Danielski (2019); Danielski & Tamanini (2020).

In our dynamical analysis, double white dwarfs are particularly interesting because unlike the planetary companion case, the white dwarf is very far from the centre of mass when its companion has comparable mass. In this scenario, pollution is governed by direct collisions between incoming comets and the white dwarfs on their orbits.

Assume we have two white dwarfs, separated by a_p on circular orbits. The Safronov number can be used to estimate how probable it is to expect collisions of incoming comets on highly eccentric orbits:

$$\Theta = \frac{v_{\text{esc}}^2}{v_c^2} = 2 \cdot \frac{M_p}{M_* + M_p} \cdot \frac{a_p}{R} \approx 2 \times 10^3 \quad (2.46)$$

where v_{esc} is the escape velocity from the companion's surface (at distance R) and v_c is the circular speed at the companion's semi-major axis. We set $R = 1R_\odot$ for the tidal radius where comets are captured by a white dwarf and $a_p = 10$ au. Since $\Theta \gg 1$, we predict that collisions into the tidal radius are unlikely (Tremaine, 2023).

In Figure 2.14, we show the pollution rate of comets into one white dwarf in a white dwarf – white dwarf binary separated by $a_p = 10$ au at various γ . In the simulation here, we directly check every timestep if a comet's distance is within a white dwarf's tidal radius. The switching point between secular integration and direct integration with REBOUND is increased to $q = 6a_p$ to accurately capture all dynamics between comets and a stellar-mass companions (see Figures 2.4, 2.6). Here, we find that the pollution rate is significantly reduced by 2.5-3 orders of magnitude compared to the Galactic tide-only case. Assuming a Solar system Oort cloud, the pollution rate is about $2 - 4 \times 10^5$ g s $^{-1}$. Note that this is just below the detection limit at $\sim 5 \times 10^5$ g s $^{-1}$. This rate is low due to a combination of effects. First, as shown earlier, $\zeta \sim 0.1$ and comets experience a precession torque reducing the effectiveness of Galactic tide in exciting incoming comets. Second, comets in the empty loss cone cannot slowly migrate inwards as they are strongly scattered through multiple encounters with the strong scattering barrier. Third, comets that can reach sufficiently low $q \approx a_p$ are still unlikely to collide with the white dwarf since the Safronov number is very high.

Next, we consider two extreme cases: a very close white dwarf – white dwarf binary and a more widely separated one. If the separation between white dwarfs is smaller, we expect the pollution rate to increase, peaking at half of the normal Galactic tide-only rate. For example, take the limit where the white dwarfs are separated by only a few solar radii, then they are both near the centre of mass and will be impacted by all incoming comets. Since there are two stars, the pollution rate (from the Galactic tide only case) will be reduced by half as comets are equally likely to collide with either star. If the separation is larger, the Safronov number, $\Theta \propto a_p$, would increase and collisions would be even more unlikely.

Thus, we expect a decrease in pollution rate as a_p increases.

Finally, the results here also give an order of magnitude estimate of Oort cloud comet pollution rate for other stellar-mass companions, assuming $M_p \sim M_*$.

2.5.5 Pollution Over Time

In this subsection, we analyse the pollution rate over time to study if the Oort cloud as a reservoir can consistently maintain the white dwarf pollution rate over a Gyr timescale.

In Figure 2.15, we show the pollution rate over time for $\gamma = 2.5$ and 3.5 in the case of Galactic tide only (no companion). During the first ~ 400 Myr, we observe a “warm-up” phase. Intuitively, this is because it takes time for comets to experience Galactic tide, migrate in q , and arrive at q_{crit} . The timescale of 400 Myr is consistent with the typical Galactic tide cycle period, which is on the order of 300 Myr (estimated in Equation 18 in [Heisler & Tremaine, 1986](#)). After the first 400 Myr, we find that the simulation rate matches well with analytic predictions. In addition, the rate stays constant with no signs of reduction over a 1 Gyr timescale. Thus, without a companion, an Oort cloud is capable of delivering materials into the white dwarf tidal disruption zone at a constant rate between $\dot{M}_Z \approx 5 \times 10^7 \text{ g} \cdot \text{s}^{-1}$ and $10^8 \text{ g} \cdot \text{s}^{-1}$ over a 1 Gyr timescale.

Figure 2.16 shows the pollution rate over time for $\gamma = 2.5$ and 3.5 in the case of Galactic tide and a planetary-mass companion. The simulation rate does not match as well with the analytic prediction (Equation 2.37). Recall that there are some limitations in the analytic predictions for white dwarf pollution rate in the presence of a companion since this framework does not include additional complicated effects induced by scattering. This is typically off by about a factor of 2-3, consistent with what is seen in the previous subsection.

Furthermore, we again find that the accretion rate does not significantly decline over a 1 Gyr timescale. Note that in the case where $\gamma = 2.5$ (bottom panel), the accretion decreases by about a factor of 3-4 over a 1 Gyr timescale. Note that in the context of white dwarf pollution rate which ranges 5 orders of magnitude, this reduction factor of 3-4 over a Gyr timescale is not significant. The reduction factor for $\gamma = 3.5$ is even less, where the accretion rate only reduces by about a factor of 2. This can be explained by the distribution of comets. In the case of $\gamma = 2.5$, there are more comets at larger semi-major axes than $\gamma = 3.5$ and thus, are easier to be ejected. Hence, the reservoir depletes quicker at low γ than at high γ . None of this is observed in the Galactic tide only case because there, comets’ semi-major axes are conserved and the reservoir does not get depleted by ejection.

Finally, there are variations over time in the accretion rate for both cases with and without planet. These variations are due to the limited number of comets in our simulation. Similar to the discussion in subsection 2.5.1, the variations over every Myr bin are because of our resolution-limited simulation ($\sim 10^7$ comets). This is about 4 orders of magnitude smaller than the actual Oort cloud population of 10^{11} comets. Scaling these to a full Oort cloud, the variations would be smaller by 2 orders of magnitude. We observe that

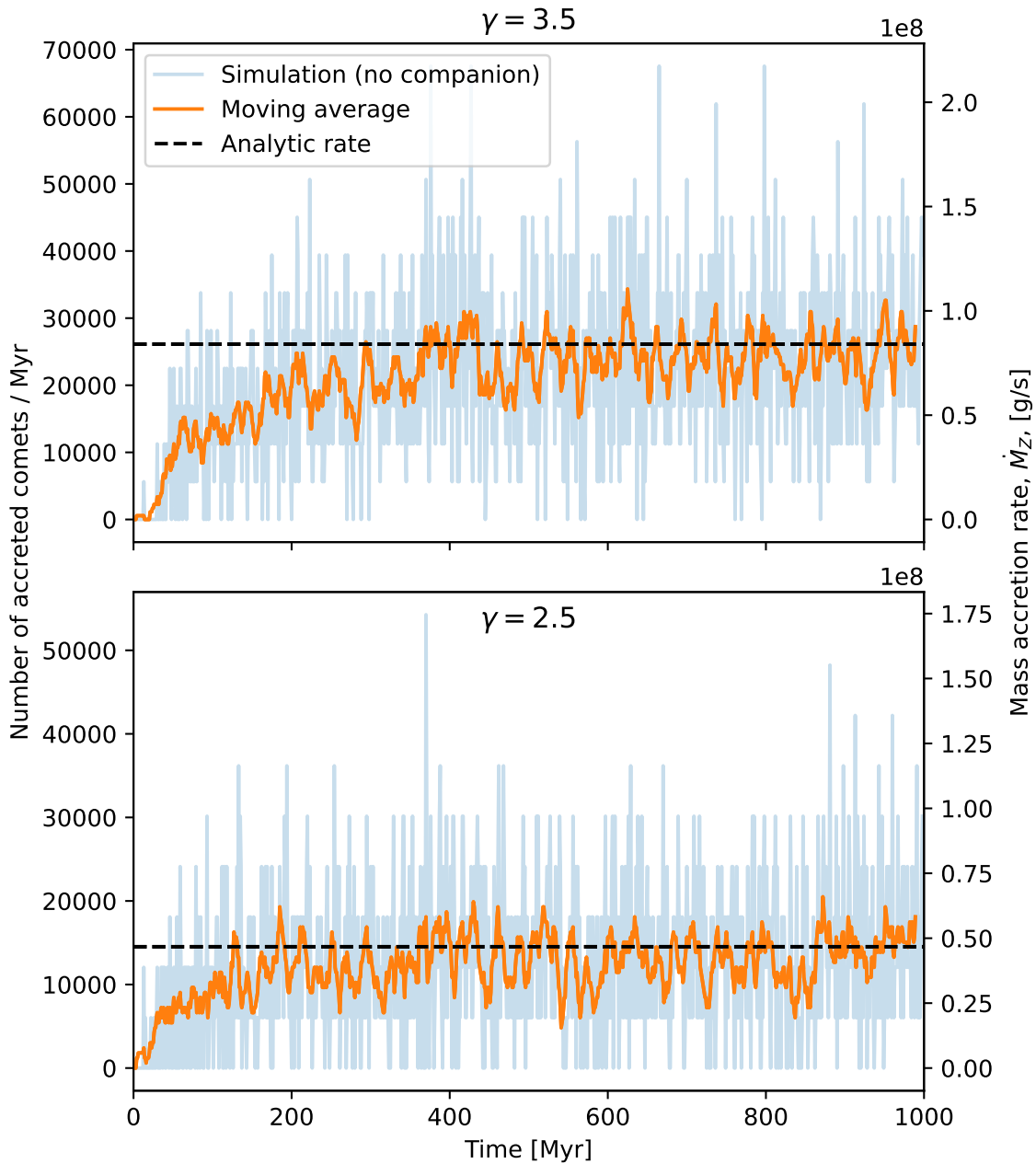


Figure 2.15: Accretion rate over a 1 Gyr timescale from Oort clouds with $\gamma = 2.5$ and 3.5 . There are no companions in this case. Accretion rates from simulations (red) is binned per Myr. Analytic rates are shown as horizontal blue lines. A moving average with a sliding window of 10 Myr is shown in grey. The accretion rate can be sustained over a 1 Gyr time period. An equivalent mass accretion rate on the right is found by assuming an Oort cloud with $N_{\text{Oort}} = 10^{11}$ comets and total cloud mass $M_{\text{Oort}} = 2M_{\oplus}$.

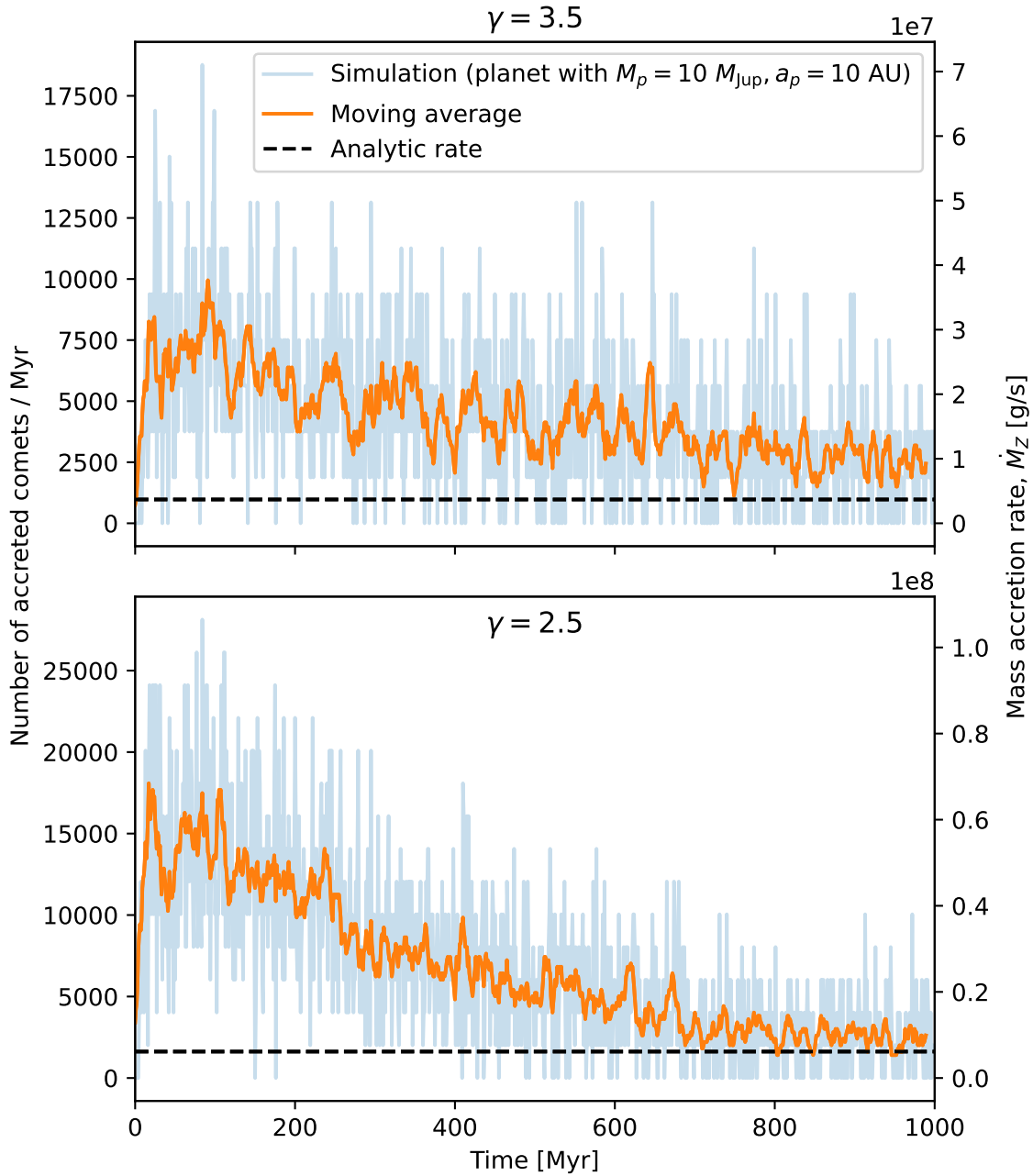


Figure 2.16: Accretion rate over a 1 Gyr timescale from Oort clouds with $\gamma = 2.5$ and 3.5 . There is a planetary-mass companion with $M_p = 10 M_{\text{Jup}}$ at $a_p = 10$ au. Accretion rates from simulations (red) are binned per Myr. Analytic expectations are shown as horizontal blue lines. A moving average with a sliding window of 10 Myr is shown in grey. The accretion rate is slightly decreased over the 1 Gyr period, but no more than 0.5 dex.

the variations per Myr bin in our simulations (Figures 2.15, 2.16) are within an order of magnitude of the mean. Thus, for a full Oort cloud, these variations would be within 10^{-1} of the mean rate.

In summary, we find that in the presence of a planetary-mass companion and Galactic tide, an Oort cloud is capable of delivering materials at a relatively constant rate $\dot{M}_Z^{(\text{planet})} \approx 1 - 3 \times 10^7 \text{ g} \cdot \text{s}^{-1}$ over a 1 Gyr timescale. Depending on γ , this rate may be reduced by a factor of 3-4 over this timescale.

2.6 Discussion

Figure 4 of [Blouin & Xu \(2022\)](#) presents observed white dwarf pollution rates for white dwarfs with ages ranging from 1 Gyr to 8 Gyr. In this Figure, they show that the pollution rate ranges between 10^5 to 10^{10} g s^{-1} , with the majority ranging between 10^6 to 10^8 g s^{-1} . They also find that pollution rates decrease by no more than one order of magnitude over the course of 8 Gyrs. Recent observations by [Mullally et al. \(2024\)](#) find giant planet candidates around two polluted white dwarfs with ages 1.5 and 5 Gyrs. These potential planets are predicted to have masses $1 - 7M_{\text{Jup}}$ and separations $10 - 35 \text{ au}$. If these planets are confirmed, they would point towards having giant planets not significantly reducing white dwarf pollution rate.

Through simulations, we find that an Oort cloud (with total number of objects and total mass like the Solar system) is capable of delivering materials into a white dwarf Roche radius at a rate from 5×10^6 to 10^8 g s^{-1} , depending on the existence of a planetary companion. These rates are above the current detection limit at $\sim 5 \times 10^5 \text{ g s}^{-1}$. Furthermore, these pollution rates can be sustained and decrease no more than a factor of 3-4 (in the existence of a planet) over a Gyr timescale. We find that the simulated rates found here can explain a significant portion of observed pollution rates (e.g., [Blouin & Xu, 2022](#)) and sustain that rate over a Gyr timescale. Our results further show that Oort cloud comets can pollute white dwarfs in evolved systems with giant planets, potentially in the white dwarf systems with candidate planets by [Mullally et al. \(2024\)](#).

In the scenario of white dwarf-white dwarf binary with separation $a_p = 10 \text{ au}$, the pollution rate is $\approx 3 \times 10^5 \text{ g s}^{-1}$, below the detection limit. This rate is significantly lower than in other cases due to a combination of precession, scattering, and the low chance of collisions. This rate can be used as an order of magnitude estimate for other stellar-mass companion cases where $M_p \sim M_*$.

We note that an advantage of the mechanism and reservoir presented here is that it is time-independent, in contrast to other works (cf. [Debes et al., 2012](#); [Mustill et al., 2014](#); [Smallwood et al., 2018](#)). The pollution rate from an Oort cloud would only decrease if the reservoir is significantly depleted. Over an 8 Gyr timescale with a comet injection rate of $\sim 10^8 \text{ g s}^{-1}$, an Oort cloud would only deplete by roughly $5 \times 10^{-3} M_{\oplus}$ worth of materials,

which is much less than the current Solar system Oort cloud reservoir of $2M_{\oplus}$. In the presence of other perturbers like a planet or stellar flybys, the Oort cloud reservoir would be depleted faster due to ejection. As shown previously, with a planet we find that the pollution rate can decrease at most by a factor of 3-4 in the course of 1 Gyr.

We further discuss below the scalability of the Oort cloud, the potential impacts of stellar flybys, concerns about using the Oort cloud as a reservoir for white dwarf pollution, the effects of very close companions, wide companions, and delivery from an accretion disc into a white dwarf.

2.6.1 Robustness of the Oort cloud

The results in this thesis can be scaled to other exo-Oort clouds with different N_{Oort} and M_{Oort} by:

$$\Gamma_{\text{total}}^{\text{new}} = \Gamma_{\text{total}} \cdot \left(\frac{N_{\text{Oort}}^{\text{new}}}{10^{11}} \right) \quad (2.47)$$

$$\dot{M}_Z^{\text{new}} = \dot{M}_Z \cdot \left(\frac{N_{\text{Oort}}^{\text{new}}}{10^{11}} \right) \left(\frac{M_{\text{Oort}}^{\text{new}}}{2M_{\oplus}} \right)^{-1}. \quad (2.48)$$

The other parameters of an Oort cloud, γ , a_1 (inner edge of the Oort cloud) and a_2 (outer edge), do not significantly affect the pollution rate. First, we studied various γ in this chapter and found that γ does not affect the pollution rate by more than a factor of 2 (Figures 2.10, 2.12, 2.14). Second, we fixed the inner semi-major axis edge at $a_1 = 3000$ au, based on the Solar system Oort cloud. O'Connor et al. (2023) find that varying a_1 changes the pollution rate by at most a factor of 4 for $10^3 \text{ au} \leq a_1 \leq 10^4 \text{ au}$. Third, we fixed the outer semi-major axis edge at $a_2 = 85000$ au. This is because we have shown that this outer edge is a natural consequence of enforcing the boundary condition of the white dwarf Hill sphere at 0.8 pc. Thus, a_2 would not be different in another Oort cloud around a typical white dwarf.

2.6.2 Stellar Flybys

Stellar flybys are an additional mechanism which can both reduce and increase pollution rate. First, a strong flyby (slow with a small impact parameter) could potentially induce strong scattering and significantly deplete an Oort cloud. We do not consider stellar flybys in this chapter, thus it is unclear to us how flybys would deplete the Oort cloud reservoir. However, Higuchi & Kokubo (2015) show that in simulations of Oort clouds with Galactic tide and impulsive stellar flybys over different γ structures, the e -folding decay timescale for the Oort cloud population is 4 – 18 Gyrs. Thus, even with stellar flybys, we still do not expect a strong (more than one order of magnitude) decrease in pollution rate within a Gyr timescale because the reservoir is not significantly depleted.

Second, distant flybys can stochastically perturb comets and cause them to diffuse into small pericentres. Hence, weak flybys can act as another mechanism, in addition to Galactic

tide, to deliver comets from the Oort cloud into small pericentre. This was first explored by [Heisler & Tremaine \(1986\)](#) and used by [O'Connor et al. \(2023\)](#) to estimate that the effects distant flybys contribute to the comet injection rate is on the order of the pollution rate from Galactic tide alone.

Third, a strong flyby can cause comet showers ([Heisler, 1990](#)). In the Solar system, these showers increase the injection rate of Oort cloud comets into $q \sim 10$ au. In the Solar system these showers have increased injection rate as much as two orders of magnitude within a few Myr – much shorter than the Galactic tidal timescale. The precession and scattering barriers we discussed earlier cannot prevent these comet showers because comets are induced into low pericentre within one orbital period. In the loss cones formulation, this is equivalent to a significant number of comets in the filled loss cone regime and are able to bypass both angular momentum and scattering barriers. In the context of exo-Oort cloud around white dwarfs, this is perhaps another mechanism to not only deliver materials but also potentially explain the observed spread in pollution rate (5 orders of magnitude).

2.6.3 Surviving Stellar Evolution

One major concern of having an Oort cloud as a potential material reservoir for white dwarf pollution is that the Oort cloud might be ejected during the evolutionary process from the main sequence to white dwarfs. A comet at 10 000 au has a typical orbital speed of ~ 0.3 km s $^{-1}$. This is lower than the typical speed the natal, anisotropic recoil kick a white dwarf experiences during its rapid mass loss phase, which is about 0.75 km s $^{-1}$ ([El-Badry & Rix, 2018](#)). The star also undergoes mass loss at the same time. Thus, it is a concern if objects in the Oort cloud can be kept bound to its central star. [O'Connor et al. \(2023\)](#) also investigate this question to find that a post-main-sequence evolution Oort cloud retains about 10% of its original objects, with a fairly complex cloud structure. Thus, an Oort cloud can remain bound, albeit with fewer materials, after an anisotropic mass loss during stellar evolution.

[O'Connor et al. \(2023\)](#) also find that the pollution rate after main-sequence evolution is reduced by about an order of magnitude for a typical kick strength of 0.75 km s $^{-1}$. Hence, if we assume a more complicated post-main-sequence evolution Oort cloud where the original Oort cloud is like our current Solar system Oort cloud, the pollution rates in this chapter are reduced by another order of magnitude. This gives the post-stellar evolution pollution rate to be in the range between 10^6 to 10^7 g s $^{-1}$, depending on the existence of a planet. If the companion is stellar-mass, the pollution rate is much lower at $\sim 3 \times 10^4$ g s $^{-1}$.

However, the mass and structure of exo-Oort clouds in other main-sequence or post-main-sequence systems are unknown. This could point to a much wider range of Oort clouds' total mass or number of objects. In addition, Solar system Oort cloud formation and characterisation remains an active area of research. For example, simulations of Solar system Oort cloud formation (e.g., [Vokrouhlický et al., 2019](#)) include a very specific

migration history of the planets following the Nice model. The Solar system’s Oort cloud total mass, number of objects, and chemical composition are heavily dependent on the early configuration of the giant planets. Thus, an exo-Oort cloud might very well be different in number of objects, mass, and chemical composition from what we currently observe of our own Oort cloud. Therefore, it is unclear how well we can extrapolate the mass of the post-main sequence Solar system Oort cloud to other white dwarf planetary systems.

With the uncertainty of formation models and complicated post-main-sequence evolution, it is unclear how exo-Oort clouds look around white dwarfs. Therefore, in this chapter, we choose to simplify by only answering the question if an exo-Oort cloud with a $n(a) \propto a^{-\gamma}$ radial density profile — like the one currently existing in the Solar system as we currently understand it — can pollute a white dwarf.

2.6.4 Cometary Composition

Another major concern for the Oort cloud as a potential material reservoir for white dwarf pollution is that we mostly observe volatiles-poor polluted white dwarf atmospheres (e.g., Jura, 2006; Jura & Xu, 2012; Doyle et al., 2019), with accreting material composition resembling of asteroids or rocky planets in the Solar system. These observed compositions are inconsistent with the volatiles-rich, icy bulk composition of typical Solar system comets. Solar system Oort cloud comets are expected to be mostly ice because they are ejected from the protoplanetary disk beyond the ice line due to interactions with Uranus and Neptune (Vokrouhlický et al., 2019). We discuss ways to reconcile these observations with our numerical predictions that Oort clouds, at least those like our own, should be able to pollute their white dwarf.

First, the composition of objects in the Oort cloud in our Solar system and especially in other exo-Oort clouds might not be composed of only icy comets. In our own Solar system, for example, Vida et al. (2023) recently observe a small rocky object with origins from the Oort cloud. Simulations of the Solar system Oort cloud indicate that about 4% of objects (up to 8×10^9 objects) are rocky asteroids (Shannon et al., 2015). In addition, our own Oort cloud is “icy” and volatile-rich because of the early configuration of the giant planets. Because of this, it is also unclear regarding other details of Oort clouds in other systems. We have observations of protoplanetary discs with diverse arrangements of giant planets configurations. These giant planets do not always stay fixed beyond the ice line. Thus, it is uncertain if objects interacting with different giant planets to be injected into exo-Oort clouds are also formed within or outside of the ice line (e.g., Doner et al., 2024). Therefore, it is problematic to assume Oort clouds around white dwarfs or even in our own Solar system to be solely composed of volatile-rich, icy comets.

To add to the complexity, we also observe some polluted white dwarfs with volatiles in their atmospheres (e.g., Farihi et al., 2013; Klein et al., 2021; Doyle et al., 2021). This includes the detection of a Kuiper Belt-analogue composition in a polluted white dwarf

(Xu et al., 2017). In addition, Johnson et al. (2022) observe a polluted white dwarf with compositions that are composed from both rocky and icy bodies. They conclude that the unusual composition can be explained if the white dwarf is polluted by two parent bodies, with a mix of Mercury-like composition and an icy Kuiper Belt-analogue. In the context of our discussion, if Oort clouds are composed of both rocky asteroids and icy comets as mentioned previously, they can potentially explain all these diverse composition observations.

Brouwers et al. (2023a) explore in detail the accretion of comets. They find that accretion can occur in two stages: the ices may sublime and accrete first before refractory minerals can reach the star. Thus, the composition signature on a white dwarf's atmosphere may vary over time in a single accretion event, potentially also explaining the composition diversity in polluted white dwarfs' atmospheres.

2.6.5 Accretion Disc Delivery

We only study mechanisms to deliver comets into the Roche radius. After a comet achieves a distance $d \leq 1R_{\odot}$, we assume that it is tidally disrupted and formed an accretion disc around a white dwarf (Koester et al., 2014). Poynting-Robertson drag can deliver materials from an accretion disc into white dwarfs at the rate 10^8 g s^{-1} (Rafikov, 2011). However, we observe pollution rate up to 10^{10} g s^{-1} on white dwarfs. It is difficult to explain material delivery at such rates from an accretion disc. Okuya et al. (2023) show that the Poynting-Robertson delivery rate can be enhanced in the existence of some volatiles, to bring the delivery rate above 10^8 g s^{-1} . Relating to our discussion of volatiles, it may be necessary to have some icy bodies to enhance the accretion disc delivery rate to explain some observed higher pollution rates.

2.6.6 Very Close Companions

So far, we only considered companions with semi-major axes on the order of $a_p = 10$ or 100 au. There are observational evidence for companions at these semi-major axes (e.g., Veras et al., 2020; Blackman et al., 2021; Mullally et al., 2024). On the other hand, Vanderburg et al. (2020) present observational evidence for a $M_p \sim 1M_{\text{Jup}}$ planet orbiting its white dwarf at $a_p \sim 4R_{\odot}$. Note that the system by Vanderburg et al. (2020) is actually in a hierarchical quadrupole system consisting of the white dwarf, the planet, and two M dwarfs. The analyses below only serves as an illustrative example of how a white dwarf with a very close-in planet would affect the dynamics of an incoming comet. In addition, Gänsicke et al. (2019); Veras (2020) present evidence for a planet at $a_p \sim 15R_{\odot}$ orbiting a volatile-rich polluted white dwarf. These observations require us to analyse the scenario of a planet on a very small orbit.

First, we analyse if the effects induced by this planet is important. For the planet found by Vanderburg et al. (2020), we have $\zeta \approx 5 \times 10^3$, assuming typical incoming comets

$a \sim 10^4$ au. Since $\zeta \gg 1$, torque induced by this planet does not overcome Galactic tide. In addition, since the planet is so close to the white dwarf, the ejection loss cone does not significantly cover phase space more than the engulfment loss cone (Equation 2.37). Thus, the ejection loss cone should not significantly reduce the pollution rate. Therefore, the existence of a close-in planet with the configurations as found by [Vanderburg et al. \(2020\)](#) cannot reduce the pollution rate of Oort cloud comets. We expect the pollution rate to be decreased by about a factor of 2 because comets are equally likely to collide into either body. This is because we have two close central bodies, and the Safronov number for this planet is $\Theta \approx 0.01 \ll 1$. Finally, the same conclusions apply to the system found by [Gänsicke et al. \(2019\)](#).

We discussed the case for close stellar companions earlier in Section 2.5.4, where we expect the pollution rate to be reduced by half. Note that for white dwarfs with close stellar companions (with separations on the order R_\odot to aus), the metal pollution on those white dwarfs can also be explained by stellar winds from their companion ([Zuckerman et al., 2003; Zuckerman, 2014](#)) and not necessarily by another reservoir like exo-Oort clouds.

We show using our analysis framework that close-in companions, either stellar or planetary, cannot significantly reduce Oort cloud comet delivery rate into a white dwarf. The analysis can be applied to other systems with varying companion masses and separations; except for when the separations are large, $a_p \geq 300$ au.

2.6.7 Widely Separated Companions

For planets or stellar-mass companions widely separated ($a_p \geq 300$ au), our analysis cannot be applied, at least for Oort clouds with an inner semi-major axis at $\sim 3\,000$ au like ours. As discussed earlier in various contexts, we typically assume that comets that encounter a companion have high eccentricity, $e \sim 1$ (or equivalently, $a \gg a_p$). Thus, we regularly expand expressions in this limit for simplifications. This assumption is also used in the analytic Galactic tide loss cone theory.

Observationally, there is evidence for distant companions, both planetary and stellar mass, around white dwarfs. [Luhman et al. \(2011\)](#) provide observational evidence for a planetary companion with mass $M_p = 7M_{\text{Jup}}$ at a separation of $a_p \approx 2\,500$ au. [Zuckerman \(2014\)](#) presents a catalogue of 17 white dwarfs with companions separated by more than 10^3 au. In addition, the white dwarf-planet system we mentioned earlier observed by [Vanderburg et al. \(2020\)](#) is in fact a hierarchical triple system. There is a distant star at $\sim 10^3$ au forming a triple system with the white dwarf-planet binary.

Relating these observations to white dwarf pollution, [Wilson et al. \(2019\)](#) find that the occurrence rate of single polluted white dwarfs and polluted white dwarfs with wide stellar companions are the same. The fact that there are polluted white dwarfs in wide binaries is in contrast with our prediction in Section 2.5.4. We expect that wide binaries should have significantly reduced pollution rates (below detection limit) due to the difficulty of direct

collisions because of a high Safronov number. An implication of this could be that Oort clouds around wide stellar binaries are not similar to ours. In addition, the existence of a distant massive object, potentially embedded within the Oort cloud itself, could change those exo-Oort cloud structures significantly from our own Solar system Oort cloud.

One dynamical study involving wide binaries around white dwarfs is performed by [Bonsor & Veras \(2015\)](#). They propose that due to Galactic tidal effects, a distant binary companion periodically becomes excited to high eccentricity bringing it closer to the white dwarf. During these close approaches, the stellar companion scatters other reservoirs, like an exo-asteroid belt or an exo-Kuiper Belt, into a white dwarf and induces pollution.

With an abundance of companions at all mass scales with orbital separations $a_p \geq 10^3$ au and observations of polluted white dwarfs in wide binaries, it remains interesting if and how these distant companions affect their Oort cloud and influence the observed white dwarf pollution rate.

2.7 Conclusion

We have studied if an exo-Oort cloud can pollute a white dwarf with Galactic tide and a companion over a 1 Gyr timescale through numerical and analytic methods. We analysed cases when there is Galactic tide only, when the companion is a star, and when the companion is a planet. We studied the dynamics of the companion, namely precession torque induced on exo-Oort cloud comets and the kick in semi-major axis they experience close encounters with the companion. We make use of a fast integration method to integrate 10^8 comets over 1 Gyr of simulation time.

The conclusions presented below assume a Solar system Oort cloud, with total cloud mass $M_{\text{Oort}} = 2M_{\oplus}$ containing $N_{\text{Oort}} = 10^{11}$ objects. These pollution rate results are scalable to other exo-Oort clouds with different masses and numbers of objects. Our main conclusions are:

1. In the absence of any companions, exo-Oort clouds like our own Solar system's can pollute white dwarfs at a rate $\sim 5 \times 10^7 - 10^8 \text{ g s}^{-1}$.
2. We find that the dimensionless quantity

$$\zeta \sim \frac{32\pi\sqrt{2}}{3} \cdot \frac{\rho_0}{M_{\text{reduced}}/a_p^3} \cdot \left(\frac{q}{a_p}\right)^{3/2} \cdot \left(\frac{a}{a_p}\right)^{7/2} \quad (2.49)$$

is a good indicator of the relative importance of the angular momentum change induced by a companion compared to that of Galactic tide (see Figure 2.3). When $\zeta \lesssim 1$, torque from a companion dominates Galactic tide and reduces comet migration. When $\zeta \gg 1$, only Galactic tide is important.

3. Stellar-mass companions with masses $M_p \geq 0.1M_\odot$ reduce the white dwarf pollution rate to $\sim 3 \times 10^5 \text{ g s}^{-1}$ due to their strong angular momentum and scattering barriers, and a low-likelihood of direct collisions with the white dwarf.
4. Planetary-mass companions significantly reduce white dwarf pollution rate as predicted by [O'Connor et al. \(2023\)](#). However, we find the simulation pollution rate to be 2-5 times higher than predicted by [O'Connor et al. \(2023\)](#). We attribute this discrepancy to some limitations in the modified loss cone theory. Namely, the modified loss cone theory assumes a 100% effective ejection barrier. The modified loss cone also cannot account for migration in comet semi-major axes, which occurs when comets interact with the planet in the diffusive scattering regime. That said, we still find that the modified loss cone is a reasonable order of magnitude estimate. With the existence of a planet and in the absence of stellar flybys, we find that the white dwarf pollution rate due to Oort cloud objects is reduced to about $\sim 10^7 \text{ g s}^{-1}$, assuming a Solar system Oort cloud.
5. The powerlaw density profile structure of the Oort cloud does not significantly affect (by more than half an order of magnitude) the pollution rate.
6. The pollution rate without a planet stays constant over a 1 Gyr timescale. The pollution rate with a planet can decrease by a factor of ~ 3 over a 1 Gyr timescale.

We discussed the advantages of the Oort cloud and the impacts of stellar flybys. We also discussed two major concerns of using the Oort cloud as a potential reservoir for white dwarf pollution: (i) the retention of Oort cloud objects after a strong anisotropic natal kick experienced by white dwarfs and (ii) observations of volatiles-poor white dwarfs. There are uncertainties in our current understanding of the Solar system and extrasolar Oort cloud's structure and composition. However, these uncertainties could potentially explain the diversity in white dwarf pollution rate and composition. Finally, we applied our analysis framework in the context of observational evidence of close companions (orbits on the order of days) to predict their minimal effects on Oort cloud pollution, and stressed how we cannot apply this framework to widely separated companions (separation $\geq 10^3 \text{ au}$).

We show that exo-Oort clouds can potentially pollute old white dwarfs at observed rates over Gyr timescales, depending on the existence of a companion and Oort cloud structures. However, one single reservoir and mechanism may not necessarily explain all instances of white dwarf pollution ([Veras et al., 2024](#)). With further observations of polluted white dwarfs and characterisation of their companions (e.g., using Gaia as shown in [Sanderson et al., 2022](#)), our results can be applied to constrain sources of white dwarf pollution.

Acknowledgements

We thank the reviewer Christopher O'Connor for helpful comments. We thank Scott Tremaine for a careful reading of the manuscript and valuable feedback. We thank Norm Murray, Sam Hadden, Dimitri Veras, Yanqin Wu, Garrett Brown, and Michael Poon for insightful discussions. This research has been supported by the Natural Sciences and Engineering Research Council (NSERC) Discovery Grant RGPIN-2020-04513.

Chapter 3

Numerical Methods: Fast Integration and Adaptive Timestep

Halley produced the Elements of the Calculation of the Motion of the two Comets...as to the place of their Nodes and Perihelia, their Inclinations to the plane of the Ecliptick and their distances from the Sun; whence he concluded it was highly probable not to say demonstrative, that these were but one and the same Comet, having a Period of about 75 years; and that it moves in an Elliptick Orb about the Sun, being when at its greatest distance, about 35 times as far off as the Sun from the Earth.

Journal Book of the Royal Society (1696)

The following text, figures and tables have been adapted from the published work in the Open Journal of Astrophysics, Volume 7 as Pham et al. (2024b) and appendix A, B, C of the published article in the Monthly Notices of the Royal Astronomical Society, Volume 530, Issue 3, pp. 2526-2547 as Pham & Rein (2024). In Pham et al. (2024b), the co-authors are Hanno Rein and David Spiegel. In Pham & Rein (2024), Hanno Rein is the co-author.

Abstract

We first present a novel integration method that is capable of speeding up simulations of massless particles in the presence of massive bodies. We performed three tests to check the accuracy of our method against the usual N-body integration setups. We verify and compare our methods in these cases: (i) the trajectory of an Oort cloud comet in the

presence of a central star, a planet, and Galactic tide, (ii) the energy kicks imparted by a massive planet on an ensemble of incoming test particles, and (iii) the dynamical effects of Solar system giant planets on the Kuiper Belt. In all cases, we find that our method speeds up integration, with the Oort cloud comet case enjoying a speed up of 1800 times.

Next, we derive a new criterion for estimating characteristic dynamical timescales in N-body simulations. The criterion uses the second, third, and fourth derivatives of particle positions: acceleration, jerk, and snap. It can be used for choosing timesteps in integrators with adaptive step size control. For any two-body problem, the criterion is guaranteed to determine the orbital period and pericentre timescale regardless of eccentricity. We discuss why our criterion is the simplest derivative-based expression for choosing adaptive timesteps with the above properties and show its superior performance over existing criteria in numerical tests. Because our criterion uses lower-order derivatives, it is less susceptible to rounding errors caused by finite floating point precision. This significantly decreases the volume of phase space where an adaptive integrator fails or gets stuck due to unphysical timestep estimates. For example, our new criterion can accurately estimate timesteps for orbits around a 50m-sized Solar System object located at 40AU from the coordinate origin when using double floating point precision. Previous methods were limited to objects larger than 10km. We implement our new criterion in the high-order IAS15 integrator which is part of the freely available N-body package REBOUND.

3.1 Introduction

A common problem of interest in N-body simulation dynamics is one describing the motion of a test particle around a system consisting of a central body with one or more massive companions. For example, such a system describes the rich orbital dynamics of satellites in the Sun-Earth-Moon system as they experience the von Zeipel-Lidov-Kozai effect ([von Zeipel, 1910; Lidov, 1962; Kozai, 1962](#)). This problem can also describe the orbital motion of asteroids and comets orbiting around a star and interacting with planets ([Pham & Rein, 2024](#)).

A numerical challenge in this problem is deciding on the simulation timestep to accurately describe the motion of these particles. In the case of an Oort cloud comet in the Solar system on a Sun-grazing orbit (e.g. [O'Connor et al., 2023; Peña-Asensio et al., 2024; Jewitt et al., 2025](#)), the length scale spans seven orders of magnitude: the comet would have a semi-major axis on the order of $\sim 10^4$ AU, interacting with the giant planets at $\sim 10^1$ AU, potentially colliding with the terrestrial planets at $\sim 10^0$ AU, and having a pericentre passage at $\sim 10^{-1} - 10^{-2}$ AU. To resolve these rich dynamics, the simulation timestep must correspond with these length scales: It must be on the order of the orbital period to resolve the semi-major axis, on the order of the orbital period of the planets to resolve interactions with them, and on the order of the pericentre timescale to describe the closest approach.

Hence, the smallest time resolution in these systems is typically many orders of magnitude smaller than the greatest timescale.

One solution is to use the smallest timestep in the problem so that all dynamics can be resolved, ensuring that dynamics at all length scales are resolved. There are many numerical integrators using fixed timesteps, such as the WHFast ([Rein & Tamayo, 2015](#)) integrator. One such fixed timestep integrator is the Wisdom-Holman integrator, which can quickly integrate problems by perturbatively splitting the problem into two components: i) resolving the Keplerian motion around the star and ii) resolving the perturbation to that motion caused by other massive bodies. These integrators require *a priori* knowledge of the timesteps to perform well. For a problem like simulating the Solar system planets, the timestep can be known in advance: a fraction of the orbital period of the innermost planet.

Yet, using a fixed, smallest timestep can become prohibitively expensive, such as in cases where one is interested in the long-term evolution of bodies over many orbital periods. In the Oort cloud comet example described above, it is often necessary to integrate over the Galactic tide timescale, which can be up to ~ 300 Myr ([Heisler & Tremaine, 1986](#)). In the case of Solar system planets, once the planets experience orbit-crossing, the timestep to resolve a potential collision can become much smaller than the orbital timestep. Using a constant, small timestep over a long integration time would cause an excessively long and expensive simulation. In addition, it is often practically impossible to predict the smallest timestep beforehand as one would need to answer the following questions *a priori* for these two cases:

1. What is the minimum pericentre distance of a comet as it experiences a random walk in angular momentum due to Galactic tide?
2. What is the smallest approach between two planets in the 9-body Solar system?

To resolve this, adaptive timestep methods, such as IAS15 ([Rein & Spiegel, 2015](#)), have been developed. As their name suggests, these methods adapt the timestep automatically so that all length scales are properly resolved per integration step. Furthermore, these methods are often able to accommodate additional physics such as planet oblateness and obliquity (e.g. [Poon et al., 2024](#)). Thus, it is of interest to further improve and speed up adaptive timestep methods due to their wide-ranging flexibility.

In Section 3.2, we present a novel simulation strategy to significantly speed up adaptive timestep integration in the central body – companion – test particle system. This speed-up is applicable when the test particle does not exert gravitational effects on the central star or companion. In Section 3.3, we present an improvement on the timestepping criterion itself. This improvement focuses on the stability of resolving close encounters.

Fast integration with REBOUND

Only 1 particle (the comet) in simulation
 Force terms are analytically calculated and
 added to the comet's acceleration at each timestep

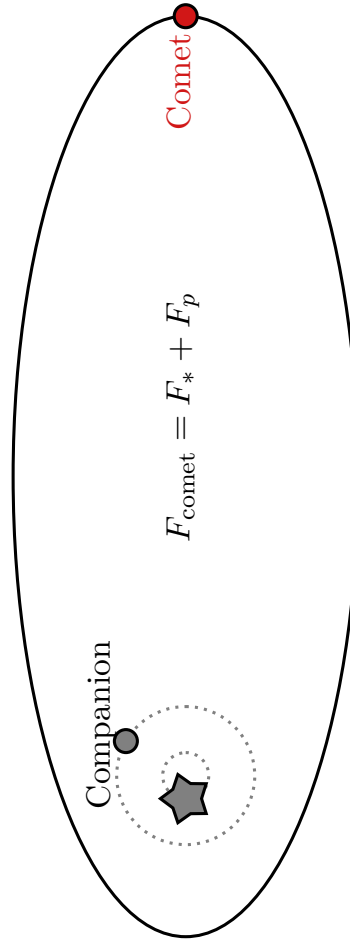


Figure 3.1: A diagram illustrating our fast, properly time-adaptive integration method in REBOUND. There is only one particle in the simulation: the comet (red). The positions of the white dwarf and its companions (shown in grey) can be calculated analytically because they are in a 2-body system. After each simulation timestep, the forces are analytically computed and added to the acceleration of the comet particle. IAS15 is used as an adaptive timestep and is capable of resolving timesteps as: large timestep when the comet is far away (the timestep is a fraction of the comet's orbital period), and small timestep when the comet is close in (fraction of the companion's orbital period). This ensures that all close encounters are properly handled while still maintaining fast integration speed.

3.2 The Fast Integration Method

We will use the star – planet – comet – Galactic tide system as the context for this section. However, we note that the method presented can be flexibly applied to any system where one is primarily interested in the motion of a test particle. As mentioned, the timestep dt for this problem spans many orders of magnitude. We would like to adaptively change the timestep between the comet’s orbital period to the planet’s orbital period to the pericentre timescale.

When setting up this system in an N-body code, such as `REBOUND`, one would add this as a $N = 3$ bodies system with a star, a planet, and a comet. However, this $N = 3$ body setup prohibits the timestep to adaptively increase beyond the planet’s orbital period. This is because the simulation always needs to resolve the planet’s orbit since it is a particle in the simulation. This is a waste of computational time when the focus is on a far-away comet at thousands of AU, but the simulation is slowly resolving the orbit of a planet at a few AU. In other words, the simulation is always resolving the smallest orbit and not actually adapting to the comet’s orbit.

Note that the behaviour described above is necessary if the comet is exerting a gravitational force on the planet or the star. In this case, we do need to resolve the constantly changing planet’s orbit. However, since the comet is a test particle and exerts no gravitational force, we know *a priori* that the planet’s orbit does not change. Thus, most of the time, we spend time resolving a Keplerian orbit of a star-planet system where there is a well-known analytic solution. Here, we develop a method to simulate just the comet so that the timestep is always adaptively changing according to the comet.

3.2.1 Orbit and Force Calculations

Now, we describe the Keplerian orbital position of the massive particles. We work in the barycentric frame of reference so that these particles orbit the centre of mass at the coordinate origin. Furthermore, in our method, the massive particles do not affect each other’s orbit. For a system with two massive particles (e.g., star and planet), our method gives an exact solution to the problem because the 2-body problem reduces to the 1-body Keplerian problem. When there are three or more bodies, our simulation will not be able to account for planet-planet interaction terms. For most systems, this is equivalent to neglecting the secular evolution of planets. The Keplerian Cartesian position (x, y, z) for particles $j > 0$ (all other massive bodies except the central star) are:

$$r_{j,x} / r_j = \cos \Omega \cos(f + \omega) - \cos(I) \sin \Omega \sin(f + \omega) \quad (3.1)$$

$$r_{j,y} / r_j = \cos \Omega \cos(f + \omega) + \cos(I) \cos \Omega \sin(f + \omega) \quad (3.2)$$

$$r_{j,z} / r_j = \sin(I) \sin(f + \omega) \quad (3.3)$$

where r_j is the distance between the massive particle $j > 0$ and the barycentre:

$$r_j = \frac{a(1 - e^2)}{1 + e \cos f} \quad (3.4)$$

where a is the semi-major axis, e is the eccentricity, f is the true anomaly. To find the true anomaly at any time t , we use Kepler's equation and calculate the mean anomaly according to:

$$m_j(t) = m_j(0) + t \sqrt{\left(G \sum_{k=0} M_k \right) / a_j^3} \quad (3.5)$$

with $m_j(0)$ as the initial mean anomaly and M_k as the mass of the body k . The orbital parameters ($a, e, I, \Omega, \omega, m_j(0)$) for a massive body j are given by the user and are fixed over the course of the simulation.

For $j = 0$ (the central star), we make use of the definition of the barycentre in the barycentric frame of reference:

$$\sum_{j=0} M_j r_{j,i} = 0; i = \{x, y, z\} \quad (3.6)$$

and since we have $r_{j,i}$ for all $j > 0$, we readily have $r_{0,i}$ as:

$$r_{0,i} = - \sum_{j=1} M_j r_{j,i}. \quad (3.7)$$

Now that we have the position of all massive particles, we can now describe the integration of the comet's orbit. First, we manually calculate and add the comet's initial Cartesian position and velocity (x, y, z, v_x, v_y, v_z at $t = 0$) into REBOUND in the barycentric frame. Then, at each timestep, the comet's acceleration is manually calculated and added to REBOUND:

$$\frac{d^2 r_i}{dt^2} = - \sum_{j=0} \left(GM_j \frac{r_{i,j}}{|r_{i,j}|^3} \right); i = \{x, y, z\} \quad (3.8)$$

where M_j is the mass of a body j , and the index j begins at $j = 0$ for the central star. $r_{i,j}$ is the distance between the comet and the massive body j :

$$r_{i,j} = r_{j,i} - r_i. \quad (3.9)$$

r_i is readily available from the comet's position in REBOUND and $r_{j,i}$ as described above.

Doing this procedure, the comet fully experiences the gravitational force of the massive bodies. Yet, at the same time, these bodies are actually not in the simulation and IAS15 does not need to resolve the other bodies. That is, the REBOUND simulation has only $N = 1$ particle as illustrated in Figure 3.1.

Finally, we note that IAS15 allows Equation 3.8 to accommodate additional effects in

the form:

$$\frac{d^2r_i}{dt^2} = -\sum_{j=0} \left(GM_j \frac{r_{i,j}}{r_{i,j}^3} \right) + F \left(r, \frac{dr}{dt}, t \right) \quad (3.10)$$

where F describes any other additional effects that might modify the equations of motion.

3.2.2 Tests

In this section, we demonstrate some verifications of our implementation and report on the speed-up achieved by this method of integration. We perform three tests of our fast integration method. The first studies the trajectory of an Oort cloud comet under the influence of a star, planet, and Galactic tide (an additional effect). Next, we study statistically the energy kick imparted by a planet on an ensemble of incoming test particles. Finally, we study the effects of multiple planets by simulating the Kuiper Belt with the Solar system's four giant planets. In each case, we compare if the fast integration method can reproduce the results of normal integration. In the end, we compare the speed-up achieved by our method.

An Oort Cloud Comet

First, we study the evolution of one test particle representative of a typical Oort cloud comet under the influence of Galactic tide with the existence of one massive planet. The test particle initially has a semi-major axis of 50 000 AU, initial pericentre of 15 AU, and the comet begins at pericentre. There is a $10^{-3}M_\odot$ massive planet on a circular orbit at 10 AU and the central star has a mass of $1M_\odot$. Furthermore, we include the full effects of vertical Galactic tide by including an additional term to the comet's z component in the equation of motion. The full equations of motion of the comet are:

$$\begin{aligned} \frac{d^2r_x}{dt^2} &= -GM_* \left(\frac{x_*}{r_*^3} \right) - GM_p \left(\frac{x_p}{r_p^3} \right) \\ \frac{d^2r_y}{dt^2} &= -GM_* \left(\frac{y_*}{r_*^3} \right) - GM_p \left(\frac{y_p}{r_p^3} \right) \\ \frac{d^2r_z}{dt^2} &= -GM_* \left(\frac{z_*}{r_*^3} \right) - GM_p \left(\frac{z_p}{r_p^3} \right) - 4\pi G\rho_0 z \end{aligned} \quad (3.11)$$

where variables with subscripts $*$ and p denote the central star and the planet, respectively. ρ_0 describes the averaged background density of gas and stars in the Galaxy. Note that as a planetary system evolves over the Galactic timescale, it oscillates up and down the Galactic plane and ρ_0 is a function of time. In this simulation, we adopt an averaged fiducial value of $\rho_0 = 0.1M_\odot \text{ pc}^{-3}$ (Holmberg & Flynn, 2000; McKee et al., 2015).

This setup is performed twice, first using the usual REBOUND setup, where there are three particles (star, planet, and test particle), then using the fast integration method presented

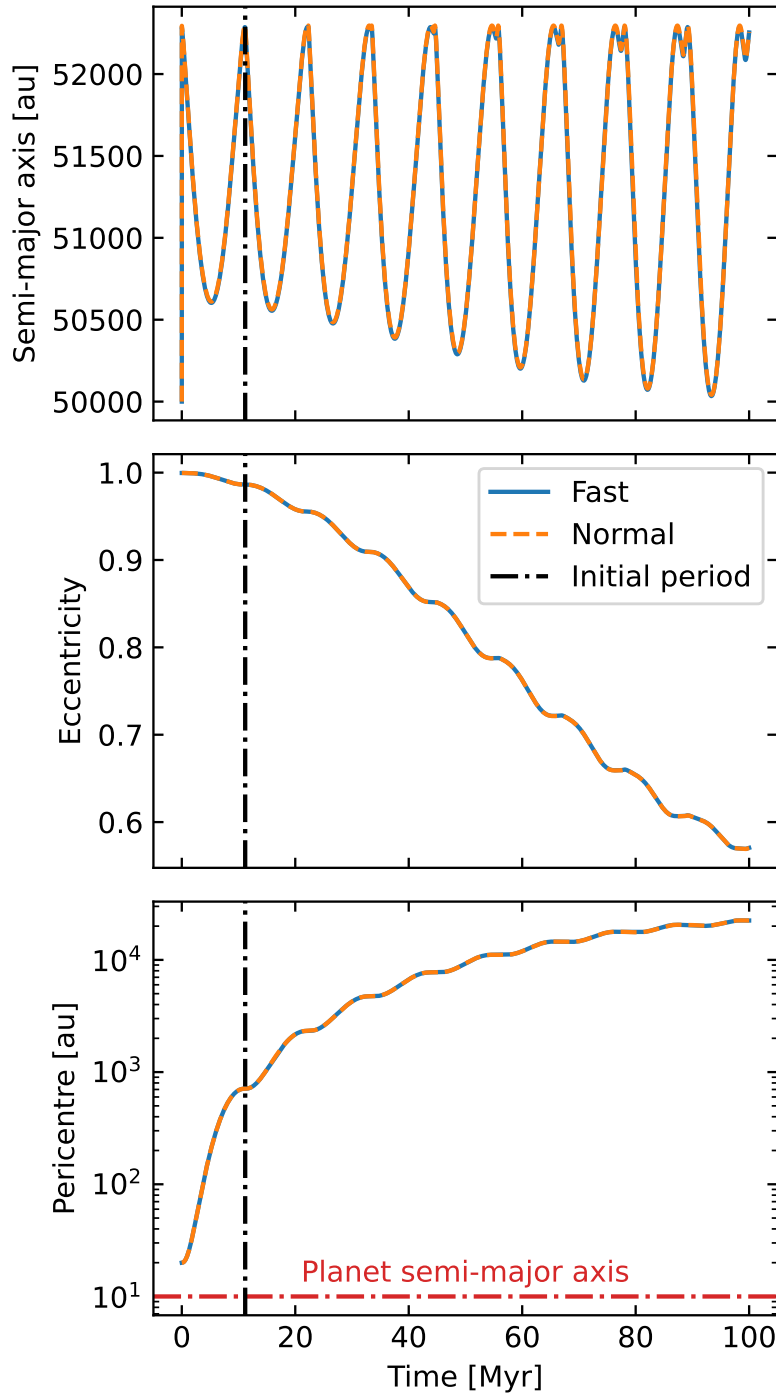


Figure 3.2: The semi-major axis (top), eccentricity (middle), and pericentre (bottom) evolution of a test particle with an initial semi-major axis at 50 000 AU and initial pericentre at 15 AU. There is a $10^{-3} M_{\odot}$ planet on a circular orbit at 10 AU and a $1M_{\odot}$ central star; there are also gravitational effects from vertical Galactic tide. The comet is started at its pericentre. The solid curve shows the results from our fast simulation method ($N = 1$ particle in the simulation), and the dashed curve shows the results from a normal REBOUND setup ($N = 3$ particles). The vertical dashed-dot line shows the initial orbital period of the comet. The fast integration method is done in 0.3 seconds walltime, whereas the usual integration method is done in 541.6 seconds.

above. In Figure 3.2, we compare the results of these two integrations, showing the semi-major axis, eccentricity, and pericentre evolution of the comet over 100 Myr. As seen, the orbital evolution compared between the two methods matches well. In the top panel where the semi-major axis is shown, we also observe that there is an initial kick in the semi-major axis. This is because the comet begins at the pericentre, near the planet. This kick is resolved and agreed by both integration methods. We find that in this setup our fast simulation method reproduces the evolution in semi-major axis (or equivalently, energy) and eccentricity (angular momentum) just as well as a typical $N = 3$ body integration.

Energy Kicks

As distant comets achieve high eccentricities, their orbits may come close to or cross the orbit of a planet. This interaction imparts an energy kick onto the planet, which we have already seen at the beginning of the top panel of Figure 3.2. We note that these energy kicks can be diffusive ($\Delta E/E \ll 1$) or scattering ($\Delta E/E \gtrsim 1$), as seen in the results in this section. For further discussion of these two regimes, we refer the reader to Figure 2.4 and discussions in the corresponding subsection in Chapter 2. Here, we study in a statistical sense how a planet can impart an energy kick, ΔE on the trajectory of incoming test particles.

To do this, we perform the integration setup as done in Figure 9.3 of Tremaine (2023). Here, there is a planet with mass 10^{-3} the mass of the central star at a semi-major axis a_p . There are 10^4 incoming test particles on parabolic orbits (initial orbital energy is 0) with a pericentre q , with randomised longitude of the ascending node (Ω), longitude of periapsis (ω), and inclination (I). These angles are drawn accordingly from an isotropic distribution of particles (i.e. ω and Ω are drawn from uniform distributions between $[0, 2\pi]$, I is drawn from a uniform distribution in $\cos I$ between $[-1, 1]$). Each incoming test particle starts at a distance $200a_p$ from the barycentre integrated over one pericentre passage. The quantity $x = 1/a$ is measured after the integration (x is equivalent to the orbital energy with a factor of 2). Then the root-mean-square change in x is measured, averaging over all test particles, at each pericentre q .

The results for this setup with the fast integration method and normal simulations are shown in Figure 3.3. As seen, σ_x for both cases match well with each other at all pericentre q . There is a slight deviation at $q = a_p$, which can be explained by the fact that these are orbits with the closest encounters to the planet. In this case, the location of the planet becomes very important to resolve the encounter length scale. Hence, the differences here can be attributed to the fact that our fast method uses the analytic solution for the planet's orbit, whereas the normal method numerically propagates the orbit in time. Finally, we compare our results with the isotropic curve in Figure 9.3 in Tremaine (2023) to find that they are consistent with each other.

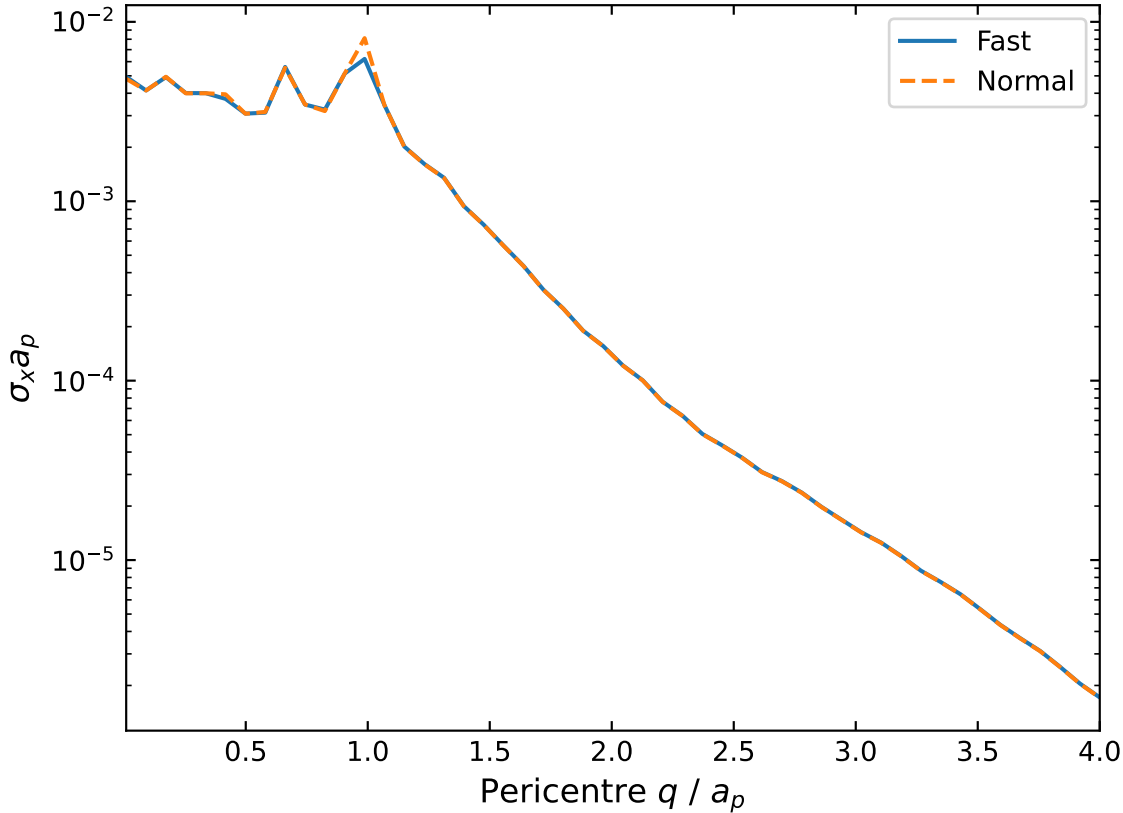


Figure 3.3: $\sigma_x = \sqrt{\langle x^2 \rangle}$ is the root-mean-square change in $x = 1/a$ over one pericentre passage. The test particles start on a parabolic orbit with a pericentre q , with random longitudes of the ascending node (Ω) and periapsis (ω) drawn from a uniform distribution. The test particle's inclinations, I , are drawn from a uniform distribution in $\cos I$. Each test particle begins at a distance $200a_p$ relative to the barycentre. There are 10^4 incoming test particles, and the system has a planet at semi-major axis a_p having mass 10^{-3} that of the stellar mass. This setup is done with the fast integration method (dashed curve) and normal integration (solid curve). The results here can be directly compared with the isotropic curve in Figure 9.3 in Tremaine (2023). To produce this plot, the fast integration method takes 45.3 seconds walltime to run, while the usual integration method takes 1116.0 seconds.

Table 3.1: Comparison of integration walltime between the fast integration method and normal integration in seconds. The speed-up factor is the ratio of normal integration time over fast integration time. The last column compares the initial test particle’s semi-major axis to the planet’s. The ‘Energy kicks’ test case initialised test particles on parabolic orbits, so a/a_p cannot be defined. In that case, we show the initial test particle distance to that of the planet.

Test case	Fast time [s]	Normal time [s]	Speed-up	a/a_p
Oort cloud trajectory	0.3	541.6	1800	5000
Energy kicks	45.3	1116.0	25	– (200)
Kuiper Belt	29.6	155	5	1-1.6

Kuiper Belt

Here, we test the accuracy of our method in the context of multiple planets. We focus on the effects of the Solar system giant planets on the Kuiper Belt. Here, 10^4 Kuiper Belt objects are initialised as test particles, with initial semi-major axes drawn from a uniform distribution between [30, 50] AU and eccentricity drawn uniformly between [0.01, 0.2]. Their initial inclinations are drawn from a Rayleigh distribution with a mean inclination of 10° , consistent with the ‘flat’ setup in Chapter 9 of [Tremaine \(2023\)](#). All other angles (Ω , ω , true anomaly) are drawn uniformly between $[0, 2\pi]$. The system contains the Sun, Jupiter, Saturn, Uranus, and Neptune as massive particles. These simulations are run for 100 Jupiter orbits.

In Figure 3.4, we show the Kuiper Belt objects’ distributions in semi-major axis, eccentricity, and inclination. The histograms show results from the fast and normal simulations. As seen, they agree well with each other, specifically with mean-motion resonances induced by the planets clearly shown in the semi-major axis histogram. Similar to the previous test, there are slight deviations between the two methods in these histograms. These differences are due to the fact that the fast integration method analytically calculates Keplerian orbits of the massive particles and does not account for planet-planet interactions, whereas the normal integration method is a true N-body integration with planets’ orbit propagated numerically.

Integration Time

Table 3.1 compares the integration time between the fast and normal integration methods. In all cases, the fast method is, as expected, faster than the normal method. Most notably, the Oort cloud trajectory case achieves a speed-up of 1800 times. This speed-up allows for the integration of many Oort cloud objects in the previous chapter.

Furthermore, there are great variations in the speed-up that can be achieved, which can

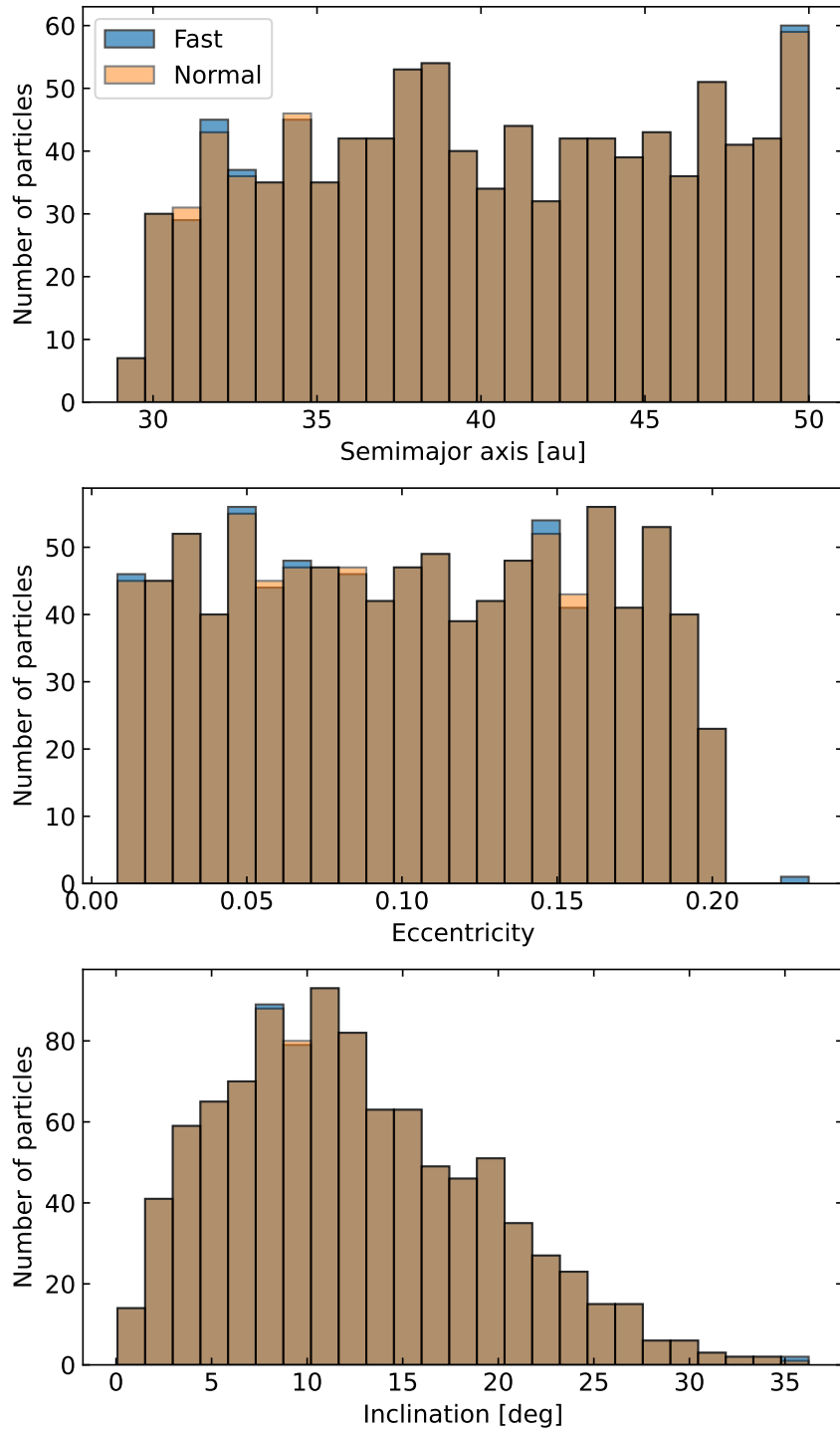


Figure 3.4: The distribution of Kuiper Belt objects (treated as test particles) after 100 Jupiter orbital periods. The 10^4 test particles are initialised on semi-major axes drawn uniformly between [30, 50] AU, eccentricity drawn uniformly between [0.01, 0.2], inclinations drawn from a Rayleigh distribution with mean inclination 10° , and all other angles drawn isotropically. The fast integration is done in 29.6 seconds walltime, and the normal integration is done in 155 seconds.

be explained by the orbital distance of the test particle. If the test particle's distance is much greater than the planet's, the timestep can become much greater. But, if the test particle is close to the planet, then the adaptive timestep of the test particle is comparable to that of the planet anyway. In other words, since the test particle is so close to the planet, IAS15 is using a small timestep to resolve such an orbit and our method does not achieve a much greater speed up compared to a simulation where the planet's orbit is resolved. This explanation can be understood through the last column of Table 3.1, where we show the initial semi-major axes of test particles in the test cases. Note that in the ‘Energy kicks’ test, particles are initialised on a parabolic orbit and a is not well-defined initially. Rather, we show the particle’s initial distance in that test case, $d(t = 0) = 200a_p$.

We conclude that our integration method performs faster than normal methods, but does so maximally for distant test particles in the regime $d/a_p \gg 1$ (d is the particle’s distance and a_p is the planet’s semi-major axis).

3.2.3 Conclusion

We present a novel fast integration method, capable of performing 5-1800 times faster than the usual N-body simulation setup. Importantly, our method accurately resolves all dynamics that N-body simulation can do. To ensure this, we perform three tests between our method and normal N-body simulation: i) the trajectory of an Oort cloud comet in the presence of a central star, a planet, and Galactic tide, ii) the energy kicks imparted by a massive planet on an ensemble of incoming test particles, and iii) the dynamical effects of Solar system giant planets on the Kuiper Belt. In all three tests, we find that our method’s results are in agreement with the normal simulation method. Finally, we find that this fast integration method is particularly efficient for distant test particles, such as Oort cloud comets typically residing at distances $10^3 - 10^5$ AU.

3.3 A New Timestep Criterion for N-body Simulations

In the course of developing the fast integration method in the previous section, we encountered a problem in how the IAS15 integrator chooses its adaptive timestep. As shown in Figure 3.5, as a distant Oort cloud comet encounters a planet, the adaptive timestep becomes prohibitively small. During the comet-planet close encounter, the timestep chosen is on the order of ~ 10 ms, which is very small compared to the pericentre timescale (dotted line, cf. Equation 3.21). To resolve this, we propose a new timestep criterion, shown as the solid curve.

In this example, we note that the smallest timescale is not the pericentre timescale, but rather the timescale to resolve the comet-planet distance during the close encounter. Hence, it is not obvious to choose a minimum timestep *a priori*, as sometimes done in the literature as a lower limit cutoff to prevent simulations from stalling. Choosing this lower bound cutoff

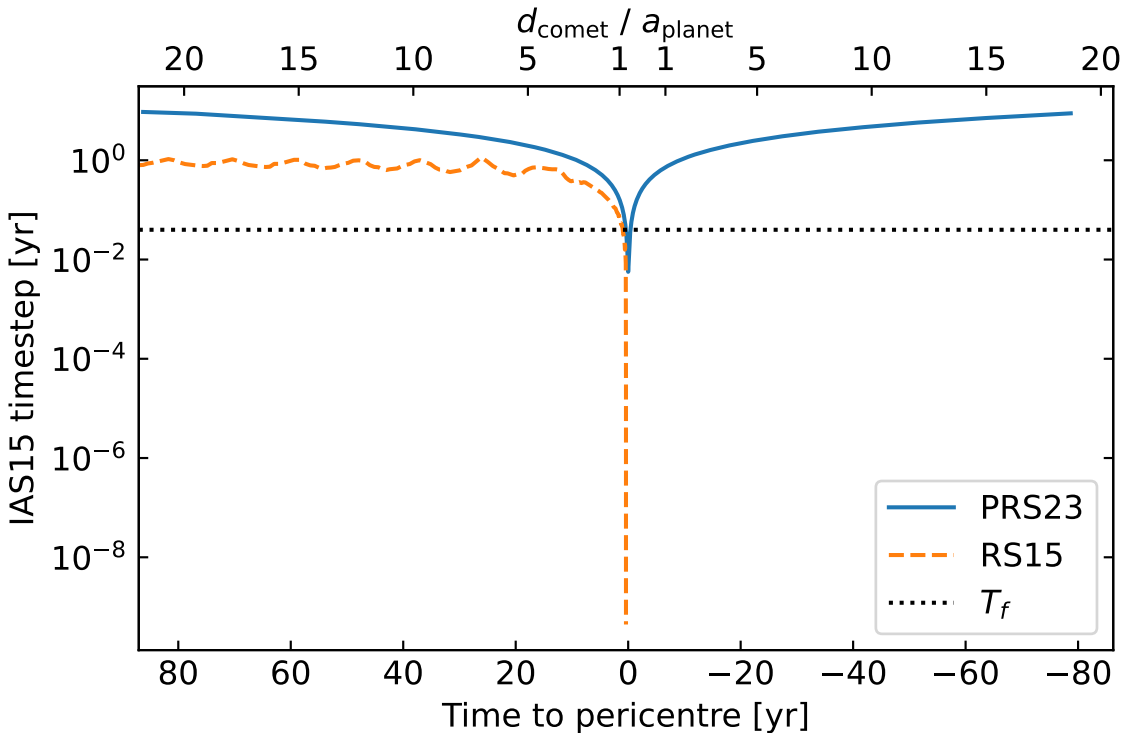


Figure 3.5: The timestep chosen by IAS15 for an Oort cloud comet encountering a planet. The dashed curve shows the timestep as originally proposed by Rein & Spiegel (2015), referred to as RS15. The solid curve is the new timestep proposed in Pham et al. (2024b) and this chapter, abbreviated as PRS23. On the top axis, we show the comet’s distance, d , relative to the planet’s semi-major axis, a_{planet} . To resolve the close encounter, RS15 chooses a prohibitively small timestep (~ 10 ms), which is much smaller than the pericentre timescale (dotted horizontal line, cf. Equation 3.21), effectively stalling the simulation.

could risk incorrect resolution of close encounters, leading to inaccurate simulation results. In this section, we discuss how to choose the timestep in practice.

We focus our discussion on IAS15, a 15th-order integrator widely used for gravitational dynamics (Rein & Spiegel, 2015). IAS15 is based on a Gauß-Radau quadrature (Everhart, 1985) and comes with an adaptive step size control that can automatically choose a timestep. IAS15 is part of the REBOUND package (Rein & Liu, 2012) and has enabled hundreds of scientific studies covering a wide range of dynamical systems, in particular those which are not well suited for symplectic integration methods¹. However, note that our results are general and the criterion we derive in Section 3.3.3 can be used in other integrators as well, for example, those aimed at simulations of stellar clusters (e.g. Nitadori & Aarseth, 2012; Wang et al., 2015).

¹Note that IAS15 converges to machine precision in most cases. If so, then IAS15 is in practice no less symplectic than an integrator which is symplectic on paper.

We start our discussion with a short summary of existing timestepping criteria often used in N-body simulations in Section 3.3.1. Then, in Section 3.3.2, we point out how rounding error due to finite floating point precision arise in the existing criterion used in IAS15. We derive and explore our new proposed timestepping criterion in Section 3.3.3. By focusing on a two-body system we analytically show that our new criterion is resolving the physically relevant timescales, especially in the limit of high eccentricity. In Section 3.3.4 we run numerical integrations with IAS15 and the new criterion. Most importantly, we will show that close encounters can now be integrated reliably even if they occur far from the coordinate origin. We summarise and conclude in Section 3.3.5.

3.3.1 Other Timestep Criteria

We begin with a review of commonly used timestep criteria used in N-body simulations. We use a notation where y denotes the particle coordinates. For readability, we ignore subtleties such as particle and coordinate indices, but come back to this issue at the end of this section. We denote time derivatives of y as follows

$$y^{(n)} \equiv \frac{d^n}{dt^n} y. \quad (3.12)$$

In principle any ratio of derivatives $y^{(m)}/y^{(n)}$ can be used to calculate a timescale τ :

$$\tau_{m,n} \equiv \left(\frac{y^{(m)}}{y^{(n)}} \right)^{1/(n-m)} \quad \forall n > m \geq 2. \quad (3.13)$$

Note that τ always has units of time. Once we have a characteristic timescale, we can multiply it by a constant dimensionless number η to calculate a timestep $dt = \eta \cdot \tau$ which can then be used in integration methods with adaptive step size control. The numerical value of η depends on the integration method and the required precision.

The simplest choice to define a timescale is to use the ratio of acceleration over jerk (the derivative of the acceleration):

$$\tau_{2,3} \equiv \frac{y^{(2)}}{y^{(3)}}. \quad (3.14)$$

This formula uses the lowest order derivatives: one cannot use the position or the velocity as it would not preserve Galilean invariance (such a criterion would use a different timestep whenever the system is boosted to a new frame moving at a constant velocity). Alternatively, some authors, e.g. Press & Spergel (1988), choose the ratio of acceleration over snap (the second derivative of the acceleration) to define

$$\tau_{2,4} \equiv \sqrt{\frac{y^{(2)}}{y^{(4)}}}. \quad (3.15)$$

The original IAS15 integrator (Rein & Spiegel, 2015), the one we aim to improve in this chapter, defines a timescale using the 2nd and 9th derivate of the position:

$$\tau_{\text{RS15}} \equiv \sqrt[7]{\frac{y^{(2)}}{y^{(9)}}} \quad (3.16)$$

with a default value² of $\eta = \sqrt[7]{5.04 \cdot 10^{-6}}$. The reasoning given by Rein & Spiegel (2015) for choosing the 9th derivative came from the fact that it is the last term in a series expansion used internally by IAS15 which allowed the authors to estimate the error of the integration scheme.

Hermite integrators (Makino & Aarseth, 1992) and Adams-Bashforth-Moulton schemes (Aarseth, 1963, 1985) are other popular tools for N-body simulations. The timestep criterion used by Aarseth (1985) is

$$\tau_{\text{A85}} \equiv \sqrt{\frac{y^{(2)}y^{(4)} + y^{(3)}y^{(3)}}{y^{(3)}y^{(5)} + y^{(4)}y^{(4)}}}. \quad (3.17)$$

The author states that this expression was derived “after some experimentation” but other than its good performance in numerical tests, we are unaware of any justification for this specific choice. Nevertheless, Aarseth (1985) correctly points out several features of this expression: it is independent of mass for two body motion and well-defined in special cases such as $y^{(2)} = 0$ or $y^{(3)} = y^{(5)} = 0$ with all particles at rest. In Section 3.3.3 below, we provide further arguments as to why this expression works well, in particular for dominant two-body motion.

Note that in all the above formulas as well as the ones below, we assume that some norm is applied to the $3N$ dimensional derivative vectors $y^{(n)}$ to obtain a scalar value. The precise choice of norm is not crucial for the discussion in this work. Often an L^2 norm, an L^∞ norm, or a combination of the two is used. For example, if $y_{a,i}^{(n)}$ refers to the n -th derivative of the Cartesian coordinate i and particle with index a , then a reasonable choice of norm is

$$|y^{(n)}| = \max_a \sqrt{\sum_{i=x,y,z} (y_{a,i}^{(n)})^2}. \quad (3.18)$$

3.3.2 Finite Floating Point Precision

Internally, IAS15 uses a series expansion to approximate trajectories during a timestep. As mentioned above, Rein & Spiegel (2015) used the highest order term in the series expansion to obtain an error estimate for the current step and then propose an optimal timestep for the next step. Although this choice was well motivated, when implemented using finite floating

²The IAS15 implementation uses an accuracy control parameter ϵ , which is related to η by $\epsilon = \eta^7 / 5400$.

point precision it is not numerically stable in many cases. The reason is that high-order derivatives in IAS15 are estimated with some finite difference method³. The precise way this is done is not important for this discussion and we refer the reader to the IAS15 paper for the details (see also [Everhart, 1985](#)). However, as an illustration, consider the following central finite difference scheme for the first derivative:

$$y^{(1)}(t) \approx \frac{y(t + dt) - y(t - dt)}{2dt}$$

The calculation of the difference in the numerator can lead to problems because dt is typically small and thus $y(t + dt) \approx y(t - dt)$. Working in double floating point precision where we have about 16 decimal digits of precision to work with, the best accuracy for the estimate of the derivative is obtained by choosing dt such that

$$\left| \frac{y(t + dt) - y(t - dt)}{y(t)} \right| \approx 10^{-8}. \quad (3.19)$$

Choosing a larger dt increases the discretisation error from the finite difference scheme. Choosing a smaller dt increases the rounding error from finite floating point precision. Now consider the case where y is offset by a constant \bar{y} . This happens frequently in N-body simulations. For example, it is common in a simulation of the Solar System to place the Sun at the origin. Then, whenever an asteroid has a close encounter with a planet it will occur at some offset \bar{y} from the origin. The close encounter distance can be very small (e.g. the Earth's radius) compared to \bar{y} (e.g. the Earth's semi-major axis). In such a case, we don't have 16 decimal digits of precision anymore. In the case of a close encounter with the Earth, we have ~ 12 digits left to work with. As a result estimates of derivatives can quickly become dominated by errors from finite floating point precision. Once the estimate for the derivative is no longer accurate, the timestep can become excessively small or excessively large, leading to stalled simulations or unphysical simulation results.

The problem described above gets worse for higher order derivatives and we quantify the effect for IAS15 in [Section 3.3.4](#). This is the main motivation why we are looking to find a criterion which uses the lowest order derivatives possible.

3.3.3 New Timestepping Criterion

We now motivate the specific combination of derivatives we choose for our new timestepping criterion. Let us start by exploring how derivatives behave in a simple eccentric two body system. We do this because the motion of a particle in an N-body simulation, at least the kind we are interested in for this work, is almost always dominated by the interaction with one other particle. For example, to first approximation the Sun orbits the Milky Way, the Earth orbits the Sun, the Moon orbits the Earth, a spacecraft orbits the Moon, and so forth.

³This is also true for other integration methods.

There are of course exceptions, but they often don't last long. Consider, for instance, the motion of a spacecraft when it leaves the Earth's Hill sphere on its way to the Moon: early in its journey, it's effectively in a hyperbolic orbit of Earth; late in its journey, it's effectively in a bound orbit of the Moon; only near the Hill sphere is it neither approximately in orbit of the Earth nor the Moon. In such a case a particle can at some point experience zero net acceleration. For as long as a particle is travelling along a straight line it has no physical timescale associated with its trajectory. In practice, this issue is resolved by making sure the timestep cannot increase by more than some fixed ratio from one step to the next⁴.

To start, let us identify two characteristic timescales in the two body problem: the orbital period T_p and the pericentre timescale T_f , which we define as

$$T_p \equiv \frac{2\pi}{n} \quad \text{and} \quad (3.20)$$

$$T_f \equiv \frac{2\pi}{n} \frac{(1-e)^2}{\sqrt{1-e^2}}, \quad (3.21)$$

where n is the mean motion (Wisdom, 2015). For circular orbits, the timescales are identical. In the limit of $e \rightarrow 1$, the pericentre timescale follows a power law, $T_f \propto (1-e)^{3/2}$.

Figure 3.6 shows the absolute values of the position and its derivatives up to $y^{(9)}$ as a function of the eccentricity at pericentre (top) and apocentre (bottom). Highly eccentric orbits are on the left-hand side, and circular orbits are on the right. We use dimensionless units such that $G = a = n = 1$. It is easy to show that at pericentre, all derivatives $y^{(n)}$ follow a power-law in the limit of $e \rightarrow 1$ with a power-law index of

$$c_n \equiv \lim_{e \rightarrow 1} \frac{\log y^{(n)}}{\log(1-e)} = 1 - \frac{3}{2}n. \quad (3.22)$$

Similarly, one can show that at apocentre the power-law index in the limit of $e \rightarrow 1$ is

$$d_n \equiv \lim_{e \rightarrow 1} \frac{\log y^{(n)}}{\log(1-e)} = \begin{cases} 0 & \text{for } n \text{ even} \\ \frac{1}{2} & \text{for } n \text{ odd} \end{cases}. \quad (3.23)$$

These fundamental results have several important implications for timestepping criteria.

First, note that up to a constant factor, any ratio of successive derivatives in the form of $\tau_{m,m+1} = y^{(m)}/y^{(m+1)}$ can be used to calculate the pericentre timescale. At pericentre, these ratios are well-behaved in both limits $e \rightarrow 1$ and $e \rightarrow 0$. The situation is more complicated at apocentre. At apocentre, the pericentre timescale is irrelevant from a timestepping point of view. However, it is imperative to keep resolving the orbital timescale even if a particle moves very slowly while it is close to apocentre. We cannot use the ratio of successive derivatives, $\tau_{m,m+1}$ as defined in Eq. 3.13, to calculate the orbital timescale because in the

⁴This is called a safety factor in IAS15 and we use a numerical value of 0.25 to limit the increase and decrease of the timestep in consecutive steps.

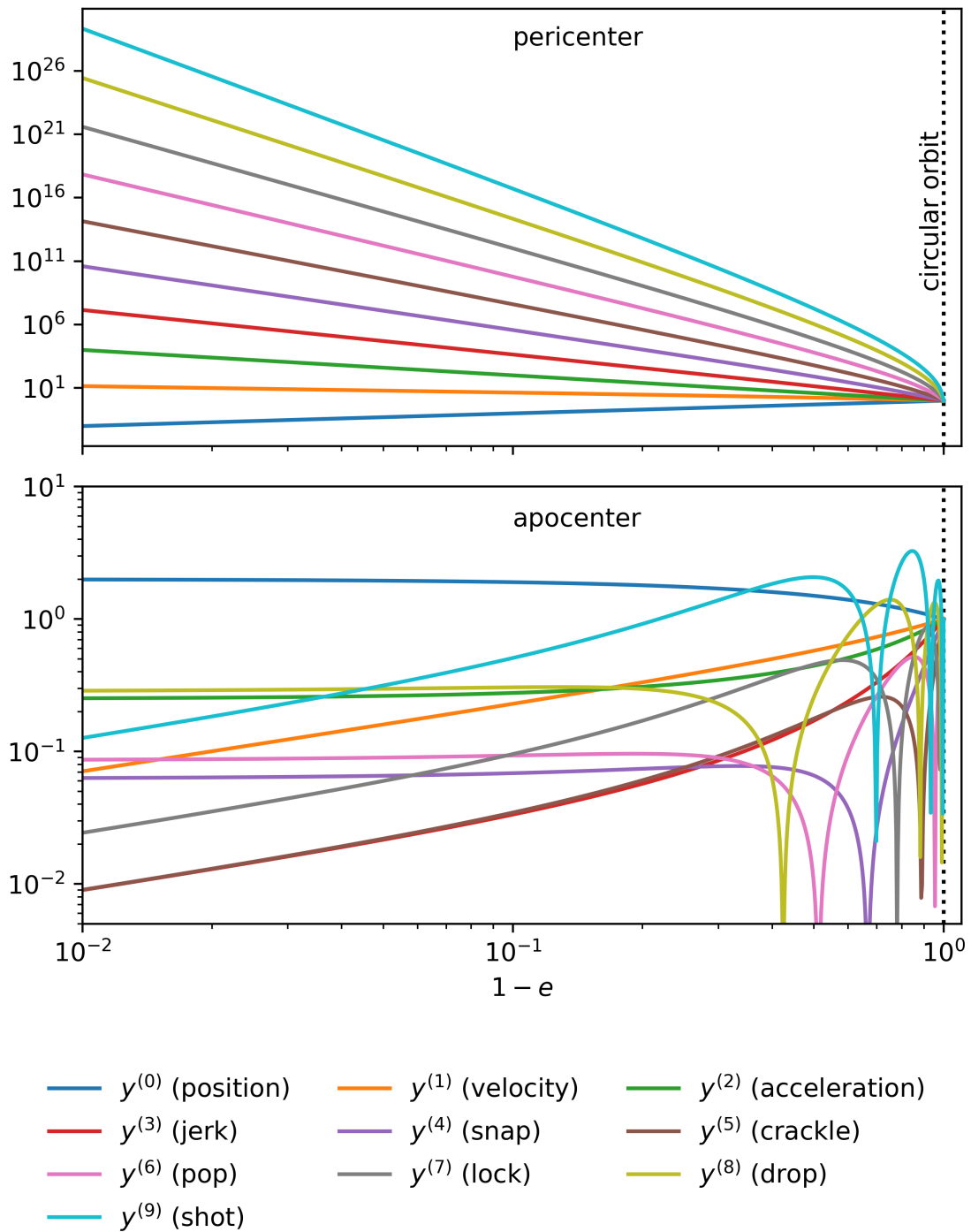


Figure 3.6: The position y and its first 9 derivatives in the eccentric two body problem. The top panel shows the values at pericentre, the bottom panel at apocentre. We use dimensionless units in which $G = a = 1$.

limit of $e \rightarrow 1$, $\tau_{m,m+1}$ tends to either 0 or ∞ but never to a finite constant. This is counter to the orbital timescale which is of course independent of e . What we can do instead, is to use $\tau_{m,m+2}$ which does converge to a constant in the limit of $e \rightarrow 1$ for all even $m \geq 2$. Note that we cannot use $m = 0$ or $m = 1$ because of Galilean invariance. We therefore have to use at least the fourth derivative $y^{(4)}$ to be able to find a well-defined orbital timescale for all eccentricities at apocentre. As one can see in Figure 3.6, this leads to another problem: Every $y^{(n)}$ with $n \geq 4$ has at least one root crossing at some e' . For example, although the timescale $\tau_{2,4}$ is well-behaved in the limit of $e \rightarrow 1$, it is ill-defined for at least one finite $e' \approx 0.4$.

With this in mind, we can now understand further failure modes of the original IAS15 timestepping criterion in addition to the finite floating point precision issue mentioned in Section 3.3.2. Recall that the original IAS15 timestepping criterion uses $\sqrt[7]{y^{(9)}/y^{(2)}}$ to estimate a timescale. Figure 3.7 shows the timestep using this old timestepping criterion at pericentre (orange line in the top panel) and apocentre (bottom panel). First, notice that the pericentre is always well resolved:

$$\lim_{e \rightarrow 1} \frac{dt_{\text{RS15}}}{T_f} \approx 0.01 \quad \text{at pericentre.} \quad (3.24)$$

This is expected given the argument above and Eq. 3.22. Second, note the spikes at apocentre for low eccentricity orbits. These are due to $y^{(9)}$ having zero crossings, visible in the bottom panel of Figure 3.6. Third, note that the timestep increases at apocentre as the eccentricity gets larger. The timestep does not converge and arbitrarily large timesteps are in principle possible:

$$\lim_{e \rightarrow 1} \frac{dt_{\text{RS15}}}{T_P} = \infty \quad \text{at apocentre.} \quad (3.25)$$

Once again, we can now understand that this is expected given Eq. 3.23: $y^{(2)}$ and $y^{(9)}$ converge to different power laws for large eccentricities at apocentre.

We also plot the timesteps defined by $\tau_{2,3}$ and $\tau_{2,4}$ in Figure 3.7 (green and red lines). Both criteria are able to accurately keep track of the pericentre timescale. Again, this is expected given Eq. 3.22. Notice that the timestep $dt_{2/3}$ diverges at apocentre, making it an unreliable choice for even moderately eccentric orbits. As we have shown above, the timestep $dt_{2/4}$ does not diverge at apocentre. However, it diverges at some $e' \approx 0.4$.

We also show dt_{A85} in Figure 3.7 (blue line). This criterion solves all of the above issues. We are now in a position to provide a justification as to why. Notice that, just like the other criteria, it estimates the pericentre timescale accurately. This is because when taking the limit $e \rightarrow 1$ in Eq. 3.17, we have $\tau_{\text{A85}} \propto (e - 1)^{3/2} \propto T_f$ as per Eq. 3.22. Similarly, using Eq. 3.23, it is easy to see that $\lim_{e \rightarrow 1} \tau_{\text{A85}}$ is a constant at apocentre and thus a constant fraction of the orbital period. We can also understand why in the bottom panel

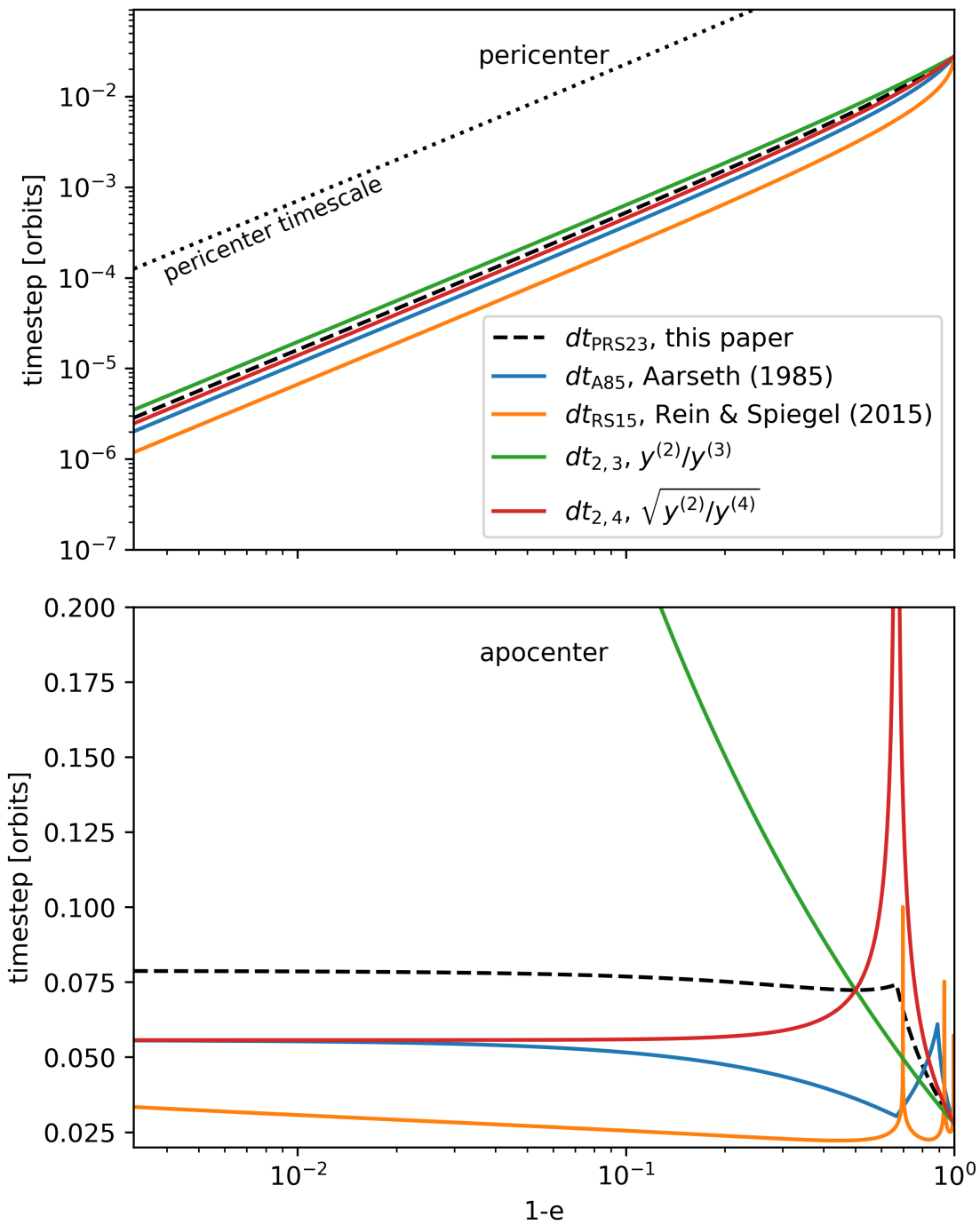


Figure 3.7: Timesteps as a function of eccentricity in an eccentric two body problem as determined by different timestepping criteria. The top panel shows the timesteps at pericentre, the bottom panel shows the timesteps at apocentre. Also shown is the pericentre timescale, defined such that it is 2π for circular orbits.

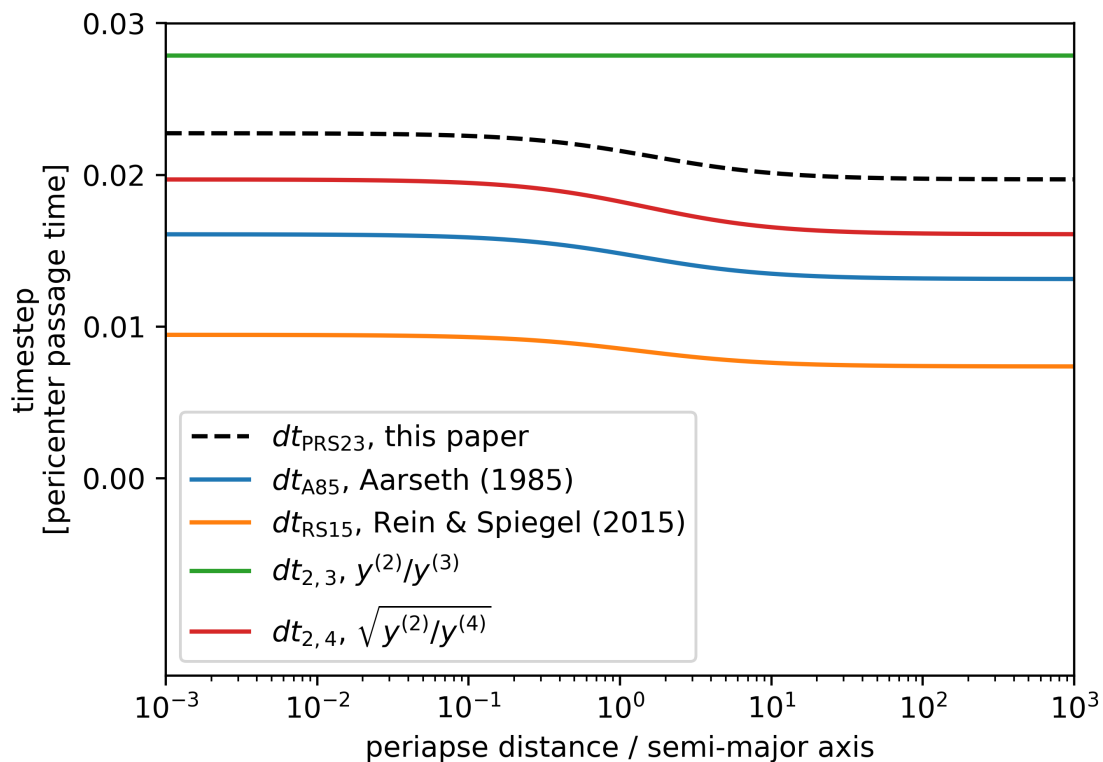


Figure 3.8: Same as Figure 3.7 but for hyperbolic orbits at pericentre. Because hyperbolic orbits do not have an orbital period, timesteps are shown in units of the pericentre passage timescale.

of Figure 3.7, the curve for τ_{A85} is non-monotonic. This is because the expression uses $y^{(4)}$ and $y^{(5)}$ which have zero crossings for some e' .

With all of this in mind, we can now finally propose our new criterion, specifically we choose

$$\tau_{\text{PRS23}} \equiv \sqrt{2} \cdot \left(\left(\frac{y^{(3)}}{y^{(2)}} \right)^2 + \left(\frac{y^{(4)}}{y^{(2)}} \right) \right)^{-1/2} \quad (3.26)$$

$$= \sqrt{\frac{2 \cdot y^{(2)} y^{(2)}}{y^{(3)} y^{(3)} + y^{(2)} y^{(4)}}}. \quad (3.27)$$

By construction, this expression avoids all the issues mentioned above. We further choose the value of η to be $\sqrt[7]{5040 \cdot \epsilon}$ so that we have

$$dt_{\text{PRS23}} = \sqrt[7]{5040 \cdot \epsilon} \cdot \tau_{\text{PRS23}}. \quad (3.28)$$

This results in identical timesteps for circular orbits using both the old and new criteria in IAS15. The scaling of dt with ϵ is also the same using both new and old criteria.

Figure 3.7 shows dt_{PRS23} as a function of the eccentricity (dashed black line). First, note that we indeed have $dt_{\text{PRS23}} = dt_{\text{RS15}}$ for circular orbits. For high eccentricities $e \rightarrow 1$, the new criterion results in timesteps about a factor of 2.3 larger. Second, note that in comparison to dt_{RS15} and $dt_{2,4}$ there are no more singularities ($dt \rightarrow \infty$) for low eccentricity orbits near apocentre. This is because the term $y^{(3)}/y^{(2)}$ remains non-zero and thus dominates when $y^{(4)}/y^{(2)}$ is zero. Third, note that in the limit of $e \rightarrow 1$, the timestep at apocentre now converges towards a constant. This is because the term $y^{(4)}/y^{(2)}$ dominates in this limit. Fourth, note that at pericentre the relevant timescale T_f remains well resolved in the limit of $e \rightarrow 1$. This is because the term $y^{(3)}/y^{(2)}$ dominates in this limit. Fifth, although dt_{PRS23} is not strictly monotonic as a function of eccentricity⁵, its local maxima at $e \approx 0.4$ is much less pronounced than in dt_{A85} .

Figure 3.8 is similar to Figure 3.7 but shows the timesteps at pericentre for hyperbolic orbits as a function of periapse distance over semi-major axis. Orbits on the right are effectively a straight line, and those on the left make an almost 180° turn. Because hyperbolic orbits have no orbital timescale, we plot the timestep in units of the pericentre passage timescale, defined as $y^{(1)}/y^{(0)}$ at pericentre (and thus consistent with the pericentre passage timescale for circular orbits). As one can see, both the new and old timestepping criterion for IAS15 as well as all the other criteria always resolve the pericentre timescale in

⁵A constant or at least a monotonic function of the eccentricity would be ideal here from a performance perspective because there is no physical timescale in the problem that has a local maxima. However, there are no free parameters to change in our current scheme. The only way to make further progress would be to include more derivatives which we can then assign different weights to or combine in other non-trivial ways. But using higher order derivatives comes at the disadvantage of making the scheme susceptible to floating point precision. For those reasons, we don't see an obvious way to improve the non-monotonicity.

hyperbolic orbits well. As for the eccentric case, the new timestepping criterion results in timesteps about 2.3 times larger for the default value of ϵ . Of course, it is straightforward to construct a hyperbolic orbit that is not resolved correctly. This is not a shortcoming of a particular timestepping criterion but simply follows from the fact that there is no timescale other than the pericentre passage timescale in the problem⁶. In practice, this is unlikely to be a problem because there are typically more than two particles being integrated at any given time. The fact that every criterion can resolve hyperbolic encounters equally well is likely a reason why authors who are mostly interested in stellar systems without binaries sometimes do not find a significant difference when testing timestepping criteria (Makino, 1991).

One disadvantage of τ_{PRS23} is that it diverges for $y^{(2)} = 0$. In practice this might not be an issue because in most implementations a timestep is only allowed to increase or decrease by some safety factor during one timestep. This safety factor is already mentioned in Aarseth (1985) and is also used in IAS15. So even if we can't estimate a timescale because instantaneously $y^{(2)} = 0$, the timestep will not blow up immediately. Note that it is reasonable to assume that $y^{(2)} = 0$ only instantaneously (e.g. at the end of one timestep). If $y^{(2)} = 0$ for more than one timestep, then the particle simply moves along a straight line for an extended period of time which implies that all the other derivatives are zero as well. In that case the integrator will have no problem integrating the particle's motion accurately regardless of the timestep. The only way to make a timestepping criterion well-defined when $y^{(2)} = 0$ and keep all the other desirable properties is to use higher derivatives, at least $y^{(5)}$ such as the criterion proposed by Aarseth (1985). However, although τ_{A85} is well-defined if $y^{(2)} = 0$, it is still not well-defined if at some point $y^{(2)} = y^{(3)} = 0$. We are unable to construct a physical scenario in which $y^{(2)} = 0$ but $y^{(3)} \neq 0$ for more than one timestep. And as we have mentioned above and will show in tests below, having higher derivatives would make any criterion more susceptible to floating point precision issues. In summary, we have good reasons to think that τ_{PRS23} is well-behaved in almost all imaginable scenarios.

As a side note, the previous timestepping criterion in IAS15 calculated the new timestep somewhat inconsistently using a mix of accelerations from the beginning of the timestep and values from the series expansion in the middle of the timestep. With τ_{PRS23} , IAS15 is now relying on the internal series expansion to consistently estimate all derivatives at the end of the timestep.

3.3.4 Tests

The discussion above provided the theoretical motivation for our specific choice for dt_{PRS23} . In this section we present results from numerical tests, verifying that simulations with our

⁶A setup that fails can be constructed by choosing the initial timestep of a hyperbolic encounter so large that the entire encounter occurs during one timestep. This is not possible for bound eccentric orbits because the orbital period puts an upper limit on the timestep.

new timestepping criterion are converged in a wide range of scenarios.

As a first test, we integrate the outer Solar System for 100 Jupiter orbits using different values of ϵ (and thus η via Eq. 3.28). The relative energy error is shown in Figure 3.9 for both the old and new IAS15 timestepping criteria. One can see that for $\epsilon \lesssim 10^{-5}$, the results are converged to machine precision. The default value of $\epsilon = 10^{-9}$ is well within this regime. Note that the relative error continues to decrease for $\epsilon < 10^{-5}$. This is because IAS15 uses compensated summation (Kahan, 1965) for some internal values. For $\epsilon \gtrsim 10^{-5}$, the error grows quickly. Because IAS15 is a 15th-order schema and the timestep is proportional to $\epsilon^{1/7}$, we have $\Delta E/E \propto \epsilon^{15/7}$. For the default $\epsilon = 10^{-9}$, the timestep corresponds to about 35 timesteps per innermost orbital period in this problem.

Next, we integrate the outer Solar System for 10^8 years, or 10^7 innermost periods. We run 12 simulations using the old timestepping criterion, dt_{RS15} , and 12 using the new criterion dt_{PRS23} . The relative energy errors of all individual simulations are shown as faint lines in Figure 3.10. We also plot the median as a stronger line. The results show that over these timescales, the energy error grows as the square root of time. This confirms that, at least under these conditions, IAS15 satisfies Brouwer's law (Brouwer, 1937) regardless of the precise timestepping criterion. Note that over much longer timescales, or by changing ϵ , IAS15 will eventually show a linear error growth. This is expected because IAS15 uses a series expansion internally. This series has to be cut off after a finite number of terms so it cannot be unbiased for all times. However, we don't expect this to matter in most astrophysical applications.

We now compare how well the new timestepping criterion, dt_{PRS23} , can determine a physically meaningful timestep in an eccentric two-body system if the system is offset from the origin. As discussed above, this is a common scenario in N-body simulations, for example, when planets orbiting a star have a close encounter with each other. For this test we initialise an eccentric two-body system on a grid with different offsets \bar{y} and eccentricities e . We plot the minimum timesteps as given by dt_{RS15} in the top panel of Figure 3.11 and those by dt_{PRS23} in the bottom panel. Physically, the minimum timestep should only depend on the eccentricity, but not the offset. However, as one can see in Figure 3.11, dt_{RS15} quickly fails to determine correct timesteps. Even at moderate offsets of only 100 times the semi-major axis, $\bar{y} = 100a$, the algorithm fails at eccentricities higher than 0.99. The reason for this is finite floating point precision as explained in Section 3.3.2. Because our new timestepping criterion, dt_{PRS23} , uses lower derivatives the reliability is much improved. We can now have offsets 10^8 times larger before finite floating point precision becomes an issue. The middle panel in the figure shows the dt_{A85} timestepping criterion. The criterion fails later than dt_{RS15} but earlier than dt_{PRS23} . This is expected because dt_{A85} uses 5th order derivatives versus 7th and 4th order for the two other criteria respectively.

In Figure 3.11 we also over-plot lines corresponding to particle orbits whose pericentre touches the planet's surface, assuming parameters for the planets in our Solar System. As

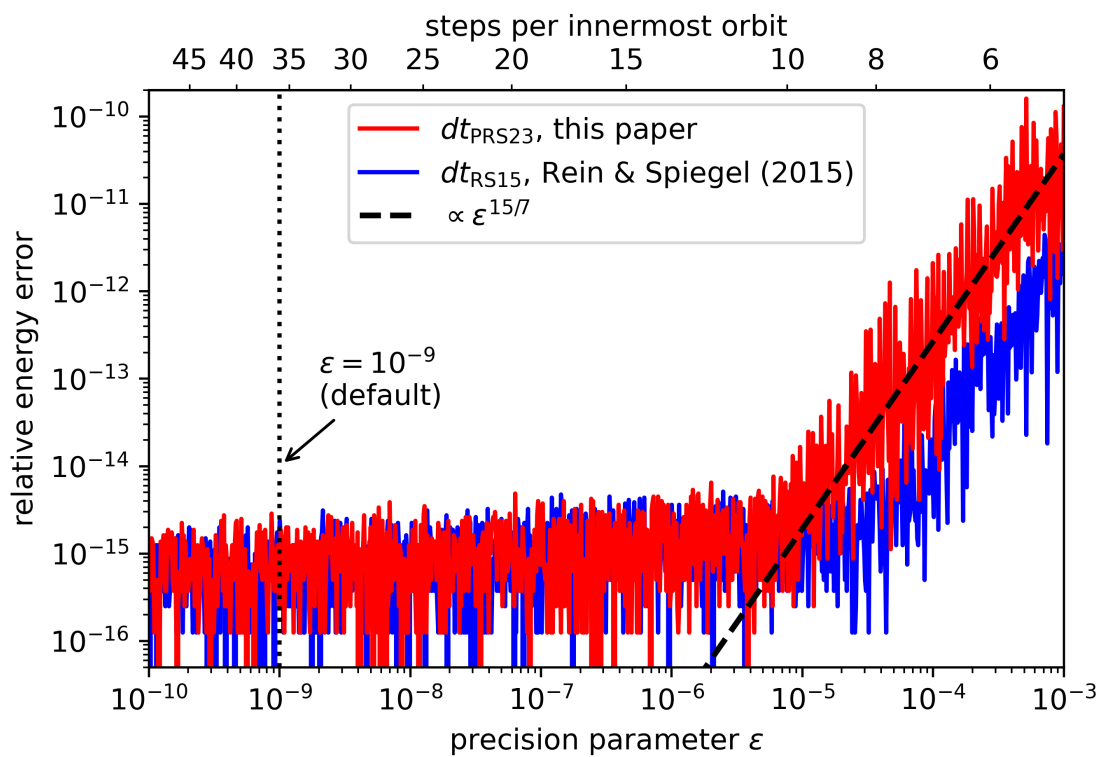


Figure 3.9: Relative energy error in simulations of the outer Solar System after 100 Jupiter orbits as a function of the accuracy control parameter ϵ . The blue curve shows the error in simulations using timesteps given by dt_{RS15} . The red curve shows the error in simulations using dt_{PRS23} . Also shown is the expected power law scaling for a 15th-order method.

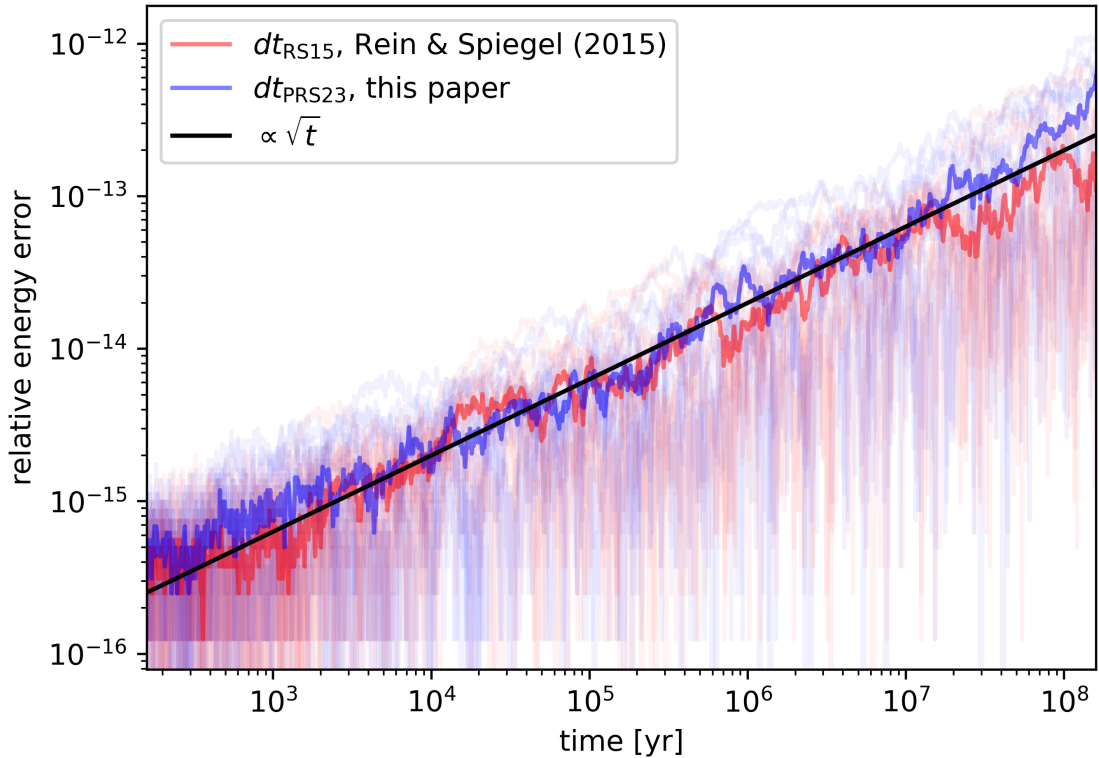


Figure 3.10: Relative energy error in 24 simulations of the outer Solar system as a function of time using the default $\epsilon = 10^{-9}$. The red curves show the error in simulations using timesteps given by dt_{RS15} . The blue curves show the error in simulations using timesteps given by dt_{PRS23} . Shown in black is the scaling expecting if the simulations follow Brouwer's law.

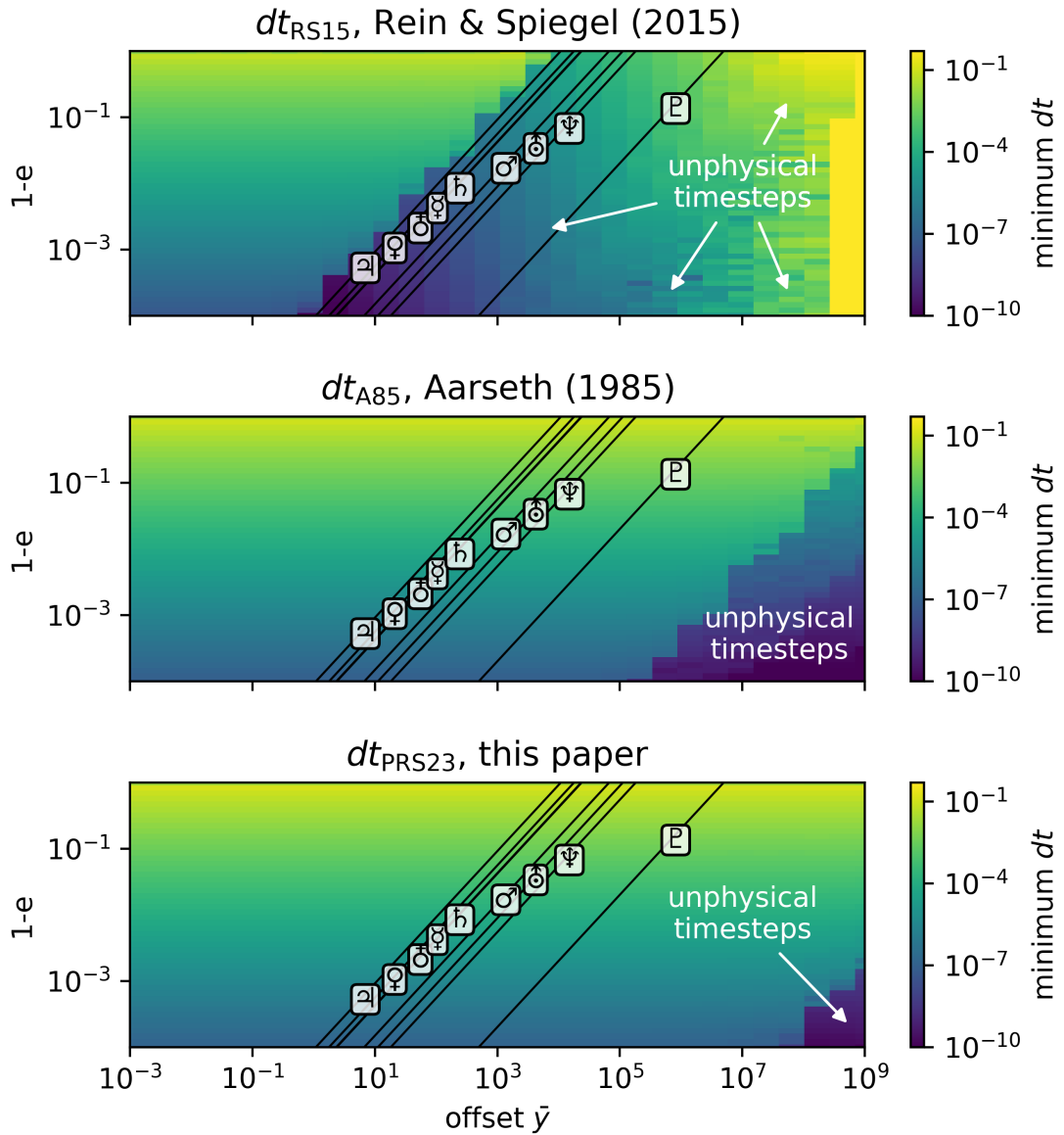


Figure 3.11: Minimal timesteps used in a two body problem as a function of eccentricity e and offset from the coordinate origin \bar{y} . We work in units where $G = a = 1$. The top, middle, and bottom panels show the minimal timesteps in simulations using dt_{RS15} , dt_{A85} , and dt_{PRS23} respectively. The diagonal lines correspond to orbits around the Solar System planets whose pericentre touches the planet's surface. Simulations using dt_{PRS23} are able to accurately calculate timesteps for offsets 10^8 times larger than simulations using dt_{RS15} .

one can see, the original dt_{RS15} criterion is not able to reliably integrate these orbits for any eccentricity and any Solar System planet which severely limits its usability. Both, dt_{A85} and dt_{PRS23} on the other hand can successfully determine the correct timescale. We therefore expect them to be able to handle most simulations in the context of the Solar System and planetary dynamics in general. Note that the problem gets worse for smaller objects further away from the central object (Pluto, planet 9, Kuiper belt objects). For example, dt_{A85} can resolve orbits around a 10 km-sized particle located at Pluto's semi-major axis. In contrast, our new criteria dt_{PRS23} can resolve orbits around particles at the same location but with a diameter as small as 50m.

Note that although the test above shows that we can resolve tight orbits around planets, the timestep chosen might not always be ideal. Our timestep criterion normalises $y^{(3)}$ and $y^{(4)}$ by comparing them to the acceleration $y^{(2)}$. There are cases where $y^{(2)}$ is dominated by the gravitational force from the central object even though the particle is in a bound orbit around a planet. This might result in a timestep that is too large. As an example, consider the Earth-Moon-Sun system. The acceleration on the Moon from the Sun is twice as large as the acceleration from the Earth. As a result, the timestep in a simulation of the Earth-Moon-Sun system is about twice as large compared to a simulation of the Earth-Moon system alone. This is clearly not physical. One can reduce ϵ if this becomes an issue. Another possible solution is to calculate τ_{PRS23} for each particle pair in the simulation and then take the minimum. However, the latter increases the computational complexity.

Whereas this chapter focuses mostly on applications related to planetary systems, the timestepping criterion by [Aarseth \(1985\)](#) was initially intended for N-body simulation of stellar clusters. Thus, as a further test we integrate a stellar cluster. We initialise the cluster as a Plummer sphere with $N = 50$ equal mass particles following the prescription of [Aarseth et al. \(1974\)](#). To better illustrate the differences between the timestepping criteria, we then replace each particle with an equal mass circular binary (we thus have $N = 100$ particles in total). We run 300 different realisations and vary the initial binary separation relative to the cluster size, $r_{\text{sep}}/r_{\text{cluster}}$. The runtime (normalised such that it is 1 for $r_{\text{sep}}/r_{\text{cluster}} = 10^{-2}$) and the relative energy errors for the timestepping criteria dt_{RS15} , dt_{A85} and dt_{PRS23} are shown in Figure 3.12 as a function of the binary separation. The dt_{RS15} criterion performs worst. It chooses a timestep that is too pessimistic (small) by an order of magnitude even for wide binaries, $r_{\text{sep}}/r_{\text{cluster}} \lesssim 10^{-2}$, and then fails catastrophically at moderately tight binaries, $r_{\text{sep}}/r_{\text{cluster}} \lesssim 10^{-8}$. As expected, our new criterion dt_{PRS23} performs significantly better, choosing the optimal timestep to resolve the binaries' orbital period down to $r_{\text{sep}}/r_{\text{cluster}} \lesssim 10^{-10}$, and never failing catastrophically in any of our tests involving stellar clusters. The dt_{A85} criterion falls once again in between the other two criteria. Note that the relative energy error increases for decreasing binary separation due to finite floating point precision as $\propto r_{\text{sep}}^{-1}$ regardless of the timestepping criteria as long as the criterion resolves the orbital period of the binaries.

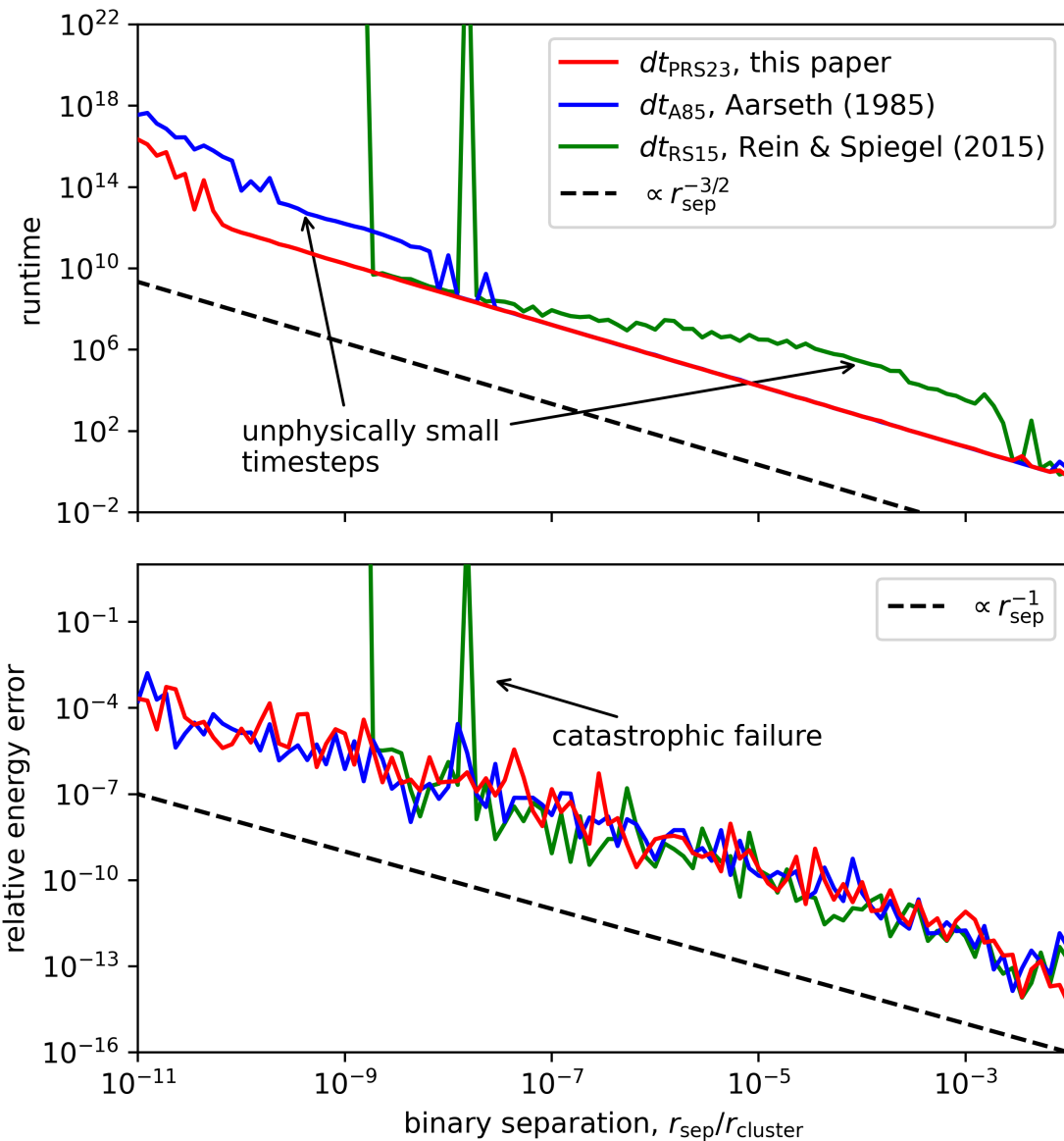


Figure 3.12: Runtime and relative energy error in a simulation of a stellar cluster with 50 binaries. The red curves show simulations using our new dt_{PRS23} criterion which performs best in this test.

We attribute the results in our cluster tests to the same issues discussed in detail above for the three body systems. Most importantly, we find that tight binaries and close encounters in stellar cluster can pose difficulties for some timestepping criteria, resulting in unphysically small timesteps and thus causing simulations to slow down significantly. Once floating point errors dominate, simulations can also fail catastrophically. This is why the criteria with the lowest order derivative, dt_{PRS23} , which is least susceptible to these errors, performs best.

3.3.5 Conclusion

In this chapter, we have described a new timestepping criterion and implemented it for the IAS15 integrator in the REBOUND N-body package. Compared to the previous timestepping criterion in IAS15, our new criterion has several significant advantages.

First, we provide a physical justification for our choice of timestep. Specifically, we choose the timestep so that for any bound orbit it is a fraction of the orbital period at apocentre and a fraction of the pericentre timescale at pericentre. In the limit of large eccentricities, these fractions are well-behaved and converge to a constant, independent of eccentricity. We have shown that our new criterion is the simplest choice (using the lowest order derivatives) that can satisfy these requirements.

Second, by using low (second, third, and fourth) order derivatives of the coordinates, we are able to avoid most issues coming from finite floating point precision. This allows us to accurately choose timesteps for particles having close encounters 10^8 times further away from the coordinate origin compared with the original timestepping algorithm in IAS15. Specifically, we can resolve orbits around a particle with a 50m diameter located at Pluto's current semi-major axis. We expect that this will be the most noticeable change for users that previously had trouble resolving tight orbits, close encounters, von Zeipel-Lidov-Kozai cycles ([von Zeipel, 1910](#); [Lidov, 1962](#); [Kozai, 1962](#)), or other scenarios where high eccentricities occur.

Third, although our criterion is similar to that of [Aarseth \(1985\)](#), it is simpler in the sense that we do not use the 5th derivative and it is therefore less susceptible to floating point precision issues.

Finally, let us make two important remarks about adaptive step size control in N-body simulations. First, it is always possible to come up with a scenario where an adaptive timestepping criterion fails. For example, if the initial timestep is orders of magnitudes too large, or timescales in a simulations change very abruptly, then any criterion will fail. So some physical intuition is always required when setting up and analysing N-body simulations with adaptive timestepping.

Second, it can be tempting to try and speed up simulations by changing the precision parameter in an adaptive scheme. For IAS15 this would involve adjusting ϵ . However, note that increasing ϵ by a factor of 10 only increases the timestep by a factor of 1.4. The energy

error on the other hand increases by a factor of 140, a consequence of IAS15 being a 15th-order scheme (see right side of Figure 3.9). Thus, one very quickly moves the integrator out of the regime where it follows Brouwer’s law. As soon as this happens, the energy error will grow linearly in time, rendering some long-term integrations unreliable. In summary, one should take great care and perform a convergence study when experimenting with larger than default timesteps in IAS15 and other high-order integrators. In most cases, the speed up of a factor of a few ($\lesssim 5$) might not be worth the extra effort.

Compared to the existing timestepping criterion in IAS15, our new criterion is better in all cases, and it will therefore become the default for new simulations. Users who wish to continue to use the old criterion can set the new `ri_ias15.adaptive_mode` flag to 1. We also implement the [Aarseth \(1985\)](#) criterion in IAS15 which can be turned on by setting `ri_ias15.adaptive_mode=3`. REBOUND and IAS15 are freely available at <https://github.com/hannorein/rebound>.

Acknowledgements

We thank Scott Tremaine and Norm Murray for insightful discussions. This research has been supported by the Natural Sciences and Engineering Research Council (NSERC) Discovery Grant RGPIN-2020-04513.

Chapter 4

Fast Radio Bursts and Interstellar Objects

I did not say and also do not believe that the matter of the comets has been created out of nothing...
Do you not daily see how large pieces of wood burn?
Weigh the ashes accurately and conclude therefrom how much matter escapes upwards.

Johannes Kepler, *Letter to Johann Georg Brengger* (1608),
translated by Baumgardt

The following text, as well as its associated figures and tables, was published in The Astrophysical Journal, Volume 977, pp. 232-236 as Pham et al. (2024a). Matthew J. Hopkins, Chris Lintott, Michele T. Bannister, Hanno Rein are co-authors.

Abstract

Fast radio bursts (FRBs) are transient radio events with millisecond-scale durations and debated origins. Collisions between planetesimals and neutron stars have been proposed as a mechanism to produce FRBs; the planetesimal strength, size and density determine the time duration and energy of the resulting event. One source of planetesimals is the population of interstellar objects, free-floating objects expected to be extremely abundant in galaxies across the Universe as products of planetary formation. We explore using the interstellar objects population as a reservoir of planetesimals for FRB production, finding that the expected interstellar objects-neutron star collision rate is comparable with the observed FRB event rate. Using a model linking the properties of planetesimals and the FRBs they produce, we further show that observed FRB durations are consistent with the

sizes of known interstellar objects, and the FRB energy distribution is consistent with the observed size distributions of Solar System planetesimal populations. Finally, we argue that the rate of interstellar object-neutron star collisions must increase with cosmic time, matching the observed evolution of the FRB rate. Thus, interstellar object-neutron star collisions are a feasible mechanism for producing FRBs.

4.1 Introduction

Fast radio bursts (FRBs) are gigahertz radio-emitting, millisecond-timescale transient events. First detected in 2007 (Lorimer et al., 2007), a large catalogue has been assembled by the Canadian Hydrogen Intensity Mapping Experiment (CHIME; CHIME/FRB Collaboration et al., 2021). The majority of known FRBs are extragalactic (Mannings et al., 2021), with only one yet known in the Milky Way (Bochenek et al., 2020; CHIME/FRB Collaboration et al., 2020). They exist in a wide range of host galaxies and local environments, but remain sparse: the inferred volumetric FRB rate for events above a threshold energy of 10^{35} erg is $(7_{-6}^{+9}) \times 10^7 \text{ Gpc}^{-3} \text{ yr}^{-1}$ (Bochenek et al., 2020). Two types are known: single (one-off) events, and repeating FRBs.

One of the many (cf. Platts et al., 2019; Zhang, 2020) proposed mechanisms to produce an FRB is a collision between a planetesimal and a neutron star, initially suggested by Geng & Huang (2015). Though neutron stars have been found to have planetary systems bound to them (Wolszczan & Frail, 1992), the radiation mechanism of Geng & Huang (2015) is specifically for unbound planetesimals, colliding on radial trajectories, as bound planetesimals are expected to interact differently (Brook et al., 2014). Dai et al. (2016) and Bagchi (2017) invoked the mechanism of Geng & Huang (2015) to explain repeating FRBs as neutron stars undergoing frequent encounters in debris disks around other stars. However, the feasibility of this scenario producing repeating FRBs at the rate observed is debated (Smallwood et al., 2019; Deng et al., 2024). Nevertheless, non-repeating FRBs may still be generated by neutron star-planetesimal collisions, if impacts can occur at a suitable rate in free space.

In this chapter, we consider the collisions between neutron stars and interstellar objects. An expected feature of planet formation (McGlynn & Chapman, 1989), interstellar objects are planetesimals unbound from the planetary systems they formed in ('Oumuamua ISSI Team et al., 2019) with a density of 10^{15} pc^{-3} in the Solar neighbourhood (Do et al., 2018) and a total number of $\sim 10^{27}$ across the Milky Way, and three discovered so far: 1I/'Oumuamua, 2I/Borisov, and 3I/Atlas. We first quantify the interstellar objects-neutron stars collision rate and consider its implications (Section 4.2). We then use the radiation mechanism of Dai et al. (2016) to compare the observed durations and energetics of FRBs to the sizes of interstellar objects (Section 4.3). Finally in Section 4.4 we discuss testable implications of FRBs being produced by interstellar object-neutron star collisions

and challenges with scaling the interstellar object-neutron star collision rate with the FRB event rate.

4.2 Interstellar Objects – Neutron Stars Collision Rate

In this section we first detail our estimate for the interstellar object-neutron star collision rate, then discuss sources of uncertainty in our estimate.

To estimate the density and velocity distribution of interstellar objects around neutron stars we make a number of assumptions. Since interstellar objects are an abundant, expected product of planetary systems (Shoemaker & Wolfe, 1984; Stern, 1990; Jewitt & Seligman, 2023), we first assume that planetary systems and therefore interstellar object populations are present in galaxies throughout the Universe. The population of interstellar objects larger than 1I/‘Oumuamua passing through the Solar system has a number density of $n_{\text{ISO}} \sim 10^{15} \text{ pc}^{-3}$ (Do et al., 2018), and a velocity distribution with a width of approximately 50 km s^{-1} (Hopkins et al., 2024). Being estimated from a single detection in a well-characterised survey this estimated number density has an uncertainty of an order of magnitude, but lacking additional constraints we assume the number density of interstellar objects around all neutron stars will be the same order of magnitude as this. For the relative velocities of neutron stars and interstellar objects, we note that upon creation neutron stars receive a large natal kick on the order of $\sim 100 \text{ km s}^{-1}$ (Lyne & Lorimer, 1994; Hobbs et al., 2005). As this is significantly larger than the interstellar object velocity dispersion around the Sun, we assume this value for the relative speed v_∞ of interstellar objects encountering neutron stars.

In the vicinity of a neutron star of mass $M_{\text{NS}} \simeq 1.4 M_\odot$ (Heger et al., 2003), interstellar objects follow hyperbolic trajectories defined by their impact parameter b and relative speed at infinity v_∞ , related to the periastron q by $b^2 = q^2 \left(1 + \frac{2GM_{\text{NS}}}{qv_\infty^2}\right)$. An interstellar object impacts the neutron star surface when it has a periastron less than the neutron star’s radius $R_{\text{NS}} \simeq 10 \text{ km}$ (Miller et al., 2021), therefore the cross-section of interstellar objects with a relative speed at infinity v_∞ colliding with the neutron star’s surface is

$$\begin{aligned} \sigma &= \pi b^2 = \pi R_{\text{NS}}^2 \left(1 + \frac{2GM_{\text{NS}}}{v_\infty^2 R_{\text{NS}}}\right) \\ &\approx 10^9 \text{ km}^2 \left(\frac{M_{\text{NS}}}{1.4 M_\odot}\right) \left(\frac{R_{\text{NS}}}{10 \text{ km}}\right) \left(\frac{v_\infty}{100 \text{ km s}^{-1}}\right)^{-2}. \end{aligned} \quad (4.1)$$

The increase in cross-section due to the second term is referred to as gravitational focusing (cf. Forbes & Loeb, 2019) and completely dominates in this high-gravity situation. Thus, taking $n_{\text{ISO}} \sim 10^{15} \text{ pc}^{-3}$, $v_\infty \sim 100 \text{ km s}^{-1}$ and $\sigma \sim 10^9 \text{ km}^2$ gives the encounter rate of a single neutron star with interstellar objects as

$$\Gamma = n_{\text{ISO}} v_\infty \sigma \sim 10^{-7} \text{ yr}^{-1}. \quad (4.2)$$

FRBs are detected over cosmological distances, with the most distant being detected at $z = 1$ (Ryder et al., 2023), thus we must consider the cosmological rate of interstellar objects-neutron stars collisions. Stars over $9M_{\odot}$ make up $\sim 0.5\%$ of all stars formed (assuming the universal initial mass function of Kroupa, 2001), have lifetimes $\lesssim 0.1$ Gyr and largely form neutron stars upon their deaths (Heger et al., 2003). Thus with approximately 10^{11} stars (e.g., Licquia & Newman, 2015), the Milky Way contains about $N_{\text{NS}} \sim 10^9$ neutron stars. For a number density of Milky Way-mass galaxies of $n_{\text{Gal}} \sim 10^7 \text{ Gpc}^{-3}$ (Blanton et al., 2003), the cosmological rate of interstellar object-neutron star collisions is

$$R_{\text{col}} = \Gamma \cdot n_{\text{Gal}} \cdot N_{\text{NS}} \sim 10^9 \text{ Gpc}^{-3} \text{ yr}^{-1}. \quad (4.3)$$

FRBs produced by interstellar object-neutron star collisions are thought to be strongly beamed by a factor $f \sim 10^{-2}$ (Dai, 2020) meaning if every 1I-sized interstellar object-neutron star collision produced an FRB the observable rate would be

$$R_{\text{obs}} = f R_{\text{col}} \sim 10^7 \text{ Gpc}^{-3} \text{ yr}^{-1}, \quad (4.4)$$

comparable to the observed rate of $(7^{+9}_{-6}) \times 10^7 \text{ Gpc}^{-3} \text{ yr}^{-1}$ (Bochenek et al., 2020).

The most significant source of uncertainty in this estimate is the average number density of interstellar objects n_{ISO} around neutron stars. In addition to the order-of-magnitude uncertainty in the number density of interstellar objects in the Solar neighbourhood, interstellar objects are not directly observable outside the Solar system so the density around different neutron stars across the local Universe may vary significantly from this value. We expect the density of interstellar objects to vary across the Milky Way (Hopkins et al., 2023) and between different galaxies (Williams et al., 2022) due to a dependence of planetesimal formation on stellar metallicity (Andama et al., 2024). Second, the natal kick that a neutron star receives (Hobbs et al., 2005; Chatterjee et al., 2005) can place them on an orbit removed from their galaxy's stars and interstellar objects, or completely eject them. Sweeney et al. (2022) model the Milky Way, predicting that 40% of neutron stars are completely ejected and the remaining neutron stars occupy a disk with a vertical scale height five times that of the stellar disk. Interstellar objects are expected to retain the same spatial distribution as their parent stars (Hopkins et al., 2024), therefore neutron star natal kicks could reduce the expected interstellar object-neutron star collision rate. This however will not be a major effect in elliptical galaxies, which make up $\sim 40\%$ of galaxies in the local universe brighter than $M_r < -19$ (Lintott et al., 2008, M_r is the r -band absolute magnitude).

Finally, the timescale for a typical collision between an interstellar object and a neutron star (Eq. 4.2) is far longer than that of repeating FRBs which occur on timescale of weeks. Thus, we find that interstellar object-neutron star collisions cannot explain repeating FRBs and this mechanism cannot be the only source of FRBs. Note that the contribution of multiple different mechanisms to the FRB population has been suggested in e.g., Gordon

et al. (2023). Furthermore, Pleunis et al. (2021) find differences in the emissions from repeaters and non-repeaters, implying repeaters and non-repeaters have different progenitors. However, we can make testable predictions from the potential subset of FRBs caused by interstellar object-neutron star collisions.

4.3 Emission Properties

We now explore the expected properties assuming the emission mechanism predicted in Geng & Huang (2015), Dai et al. (2016) and Dai (2020). When the tidal forces on the planetesimal exceed its tensile strength s , it will be disrupted. This has been observed in the Solar System, for example in the tidal disruption of comet Shoemaker-Levy 9 by Jupiter (Boss, 1994). Small bodies in the Solar System – like asteroids and comets – are rubble piles (e.g., Asphaug & Benz, 1994; Walsh, 2018) with a low tensile strength. Colgate & Petschek (1981) use a tensile strength $s \sim 10^9$ Pa and this value is continued in later works (such as Geng & Huang, 2015; Dai et al., 2016; Siraj & Loeb, 2019). However, asteroids and comets have significantly lower values, $s \sim 500$ Pa (as constrained by spacecraft measurement and population analysis e.g., Greenberg et al., 1995; Attree et al., 2018; Scheeres, 2018). Likewise, the compressive strength, $P_0 \sim 100$ MPa (e.g., Jenniskens et al., 2012; Flynn et al., 2018; Pohl & Britt, 2020), is three orders of magnitude lower than in Colgate & Petschek (1981). We use these current estimates of tensile and compressive strengths in the context of the Dai et al. (2016) emission mechanism.

An interstellar object-neutron star collision produces homogenous tidal disruption, in contrast to a Shoemaker-Levy 9-like disruption. On a highly-elliptical orbit around Jupiter, Shoemaker-Levy 9 passed close enough to the planet at perijove to partially disrupt into several fragments in 1992 (Nakano et al., 1993). However, it then continued on its orbit, far enough from Jupiter that no more disruption events occurred, for an additional two years before colliding with the planet in 1994 (Levy, 1998), allowing the fragments to drift a significant distance apart. In an interstellar object-neutron star collision as modelled in Colgate & Petschek (1981), Geng & Huang (2015) and Dai et al. (2016), the planetesimal falls radially onto the neutron star, impacting the surface very shortly after fragmentation begins. As it approaches the neutron star and the tidal forces on it continually increase the planetesimal will go through a rapid sequence of disruptions, with each generation of fragments undergoing their own fragmentation each time the remaining distance to the neutron star decreases by a factor of $2^{-2/9} \simeq 0.85$ (Colgate & Petschek, 1981). Thus, the planetesimal will completely disrupt into a mostly-homogeneous stream of material, and we expect interstellar object-neutron star collisions to produce largely unstructured FRBs, without subbursts. This is the case even for contact binaries such as (486958) Arrokoth or 67P/Churyumov–Gerasimenko, made up of two distinct lobes held together by mutual gravity (Scheeres, 2007), as the tidal force required to separate two lobes is the same order

of magnitude as that required to disrupt each lobe individually.

After disruption, the time difference between the arrival of the leading and trailing edge of the disrupted planetesimal fragments is given by Colgate & Petschek (1981), with ρ and R as the density and radius of the planetesimal:

$$\Delta t \simeq 4 \text{ ms} \left(\frac{M_{\text{NS}}}{1.4 M_{\odot}} \right)^{-1/3} \left(\frac{\rho}{3 \text{ g cm}^{-3}} \right)^{1/6} \cdot \left(\frac{s}{500 \text{ Pa}} \right)^{-1/6} \left(\frac{R}{1 \text{ km}} \right)^{4/3}. \quad (4.5)$$

This relates planetesimal radius to the resulting FRB duration. In Fig. 4.1, we show the histogram of FRBs' duration from CHIME Catalog 1 (CHIME/FRB Collaboration et al., 2021) with equivalent planetesimal radii, R . Note that there is an apparent cutoff in FRB pulse duration at ~ 1 ms due to CHIME's time resolution (CHIME/FRB Collaboration et al., 2021). The distribution plotted here is subject to detection bias: as discussed later, the longer FRB pulses produced by larger interstellar objects are also brighter, and therefore more detectable. Though a full model of the detection bias present in CHIME is beyond the scope of this work, we can qualitatively say that the distribution plotted in Fig 4.1 will be weighted towards longer pulse lengths and larger interstellar object radii than the underlying distribution. However, the observed range of FRB durations corresponds to planetesimal radii $400 \text{ m} \lesssim R \lesssim 10 \text{ km}$, still broadly consistent with the sizes of the two observed interstellar objects (Jewitt et al., 2017; Hui et al., 2020).

Using the updated value for tensile strength we can reinterpret the potential asteroidal cause of FRB 200428, first postulated in Dai (2020). FRB 200428 consists of two distinct subbursts of 0.6ms and 0.3ms separated by a large gap of 29ms (See Fig. 1 of CHIME/FRB Collaboration et al., 2020). Assuming FRB 200428 was caused by an interstellar object-neutron star collision, Dai (2020) suggests that these subbursts were caused by two major fragments of a single body, split through tidal disruption during infall. As discussed earlier in this section, we expect instead that tidal disruption during infall onto a neutron star will not create two major fragments but instead a mostly-homogeneous stream of material. Thus, we tentatively suggest instead that the large and complete separation of the sub-bursts is evidence that the colliding interstellar object was a binary: two separate bodies of radius 200m and 100m respectively, with a separation of several kilometres. Binaries are common within the Solar system (Margot et al., 2002; Walsh et al., 2008; Fraser et al., 2017), but the potential existence of binary interstellar objects presents a fascinating opportunity for study. If formed as a binary before ejection from their home planetary systems, the ejection mechanism must be gentle enough to allow the constituent bodies to remain gravitationally bound. McDonald & Veras (2023) find that ejection by scattering off planets disrupts all binary asteroids; however, ejection mechanisms acting at larger stellocentric distances, such as stellar flybys (Pfalzner et al., 2021) or the effect of the Galactic tide on the outer edges of exo-Oort clouds (Brasser et al., 2010; Kaib et al., 2011) may be sufficiently gentle. Alternatively, binaries could perhaps be formed in the tidal disruption events that may be

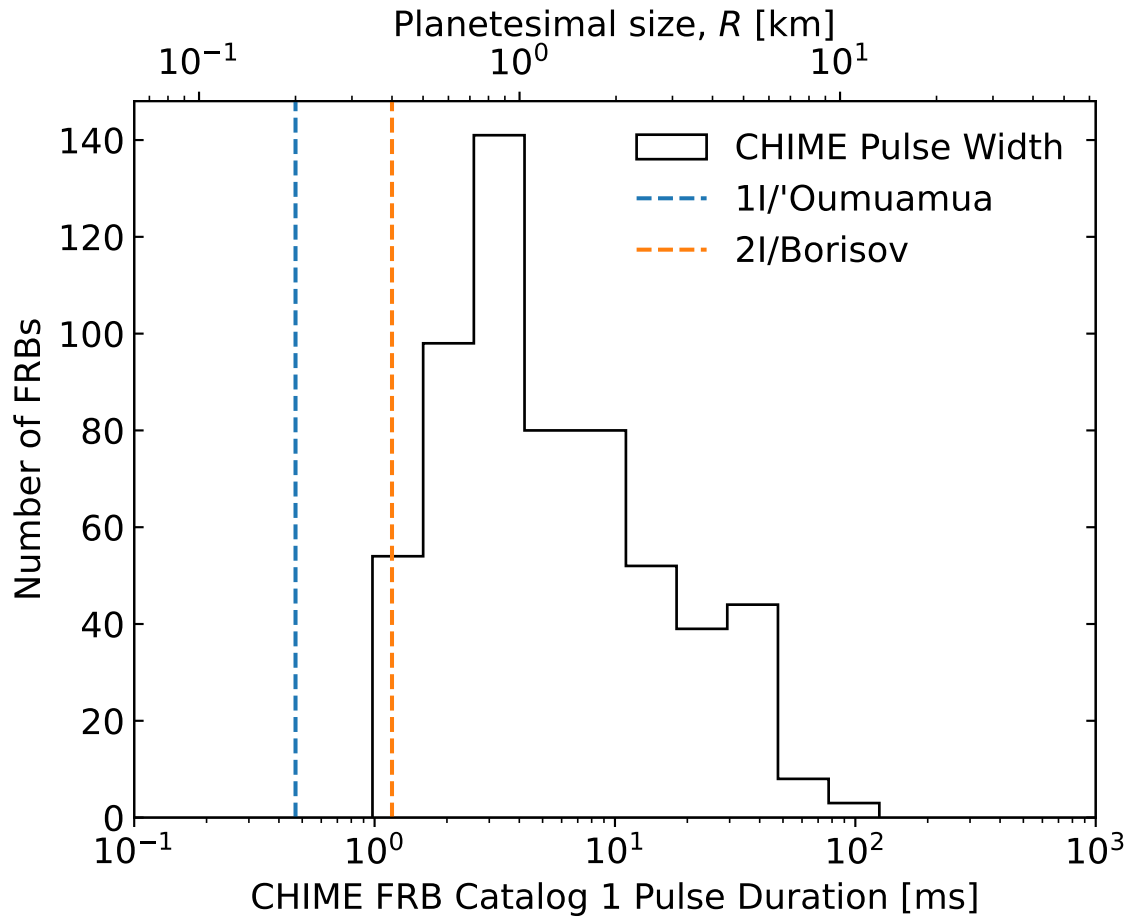


Figure 4.1: The CHIME Catalog 1 distribution of FRB boxcar pulse width. On the top axis, we show the equivalent planetesimal size, R , assuming tensile strength $s = 500$ Pa and density $\rho_0 = 3$ g cm $^{-3}$. Dashed vertical lines show the estimated sizes of two observed interstellar objects, 1I/'Oumuamua and 2I/Borisov. The apparent sudden cutoff in FRB pulse duration at 10^0 ms is due to CHIME's time resolution (0.983 ms, [CHIME/FRB Collaboration et al., 2021](#)).

Table 4.1: Planetesimal size distributions power-law exponents q and the resultant predicted interstellar object-neutron star collision energy distribution exponent γ , compared to the observed FRB energy distribution exponent.

q	γ	Description
2.5	1.38	Main asteroid belt (Gladman et al., 2009)
2.8	1.45	Streaming instability (Simon et al., 2016)
3.5	1.63	Faint TNOs (Lawler et al., 2018)
	$1.3^{+0.7}_{-0.4}$	Observed FRBs (Shin et al., 2023)

the source of some interstellar objects ([Walsh & Richardson, 2006](#); [Ćuk, 2018](#); [Zhang & Lin, 2020](#)). An interesting prediction of connecting FRB subbursts to binary interstellar objects is that they should be largely limited to two subbursts, since triple (and higher) asteroids are much rarer. We find that of the non-repeating FRBs in the CHIME Catalog 1, there are 450 events consisting of one burst, 19 events with two subbursts, and only 5 events with more than two subbursts. As discussed above interstellar object-neutron star collisions cannot be the source of all FRBs, but if they are the source of some, then FRBs may potentially be a probe for studying interstellar objects well beyond the limits of the Solar System.

Now we relate the luminosity distribution of FRBs to possible size distributions of interstellar objects. Under the [Dai et al. \(2016\)](#) mechanism most of the energy is released at frequency ~ 1 GHz, consistent with FRBs energy spectrum. The luminosity is given by

$$L_{\text{tot}} \sim 2.5 \times 10^{36} \text{ erg s}^{-1} \left(\frac{P_0}{100 \text{ MPa}} \right)^{2/5} \left(\frac{s}{500 \text{ Pa}} \right)^{4/15} \\ \cdot \left(\frac{R}{1 \text{ km}} \right)^{8/3} \left(\frac{\rho}{3 \text{ g cm}^{-3}} \right)^{-2/3} \left(\frac{M_{\text{NS}}}{1.4 M_{\odot}} \right)^{19/12} \\ \cdot \left(\frac{\mu_B}{10^{30} \text{ G cm}^3} \right)^{3/2} \left(\frac{d}{10 \text{ km}} \right)^{-23/4} \left(\frac{\rho_c}{10^6 \text{ cm}} \right)^{-1} \quad (4.6)$$

where $\mu_B = B_{\text{surface}} R_{\text{NS}}^3$ is the magnetic dipole moment, B_{surface} is the field strength at the neutron star's surface, ρ_c is the curvature radius near the neutron star, and d is the distance from the ionized planetesimal fragments to the neutron star centre. The strong dependence on d implies that most of the energy is released near the neutron star's surface at $d \simeq R_{\text{NS}} \simeq 10$ km. This emission is strongly beamed by a factor $f \sim 1/100$, so the isotropic-equivalent energy emission is given by $E_{\text{isotropic}} \sim L_{\text{tot}} \Delta t / f$. Observed FRBs have isotropic energy emission typically between $10^{35} - 10^{41}$ erg ([CHIME/FRB Collaboration et al., 2020](#); [Kirsten et al., 2024](#)), equivalent to planetesimal sizes $0.5 - 10$ km at typical pulsar magnetic field strengths, consistent with sizes inferred from FRB time duration.

The observed isotropic energy distribution of FRBs appears to follow a power law:

$$\frac{dN}{dE_{\text{isotropic}}} \propto E_{\text{isotropic}}^{-\gamma} \quad (4.7)$$

with γ inferred to be $1.3^{+0.7}_{-0.4}$ by [Shin et al. \(2023\)](#). Planetesimal size distributions are typically also treated as power laws or composite power laws:

$$\frac{dN}{dR} \propto R^{-q} \quad (4.8)$$

with streaming instability modelling predicting $q \approx 2.8$ ([Simon et al., 2016](#)), and observations of Solar system populations finding values of $q \approx 2.5$ for the main asteroid belt ([Gladman et al., 2009](#)) and $q \approx 3.5$ for faint trans-Neptunian objects (e.g., [Lawler et al., 2018](#)). The interstellar object size distribution is completely unconstrained, but assuming interstellar objects have a similar power-law size distributions to Solar system populations we can relate the interstellar object power law exponent to the expected interstellar object-neutron star isotropic energy distribution exponent. Since $E_{\text{isotropic}} \propto L_{\text{tot}}\Delta t \propto R^4$, γ is related to q by $\gamma = (3 + q)/4$.

[Table 4.1](#) compares the expected values of γ for interstellar object-neutron star collision isotropic energy distributions assuming different planetesimal size distributions to the observed FRB distribution. Ideally, we would compare our predictions for γ to the energy distribution of exclusively single pulses from non-repeating FRBs, as this is the type of FRB that model predicts. However, the sample used by [Shin et al. \(2023\)](#) includes repeating FRBs, albeit only the first detected burst from each, and uses the combined energy released in the small number of FRBs with multiple pulses. Since the majority of bursts are single pulses from non-repeaters we do not expect this to change the value of γ by a significant amount and find that the power-law scalings are within the uncertainty of observed FRB rates.

4.4 Discussion

First, both neutron stars and interstellar objects are long-lived and build up over time, meaning that the rate of interstellar object-neutron star collisions is decoupled from the current star formation rate. This is in direct contrast to magnetars, a commonly-invoked FRB source (e.g., [Metzger et al., 2019](#); [Wadiasingh & Timokhin, 2019](#); [Margalit et al., 2019](#)), which have short lifetimes of 10 kyr ([Mondal, 2021](#)) meaning they are only present when and where star formation is actively occurring. Several recent studies have found the redshift dependence of the FRB rate to be inconsistent with the evolution of the cosmic star formation rate (e.g., [Hashimoto et al., 2020a, 2022](#); [Zhang & Zhang, 2022](#); [Tang et al., 2023](#); [Lin et al., 2024](#); [Lin & Zou, 2024](#); [Zhang et al., 2024](#); [Chen et al., 2024](#)), and FRBs cannot only originate from short-lived objects like magnetars. Instead of decreasing with cosmic

time like the star formation rate (Madau & Dickinson, 2014) the FRB rate is increasing, as would be expected from long-lived progenitors.

Second, a small number of FRBs have been localised to their host galaxies, and though the majority of this sample is found in star-forming galaxies, those that originate in quiescent galaxies are unlikely to be from young progenitors (Gordon et al., 2023). If interstellar object-neutron star collisions are the source of a significant fraction of FRBs, we additionally would expect the reduced rate of interstellar object-neutron star collisions from disk galaxies as neutron star natal kicks cause a dependence of FRB rate on host galaxy morphology.

Therefore, we expect that insights into interstellar object-neutron star collisions as a production mechanism will be constrained as more events are found and localised by SKA, CHIME, CHORD, and ASKAP (Vanderlinde et al., 2019; Hashimoto et al., 2020b; Bhandari et al., 2020; Michilli et al., 2023).

A final issue remains: the rate of observable interstellar object-neutron star collisions of $\sim 10^7 \text{ Gpc}^{-3}\text{yr}^{-1}$ that we calculate in Section 4.2 is not directly comparable to the rate of FRBs of $(7^{+9}_{-6}) \times 10^7 \text{ Gpc}^{-3} \text{ yr}^{-1}$ inferred by Bochenek et al. (2020). The rate we calculate corresponds to 11-sized interstellar objects colliding with all neutron stars, whereas the observable FRB rate inferred by Bochenek et al. (2020) corresponds to FRBs of at least the energy of FRB 200428, with an isotropic-equivalent energy release of $2 \times 10^{35} \text{ erg}$. Ideally, we would use a combination of the interstellar object size distribution and neutron star magnetic field distribution to calculate the rate distribution of interstellar object-neutron star collision energies and compare the observable interstellar object-neutron star collision rate at the energy of FRB 200428. However, given that the interstellar object size distribution is not well constrained, this is beyond the scope of this work.

4.5 Conclusion

The progenitors and emission mechanisms of FRBs are debated. We revisit the emission mechanism of Geng & Huang (2015) and Dai et al. (2016) which postulates FRBs are caused by collisions between neutron stars and planetesimals, and investigate the implications of these planetesimals being interstellar objects. As products of planetary formation, interstellar objects are common in the Milky Way and expected to be abundant across the Universe. We have demonstrated that the expected interstellar object-neutron star collision rate is consistent with the cosmic rate of FRBs within the order-of-magnitude uncertainties. Using updated planetesimal properties such as tensile strength, we have shown that observed FRB durations and energetics correspond to collisions with planetesimals of sizes in the range 0.4 – 10 km, consistent with the two observed interstellar objects. We have tentatively suggested FRBs with sub-bursts such as FRB 200428 could be caused by collisions with binary interstellar objects. Finally, we have discussed the testable implications of interstellar object-neutron star collisions producing FRB-like signals on the redshift dependence of

the FRB rate, and the morphology of galaxies which host FRBs. Thus collisions between interstellar objects and neutron stars are feasible progenitors of one-off FRBs.

Acknowledgements

We thank the anonymous reviewer for their insightful comments. We would like to thank Jocelyn Bell Burnell, Ayush Pandhi, and Alexander Andersson for insightful and helpful discussions. MJH acknowledges support from the Science and Technology Facilities Council through grant ST/W507726/1.

Chapter 5

Post-Main Sequence Evolution of Cometary Volatiles

The question relative to the constitution of Comets is one of the most interesting in the whole range of celestial physics...

And although it must be acknowledged that little progress has hitherto been made towards obtaining a satisfactory solution of these questions, still a multitude of facts have been disclosed by the observations of astronomers, which have formed the groundwork of much ingenious speculation...

Robert Grant, *History of Physical Astronomy* (1852)

This chapter will be submitted for peer-reviewed publication. The authors are Dang Pham and Hanno Rein.

Abstract

Observations of white dwarfs reveal pollution from bodies with rocky, Earth-like composition. A variety of dynamical models propose that debris discs at various distances can be dynamically induced to bring planetesimals to pollute the central white dwarf. It is assumed that these discs are thermally processed due to the intense asymptotic giant branch before the star becomes a white dwarf. To fully study the volatile budget in various planetesimal reservoirs in evolved Solar system and exoplanetary systems, it is necessary to study the chemical and dynamical evolution of these small bodies during the luminous post-main sequence stellar evolution. In this chapter, we first develop a new simulation capable of

simulating comets on highly eccentric orbits around an evolving post-main sequence star, which can rapidly change in luminosity and mass. This simulation couples dynamical, stellar, thermal, and volatile ices evolution, employing an adaptive timestep scheme with an implicit-explicit integrator switching criterion. We use this method to simulate the long-term evolution of cometary volatiles and hypervolatiles in the Solar system Kuiper Belt and Scattered Disc, and in circular debris discs around Sun-like stars. We find that the Kuiper Belt is depleted of all volatiles like CO and CO₂, while the Scattered Disc can retain some fraction of these volatiles depending on the comets' size and distance. For comets in circular debris discs, we found a similar result with varying degrees of volatile retention. Our results show that recently proposed debris discs of planetesimals to produce white dwarf pollution would have consistent composition with observed volatile-depleted white dwarf spectra.

5.1 Introduction

In a few billion years, the Sun will become a white dwarf, a degenerate stellar core, a remnant of stellar evolution. Observations of white dwarf atmospheres found that about 20-50% of white dwarfs exhibit signs of recent or ongoing metal accretion from an external body (Zuckerman et al., 2003; Koester et al., 2014; Wilson et al., 2019; Blouin & Xu, 2022). There are many dynamical theories on the possible reservoirs of white dwarf pollutants, ranging from asteroids to planets, with a variety of mechanisms to deliver these bodies to the white dwarf (e.g. Debes & Sigurdsson, 2002; Mustill et al., 2014; Smallwood et al., 2018; Maldonado et al., 2020; Trierweiler et al., 2022; O'Connor et al., 2022; Veras et al., 2024). Studying the atmosphere of polluted white dwarfs grants an unprecedented opportunity to analyse the bulk composition of exoplanetary bodies. The observed white dwarf spectra show diverse composition typically representing rocky Earth-like bodies (Jura, 2006; Jura & Xu, 2012; Doyle et al., 2019; Putirka & Xu, 2021; Xu & Bonsor, 2021; Rogers et al., 2024). The observed composition on white dwarfs are different from those of current Solar system comets due to the much lower abundance of observed C and O (e.g. Xu & Bonsor, 2021; Rogers et al., 2024). That being said, there are some white dwarfs exhibiting cometary composition (Farihi et al., 2013; Klein et al., 2021; Doyle et al., 2021), most notably a Kuiper Belt-analogue in Xu et al. (2017). There is also an observation of a polluted white dwarf exhibiting pollution signals from both rocky and icy bodies (Johnson et al., 2022).

A variety of scenarios have recently been proposed in the literature using a debris disc of rocky planetesimals to pollute white dwarfs (e.g. O'Connor et al., 2022; Akiba et al., 2024). It is sometimes assumed that comets in these debris discs could be depleted of volatiles during the post-main sequence evolution stages when the central star's luminosity can reach up to $5000L_{\odot}$. The processing of volatile content during post-main sequence evolution in various populations of comets has been studied by Jura & Xu (2010); Stone et al. (2015); Malamud & Perets (2016, 2017a,b); Harrison et al. (2021); Levine et al. (2023); Li et al.

(2024). All of these works have the primary goal of studying the resulting volatile content of comets after post-main sequence evolution to explain the observed rocky composition of polluted white dwarf atmospheres. The final delivery of the tidally disrupted comets and their surviving volatile content (if there are any) into white dwarfs are studied by [Brouwers et al. \(2023a,b\)](#).

In the existing literature that we are aware of, there is gap in understanding the volatile contents of many cometary population for a few reasons. First, some articles only track the evolution and retention of only H₂O ices, which is the most difficult volatile to sublimate. Using the fraction of final H₂O to trace other cometary molecules leads to an overestimation of other volatiles like CO₂ and hypervolatiles like CO. Second, some previous works on post-main sequence volatile processing of comets consider comets on circular orbits or use orbit-averaged equilibrium temperature for eccentric orbits. Considering only circular orbits neglects the volatile evolution of comets on eccentric orbits, which encompasses the majority of the Solar system Scattered Disc and Oort cloud. The use of orbit-averaged equilibrium temperature can become inappropriate for some orbits, as discussed in [Quirrenbach \(2022\)](#). Third, some works assume that comets instantly reach equilibrium temperature given a particular stellar luminosity. This is not a good assumption when some of the brightest stellar evolution phases occur on very fast timescales. In addition, these works often do not couple the mass evolution of ices, which can change the thermal conductivity of a comet, to the thermal evolution. Fourth, some works perform various order of magnitude estimates (typically by taking the ratio of energy required to sublimate a comet full of a particular ice species divided by the total energy a comet receives). However, these estimates are often inaccurate because they neglect blackbody re-radiation from the top layers of a comet (which significantly reduces the energy input-output budget). Fifth, these order of magnitude estimates assume that comets' thermal properties are constant, uniform, and homogeneous. These assumptions are not made in Solar system comet modeling ([Huebner et al., 2006](#)) because comets can vary significantly between their nuclei cores and surface. Sixth, some works “scale out” the known boundaries of Solar comets (e.g., what is the distance of equivalent flux of a present-day 30 AU comet when the Sun becomes a 5000 L_{\odot} star). This estimate, unfortunately, fails to quantitatively describe the exact volatile fraction for a comet of a given size.

For these reasons, it is currently unclear what are the volatile content of species like CO and CO₂ ices for comets on eccentric and circular orbits after post-main sequence stellar evolution. Since various reservoirs small bodies are expected by many dynamical models to pollute white dwarfs ([Alcock et al., 1986; Stephan et al., 2017; O'Connor et al., 2022, 2023; Pham & Rein, 2024; Akiba et al., 2024](#)), it is important to understand the volatile budget of these comets to interpret the observed lack of C abundance on bodies that are polluting white dwarfs.

In this work, we contribute to the existing literature by fully coupling dynamical, stellar,

thermal, and mass evolution for comets over the last 400 Myr stellar evolution. In this work, we specifically track the evolution of water, CO, and CO₂ ices. We use the theory and develop upon the extensive literature on the processing of volatiles in the early Solar system (e.g. Mekler et al., 1990; Prialnik, 1992; Tancredi et al., 1994; Orosei et al., 1999; Choi et al., 2002; Huebner et al., 2006; Prialnik & Merk, 2008; Guilbert-Lepoutre et al., 2011; Davidsson, 2021; Gkotsinas et al., 2022, 2024). However, our problem is different from these works because the star can become orders of magnitude brighter than the young Sun, losing mass, and our comets are often much more distant. Thus, we develop a new numerical code capable of handling the most eccentric comet orbiting around a rapidly changing star during the asymptotic giant branch where the star’s luminosity can reach up to $5000L_{\odot}$ and the star rapidly loses 30% of its mass. Then, we study the retention of CO and CO₂ for the following populations: Solar system-like Kuiper Belt and Scattered Disc, and initially circular debris discs. This allows us to answer the questions of the volatile content in future Solar system comets and the volatile content of extra-solar debris discs for white dwarf pollution.

In section 5.2, we present the analytic theory of thermal and ice evolution modelling used in this chapter. The modelling is based on the Solar system comet modelling literature, particularly from Prialnik (1992); Prialnik et al. (2004); Huebner et al. (2006); Guilbert-Lepoutre et al. (2011); Davidsson (2021); Gkotsinas et al. (2024). We present an approximation to gas sublimation and transport to speed up simulation, and discuss this in context of another approximation in the literature. In section 5.3, we study the various timescales associated with our problem, which become important in our numerical methods. In section 5.4, we describe the numerical method developed to appropriately simulate eccentric comets around a post-main sequence star. We also perform several tests to demonstrate the capability of our methods.

In section 5.5, we use this simulation for the two populations previously described. We also discuss our results in context of recently proposed close-in planetesimal reservoirs (debris discs between $10 - 10^3$ AU) for white dwarf pollution (O’Connor et al., 2022; Akiba et al., 2024). In section 5.6, we discuss our results for polluted white dwarfs by showing icy body pollution spectra signature. We further discuss dynamics not included (planets and white dwarf natal kick) and a missing cometary evolution aspect (serpentinisation). We summarise our work in section 5.7.

Commonly-used variables in this work are summarised in Table 5.1. Other variables are defined where they are used. Cometary constants used are in Table 5.2 and Table 5.4.

5.2 Analytic Theory: Thermal and Ice Evolution

Modelling the interior evolution of a comet entails coupling thermal and volatile (in gaseous and solid forms) evolution. The equations of state describing such evolution have been

developed extensively in previous works (Prialnik, 1992; Prialnik et al., 2004; Huebner et al., 2006; Davidsson, 2021). This typically entails a partial differential equation to describe the temperature evolution, and mass-continuity equations to govern the production and transport of gas. In this section, we will describe the governing equations modeled in our simulation, and any relevant approximations done. In Table 5.1, we list the symbols used in this chapter, their definitions, and associated SI units as a reference.

We model our comet as a spherical, porous aggregate with dust, H₂O (consisting of amorphous ice, crystalline ice, and water vapour phases), and other volatiles (solid and gaseous phases). There are a few parameters to describe this porous medium: Porosity (ψ), average pore radius (r_p), and tortuosity (ξ) — all of these quantities are assumed to be uniform and unchanging. The values we used are shown in Table 5.2. These values are from typical values used in existing comet modelling literature (e.g. Huebner et al., 2006; Guilbert-Lepoutre et al., 2011; Davidsson, 2021; Gkotsinas et al., 2024).

5.2.1 Thermal Evolution

The general equation governing a comet's thermal evolution has the form of an advection-diffusion equation with a source (cf. Prialnik, 1992; Prialnik et al., 2004; Huebner et al., 2006):

$$\rho_{\text{bulk}} c \frac{\partial T}{\partial t} - \vec{\nabla} \cdot (\kappa(r) \vec{\nabla} T) + \sum_n c_n \vec{J}_n \cdot \vec{\nabla} T = \mathcal{S} \quad (5.1)$$

where \mathcal{S} is the source term, the index n runs over all gaseous components of the comet, and all other variables as described in Table 5.1. The bulk specific heat and density are described in Section 5.2.2 since they evolve over time as ices evolve.

First, we make the simplification that the comet is spherical and the long-term thermal evolution can be approximated by only solving this equation in one dimension. We also assume that all points on the surface receive equal flux and have the same surface temperature (i.e. the fast-rotator and plane-parallel approximations, cf. Huebner et al., 2006). The justification for these approximations originates from the fact that we are interested in the thermal evolution over 400 Myr. In other words, over the 10⁸ years timescale, the following effects are negligible and can be averaged out: diurnal variations and latitudinal effects. A comet's rotation period is typically on the order of hours to days, thus the differential heating timescale is also on that order, which is much less than the Myr timescale. The latitudinal effects due to the comet's shape can be ignored because the thermal timescale to propagate heat through a spherical comet is comparable to that in a non-spherical comet, when both are compared against the 400 Myr timescale.

Second, we neglect the advection term, as is done in some cometary evolution codes (cf. Huebner et al., 2006). This term describes the heat transport from the movement of gas (\vec{J}_n describes the mass flux of a gaseous species n). This is often neglected in cometary models because the heat capacity of solids is much greater than that of the gaseous phase.

Table 5.1: List of symbols used and their associated SI units in this chapter.

Symbol	Description	Units [SI]
a	Semi-major axis	m
A_j, B_j	Saturated vapour pressure constants	Pa, K
\mathcal{A}	Surface albedo	—
c	Bulk specific heat	J kg ⁻¹ K ⁻¹
c_j	Specific heat of a species j	J kg ⁻¹ K ⁻¹
dt	Simulation timestep	s
d_H	Heliocentric distance of comet	m
e	Eccentricity	—
E_i	Energy from quantity i	J
f_j	Fraction of trapped gas j in amorphous ice	—
G	Surface heat input and output	K s ⁻¹
h	Hertz factor	—
J_j	Gas transport flux for j	kg m ⁻³ s ⁻¹
L_*	Stellar luminosity	J s ⁻¹
M_*	Stellar mass	kg
\mathcal{P}	Saturated vapour pressure	Pa
m_j	Mass of molecule j	kg
q_j	Sublimation rate of gas j	kg m ⁻³ s ⁻¹
r	Radial distance ($r = R$ is surface)	m
Δr	Grid cell size	m
r_p	Average pore radius	m
T	Temperature	K
\mathcal{S}	Other heat sources (radioactivity, etc.)	J kg ⁻¹ m ⁻³
X_j	Mass fraction of j	—
x_j	Volume fraction of j	—
β	Grid steepness	—
ϵ	Emissivity	—
κ	Bulk thermal conductivity	J s ⁻¹ m ⁻¹ K ⁻¹
κ_j	Thermal conductivity of species j	J s ⁻¹ m ⁻¹ K ⁻¹
λ	crystallisation rate	s ⁻¹
ψ	Porosity	—
ϕ	Russell correction factor	—
$\rho_j(r)$	Density of j at a grid point r	kg m ⁻³
$\tilde{\rho}_j$	Specific density of j	kg m ⁻³
ρ_{bulk}	Bulk density of comet	kg m ⁻³
τ_i	Timescale for a process i	s
ξ	Tortuosity	—
k_B	Boltzmann constant	J K ⁻¹
G	Gravitational constant	m ³ kg ⁻¹ s ⁻²
σ	Stefan-Boltzmann constant	J s ⁻¹ m ⁻² K ⁴

Table 5.2: List of constants in our simulation, their values, and the references to publications where these values are used and/or measured. We refer the reader to Table 5.1 for the definitions of these constants. The first half of this table are values inferred from comet properties through modelling. The second half of the table are for laboratory measured values.

References: K75 ([Klinger, 1975](#)), K80 ([Klinger, 1980](#)), K81 ([Klinger, 1981](#)), ES83 ([Ellsworth & Schubert, 1983](#)), H06 ([Huebner et al., 2006](#)), G11 ([Guilbert-Lepoutre et al., 2011](#)), GB12 ([Gundlach & Blum, 2012](#)).

Symbol	Value used in our model [SI]	Reference(s)
r_p	10^{-5} [m]	H06
ψ	0.6	H06
ξ	1	H06
h	10^{-2}	G11, GB12
\mathcal{A}	0.95	H06
ϵ	0.05	H06
$\tilde{\rho}_{\text{H}_2\text{O}}$	$917 \text{ [kg m}^{-3}\text{]}$	H06
$\tilde{\rho}_{\text{dust}}$	$3250 \text{ [kg/m}^3\text{]}$	H06
$c_{\text{H}_2\text{O}}$	$7.49T + 90 \text{ [J kg}^{-1} \text{ K}^{-1}\text{]}$	K81
c_{dust}	$1200 \text{ [J kg}^{-1} \text{ K}^{-1}\text{]}$	ES83
$\kappa_{\text{crystalline}}$	$567/T \text{ [J m}^{-1} \text{ s}^{-1} \text{ K}^{-1}\text{]}$	K75
$\kappa_{\text{amorphous}}$	$2.34 \times 10^{-3}T + 2.8 \times 10^{-2} \text{ [J m}^{-1} \text{ s}^{-1} \text{ K}^{-1}\text{]}$	K80
$\kappa_{\text{dust}} \text{ (Silicate)}$	$10 \text{ [J m}^{-1} \text{ s}^{-1} \text{ K}^{-1}\text{]}$	H06

Table 5.3: Parameters of long-lived radioactive isotopes. This selected list of relevant long-lived isotopes are from [De Sanctis et al. \(2001\)](#) with values from [Carmichael \(1984\)](#).

Isotope	X_{rad}	$\tau_{\text{rad}} [\text{years}]$	$H_{\text{rad}} [\text{J kg}^{-1}]$
^{40}K	1.2×10^{-6}	1.80×10^9	1.66×10^{12}
^{232}Th	6.0×10^{-8}	2.02×10^{10}	1.68×10^{13}
^{235}U	9.0×10^{-9}	1.02×10^9	1.82×10^{13}
^{238}U	2.9×10^{-8}	6.45×10^9	1.92×10^{13}

Third and most importantly, we make the crucial assumption that $\mathcal{S} = 0$, following previous works like [Gkotsinas et al. \(2022, 2024\)](#) where the authors are similarly interested in long-term modelling of comet volatiles. If not neglected, this source term \mathcal{S} includes the heat changes during phase transitions and radioactive heating. Radioactive heating will be discussed in the following subsection. Of these two heat changes, those from phase transitions are the most important and also most difficult to model. This is because crystallisation (exothermic), sublimation (endothermic), and condensation (exothermic) of volatiles can occur rapidly and act as significant sources and sinks of energy. Because we are ignoring these heat changes, our simulation does not accurately describe the thermal evolution when rapid sublimation and recondensation occur. This is an acceptable caveat for our purpose of studying the long-term depletion of volatiles, especially as we are not interested in a particular short cometary outburst, which is when rapid sublimation occurs (or the subsequent recondensation as the temperature decreases when a comet travels away from the star). Crystallisation releases heat, but this process is irreversible and cannot be a constant source of energy for comets.

Radioactivity

We also ignore contributions from radio-nuclides because the major source of radiogenic heating is typically from one isotope, ^{26}Al , which has a decay timescale on the order of $\sim 10^5$ years ([Browne et al., 1986](#)). When compared to the main sequence timescale of even the most massive progenitors of white dwarfs (~ 300 Myr), this source of energy in comets would be depleted long before the post-main sequence stellar evolution stage. Other radioactive species exist in comets and can be long-lived ($\sim \text{Gyr}$) until post-main sequence evolution. However, because their half-life is long, their energy production should be negligible compared to the energy received from the star over the course of one orbit, which is the timescale on which significant temperature changes in our cases.

We now quantify the contribution of radioactive heating to that by stellar flux. The total stellar irradiation energy received over one orbit can be estimated by:

$$E_* = (4\pi R^2)\tau_{\text{period}} \int_0^{2\pi} d\nu \frac{L_*(1-\mathcal{A})}{4\pi d_H^2} \approx \frac{L_*(1-\mathcal{A})(4\pi R)^2}{(GM_*a(1-e^2))^{1/2}} \quad (5.2)$$

where τ_{period} is the orbital period and ν is the orbital true anomaly. The approximation assumes no perturbations to the stellar luminosity and the Keplerian orbit over one orbit. Then the energy contribution from radioactivity compared to the stellar flux is:

$$\frac{E_{\text{radio}}}{E_*} = \frac{R}{6} \rho_{\text{dust}} H_{\text{rad}} X_{\text{rad}} \frac{a^2(1-e^2)^{1/2}}{L_*(1-\mathcal{A})} \left(\exp\left(\frac{-\tau_{\text{period}}}{\tau_{\text{rad}}}\right) \middle/ \tau_{\text{rad}} \right) \quad (5.3)$$

$$\approx 10^{-2} \times (1-e^2)^{1/2} \left(\frac{a}{10^3 \text{ AU}} \right)^2 \left(\frac{R}{50 \text{ km}} \right) \times \\ \left(\frac{L_*}{10L_\odot} \right)^{-1} \left(\frac{\tau_{\text{rad}}}{1.8 \times 10^9 \text{ yr}} \right)^{-1} \left(\frac{X_{\text{rad}}}{10^{-6}} \right) \left(\frac{H_{\text{rad}}}{1.66 \times 10^{12} \text{ J kg}^{-1}} \right) \quad (5.4)$$

where H_{rad} is the energy released per unit mass. In the approximation, we assumed typical values for ${}^{40}\text{K}$, which is the most abundant long-lived isotope. We also used the typical amount of dust in a comet ($\sim 250 \text{ kg m}^{-3}$). The exponential term is of order unity, which is true for long-lived isotopes of comets on distant orbits as far as 10^5 AU . In Table 5.3, we show values of other long-lived isotopes (values from Carmichael, 1984). The selected list of relevant long-lived isotopes in comets are from De Sanctis et al. (2001).

As seen from Equation 5.3, around a $10L_\odot$ star, comets on circular orbits with $a < 1000 \text{ AU}$ have $E_{\text{radio}}/E_* \ll 1$ and radioactive isotopes can be ignored. However, comets on circular orbits at greater distances should include radioactivity in the heat equation source term. Finally, our estimate of E_{radio}/E_* is only valid when $\tau_{\text{period}} \ll \tau_{\text{rad}}$. This condition is true for all Solar system comets when compared with long-lived isotopes decay time. However, when this condition is not satisfied (i.e. with short-lived isotopes), a long-period comet can have radioactive heating be dominant during its apocentre and then have solar flux heating be dominant during the pericentre passage.

Heat Equation and Boundary Conditions

With these simplifications, the heat equation simplifies to a diffusion equation, as typically solved by previous works on long-term comet evolution (e.g., Jura & Xu, 2012; Gkotsinas et al., 2022; Levine et al., 2023; Gkotsinas et al., 2024; Li et al., 2024):

$$\rho_{\text{bulk}} c \frac{\partial T}{\partial t} - \frac{1}{r^2} \frac{\partial}{\partial r} \left(\kappa(r) r^2 \frac{\partial T}{\partial r} \right) = 0 \quad (5.5)$$

where the radial coordinate r is set up such that $r = 0$ is at the centre and $r = R$ is the surface of the comet. In this equation, bulk density is ρ_{bulk} , heat capacity is c , and thermal conductivity is κ , which controls how effectively heat can be transported via conduction.

This partial differential equation is subjected to the Neumann boundary condition at the centre:

$$\frac{\partial T}{\partial t} \Big|_{r=0} = 0 \quad (5.6)$$

and at the surface:

$$\frac{\partial T}{\partial t} \Big|_{r=R} = \left((1 - \mathcal{A}) \frac{L}{4\pi d_H^2} - \epsilon \sigma T(r=R)^4 \right) / (\kappa|_{r=R}) \equiv G(t). \quad (5.7)$$

This boundary condition assumes the “fast-rotator” and plane-parallel approximations, such that all points on the comet’s surface receive equal flux. The star’s luminosity L_* and the comet’s heliocentric distance d_H are both functions of time resulting in a time-varying boundary condition for our heat equation.

Thermal Conductivity

The remaining variables needed to solve the heat equation are: ρ_{bulk} , c , and κ . For these variables, we only consider the contribution from water and dust, since they are the most abundant components by one order of magnitude in comets. In addition, they evolve over time as amorphous and crystalline water ice changes over time, which will be discussed in the next section.

First, since the comet is a porous body made up of mostly dust and water, the bulk density at a grid point r is:

$$\rho_{\text{bulk}}(r) = (1 - \psi) \left(\frac{X_{\text{H}_2\text{O}}(r)}{\tilde{\rho}_{\text{H}_2\text{O}}} + \frac{X_{\text{dust}}(r)}{\tilde{\rho}_{\text{dust}}} \right)^{-1} \quad (5.8)$$

where X_i is the mass fraction of the component i . For H_2O , we sum the contribution from amorphous and crystalline ice since they have the same density. $\tilde{\rho}$ is the specific density, with values for water and dust shown in Table 5.2.

Next, the bulk heat capacity at a specific grid point r is weighted by the mass fraction of each individual component’s heat capacity (Guilbert-Lepoutre et al., 2011):

$$c(r) = X_{\text{H}_2\text{O}}(r)c_{\text{H}_2\text{O}} + X_{\text{dust}}(r)c_{\text{dust}} \quad (5.9)$$

where the values for the heat capacities $c_{\text{H}_2\text{O}}$ and c_{dust} are given in Table 5.2.

A porous medium can be modelled as a material with two phases with two conductivities:

$$\kappa(r) = \kappa_{\text{pores}}(r) + \phi h \kappa_{\text{solid}}(r). \quad (5.10)$$

The first term describes heat transfer from the empty pores through thermal radiation:

$$\kappa_{\text{pores}}(r) = 4r_p \epsilon \sigma T(r)^3. \quad (5.11)$$

The second term describes heat conduction through the solid mixture of dust and water ice. The heat conductivities of solid materials are averaged over the occupying volume of

each component (Guilbert-Lepoutre et al., 2011):

$$\kappa_{\text{solid}}(r) = x_{\text{H}_2\text{O}} ((1 - X_{\text{crystalline}})\kappa_{\text{amorphous}} + X_{\text{crystalline}}\kappa_{\text{crystalline}}) + x_{\text{dust}}\kappa_{\text{dust}} \quad (5.12)$$

where x_i is the volume fraction of a component i . Note that the thermal conductivities $\kappa_{\text{amorphous}}$ and $\kappa_{\text{crystallisation}}$ can have very different values (cf. Table 5.2). There are two correction factors for κ_{solid} , h and ϕ . ϕ is the Russell correction factor (Russell, 1935) to account for the fact that the medium is porous:

$$\phi = \frac{\psi^{2/3}k + (1 - \psi^{2/3})}{\psi - \psi^{2/3} + 1 - \psi^{2/3}(\psi^{1/3} - 1)k} \quad (5.13)$$

where ψ is the porosity and $k = \kappa_{\text{pores}}/\kappa_{\text{solid}}$. h is the Hertz factor, additionally accounting for the reduction of the solid grain cross-section in a porous medium. This value can range from 10^{-4} to 10^{-1} ; we choose $h = 10^{-2}$, consistent with Guilbert-Lepoutre et al. (2011); Gundlach & Blum (2012); Davidsson (2021); Gkotsinas et al. (2022). We refer the reader to Shoshany et al. (2002); Prialnik et al. (2004); Huebner et al. (2006); Davidsson (2021) for more on Hertz factor and conductivity modelling.

5.2.2 Ice Evolution

In our model, dust and water are the two main components and their evolution directly affects the thermal conductivity κ . Like most previous works (e.g., Choi et al., 2002; Prialnik & Merk, 2008; Guilbert-Lepoutre et al., 2011; Malamud & Perets, 2017a; Gkotsinas et al., 2024), we assume that the dust content stays constant (i.e., no dust outflow in our model):

$$\frac{\partial \rho_{\text{dust}}}{\partial t} = 0. \quad (5.14)$$

We model water in a comet in three phases: amorphous ice, crystalline ice, and water vapour. As the comet heats up, amorphous ice transitions into crystalline ice in an exothermic process called crystallisation. However, this phase change is irreversible, and thus only occurs once and cannot supply a long-term source of energy for a comet. That being said, it is still important to model this process because the thermal conductivity of amorphous and crystalline ice can be very different, cf. Table 5.2. As temperature increases, eventually crystalline ice sublimates into water vapour, at which point the gas can be transported through the pores and can escape the comet. Technically, amorphous ice can also spontaneously sublime into vapour, but this occurs at a negligible rate since amorphous ice can only exist at low temperatures. The transitions between amorphous-crystalline-vapour are

modelled through the following equations:

$$\frac{\partial \rho_{\text{amorphous}}}{\partial t} = -\lambda(T)\rho_{\text{amorphous}} \quad (5.15)$$

$$\frac{\partial \rho_{\text{crystalline}}}{\partial t} = (1-f)\lambda(T)\rho_{\text{amorphous}} - q_{\text{H}_2\text{O}} \quad (5.16)$$

$$\frac{\partial \rho_{\text{vapour}}}{\partial t} + \vec{\nabla} \cdot \vec{J}_{\text{H}_2\text{O}} = q_{\text{H}_2\text{O}} \quad (5.17)$$

where $f = \sum_i f_i$ is the sum of all trapped volatile i in amorphous ice. These gases are released when water ice is crystallised. The rate at which amorphous ice spontaneously transitions into crystalline ice is measured by [Schmitt et al. \(1989\)](#):

$$\lambda(T) = 1.05 \times 10^{13} \exp\left(\frac{-5370 \text{ K}}{T}\right) \text{ s}^{-1}. \quad (5.18)$$

$q_{\text{H}_2\text{O}}$ describes the sublimation rate of crystalline ice into water vapour. $\vec{J}_{\text{H}_2\text{O}}$ is the flow of water vapour through the pores.

The sublimation rate q_i of a species i is ([Mekler et al., 1990](#); [Tancredi et al., 1994](#); [Davidsson, 2021](#)):

$$q_i = \frac{3(1-\psi)}{r_p} \sqrt{\frac{m_i}{2\pi k_B T}} (\mathcal{P}_i - P_i) \quad (5.19)$$

where \mathcal{P}_i is the saturated vapour pressure and is found via the Clausius-Clapeyron equation:

$$\mathcal{P}_i = A_i \exp(-B_i/T) \quad (5.20)$$

Measured values of A_i and B_i for relevant volatiles are shown in Table 5.4 (values from Table 4 in [Prialnik et al., 2004](#)). P_i is the partial vapour pressure which can be found through the ideal gas law. When the $P_i < \mathcal{P}_i$ then net sublimation occurs. Otherwise, the term becomes negative and the gas recondenses.

The mass flux \vec{J} can be modelled as Knudsen (molecular) flow or as Poiseuille (continuous) flow. In Knudsen flow, the collisions between particles and the pore walls are more frequent than collisions between particles. [Prialnik et al. \(2004\)](#) showed that when the average pore size is less than 1 mm, which is our regime with $r_p = 10^{-5} \text{ m}$, the gas flow is dominantly Knudsen flow and \vec{J} has the form ([Mekler et al., 1990](#); [Huebner et al., 2006](#)):

$$\vec{J} = \vec{J}_{\text{Knudsen}} = -\frac{8\psi r_p^3}{3\xi^2} \left(\frac{m}{2\pi k_B T}\right)^{1/2} \vec{\nabla} \left(\frac{P}{\sqrt{T}}\right) \quad (5.21)$$

where m is the mass of the gas molecule, and P is the local gas pressure at r found through the ideal gas law. Finally, when multiple gases are transported, they are treated independently of each other. This is strictly valid in Knudsen flow.

The evolution of other volatiles is treated similarly, except that they are presumed to

only exist in solid and gaseous forms. The evolution of a volatile i is described by:

$$\frac{\partial \rho_{i,\text{solid}}}{\partial t} = -q_i \quad (5.22)$$

$$\frac{\partial \rho_{i,\text{gas}}}{\partial t} + \vec{\nabla} \cdot \vec{J}_i = q_i + f_i \lambda(T) \rho_{\text{amorphous}}. \quad (5.23)$$

In the second expression, a volatile gas can be produced via the sublimation of the solid form or upon crystallisation of water ice where a fraction of the trapped gas is released.

5.3 Timescales

We now discuss the timescales for the physical processes considered in this chapter. The timescales discussed here can be summarised in three categories:

1. Cometary: thermal, crystallisation, sublimation, gas transport, surface flux.
2. Orbital: orbital period, pericentre timescale.
3. Stellar: mass loss timescale, luminosity change timescale

This discussion will support the following section on numerical methods, as it affects the timestep choices in our simulation.

5.3.1 Cometary Timescales

The timescales for heat production and absorption processes (crystallisation, sublimation and condensation) are strongly dependent on temperature. The crystallisation timescale for water amorphous ice to transition into crystalline ice is:

$$\tau_{\text{crystallisation}} = \frac{1}{\lambda(T)} \approx 9.54 \times 10^{-14} \exp\left(\frac{5370 \text{ K}}{T}\right) [\text{s}]. \quad (5.24)$$

Likewise, the timescale for sublimation (or condensation) of a species i is (Prialnik et al., 2004):

$$\tau_{\text{subl},i} = \frac{\rho_i r_p}{3(1-\psi)A_i} \exp\left(\frac{B_i}{T}\right) \left(\frac{m_i}{2\pi k_B T}\right)^{-1/2} \quad (5.25)$$

where m_i is the mass of a species i (see Table 5.4 for values). Here, ρ_i can be ignored for order of magnitude purposes, since typical volatile densities in comets are negligible when compared to other terms for typical temperatures and porous structure constants ($\psi = 0.6$, $r_p = 10^{-5}$ m).

The timescale to transport a parcel of gaseous species i over a distance Δr is

$$\tau_{\text{gas},i} = \frac{J_i}{dJ_i/dt} \sim \frac{\Delta r^2}{\psi r_p} \left(\frac{2\pi m_i}{k_B T}\right)^{1/2} \quad (5.26)$$

Table 5.4: Constants A, B for the saturated vapour pressure (Equation 5.20) and molecule masses for H₂O, CO, and CO₂. Values of A, B are from Table 4 in Prialnik et al. (2004).

Molecule	Mass [kg]	A [Pa]	B [K]
H ₂ O	2.991×10^{-26}	3.56×10^{12}	6141.667
CO ₂	7.309×10^{-26}	1.079×10^{12}	3148
CO	4.651×10^{-26}	1.12×10^9	764.16

where Knudsen flow is used, as mentioned earlier. Unlike the previous two timescales, $\tau_{\text{gas},i}$ does not vary exponentially with temperature and is more dependent on the distance over which the gas needs to be transported.

Next, we find the timescale for heat to diffuse through the comet and also the timescale for heat to diffuse through the smallest cell in the comet. These two timescales set the upper and lower bounds of the thermal diffusion process. Note that unlike the other timescales so far, the thermal timescales are independent of temperature.

It can be shown that for a constant value of $\kappa/c\rho_{\text{bulk}}$, the diffusion equation (Equation 5.5) admits a solution of the form:

$$T(r, t) \propto \exp\left(-t \cdot \frac{\pi^2 \kappa}{R^2 c \rho_{\text{bulk}}}\right) j_0\left(\pi \cdot \frac{r}{R}\right) \quad (5.27)$$

where j_0 is the zeroth-order spherical Bessel function of the first kind. From this, we identify the characteristic timescale for heat to be transported over a comet with size R as:

$$\tau_{\text{thermal,bulk}} = \frac{R^2 c \rho_{\text{bulk}}}{\pi^2 \kappa} \approx 3 \times 10^5 \text{ yr} \left(\frac{R}{1 \text{ km}}\right)^2 \left(\frac{\kappa/c\rho_{\text{bulk}}}{10^{-8} \text{ m}^2 \text{ s}^{-1}}\right)^{-1} \quad (5.28)$$

where in the last equality, we use typical values for the bulk properties of comets: $\rho = 500 \text{ kg/m}^3$, $c = 2000 \text{ J kg}^{-1} \text{ K}^{-1}$, $\kappa = 10^{-2} \text{ W K}^{-1} \text{ m}^{-1}$ (Huebner et al., 2006; Gundlach & Blum, 2012; Steckloff et al., 2021; Levine et al., 2023). We note that the assumption that $\kappa/c\rho_{\text{bulk}} = \text{constant}$ is not valid in our simulation because κ , c , and ρ_{bulk} all change as water ice crystallises, sublimates, and are lost. That being said, the values of $\kappa/c\rho_{\text{bulk}}$ over the whole comet do not vary significantly more than one order of magnitude in our simulations. Thus, we find that this simple estimate gives the correct order of magnitude for the heat transfer timescale throughout the comet.

Related to the thermal timescale, but instead of heat transfer through the comet, is one where the heat transfer is between the grid cells in the simulation. This is described by the Courant-Friedrichs-Lowy timescale:

$$\tau_{\text{CFL}} = \frac{\Delta r^2 c(r) \rho(r)}{2\kappa(r)} \sim 1 \text{ yr} \left(\frac{\Delta r}{1 \text{ m}}\right)^2 \left(\frac{\kappa/c\rho_{\text{bulk}}}{10^{-8} \text{ m}^2 \text{ s}^{-1}}\right)^{-1}. \quad (5.29)$$

This timescale must always be resolved to accurately and stably resolve the heat transfer through the smallest grid cell Δr . The determination of the smallest grid size Δr will be discussed later, but they typically range from ~ 1 m up to ~ 300 m, depending on the comet size and orbit. Again, we use the bulk density, heat capacity and thermal conductivity over the whole comet to illustrate the order of magnitude values of this timescale here. In the simulation, we ensure that those quantities are measured at that cell and not over the whole comet.

The timescales mentioned so far in this section which govern the thermal and mass evolution of the comet are shown in Figure 5.1. As seen here, the sublimation and crystallisation timescales can change very quickly over many orders of magnitude as a comet changes its temperature. Furthermore, we note that all of these timescales cover a large range of at least 4-5 orders of magnitude.

Finally, there is also the timescale on which the surface layer changes over the course of an orbit and as the star's luminosity. To first order, the quickly changing component of Equation 5.7 is

$$\left. \frac{\partial T}{\partial t} \right|_{r=R} = G(t) \sim \mathcal{O}(L_*/d_H^2) \quad (5.30)$$

and thus, the boundary condition timescale can be estimated as

$$\tau_G(t) = \min \{ \tau_L(t), \tau_{\text{distance}^{-2}}(t) \} \quad (5.31)$$

where τ_L is the timescale on which the star's luminosity changes and $\tau_{\text{distance}^{-2}}$ is the timescale to resolve the $1/\text{distance}^2$ relationship for the flux. The values for τ_L will be discussed in Section 5.3.3. How to choose the value for $\tau_{\text{distance}^{-2}}$ will be discussed in Section 5.4.1. At this point, we note that G also contains a dependency on the surface temperature ($\propto T^4$). There are two cases for changing T at the surface: as a response to changing surface flux or through heat transfer from the core outward. In the first case, if we resolve τ_L and $\tau_{\text{distance}^{-2}}$, then we also resolve the changing temperature timescale. In the second case, the heat transfer timescale outward for the surface grid cell is already considered with τ_{CFL} (Equation 5.29).

5.3.2 Orbital Timescales

Consider a gravitational simulation of an eccentric comet: at large distances, the simulation must resolve timesteps which are a fraction of an orbital period, but when the comet comes close to the central star the timesteps should be much smaller to resolve the much smaller length scale involved. Because we couple our thermal evolution with N-body gravitational simulation with adaptive timesteps, these wide-ranging timesteps are all relevant to our simulation¹.

¹In this work, we do not consider the effects of planets on the orbital evolution of post-main sequence comets. For completeness, however, we note that there are other timescales that may be important when

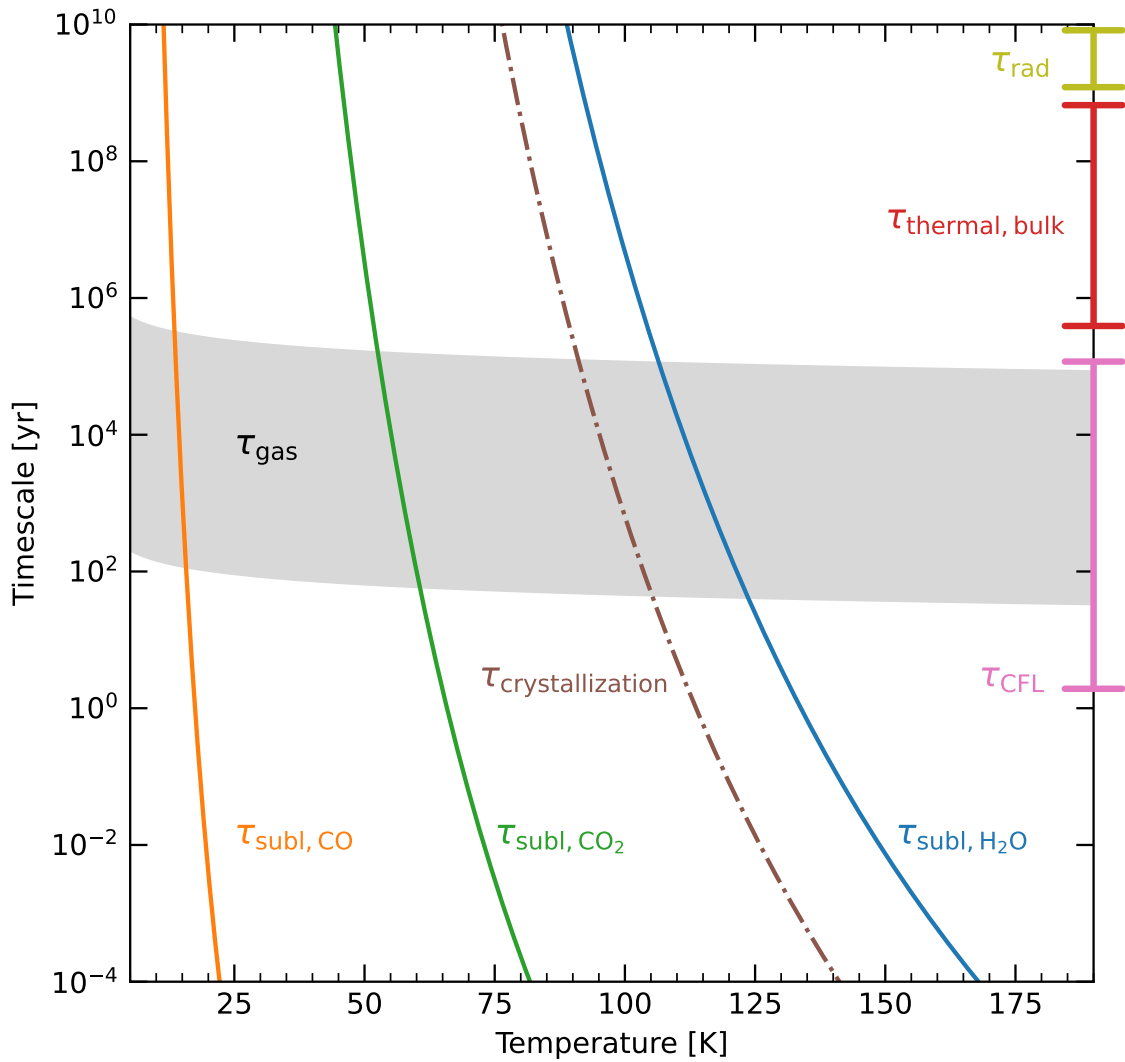


Figure 5.1: The relevant timescales for the internal evolution of comets in our simulation: sublimation for CO, CO₂, H₂O crystalline ice (solid curves, τ_{subl}), gas transport to surface timescale (shaded area, τ_{gas}), crystallisation timescale (dashed dot curve, $\tau_{\text{crystallisation}}$), the bulk thermal timescale to transfer heat from the surface to a comet's centre ($\tau_{\text{thermal,bulk}}$), and the Courant-Friedrichs-Lowy timescale (τ_{CFL}). τ_{gas} strongly depends on the distance to transport and the temperature of the gas, resulting in the spread shown here. $\tau_{\text{thermal,bulk}}$ and τ_{CFL} are only shown as bars indicating their potential timescales because they are independent of temperature (they are dependent on either the size of the comet or the minimum grid cell size). For completeness, we also show the timescales of long-lived radioactive nuclides (τ_{rad} , cf. Table 5.3). This figure closely follows Figure 5.3 in Huebner et al. (2006).

The pericentre timescale of a comet can be defined as (Rein & Tamayo, 2015):

$$\tau_{\text{peri}} = 2\pi \sqrt{\frac{a^3}{GM_*} \frac{(1-e)^2}{1-e^2}} \quad (5.32)$$

where a is the orbital semi-major axis, and e is the orbital eccentricity. In an eccentric orbit, τ_{peri} can be many orders of magnitude less than the orbital period. When $e = 0$, this timescale recovers the orbital period.

In Figure 5.2, we show the pericentre timescale as a function of pericentre distance and semi-major axis. Here, we find that the pericentre timescale spans six orders of magnitude, depending on the pericentre distance and semi-major axis. The most eccentric Oort cloud comets will experience vastly orbital timescales as they travel between pericentre and apocentre.

5.3.3 Stellar Timescales

The progenitors of white dwarfs have main sequence lifetimes as low as 300 Myr for massive stars, 10 Gyr for Sun-like stars, and even longer for less massive stars. We focus on the last 400 Myr evolution of Sun-like stars in this chapter, but the numerical methods developed here can be applied for any stellar evolution.

At the beginning of the 400 Myr time period we are focusing on, a Sun-like star has already left the main sequence and has a luminosity on the order of $10L_\odot$. For the next 400 Myr, they continue to evolve and increase in luminosity. During this process, their luminosity can increase up to $\sim 5 \times 10^4 L_\odot$ during the Helium flash (at around the 250 Myr mark in our simulation) and asymptotic giant branch (AGB, at around the 360-390 Myr point). During these events, the star also rapidly loses its mass, where at the end of the AGB stage the star would rapidly lose $\sim 30\%$ its mass.

In this chapter, we use the evolutionary track for the $1M_\odot$ model star from pre-computed MESA Isochrones & Stellar Tracks (MIST, Dotter, 2016; Choi et al., 2016)². In Figure 5.3, we plot the stellar luminosity change timescale, τ_L :

$$\tau_L = \frac{L_*}{dL_*/dt} \quad (5.33)$$

there is a planet (or more). The existence of a planet would require an integrator to consider the orbital period of this planet to properly resolve any potential close encounters. In multi-planet systems, such as the Solar system, the secular timescale is the long timescale on which planets affect each other's orbits. Lastly, the much longer timescale is the onset of chaos. At and beyond this last timescale, simulations for multi-planetary systems will need to be done statistically (multiple realisations) due to their sensitivity to initial condition.

²Stellar mass loss from our MESA model is isotropic. Currently, literature find observational indications that the mass loss is anisotropic (e.g. El-Badry & Rix, 2018). The main problem with not modeling anisotropic mass loss is that this process can induce an anisotropic kick to the star, which would affect the orbits of comets. This effect is particularly important for the dynamics of Oort cloud comets (O'Connor et al., 2023). This is because comets at distances > 1000 AU have orbital speed comparable to the stellar kick ($v_{\text{kick}} \sim 0.75 \text{ km s}^{-1}$).

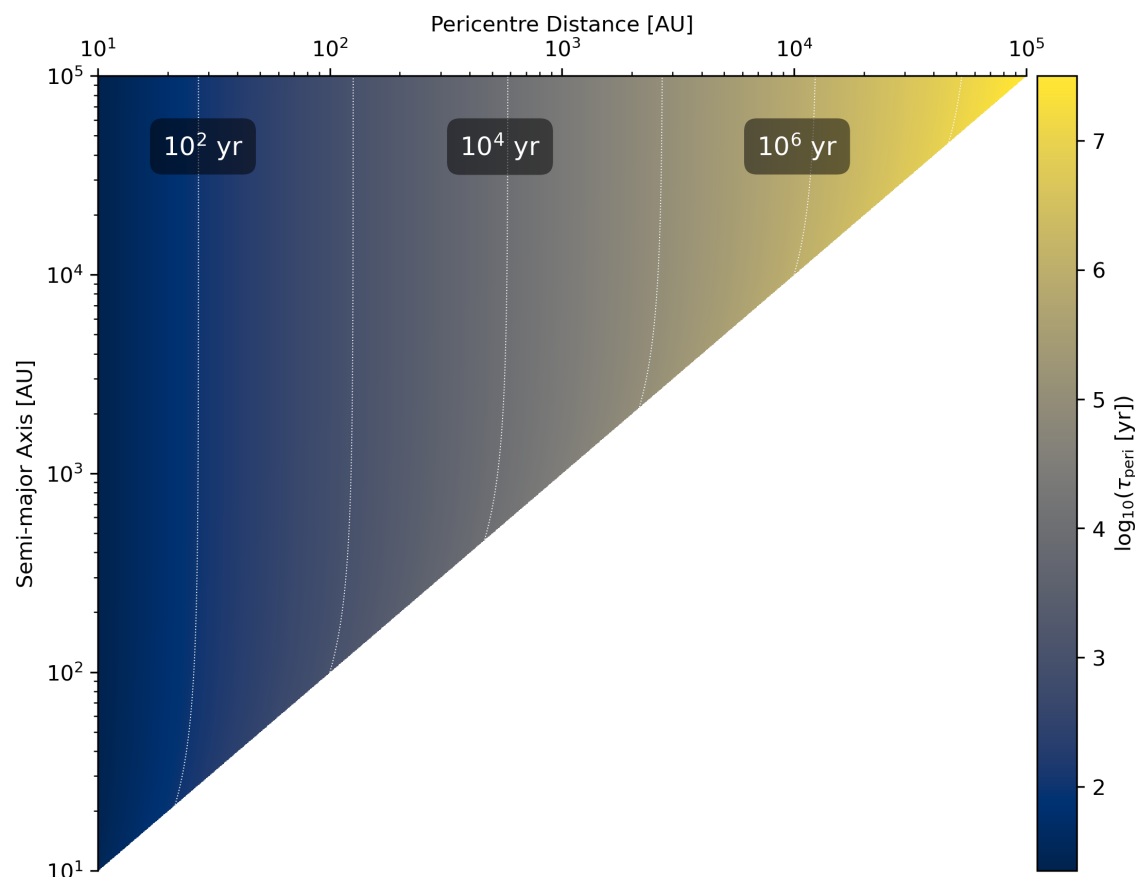


Figure 5.2: The pericentre timescale (τ_{peri}) as a function of pericentre distance and semi-major axis. The contours outline the timescale order of magnitude value. As seen, τ_{peri} can be many orders less than the orbital period, especially for a very eccentric orbit like those from the Oort cloud (with semi-major axes between $3000 - 10^5$ AU).

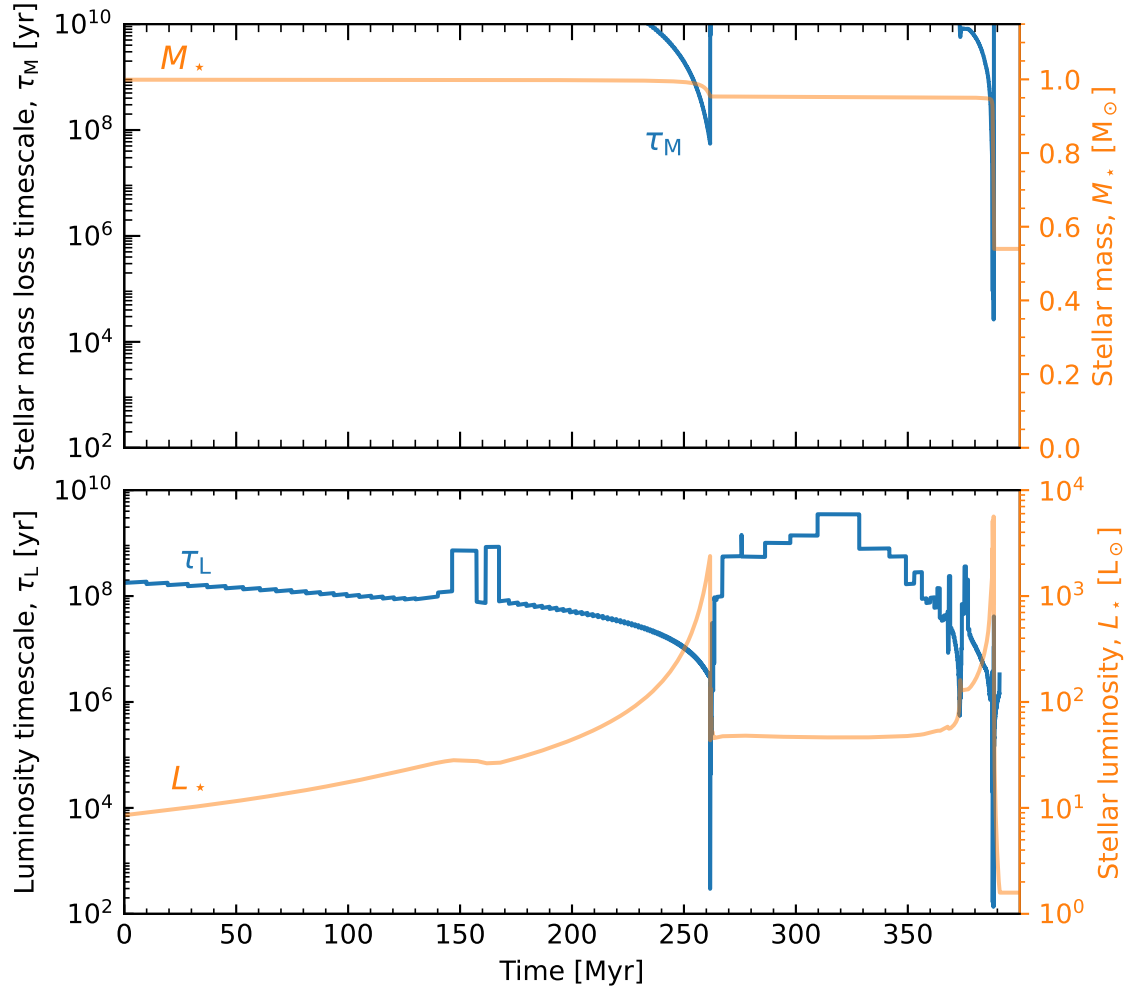


Figure 5.3: The stellar mass loss timescale, τ_M , (top) and luminosity change timescale, τ_L , (bottom) for the last 400 Myr evolution of a $1M_\odot$ star before it becomes a white dwarf. The luminosity and mass of the star (orange curves with values corresponding to the right y-axis) are taken from the MESA Isochrones & Stellar Tracks (MIST, Dotter, 2016; Choi et al., 2016).

and the mass loss timescale, τ_M :

$$\tau_M = \frac{M_*}{dM_*/dt}. \quad (5.34)$$

In the same plot, stellar luminosity (L_*) and mass (M_*) are shown to demonstrate how much and how fast these values can change. As seen, these quantities can evolve significantly over a short amount of time: as low as 10^2 years for L_* and as low as 10^5 years for M_* .

5.4 Simulation Methods

5.4.1 N-body coupling and Inverse-square Law Timescale

We couple our thermal-mass evolution code with `REBOUND` (Rein & Liu, 2012), a numerical N-body simulation code. The first advantage of this coupling is that it allows our code to be able to be used in many circumstances where a comet's orbit changes over time, e.g., the formation and volatile content of Kuiper Belt objects as they interact with migrating planets³. In addition, `REBOUND` can include other effects (beyond those from planets) that affect a planet's orbit, such as Galactic tide, general relativity, and disc migration with the package `REBOUNDx` (Tamayo et al., 2020).

The main advantage of coupling is that N-body codes are often capable of adaptive timestepping, allowing them to calculate the changing gravitational timescale over the course of an eccentric orbit. Specifically, the goal of an adaptive timestep method is to have a large timestep when an object is distant from massive objects while reducing the integration timestep significantly to resolve any close encounters with massive bodies. This behaviour is fortunate for us as both gravity and flux scale $\propto 1/\text{distance}^2$. Hence, over one orbit with constant luminosity, gravity and flux vary with the same timescale. Therefore, if we can solve the gravitational timescale at each point in the orbit, we also automatically have the $\tau_{\text{distance}-2}$ timescale for the flux. This completes Equation 5.31, allowing us to resolve how fast the comet's surface boundary condition changes over time. If this fast-changing flux is not resolved over one orbit, the heat equation behaviour becomes very stiff and gives unstable results.

In this work, to resolve gravity (and $\propto \text{distance}^{-2}$ laws) we will use the IAS15 integrator (Rein & Spiegel, 2015) with the timestep scheme described in Pham et al. (2024b). Briefly, the scheme adaptively increases and decreases the timestep used in N-body gravitational simulation, such that pericentre passage and close encounters are resolved properly with low timesteps, while objects at large distances enjoy greater timesteps. In the context of flux, during the pericentre passage, the timestep decreases matching how an incoming comet would rapidly receive increasing flux. Vice versa, when a comet approaches the apocentre, the timescale increases matching the lowered flux.

³The radioactive heating term in \mathcal{S} (Equation 5.5) should be included for any models involving the formation of these objects, since ^{26}Al can be a significant source of energy for the first 10^5 years.

Another advantage of coupling with a time-adaptive integrator is that this makes our simulation time-adaptive, greatly improving simulation speed. Finally, we remark that any time-adaptive scheme that properly resolves the $1/\text{distance}^2$ relationship should also work for this purpose (e.g., Aarseth, 1985). We use the criterion in Pham & Rein (2024) because it uses the lowest order derivatives possible and consequently, is shown to be least susceptible to floating point precision error. To this end, we refer the reader to Pham & Rein (2024) for further discussions on the mechanisms of this adaptive timestepping routine, how it resolves the pericentre and apocentre, and floating point precision error.

5.4.2 Simulation Grid

To properly resolve the rapidly increasing flux during pericentre passages, we need a grid with a cell size less than or equal to the thermal depth that can be reached over the pericentre passage timescale. We can define the thermal depth length as

$$\Delta r_{\text{thermal}} = \pi \left(\tau_{\text{peri}} \frac{\kappa(R)}{c(R)\rho(R)} \right)^{1/2} \sim 20 \text{ m} \left(\frac{\tau_{\text{peri}}}{10^2 \text{ yr}} \right)^{1/2} \left(\frac{\kappa/c\rho_{\text{bulk}}}{10^{-8} \text{ m}^2 \text{ s}^{-1}} \right)^{1/2} \quad (5.35)$$

where κ , c , and ρ are values calculated at the surface in the simulation. The values shown in the above equation are from using the bulk comet properties to estimate the order of magnitude value for illustrative purposes. τ_{peri} is from Equation 5.32 with values shown in Figure 5.2.

As seen, the thermal resolution needed to be resolved can be quite small, compared to comet sizes ($R \sim 1 - 50$ km). Setting up a grid with uniform-sized cells could lead to a big grid, potentially causing prohibitively long runtime due to the number of equations being solved. Let N_v be the number of volatile species excluding water, then at each cell, we are solving $1 + 3 + 2N_v$ equations — one for the heat equation, three for the H₂O mass-continuity equations, and 2 mass-continuity equations for each volatile species. Now, denote the number of grid cells as N_r , then we are potentially solving up to $(4 + 2N_v) \cdot N_r$ coupled equations simultaneously. Thus, a large N_r from a fine grid will significantly increase computational cost.

To resolve this, we use a non-uniform, hyperbolic tangent grid (for other applications and properties of this grid choice, we refer the reader to Thompson et al., 1999). Here, each grid point r is generated by:

$$r(\zeta; \beta) = R \cdot \left(1 - \frac{\tanh(\beta(1 - \zeta))}{\tanh \beta} \right) \quad (5.36)$$

where $\zeta \in [0, 1]$ is a uniform grid with N_r points, while the resulting grid is $r \in [0, R]$ with the same number of grid points. The parameter β describes how “stretchy” (or “steep”) the grid will be. The simulation code automatically chooses β , such that the grid is “locally

uniform” ($\Delta r_+ \simeq \Delta r_-$); specifically, we enforce the condition:

$$\frac{\Delta r_+}{\Delta r_-} \geq 0.9 \quad (5.37)$$

where $\Delta r_+ = r_{i+1} - r_i$ and $\Delta r_- = r_i - r_{i-1}$. This condition is highly desirable for the non-uniform finite difference error term, which is second-order in error.

The number of grid points, N_r , is automatically determined together with β to enforce the condition that the smallest grid cell size is always strictly less than the pericentre thermal depth ($\Delta r_{\text{thermal}}$). Often, our simulation’s smallest grid size is smaller than $\Delta r_{\text{thermal}}$ by a factor of a few to guarantee that heat transfer during pericentre is properly resolved.

In Figure 5.4, we show an example of the thermal evolution and the grid used for a simulation for a 5 km Oort cloud comet on a highly eccentric orbit (semi-major axis 20 000 AU, pericentre distance 3 AU) around a highly luminous star ($L_* = 10^3 L_\odot$, $M = 1M_\odot$) over 20 Myr. As seen, the heat transport from the surface reaches the centre of the comet as expected from the analytic value of $\tau_{\text{thermal,bulk}}$. The grid has varying cell sizes, with gradually smaller cells as we approach the surface, ensuring that the surface layers with the fastest temperature changes are most finely resolved. There are many grid cells at the surface, each of which has a smaller grid size than the pericentre thermal depth, allowing proper heat transport over one pericentre passage. We can clearly observe the rapidly changing surface temperature after each pericentre passage. These temperature changes can be very fast, especially for cases like this where the orbit is highly eccentric and the star is highly luminous.

5.4.3 Finite Difference

Given a function $\mathcal{F}(r, t)$, we discretise the spatial component such that $\mathcal{F}(r, t) \approx \mathcal{F}(r_i, t) \equiv \mathcal{F}_i$ over a non-uniform grid with grid points r_i , $i = 0, 1, 2, \dots, N_r - 1$. The finite differences with respect to r are:

$$\frac{\partial \mathcal{F}}{\partial r} = \frac{\mathcal{F}_{i+1} - \mathcal{F}_{i-1}}{\Delta r_+ + \Delta r_-} \quad (5.38)$$

$$\frac{\partial^2 \mathcal{F}}{\partial r^2} = \frac{4(\mathcal{F}_{i+1}\Delta r_- + \mathcal{F}_{i-1}\Delta r_+ - f_i \cdot (\Delta r_+ + \Delta r_-))}{(\Delta r_+ + \Delta r_-)(\Delta r_+^2 + \Delta r_-^2)} \quad (5.39)$$

and both of these finite differences have the error scaling as:

$$\text{error} \propto \begin{cases} \mathcal{O}(\max\{\Delta r_+, \Delta r_-\}^2), & \Delta r_+ \simeq \Delta r_- \\ \mathcal{O}(\max\{\Delta r_+, \Delta r_-\}), & \text{otherwise} \end{cases}. \quad (5.40)$$

We emphasise that this discretisation has a strong dependency on grid spacing and that the grid should be “locally uniform” ($\Delta r_+ \simeq \Delta r_-$) to ensure quadratic error scaling instead of linear. Applying this spatial discretisation scheme to the heat equation turns it into an

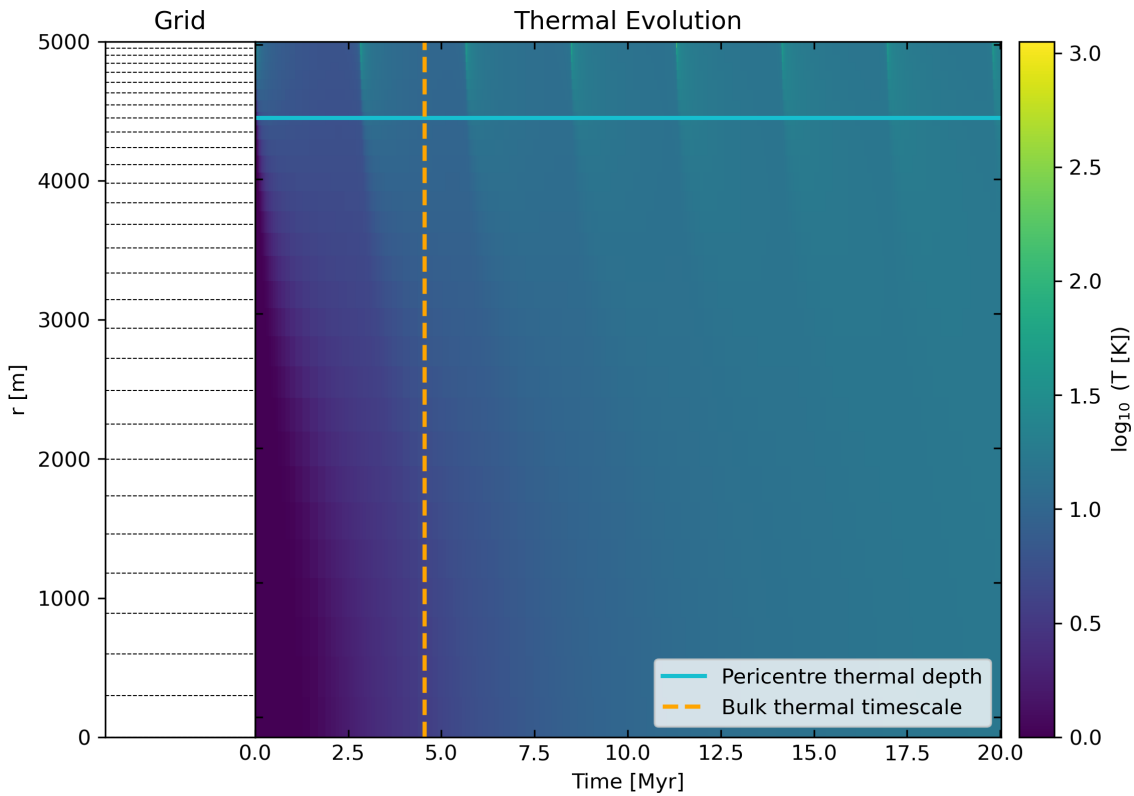


Figure 5.4: An example simulation of a 5 km Oort cloud comet with semi-major axis 20 000 AU and pericentre 3 AU. The central star is $1M_\odot$ and has a luminosity of $10^3 L_\odot$. On the left is the non-uniform, hyperbolic tangent grid used in this simulation. On the right is the temperature evolution in $\log_{10} T [\text{K}]$. The solid horizontal line shows the pericentre thermal depth ($\Delta r_{\text{thermal}}$), which is the length that heat is transported from the surface over one pericentre passage. The dashed vertical line shows the bulk thermal timescale ($\tau_{\text{thermal,bulk}}$), which is the timescale to transport heat from the surface to the centre. The streaks at the top show the increase heat from the surface from increasing stellar irradiation every time the comet approaches pericentre. As seen, the simulation is capable of properly resolving the rapidly changing surface boundary condition when this happens. After the pericentre, we can see that the heat is propagated inward.

ordinary differential equation. We are left with solving the set of equations at each grid point r_i :

$$\frac{\partial T_i}{\partial t} = \mathcal{F}_{i,T}(t; r_{i+1}, r_i, r_{i-1}; T_{i+1}, T_i, T_{i-1}; \rho_{\text{dust}}, \rho_{\text{amorphous}}, \rho_{\text{crystalline}}, \dots) \quad (5.41)$$

$$\frac{\partial \rho_{i,\text{amorphous}}}{\partial t} = \mathcal{F}_{i,\text{amorphous}}(T_i, \rho_{i,\text{amorphous}}) \quad (5.42)$$

⋮

and so on with other mass-continuity equations for water and other volatiles as previously mentioned. Note that the temperature equation has dependencies on the density of volatiles and water because they affect the heat conductivity term. In addition, the temperature and masses at each grid point depend on the values of these quantities at nearby grid points. Therefore, we currently have $(4 + 2N_v)N_r$ coupled ordinary differential equations to solve.

5.4.4 Approximating Sublimation and Gas Transport

Resolving the small gas sublimation and transport timescales can be extremely costly (cf. Figure 5.1). In addition, fully simulating all volatiles for transport greatly increases the number of coupled ordinary differential equations. To resolve this, we present two different approximation methods to resolve the gas sublimation-transport process. Both methods are implemented in our code, and we find that they give similar results in terms of volatile evolution.

Method 1

We now make two crucial approximations to reduce the complexity and runtime of our computation.

First, we approximate that a solid component automatically evaporates into gas when it reaches a certain critical temperature threshold. This is the same approximation that was made in Gkotsinas et al. (2022) to study the long-term evolution of Jupiter-family comets during the early evolution of the Solar system. This approximation is needed because sublimation (and condensation) is a strong exponential function of temperature and reaches very low timescales. If our simulation does not resolve these timescales correctly, they will introduce significant stiffness to the equations and numerical error. However, resolving these low timescales would significantly reduce the simulation speed⁴. In addition, sublimation and condensation can occur multiple times over one orbit so these processes would occur frequently. Constantly having timesteps on the order of 10^{-5} years would cause massive computational costs, prohibiting us from simulating for 400 Myr. As a result, we determine

⁴Note that we do not make the instant sublimation approximation for crystallisation, although sublimation also reaches very low timescales at high temperatures. This is because crystallisation only occurs once at each grid cell and does not incur computational costs multiple times.

that volatiles sublime instantly when the following conditions are met (see Figure 5.1):

- hypervolatiles like CO sublimate rapidly when $T \gtrsim 30$ K
- volatiles like CO₂ sublimate when $T \gtrsim 100$ K
- H₂O sublimate when $T \gtrsim 180$ K.

Note that the temperatures chosen are a few degrees higher than what's needed in Figure 5.1 to ensure instant sublimation. In addition, these conditions are consistent with the conditions used by Gkotsinas et al. (2022) to determine when volatile species are depleted. This approximation removes the dependency on the q terms in the mass-continuity equations for water and other volatiles.

Second, we simplify the gas transport term J to reduce the number of equations needed to be solved. The timescale on which gas can be transported from some point r to the surface is τ_{gas} (Equation 5.26). Hence, if a cell has reached a temperature high enough for sublimation for a particular volatile species *and* if that temperature is sustained over τ_{gas} , we can say that the volatile species is lost from the comet. If at the temperature drops below the critical temperature, we assume that the gas has re-condensed.

With this, both the J and q terms are removed from the mass-continuity equations. Hence, the following equations remain for us to solve as coupled ordinary differential equations: the heat equation and the mass-continuity equations for water ices

$$\frac{\partial \rho_{\text{amorphous}}}{\partial t} = -\lambda(T)\rho_{\text{amorphous}} \quad (5.43)$$

$$\frac{\partial \rho_{\text{crystalline}}}{\partial t} = \lambda(T)\rho_{\text{amorphous}}. \quad (5.44)$$

The densities ρ_{vapour} for water and $\rho_{j,\text{gas}}$ for a volatile species j are tracked through the temperature changes according to the described scheme. $\rho_{j,\text{solid}}$ at each grid point is assumed to stay constant until temperature is high enough and sustained long enough for them to be sublimated and lost from the comet. This now leaves us with $3N_r$ coupled differential equations to solve.

In Figure 5.5, we show an example simulation run with this sublimation-transport approximation. The simulation shown here is for a 5 km comet with semi-major axis of 30 AU, pericentre of 1 AU, around a $10^3 L_\odot$ star and simulated over 1 Myr. Initially, the comet's temperature is uniform and is set at 10 K. Initially, all H₂O are assumed to be in amorphous ice form. As seen in the top panel, as the comet heats up, amorphous ice is transformed into crystalline ice. In the bottom panel, we observe a layer of crystallised water ice. Toward the surface, we find the sublimation front of water ice where the temperature is high enough for H₂O to sublimate and is sustained long enough to be transported to the surface, according to the sublimation-transport approximation described.

We note that a major caveat of this approach is that we fail to account for the case where the gas is hot enough for sublimation, but the temperature is sustained over a lesser time

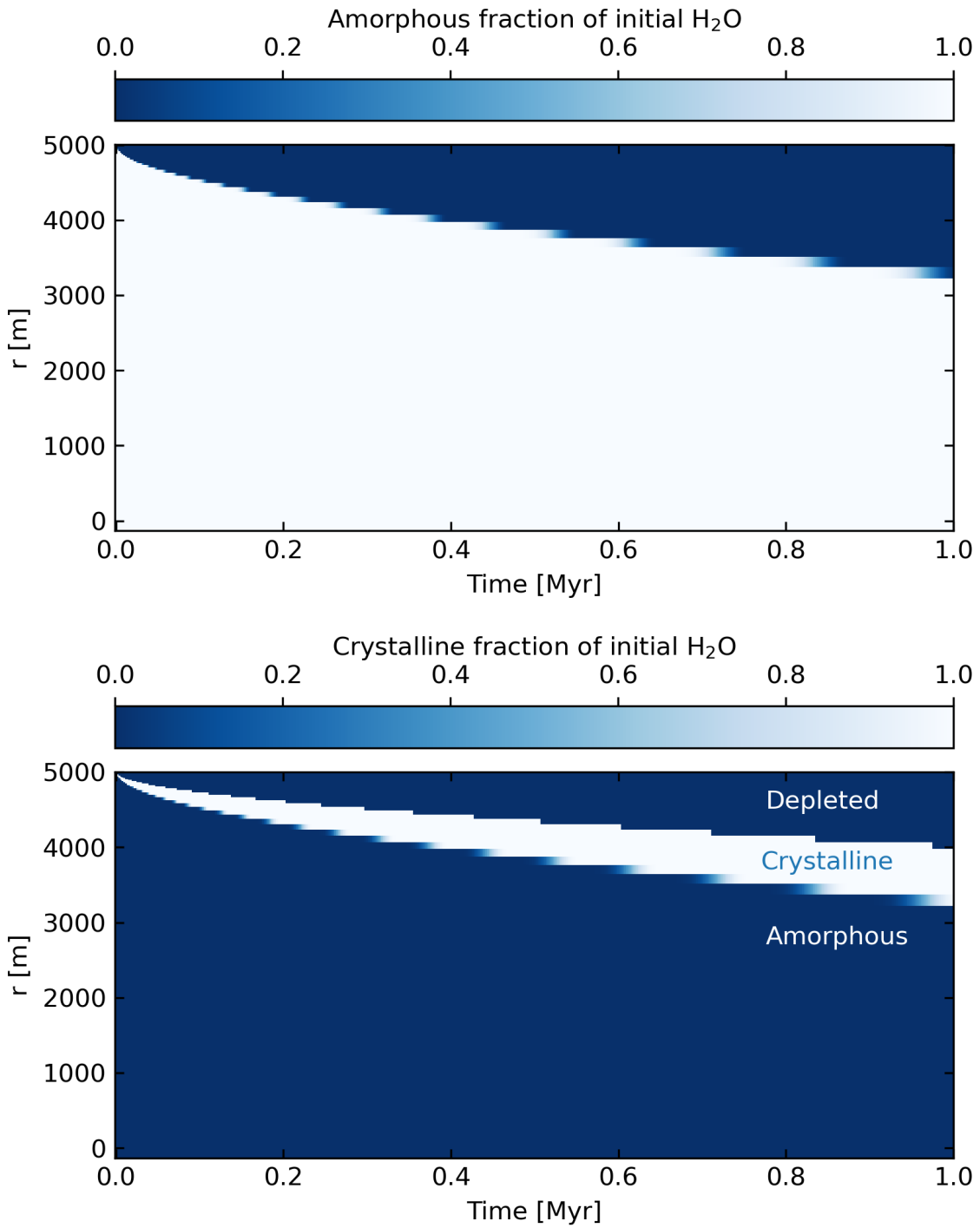


Figure 5.5: The fraction of amorphous ice relative to all initial H₂O ices (top) and the same for crystalline ice (bottom) over time in a 5 km comet with semi-major axis of 30 AU, pericentre of 1 AU, around a $10^3 L_\odot$ star. The comet is initially cold (10 K uniformly throughout) and initially all H₂O are in the amorphous form. The top panel shows amorphous ice transitioning to crystalline ice. The bottom panel shows the crystallised ice layer and the ablated front near the surface where all H₂O are lost.

than τ_{gas} . In this case, a parcel of gas from below the sublimation front is transported over a distance and then recondenses. This process is not accounted for in our approximation, though has been observed in other comet simulations (e.g. [Davidsson, 2021](#)). For our purpose, ignoring transport-recondensation is an acceptable caveat because we are only interested in how much a volatile species is lost in bulk from the comet and not about where they are. We consider that our method gives a first-order, physically motivated approximation for volatiles lost.

Method 2

There is another approximation which has a similar caveat of neglecting the internal transport-recondensation effect. This method has been developed in [Schorghofer \(2008, 2010, 2016\)](#); [Schörghofer & Hsieh \(2018\)](#) and most recently used in [Gkotsinas et al. \(2024\)](#) to study cometary volatile processing in the early Solar system. Both their scheme and ours seek to find simplifications to the gas transport term J_j and sublimation term q_j for a volatile species j .

This approximation reduces the gas transport equation to a differential equation describing the distance r_i at which a volatile ice j retreats from the surface of the comet in the form:

$$\frac{dr_i}{dt} = \mathcal{D} \frac{\rho_{i,\text{sat}}}{\rho_i} \left(r_i \cdot \left(1 - \frac{r_i}{R} \right) \right)^{-1}. \quad (5.45)$$

Here, the distance $r = r_i$ is the sublimation front, beyond which all volatile ice is assumed to be ablated. ρ_i is the ice density of the volatile at the distance $r = r_i$. $\rho_{i,\text{sat}}$ is the saturated vapour pressure density, defined as the density calculated from the ideal gas law given the temperature at the sublimation front and the saturated vapour pressure (\mathcal{P}_j , Equation 5.20). \mathcal{D} is the gas diffusion coefficient, defined as (cf. [Guilbert-Lepoutre, 2014](#); [Schörghofer & Hsieh, 2018](#); [Gkotsinas et al., 2024](#)):

$$\mathcal{D} = \frac{\pi}{8 + \pi} \frac{\psi}{1 - \psi} \frac{v_{\text{therm}}}{\xi} r_p \quad (5.46)$$

where $v_{\text{therm}} = \sqrt{(8k_B T)/(\pi m)}$ [m s⁻¹], and other constants as defined in Table 5.1.

Now, all variables are functions of temperature. Our simulation always resolve the timescales on which temperature change over one timestep, through either the Courant-Friierichs-Lowy condition or the rate at which surface flux changes (see the next section on how we resolve the smallest relevant timescales). Hence, over a timestep dt , the temperature does not significantly change over this timescale. Thus, we use the average temperature between timesteps, \bar{T} , at the sublimation front r_i to calculate all terms with a temperature dependence. This allows the differential equation to be solved analytically through

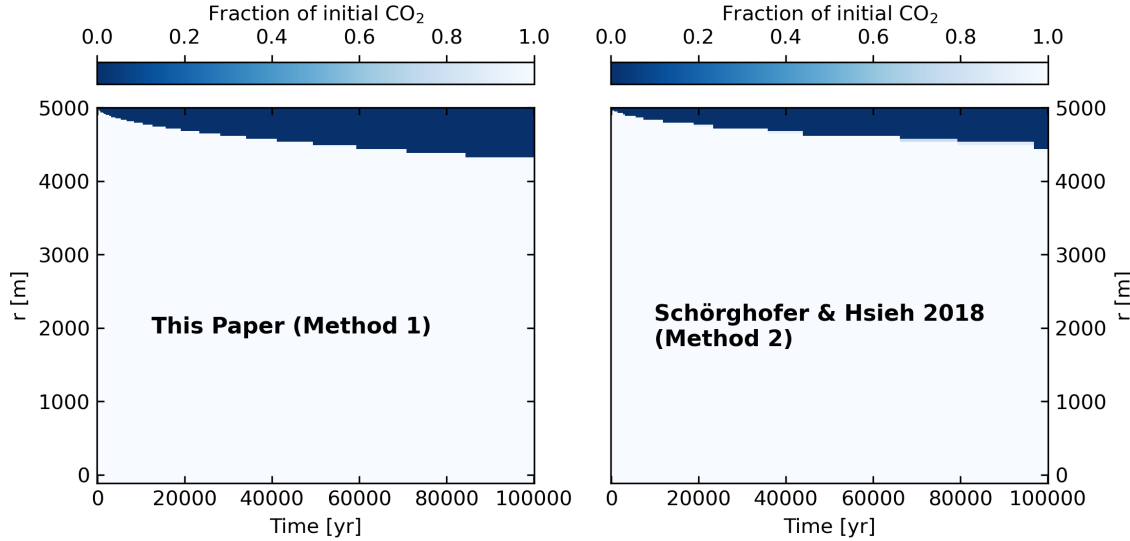


Figure 5.6: The fraction of CO_2 ice relative to initial CO_2 ice over time in a 5 km comet with semi-major axis of 30 AU, pericentre of 1 AU, around a $10^3 L_\odot$ star. The comet is initially cold (10 K uniformly throughout). The left panel shows approximation method 1 for gas sublimation-transport used in this work, the right panel shows the method by Schörghofer & Hsieh (2018) (method 2).

separation of variables, yielding the solution:

$$\frac{R^2}{6} - \frac{r_i^2}{2} + \frac{r_i^3}{3R} = \frac{\mathcal{D}(\bar{T})\rho_{i,\text{sat}}(\bar{T})}{\rho_i} dt \quad (5.47)$$

where dt is the timestep. This cubic equation admits one physical root (Schörghofer & Hsieh, 2018):

$$\frac{r_i}{R} = \frac{1}{2} + \cos\left(\frac{1}{3}\arccos\left(2\frac{t}{t_D} - 1\right) - \frac{2\pi}{3}\right) \quad (5.48)$$

where the timescale

$$t_D(\bar{T}) = \frac{R^2}{6\mathcal{D}(\bar{T})} \frac{\rho_i}{\rho_{i,\text{sat}}(\bar{T})} \quad (5.49)$$

can be thought of as the characteristic timescale to deplete the entire comet with radius R if the temperature stays constant at $T = \bar{T}$.

After each timestep, we calculate the sublimation fronts of water and other species through these equations. Cells at radii $r > r_i$ are fully depleted of volatiles, while the cell at the sublimation front is partially depleted. Cells below the sublimation front are not altered. Hence, similar to approximation 1, this approximation does not account for the internal transport and recondensation of gas below r_i .

Method Comparison

Both methods mentioned are implemented in our code. In Figure 5.6, we present the sublimation of CO₂ ice in a 5 km comet with semi-major axis of 30 AU, pericentre of 1 AU, around a $10^3 L_\odot$ star. In this figure, the two methods are shown and we find that there are negligible differences between them. There is a small difference in how fast volatiles are sublimated, where method 2 evaporates volatiles slightly slower. This can be attributed to the fact that method 1 assumes Knudsen flow, whereas method 2 calculates the diffusion coefficient \mathcal{D} under a slightly different method. There are a few different ways to find \mathcal{D} , but [Guilbert-Lepoutre \(2014\)](#) found that these differences expressions for \mathcal{D} are no more than order unity.

5.4.5 Method of Lines, Timestep Limit, and Integrator Switching

Solving a partial differential equation by discretising all spatial components and turning it into an ordinary differential equation is called the method of lines (a method of solving partial differential equations and is recently used to solve the heat equation in comets in [Levine et al., 2023](#)). We use integrators from `solve_ivp` in the `scipy` package ([Virtanen et al., 2020](#)) to solve our set of $3N_r$ coupled ordinary differential equations.

We now describe how each simulation timestep is performed. At each step, we first integrate one gravitational step with `REBOUND` using the IAS15 integrator, recording the timestep taken there as dt_{IAS15} . Now, we solve temperature-mass differential equations using the integrators in `solve_ivp`. At each simulation step, we set the maximum timestep limit that an integrator can take by calculating the following timescales:

$$dt_{\max} = \min\{\tau_L, \tau_{\text{CFL}}, \tau_{\text{crystallisation}}, dt_{\text{IAS15}}\}. \quad (5.50)$$

This is the maximum timestep because the `solve_ivp` integrators have a time-adapted scheme internally. So in reality, the true timestep is even shorter than dt_{\max} , ensuring proper resolutions of surface flux and temperature variations, heat transfer, and mass evolution. We also keep track of how much mass is sublimated and lost through the sublimation-transport approximation.

There are six integrators currently implemented in `solve_ivp`, three of which are explicit schemes, two of which are implicit, and LSODA can automatically switch between implicit-explicit depending on the stiffness of the problem. Implicit integrators have the advantage of numerical stability but come with an increased computational cost. Explicit integrators are cheaper but are at risk of numerical instability. It is especially important to respect the Courant-Friierichs-Lewy condition with explicit methods. For our simulation, we use a combination of integrators to ensure computational speed and stability⁵. When the surface

⁵Implicit integrators are guaranteed to be A-stable. That is, for any values and with any timestep, these methods do not fail (their stability region is unbounded). In contrast, explicit methods have bounded

condition varies strongly between simulation steps ($\Delta G \sim G$), satisfying the condition:

$$\frac{\Delta G}{G} \geq 0.5 \quad (5.51)$$

then we always use the RADAU implicit integrator (Hairer & Wanner, 1999). When this condition is not satisfied, the problem is less likely to be stiff and we use LSODA (Petzold, 1983) to speed up our integration. This integrator uses an explicit integration scheme for speed, but can automatically switch to an implicit method when stiffness is detected. As a failsafe, if an integrator fails to achieve the desired accuracy tolerance for whatever reason, the maximum timestep is reduced and the timestep is re-attempted with an implicit integrator.

5.4.6 A Long-term Evolution Simulation

In Figures 5.7, 5.8, and 5.9, we show the simulation results for a fully coupled stellar - orbital dynamics - thermal - mass evolution for a comet over the last 400 Myr of post-main sequence stellar evolution. This comet is 30 km in radius at an initial semi-major axis of 400 AU and with an initial pericentre distance of 30 AU, representative of a large comet in the current Solar system's Scattered Disc.

In Figure 5.7, the top panel shows the stellar mass and luminosity over time from the pre-computed $1 M_{\odot}$ star model in MESA Isochrones & Tracks (Dotter, 2016). In the middle panel, we show the semi-major axis and eccentricity of the comet. The comet has an initial orbital period of $\tau_{\text{period}} \approx 8000$ years. As seen in this panel, the first stellar mass loss at ~ 260 Myr does not affect the comet's eccentricity but moves the semi-major axis outward. This can be understood by comparing the orbital period with the mass loss timescale, τ_M , in Figure 5.3. $\tau_M \sim 10^8$ years during this first mass loss, which is much longer than the comet's orbital period. That is, over the course of one comet orbit, the star's mass is relatively stable. This is the strong adiabatic mass loss limit, where the comet's eccentricity remains unchanged, while the semi-major axis changes according to:

$$a_{\text{new}} = \frac{M_{\text{old}}}{M_{\text{new}}} a_{\text{old}}. \quad (5.52)$$

This is typically used in previous works where the comet's evolution does not couple with stellar evolution (e.g. in Jura & Xu, 2010). However, the second mass loss during the asymptotic giant branch pulses at 360 – 400 Myr highlights the limitation of this approach. During this mass loss, the star loses mass on the timescale $\tau_M \sim 3 \times 10^4$ years (Figure 5.3), which is only a few times more than the orbital period of the comet. Here, the adiabatic

regions for stability and timesteps have to be carefully chosen. That being said, the timestep cannot be arbitrarily large for implicit integrators or the accuracy will still be impacted. Thus, implicit integrators are preferred when differential equations are “stiff”. Unfortunately, implicit integrators are more computationally expensive compared to explicit integrators and thus, we use a switching scheme to balance stability and speed.

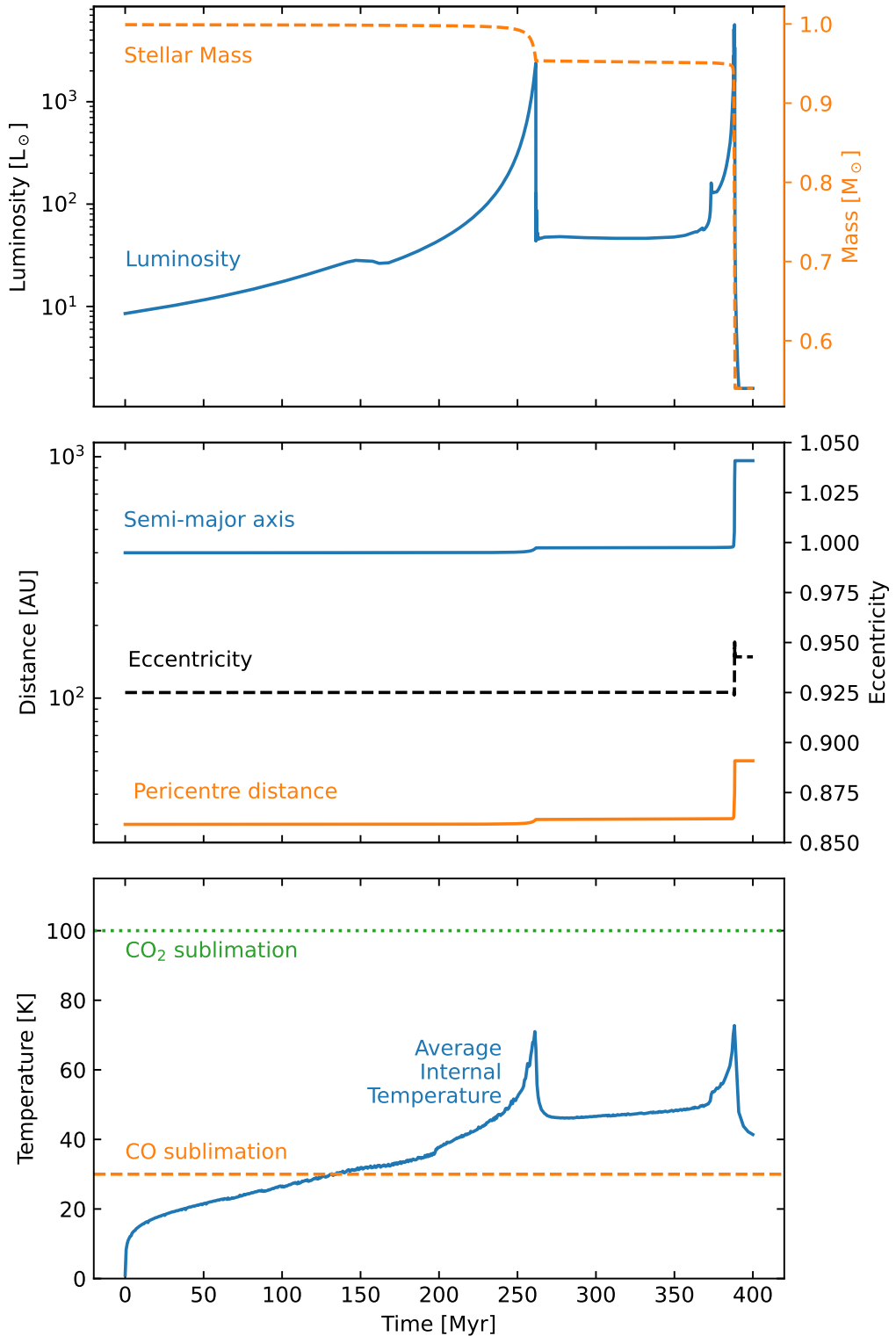


Figure 5.7: A summary of a long-term comet evolution coupled with stellar evolution. *Top:* Mass and luminosity changes during the last 400 Myr of stellar evolution for a Sun-like $1 M_{\odot}$ star. *Middle:* The orbital evolution of a comet around this star with an initial orbit at 400 AU and pericentre distance of 30 AU, typical of a Solar system Scattered Disc object. *Bottom:* The average internal temperature of the comet over time. As seen, the temperature is sufficiently high to sustain CO sublimation.

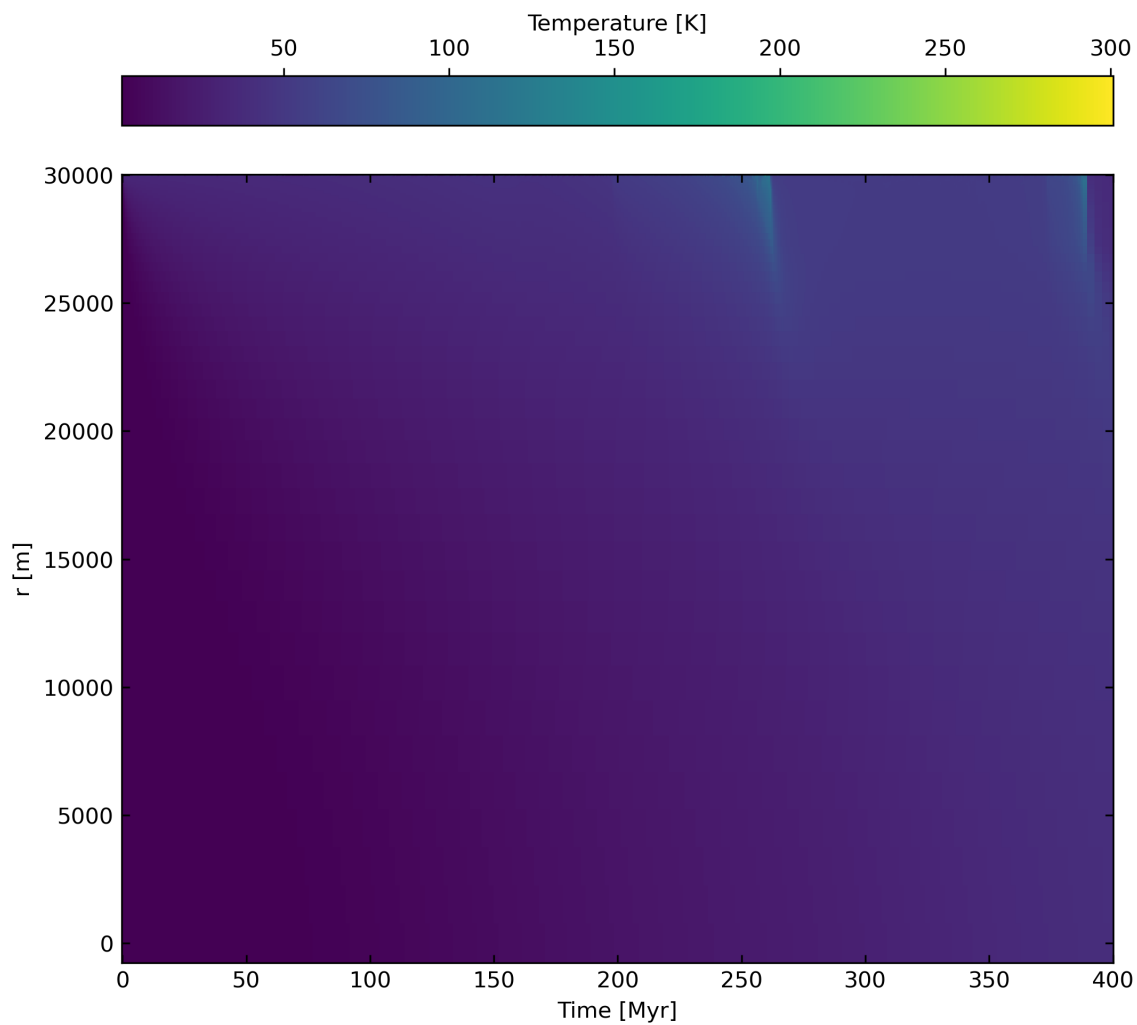


Figure 5.8: The temperature evolution over the last 400 Myr evolution of a 30 km radius comet with an initial semi-major axis of 400 AU and initial pericentre distance of 30 AU. We can observe that our numerical method properly resolves the heat transfer throughout the comet, even during the most luminous stellar evolution phases when the received stellar flux increases by 2.5 orders of magnitude over a timescale on the order of $10^2 - 10^3$ years (cf. top panel of Figure 5.9).

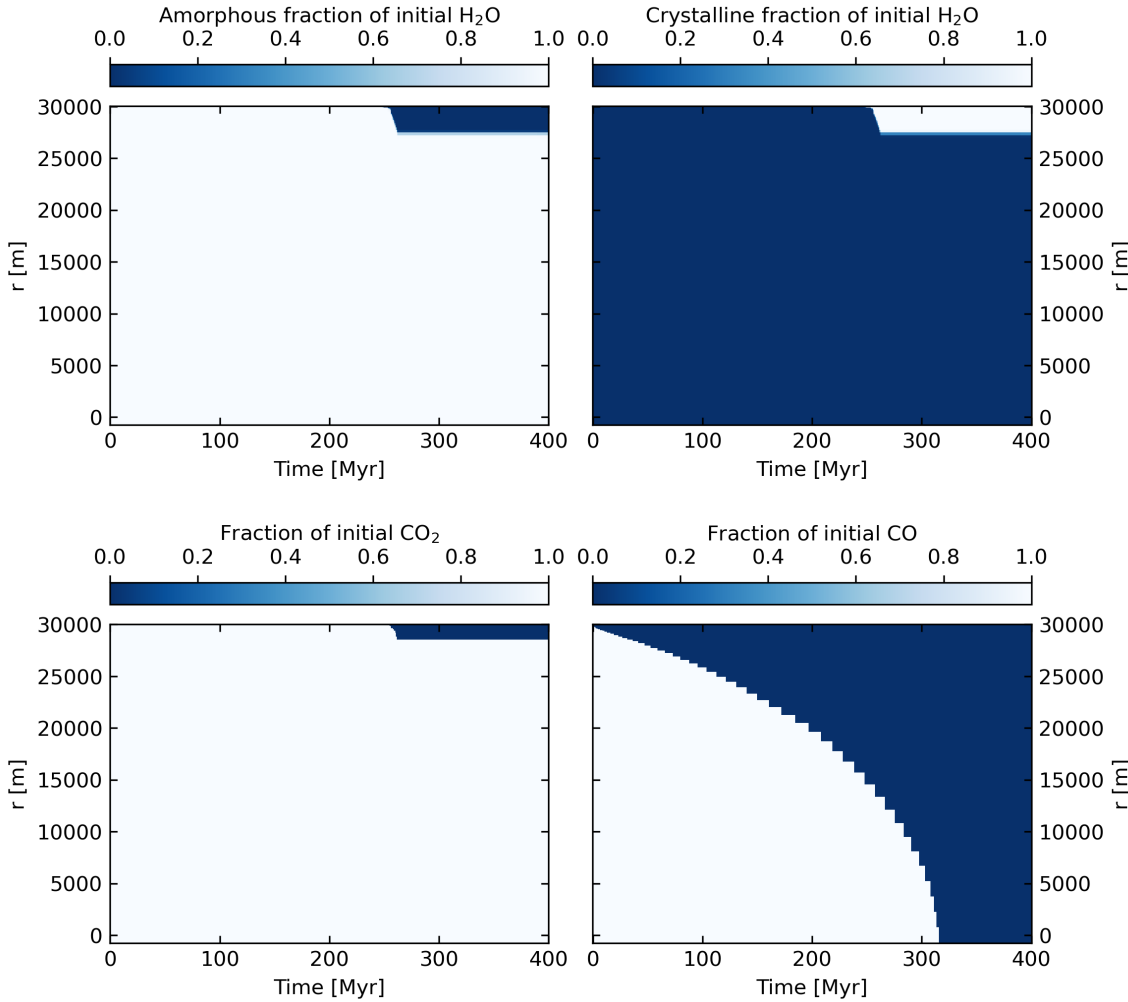


Figure 5.9: Four panels showing the evolution over the last 400 Myr of stellar evolution of amorphous H₂O ice (top left), crystalline H₂O ice (top right), CO₂ ice (bottom left), and CO ice (bottom right). All panels show the fraction of volatiles relative to their initial abundance. The comet has an initial semi-major axis of 400 AU and pericentre distance of 30 AU. Initially, all H₂O ices are in amorphous form.

mass loss assumption is weakened and there is some eccentricity evolution. Coupling with N-body allows us to accurately consider the orbital evolution induced by stellar evolution for any comets. We now compare the N-body evolution of this comet with the analytic work by Veras et al. (2011), where the authors analytically study the orbital evolution of a test particle when the star experiences a constant mass loss. Our simulation and their analytic calculation show that eccentricity evolution is not monotonic. However, the analytic work does not predict the eccentricity to decrease when it is close to 1. We attribute this difference to the assumption in Veras et al. (2011) where mass loss occurs at a constant rate, whereas our mass loss follows the MESA model (which does not occur at a constant rate).

In the bottom panel of Figure 5.7, we plot the mean internal temperature (not including the surface temperature) of the comet. Comparing this panel to the top panel of the same Figure, we find that the comet’s temperature is coupled to the stellar luminosity as expected. Further, the temperature is sufficiently high to sustain CO sublimation, but not enough to sublime CO₂. In Figure 5.8, we plot the temperature of all the comet’s grid cells over the entire time evolution. We show that our simulation is capable of resolving the heat propagation through the comet during the most intense stellar luminosity ($L_* \sim 10^4 L_\odot$).

Finally, in Figure 5.9, we plot the fraction of amorphous, crystalline, CO₂, and CO ices over time. The fractions of amorphous and crystalline ices are normalised to all initial H₂O ices. In this plot, we observe that the temperature is low enough to sustain amorphous ice throughout the whole comet until ~ 250 Myr, at which point the top surface layer of ice crystallises. Note that because of this crystallisation, the heat conductivity κ also changes. Observing the crystalline ice panel, we find that this top layer of crystalline ice remains as ice and is not lost. Even though the surface temperature does become sufficiently high to instantly sublime water, the time over which these temperatures can be sustained is not long enough to transport water vapour to the surface to be lost from the surface. Observing the CO and CO₂ plots, we find that CO is completely depleted while only the top layer of CO₂ is lost.

5.5 Volatile Content: Kuiper Belt and Scattered Disc

In this section, we first discuss why we only simulate comets with semi-major axes less than 1000 AU in this chapter. Next, we describe details of simulations done, and then we show the results of these simulations. Finally, we discuss our results in context of recently proposed reservoirs of white dwarf polluting bodies.

5.5.1 Comets at Distances Less Than 1000 AU

Here, we show the simulation results for comets whose orbits are under the adiabatic mass-loss limit ($\tau_{\text{period}} \gtrsim \tau_M$):

$$a \lesssim \left(GM_* \left(\frac{\tau_M}{2\pi} \right)^2 \right)^{1/3} \approx 10^3 \text{ AU} \left(\frac{\tau_M}{3 \times 10^4 \text{ years}} \right)^{2/3} \left(\frac{M_*}{1M_\odot} \right)^{1/3}. \quad (5.53)$$

Comets beyond the adiabatic limit are considered under the impulsive limit. The evolution of comets under the impulsive limit has to be done statistically since these comets experience a velocity kick which depends on their location in their orbit. For example, a distant Oort cloud comet at apocentre while the star rapidly loses 30% of its mass would experience a very different velocity kick compared to a similar comet at pericentre. Thus, for comets under the impulsive limit, we need to simulate a population of comets to average over orbital phases. Furthermore, comets beyond 3000 AU begin to strongly experience the Galactic tide and stellar flybys, which can significantly affect the orbits of comets (Heisler & Tremaine, 1986; Heisler, 1990; O'Connor et al., 2023; Pham & Rein, 2024). In addition, we made the assumption that radioactivity is negligible because comets on circular orbits with semi-major axes less than 1000 AU have $E_{\text{radio}}/E_* \ll 1$ (cf. Equation 5.3). More distant comets will require radioactivity modelling in the heat equation source term. All of these factors are beyond the scope of the current work and will be considered in a subsequent study.

5.5.2 Simulation Setup

For comets in this chapter, we consider two cases: a Solar system-like configuration with Kuiper Belt and Scattered Disc comets, and initially circular debris discs of comets. The details of initial semi-major axes and pericentres considered are summarised in Table 5.5. Comet sizes 1, 5, 10, 20, 30, 40, and 50 km are simulated, representing the ranges of body we consider appropriate for the thermal-mass evolution previously described. Other than H₂O, we consider the evolution of CO representing hypervolatiles and CO₂ representing other volatiles.

Initially, all H₂O ices are in their amorphous form. Other volatile ices are initially in their solid form. The initial abundances in our setup for dust-to-ice, CO-to-water, and CO₂-to-water ratios are commonly used values in Solar system comet simulations, typically found through measurements or modeling (Bockelée-Morvan et al., 2004; Huebner et al., 2006; Britt et al., 2006; Gkotsinas et al., 2022, 2024). All of these components are distributed uniformly throughout the comet. We set no trapped gas in amorphous ice because the fraction of occluded gas in amorphous ice is constrained to be much lower than the non-occluded volatile ice (e.g., $f \sim 0.001$ in Prialnik et al., 1995; Huebner et al., 2006). Furthermore, how much gas are trapped and the nature of this trapping in amorphous ice are still open questions (e.g. Ninio Greenberg et al., 2017; Prialnik & Jewitt, 2022). The

Table 5.5: The orbital initial conditions and radii (top) for comets in our simulations and initial conditions common to all comets (bottom). No gas are trapped in amorphous ice (f_{CO} , f_{CO_2} zero). The dust-to-water, CO-to-water, and CO₂-to-water ratios are from typical values in the literature (e.g. Bockelée-Morvan et al., 2004; Huebner et al., 2006; Britt et al., 2006; Gkotsinas et al., 2024). The initial temperature is set to be 10 K.

Simulation	Radius [km]	Initial Semi-major axis [AU]		Initial Pericentre [AU]		
Solar system-like	[1,50]	[30, 1000]		30		
Debris discs	[1,50]	[30, 1000]		Circular orbits		
ρ_{bulk} [kg m ⁻³]	$X_{\text{dust}}/X_{\text{H}_2\text{O}}$	$X_{\text{CO}}/X_{\text{H}_2\text{O}}$	$X_{\text{CO}_2}/X_{\text{H}_2\text{O}}$	f_{CO}	f_{CO_2}	T_0 [K]
500	1	0.1	0.1	0	0	10

initial temperature is also set uniformly across the comet at a value of 10 K, roughly the equilibrium temperature for a comet on a circular orbit at 1000 AU around a $10L_\odot$ star. Simulations are run over the last 400 Myr of stellar evolution for a Sun-like $1M_\odot$ star, where at the end the star becomes a white dwarf.

5.5.3 Results

In Figure 5.10, we show the volatile content of CO and CO₂ for the Solar system Kuiper Belt and Scattered Disc comets after the 400 Myr post-main sequence evolution. As seen, both species are depleted in the Kuiper Belt, with only a very small trace amount of CO₂ remaining ($\sim 5\%$). The Scattered Disc comets are also largely deprived of hypervolatiles like CO, with the exception of the largest comets (40–50 km) which retain about 20 – 40% of their original hypervolatile content. However, volatiles like CO₂ are more likely to be retained in the Scattered Disc, depending on the comet size. Thus, if the Kuiper Belt planetesimals pollute the Solar white dwarf in 5 billion years, the pollution signature will be largely rocky. The Scattered Disc, on the other hand, might produce some volatile signatures in the atmosphere of our future white dwarf. However, the volatile content will be much less than what we would expect from current Kuiper Belt and Scattered Disc comets. Here, we note that the curves are apparently non-monotonic for small comets (radii 1–5 km) and large distances (> 700 AU). This is because these comets can have very sparse grids due to their size and distances (they are at greater distances so do not need a fine grid resolution at the surface). Small comets are much more susceptible to having a very sparse grid, and thus exhibits non-monotonic behaviours in the figure. To confirm this, we enforce a minimum grid cell size to test small comets in this regime which causes the apparent non-monotonicity to disappear.

In Figure 5.11, we likewise plot the volatile content, but now for comets on initially circular orbits at various distances. We discuss this result in the context of recently proposed literature on white dwarf pollution sources. In O'Connor et al. (2022), planetesimals in a

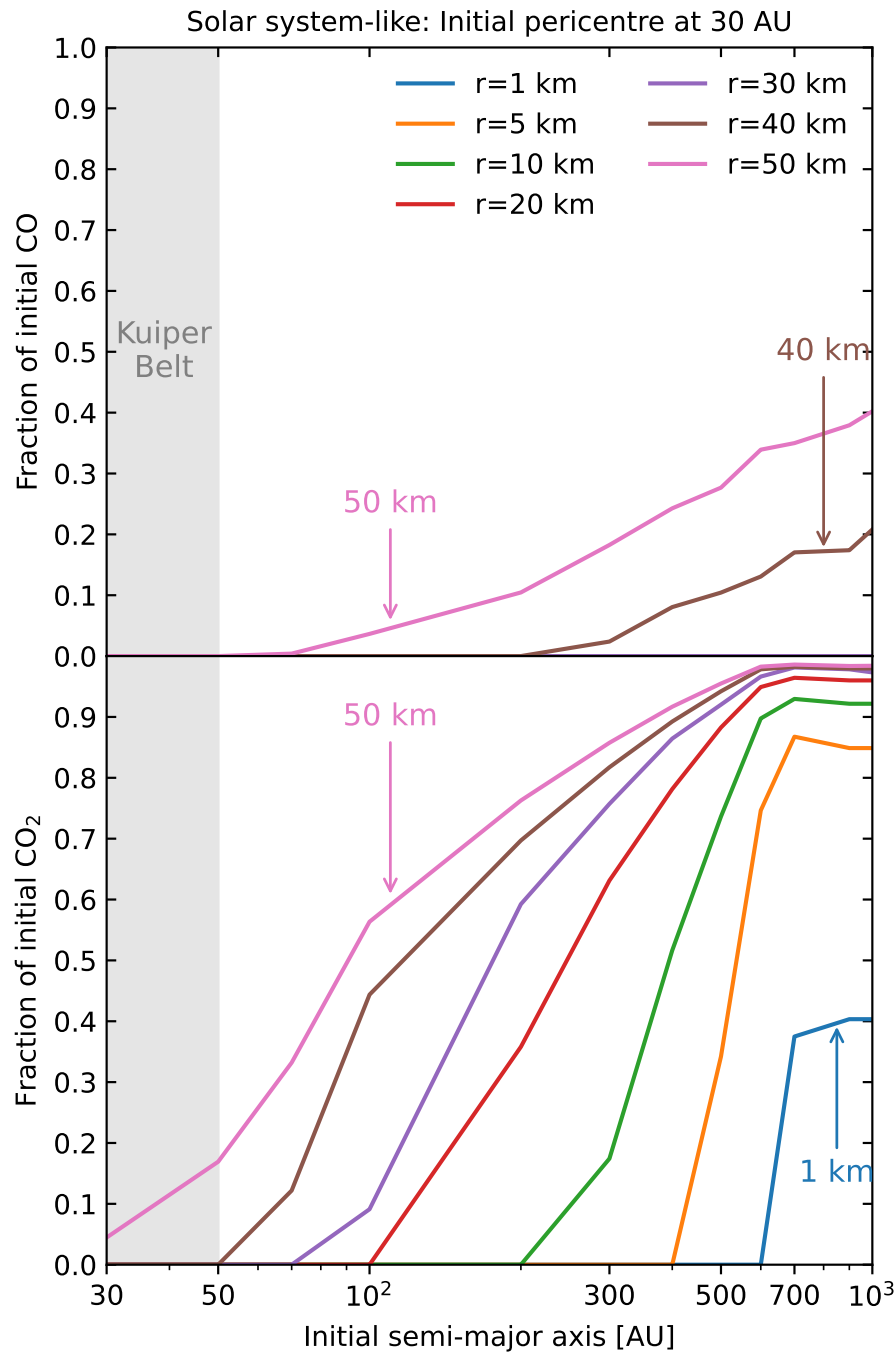


Figure 5.10: The volatile content for CO (top) and for CO₂ (bottom) as a function of initial semi-major axis after 400 Myr of post-main sequence stellar evolution for a Sun-like star. The curves are for various comet sizes. Initially, all comets have a pericentre distance of 30 AU. This setup represents the current Solar system Kuiper Belt (shaded in grey) and Scattered Disc.

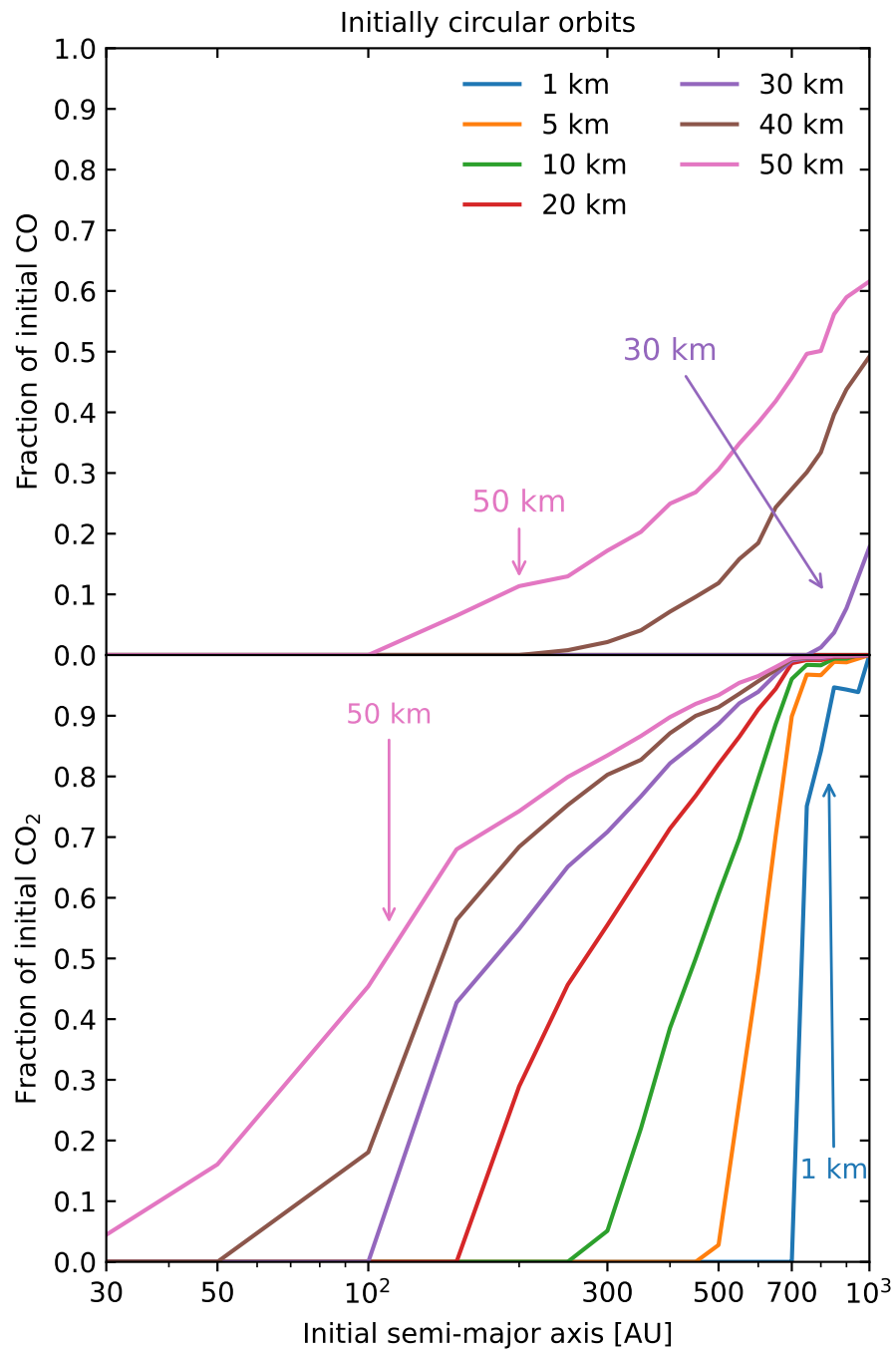


Figure 5.11: The volatile content for CO (top) and for CO₂ (bottom) as a function of initial semi-major axis after 400 Myr of post-main sequence stellar evolution for a Sun-like star. The curves are for various comet sizes. Initially, all comets have circular orbits, representing comets in circular debris discs.

debris disc at tens of AUs are delivered to the white dwarf through secular chaos induced by an inner giant planet. The pollution rate increases sharply by several orders of magnitude right after the post-main sequence evolution, then decreases to a constant rate. In this scenario, all volatiles and hypervolatiles are depleted. In [Akiba et al. \(2024\)](#), debris discs between 30-240 AU are delivered to the white dwarf through the white dwarf's natal kick during its asymptotic giant branch phase. The pollution rate in [Akiba et al. \(2024\)](#) also receives a sharp increase initially during the asymptotic giant branch. In this scenario, hypervolatiles are depleted in comets with radii < 50 km, while volatiles are depleted in comets with radii < 20 km. In both cases, significant volatile depletion of the debris discs points consistently to observations of the lack of volatiles in most young, polluted white dwarfs ([Xu & Bonsor, 2021](#)).

5.5.4 Water Retention

Since this work is focused on understanding non-water evolution to understand the abundance of Carbon on white dwarfs, we do not fully model water evolution. In particular, as compared to [Malamud & Perets \(2016, 2017a,b\)](#), our water evolution model does not include the production of liquid water or the serpentinisation of water with rocks (a process where water can chemically bind with rocks). Furthermore, [Malamud & Perets \(2016\)](#) fully models the movement of gas to describe the sublimation front on a surface comet, whereas we use the surface ice retreat approximation by [Schörghofer & Hsieh \(2018\)](#). This last difference would produce the greatest effects, since their model allows differentiation in comets. The approximation by [Schörghofer & Hsieh \(2018\)](#) does not naturally allow this feature, which could concentrate more volatiles near the surface where they would be sublimated much easier. Due to these modeling differences, we found that our comets retain about 1-15% more water at the end, as compared to [Malamud & Perets \(2016\)](#), which is probably due to the difference in the sublimation modeling. We show our results for the final fraction of H_2O in Figure 5.12 where all comets are initially in circular orbits, similar to [Malamud & Perets \(2016\)](#). This Figure can be compared directly to the results in Figure 4 of [Malamud & Perets \(2016\)](#).

Prior to the model developed by [Malamud & Perets \(2016\)](#), [Jura & Xu \(2010\)](#) presented a major advancement in this field. However, there are a few limitations in this study which is discussed in details in [Malamud & Perets \(2016\)](#). The greatest problems are the assumption that bodies reach equilibrium temperature instantly, comets have homogeneous thermal properties throughout, and extrapolating vaporisation temperature causing their vaporisation temperature to be much greater than what is typical in comet modeling literature. The work by [Stone et al. \(2015\)](#) estimated the water content for comets using an order of magnitude approach. However, since they neglected the blackbody re-radiation from the top layers of comets, their Equation 11 predicts that 10 km comets around the current Sun ($1L_\odot$) completely evaporates within 500 000 years. Because of these modeling

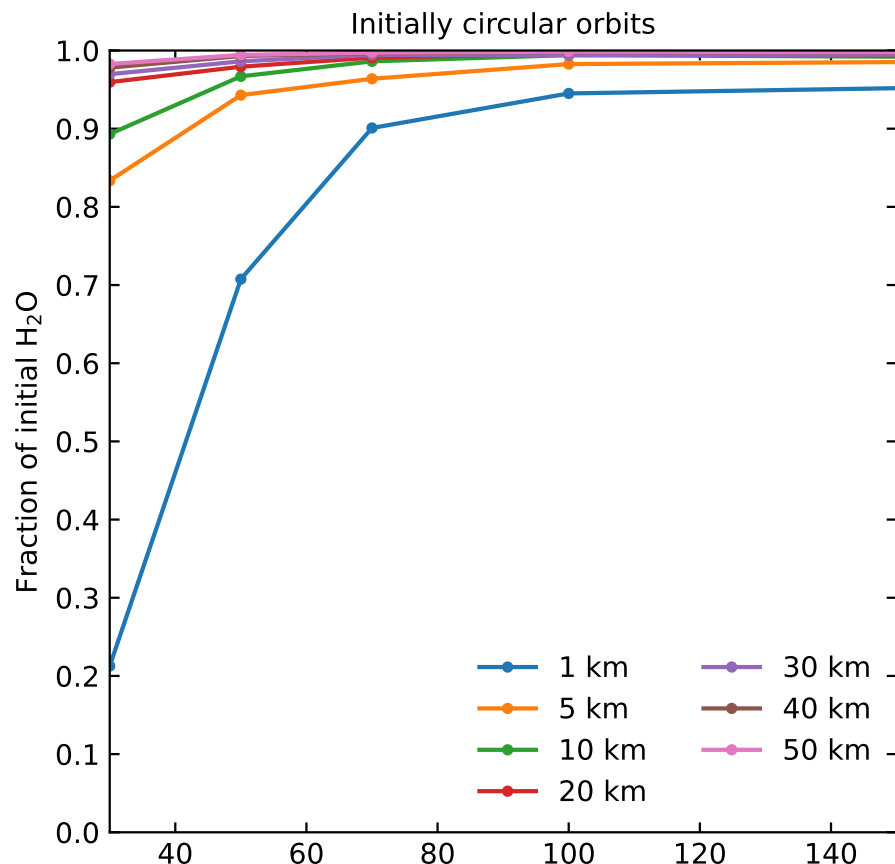


Figure 5.12: The volatile content for H_2O as a function of initial semi-major axis after 400 Myr of post-main sequence stellar evolution for a Sun-like star. The curves are for various comet sizes. Initially, all comets have circular orbits, representing comets in circular debris discs.

differences, our water retention results differ greatly to that in [Jura & Xu \(2010\)](#) and [Stone et al. \(2015\)](#).

5.6 Discussion

In this section, we first discuss why we do not include the existence of planets or the white dwarf natal kick, and why we do not expect these dynamical effects to affect the final volatile budget after stellar evolution. Next, we discuss the lack of water serpenisation in our simulation and the water budget in comets. Then, we discuss the application of our findings to existing polluted white dwarf with showing pollution coming from icy bodies.

First, we do not consider the existence of a planet, which is often invoked to deliver planetesimals from debris discs to the white dwarf. This is because there is a large parameter space of possible configurations invoking many dynamical mechanisms (e.g. [Debes & Sigurdsson, 2002](#); [Mustill et al., 2014](#); [Smallwood et al., 2018](#); [Maldonado et al., 2020](#); [Trierweiler et al., 2022](#); [O'Connor et al., 2022, 2023](#); [Pham & Rein, 2024](#); [Veras et al., 2024](#)). However, we expect that the inclusion of a planet would not significantly alter volatile content as found in Figures 5.10 and 5.11. This is because the comet-planet interaction is typically important after the asymptotic giant branch mass loss, where the star loses a significant amount of mass, inducing many dynamical scenarios for comet-planet interactions. This is towards the very end of our simulation (see the top panel in 5.7) and is unlikely to significantly deplete comets. Furthermore, this comet-planet interaction would affect the orbital eccentricity. Yet, the volatile content in both Figures 5.10 and 5.11 are quite similar, despite having very different eccentricities. Thus, we do not expect the inclusion of a planet to significantly alter the orbit of comets.

Second, we do not consider the white dwarf natal kick. During the asymptotic giant branch, white dwarfs might experience a kick on the order of $\sim 1 \text{ km s}^{-1}$ ([El-Badry & Rix, 2018](#)). This kick would excite a comet's orbital eccentricity; but as previously mentioned, the final volatile content are relatively similar even for very different eccentricities. Hence, we again do not expect very different results with the inclusion of the kick.

Third, we do not show the final water content in comets, although water ices are accounted for in the simulation. Specifically, we track the crystallisation, sublimation, and transport of water ices for thermal conductivity purposes. However, the retention of water is more complicated than just sublimation and transport (which are sufficient for other volatiles). Water can undergo a process called serpentinisation, a chemical reaction that can bind water to rocks on a molecular level. The post-main sequence retention of water content in comets with serpenisation has been done in [Malamud & Perets \(2016, 2017a,b\)](#).

Fourth, using our results, we can begin to constrain the potential reservoirs of white dwarfs exhibiting comet-like or water-rich compositions, like those in [Farihi et al. \(2013\)](#); [Raddi et al. \(2015\)](#); [GentileFusillo et al. \(2017\)](#); [Xu et al. \(2017\)](#); [Hoskin et al. \(2020\)](#); [Klein](#)

et al. (2021); Doyle et al. (2021); Johnson et al. (2022). For example, our results show that comet-like planetesimals must have originated at large distances ($>700\text{--}900$ AU) to retain a Solar system comet composition, depending on the comet size. Combining this with various dynamical theories and limits, it is then possible to infer which reservoirs are primary contributors to which white dwarf. On the other hand, Xu et al. (2017) found a polluted white dwarf exhibiting spectra similar to that of a Kuiper Belt body. The mass of the parent polluting body is $\sim 1 \times 10^{22}$ g, which corresponds to a radius of $100 - 150$ km, depending on density. Based on our results, this observation is expected since such a large body would be very likely to retain a high fractional amount of volatiles and hypervolatiles.

Fifth, we find that the same reservoir of planetesimals can produce vastly different cometary compositions. For example, a circular debris disc at 200 AU would have both larger, icy bodies (>20 km) and smaller, rocky-like bodies. This could explain the observation in (Johnson et al., 2022) where the observation of a white dwarf can be explained if it accreted a mixture of rocky and icy bodies. Of course, this can also be explained if there are several progenitor reservoirs to pollute white dwarfs, as mentioned in Veras et al. (2024).

5.7 Conclusion

In this chapter, we developed a numerical code that is capable of integrating over the last 400 Myr of post-main sequence stellar evolution for any comet orbits. Our numerical code couples the dynamical, stellar, thermal, and mass evolution. Various timescales associated with these processes are discussed, and an adaptive timestep criterion is used to resolve all of them accurately. The numerical method also uses a non-uniform grid spacing, with the smallest grid scale at the surface having a resolution as small as a few meters. We found a criterion to switch between implicit and explicit integrators to ensure proper resolution of stellar flux for comets on very eccentric orbits or when the stellar luminosity changes rapidly with values up to $\sim 5000L_\odot$ during the asymptotic giant branch. For the mass evolution, we track the crystallisation, sublimation, and gas mass loss of amorphous and crystalline H₂O, CO, and CO₂ ices. We develop a numerical approximation to sublimation and gas transport to speed up our simulation. We show several tests to demonstrate the capability of our simulation, the most extreme being an Oort cloud comet at 20 000 AU with pericentre reaching 3 AU around a 10^3L_\odot star.

With this method, we then study the volatile content of CO, representing hypervolatile species, and CO₂, representing other volatiles. We study the following populations of comets: (i) Solar system-like Kuiper Belt and Scattered Disc, and (ii) comets on initially circular debris discs at various distances. In both cases, we find that CO is completely depleted, except for the largest objects (40-50 km) at distances $> 100 - 300$ AU. CO₂ can be retained in various amounts, depending on the comet size and distance, as shown in Figures

[5.10](#) and [5.11](#). In the context of existing literature on possible planetesimal reservoirs for white dwarf pollution, the volatile depletion we found for comets at distances less than 200 AU are consistent with the observed lack of volatiles on white dwarf atmospheres.

Acknowledgement

We thank Scott Tremaine and Norm Murray for insightful discussions. This research has been supported by the Natural Sciences and Engineering Research Council (NSERC) Discovery Grant RGPIN-2020-04513.

Chapter 6

Conclusion

There will come a day when the passage of time and the efforts of a longer stretch of human history will bring to light things that are now obscure. One lifetime, even if it can be wholly devoted to astronomy, is not sufficient for the investigation of such important matters...

There will come a day when our descendants are astonished that we did not know such obvious facts.

Lucius Annaeus Seneca, *On Comets in Natural Questions* (ca. 62)
translated by Hine

The reciprocity of puzzling astronomical observations and theoretical astrophysical predictions has moved modern scientific pursuits in the last few centuries, as demonstrated through the works by [Kepler \(1609\)](#); [Newton \(1687\)](#); [Le Verrier \(1843\)](#); [Einstein \(1915\)](#). One major domain of astronomy and astrophysics is the study of planets, which has enjoyed its status simultaneously as the oldest field of astronomy, starting with the works studying the motion of Solar system planets by [Kepler \(1609\)](#), and the youngest field, starting with the discovery of exoplanets by [Wolszczan & Frail \(1992\)](#); [Mayor & Queloz \(1995\)](#). Over four centuries, astronomers discovered a variety of phenomena on astronomical objects over the entire electromagnetic radiation spectrum, ranging from the densest and heaviest stars to the smallest and least dense comets (e.g., [van Maanen, 1917](#); [Bockelée-Morvan et al., 2004](#); [Lorimer et al., 2007](#); [Bell Burnell, 2017](#); [Blouin & Xu, 2022](#)). During this same time, astrophysicists developed a variety of techniques, ranging from analytical (e.g., [Newton, 1687](#); [Hamilton, 1833](#); [von Zeipel, 1910](#)) to numerical (e.g., [Newton, 1687](#); [Euler, 1768](#); [Runge, 1895](#); [Wisdom & Holman, 1991](#)).

Recent observations leave new problems requiring explanations, motivating two questions which lie at the heart of this thesis:

1. How do small bodies like comets evolve over billions of years and eventually interact with stellar remnants?
2. Knowing how small bodies evolved, can we use observed phenomena from compact objects to probe the properties of planetesimals across the Universe?

This thesis contributes to the development of numerical methods, and applying both analytical and numerical techniques to explain some of the recent observations of white dwarf pollution and fast radio bursts.

We study the effects of comets on white dwarf pollution in Chapters 2 and 5. In Chapter 2, we demonstrated that Oort cloud comets can sustain white dwarf pollution rates over gigayear timescales, provided no close stellar companion disrupts their delivery. This connects directly to our thermal models in Chapter 5, where we demonstrated that comets would need to be distant or very large to retain a volatile composition resembling the current Solar comets. Combining these findings, we can quantify that the few observations of volatiles-rich white dwarf pollution spectra must have originated from bodies that have radius $\gtrsim 100$ km or from distant, pristine regions. Conversely, the predominantly rocky white dwarf pollution observations are not surprising in the context of our finding that comets in the Solar system's Kuiper Belt, Scattered Disc, and debris discs at distances < 1000 AU are all thermally processed at various fractions. Thus, the dynamical and thermal histories of small bodies converge to explain spectroscopic observations of white dwarfs. This is particularly exciting in the context of with upcoming observations like from the DESI survey, which is expected to deliver orders of magnitude more polluted white dwarf spectra over a wide range of ages.

In Chapter 4, we study another avenue to probe the phenomenology of small bodies in the Universe by studying if collisions by interstellar objects on neutron stars explain fast radio bursts. Specifically, we study the observational implications of this reservoir of energy through calculating the event rate across cosmic distances, event duration, distribution of fast radio bursts energy, subburst statistics, and expected host galaxy morphology. Since a lot of these predictions are motivated by Solar system small bodies properties, an exciting reverse consequence is that we can potentially probe small bodies across the Universe with fast radio bursts. However, further observational works remain to be done to falsify our predictions. We expect this to be done with upcoming radio telescopes like CHORD and ASKAP capable of more and better fast radio bursts localisation.

The mentioned results require developments of novel numerical tools in Chapters 3 and 5, many of which have applications beyond this thesis. Namely, the new fast integration scheme and improved adaptive timestep criterion allowed us to speed up N-body simulations of a test particle in the presence of a massive planet, and improve simulation stability. These tools are not only key to our Oort cloud and comet evolution results but are also broadly applicable to other problems involving extreme eccentricities or close encounters. Some other applications are the error in a close encounter between an asteroid and a planet,

timesteps in gravitational evolution of a cluster of stars, or the speedup in any simulations involving a distant test particle and an interior star-planet system. In addition, we developed a new long-term comet evolution code which couples stellar, dynamical, thermal, mass processes. This allowed us to study the content in comets on the most eccentric orbits around the most luminous stars, while also applicable to any studies involving long-term evolution of comets facing rapid changes in received stellar flux.

Small bodies like comets are fossils of planetary formation, evolution, and their fates are deeply connected with the life cycles of stars. They also highlight that to interpret present-day observations, from polluted white dwarfs to fast radio bursts, we must understand the coupled dynamical and thermal histories of planetesimals across cosmic time. Looking forward, these studies open up rich avenues for exploration. The diversity of exo-Oort cloud structures, the detailed volatile evolution of comet populations, the potential role of small bodies in delivering water to planets around white dwarfs, and the further testing of fast radio burst progenitor models all await future work. By continuing to refine both our theories and our computational tools, along with more observations, we move closer to answering the questions central to this thesis.

6.1 Future Research Directions

Much remains to be done on the topics of this thesis¹.

In Chapter 2, we assumed a Solar system-like Oort cloud around other stars, though with varying density profile powerlaw indexes. However, with the wide-range of planetary system architecture and no observational detections of exo-Oort clouds, it is imperative to study how Oort clouds around other stars evolve. Since Oort clouds are byproducts of planet formation and there are many diverse planetary configurations, exo-Oort clouds could be very different than the Solar Oort cloud. Studying this diversity is especially important in the upcoming few years, as observations with the Simons Observatory may reveal the existence of exo-Oort clouds around other stars through infrared excess. Understanding the dynamical formation and evolution of these Oort clouds over time would complement these detections (or even lack thereof). Furthermore, understanding if and how exo-Oort clouds are formed can inform us on the prevalence of Oort cloud pollution on white dwarfs.

In Chapter 3, we developed numerical methods that are capable of quickly studying a massive number of test particles under the interactions with planets and a central star. A direction for future research here is applying this method to the need for evolving Oort cloud structures as the central star evolves from protostar to white dwarf. Performing a large number of simulations with the fast numerical methods will allow us to study more systems than before. In addition, the adaptive timestep scheme developed can be improved. It is always possible to find a case where adaptive timestep fails, such as when a body is

¹This is not stated for my own future employment purposes.

under multiple gravitational forces but they may cancel to be near zero. This can be a problem as the adaptive timestep might stall.

In Chapter 4, we must note that we assumed a radio-emission mechanism that is previously analytically developed. It remains necessary to verify this mechanism with simulations to further understand how the radiation is emitted and its characteristics. Furthermore, additional observations and localisations of fast radio bursts can falsify the proposed radiation progenitor mechanism.

In Chapter 5, we developed a numerical method that is capable of integrating all cometary orbits, even the most eccentric Oort cloud comets. However, to properly study Oort cloud volatile content will require a statistical approach. That is, multiple Oort cloud objects at a semi-major axis will need to be simulated because they are beyond the adiabatic limit. Thus, we plan to extend our work to sample over Oort cloud orbits to investigate how the Solar Oort cloud volatile content evolves over time. This will be an important to verify our previous assumption that exo-Oort clouds are pristine reservoirs of volatiles.

Beyond the specific scopes of each chapter, since comets are fossilised remnants of protoplanetary disc, studying their composition by using polluted white dwarf spectra as cosmic spectrometers give insights into the composition of early planetary systems. Likewise, indirect inference on the size distribution of comets in the Universe potentially through fast radio bursts could shed light into the physics of streaming instability. In addition, the questions of comets in evolved stellar systems can have implications on the detection of water, volatiles and potentially life on white dwarf exoplanets. Constraining where water and volatiles rich comets may occur and how they collide with planets around white dwarfs might allow us to predict the rate at which planets around white dwarfs are “re-watered” by comets. This could grant a planet like Earth a second chance for life, after the highly luminous post-main sequence star ablates much of the surface water.



I TE hujus laboriosæ Methodi pertæfum fuerit, jure mei te mifereat, qui eam ad minimum septuagies ivi cum plurima temporis jactura, & mirari defines hunc quintum jam annum abire...

If the wearisome method has filled you with loathing, it should more properly fill you with compassion for me, as I have gone through it at least seventy times at the expense of a great deal of time, and you will cease to wonder that the fifth year has now gone by...

Johannes Kepler, *Astronomia Nova* (1609)
translated by Donahue

Bibliography

- Aarseth, S. J. 1963, MNRAS, 126, 223, doi: [10.1093/mnras/126.3.223](https://doi.org/10.1093/mnras/126.3.223)
- . 1985, in Multiple Time Scales, ed. J. Brackbill & B. Cohen (Academic Press), 377–418
- Aarseth, S. J., Henon, M., & Wielen, R. 1974, A&A, 37, 183
- Akiba, T., McIntyre, S., & Madigan, A.-M. 2024, ApJ, 966, L4, doi: [10.3847/2041-8213/ad394c](https://doi.org/10.3847/2041-8213/ad394c)
- Alcock, C., Fristrom, C. C., & Siegelman, R. 1986, ApJ, 302, 462, doi: [10.1086/164005](https://doi.org/10.1086/164005)
- Ambartsumian, V. A. 1937, Azh, 14, 207
- Andama, G., Mah, J., & Bitsch, B. 2024, A&A, 683, A118, doi: [10.1051/0004-6361/202348899](https://doi.org/10.1051/0004-6361/202348899)
- Andrews, S. M., Huang, J., Pérez, L. M., et al. 2018, ApJ, 869, L41, doi: [10.3847/2041-8213/aaf741](https://doi.org/10.3847/2041-8213/aaf741)
- Armitage, P. J. 2007, arXiv e-prints, astro, doi: [10.48550/arXiv.astro-ph/0701485](https://doi.org/10.48550/arXiv.astro-ph/0701485)
- Asphaug, E., & Benz, W. 1994, Nature, 370, 120, doi: [10.1038/370120a0](https://doi.org/10.1038/370120a0)
- Attree, N., Groussin, O., Jorda, L., et al. 2018, A&A, 611, A33, doi: [10.1051/0004-6361/201732155](https://doi.org/10.1051/0004-6361/201732155)
- Bagchi, M. 2017, ApJ, 838, L16, doi: [10.3847/2041-8213/aa65c9](https://doi.org/10.3847/2041-8213/aa65c9)
- Belczynski, K., & Taam, R. E. 2008, ApJ, 685, 400, doi: [10.1086/590551](https://doi.org/10.1086/590551)
- Bell Burnell, J. 2017, Nature Astronomy, 1, 831, doi: [10.1038/s41550-017-0323-x](https://doi.org/10.1038/s41550-017-0323-x)
- Bhandari, S., Sadler, E. M., Prochaska, J. X., et al. 2020, ApJ, 895, L37, doi: [10.3847/2041-8213/ab672e](https://doi.org/10.3847/2041-8213/ab672e)
- Blackman, J. W., Beaulieu, J. P., Bennett, D. P., et al. 2021, Nature, 598, 272, doi: [10.1038/s41586-021-03869-6](https://doi.org/10.1038/s41586-021-03869-6)

- Blanton, M. R., Hogg, D. W., Bahcall, N. A., et al. 2003, ApJ, 592, 819, doi: [10.1086/375776](https://doi.org/10.1086/375776)
- Blouin, S., & Xu, S. 2022, MNRAS, 510, 1059, doi: [10.1093/mnras/stab3446](https://doi.org/10.1093/mnras/stab3446)
- Bochenek, C. D., Ravi, V., Belov, K. V., et al. 2020, Nature, 587, 59, doi: [10.1038/s41586-020-2872-x](https://doi.org/10.1038/s41586-020-2872-x)
- Bockelée-Morvan, D., Crovisier, J., Mumma, M. J., & Weaver, H. A. 2004, in Comets II, ed. M. C. Festou, H. U. Keller, & H. A. Weaver, 391
- Boe, B., Jedicke, R., Meech, K. J., et al. 2019, Icarus, 333, 252, doi: [10.1016/j.icarus.2019.05.034](https://doi.org/10.1016/j.icarus.2019.05.034)
- Bonsor, A., & Veras, D. 2015, MNRAS, 454, 53, doi: [10.1093/mnras/stv1913](https://doi.org/10.1093/mnras/stv1913)
- Boss, A. P. 1994, Icarus, 107, 422, doi: [10.1006/icar.1994.1035](https://doi.org/10.1006/icar.1994.1035)
- Bouvard, A. 1821, Tables astronomiques publiees par le Bureau des Longitudes de France
- Brasser, R., Higuchi, A., & Kaib, N. 2010, A&A, 516, A72, doi: [10.1051/0004-6361/201014275](https://doi.org/10.1051/0004-6361/201014275)
- Britt, D. T., Consolmagno, G. J., & Merline, W. J. 2006, in 37th Annual Lunar and Planetary Science Conference, ed. S. Mackwell & E. Stansbery, Lunar and Planetary Science Conference, 2214
- Brook, P. R., Karastergiou, A., Buchner, S., et al. 2014, ApJ, 780, L31, doi: [10.1088/2041-8205/780/2/L31](https://doi.org/10.1088/2041-8205/780/2/L31)
- Brouwer, D. 1937, AJ, 46, 149, doi: [10.1086/105423](https://doi.org/10.1086/105423)
- Brouwers, M. G., Bonsor, A., & Malamud, U. 2023a, MNRAS, 519, 2646, doi: [10.1093/mnras/stac3316](https://doi.org/10.1093/mnras/stac3316)
- Brouwers, M. G., Buchan, A. M., Bonsor, A., et al. 2023b, MNRAS, 519, 2663, doi: [10.1093/mnras/stac3317](https://doi.org/10.1093/mnras/stac3317)
- Browne, E., Firestone, R. B., & Virginia, S. S. 1986, Table of Radioactive Isotopes (New York; Wiley)
- Caiazzo, I., & Heyl, J. S. 2017, MNRAS, 469, 2750, doi: [10.1093/mnras/stx1036](https://doi.org/10.1093/mnras/stx1036)
- Carmichael, R. S. 1984, CRC handbook of physical properties of rocks. Volume III (CRC Press)
- Chatterjee, S., Vlemmings, W. H. T., Brisken, W. F., et al. 2005, ApJ, 630, L61, doi: [10.1086/491701](https://doi.org/10.1086/491701)

- Chen, J. H., Jia, X. D., Dong, X. F., & Wang, F. Y. 2024, ApJ, 973, L54, doi: [10.3847/2041-8213/ad7b39](https://doi.org/10.3847/2041-8213/ad7b39)
- CHIME/FRB Collaboration, Andersen, B. C., Bandura, K. M., et al. 2020, Nature, 587, 54, doi: [10.1038/s41586-020-2863-y](https://doi.org/10.1038/s41586-020-2863-y)
- CHIME/FRB Collaboration, Amiri, M., Andersen, B. C., et al. 2021, ApJS, 257, 59, doi: [10.3847/1538-4365/ac33ab](https://doi.org/10.3847/1538-4365/ac33ab)
- Choi, J., Dotter, A., Conroy, C., et al. 2016, ApJ, 823, 102, doi: [10.3847/0004-637X/823/2/102](https://doi.org/10.3847/0004-637X/823/2/102)
- Choi, Y.-J., Cohen, M., Merk, R., & Prialnik, D. 2002, Icarus, 160, 300, doi: [10.1006/icar.2002.6976](https://doi.org/10.1006/icar.2002.6976)
- Cohen, C. J., & Hubbard, E. C. 1965, AJ, 70, 10, doi: [10.1086/109674](https://doi.org/10.1086/109674)
- Cohen, C. J., Hubbard, E. C., & Oesterwinter, C. 1973, Celestial Mechanics, 7, 438, doi: [10.1007/BF01227509](https://doi.org/10.1007/BF01227509)
- Colgate, S. A., & Petschek, A. G. 1981, ApJ, 248, 771, doi: [10.1086/159201](https://doi.org/10.1086/159201)
- Columba, G., Danielski, C., Dorozsmai, A., Toonen, S., & Lopez Puertas, M. 2023, A&A, 675, A156, doi: [10.1051/0004-6361/202345843](https://doi.org/10.1051/0004-6361/202345843)
- Ćuk, M. 2018, ApJ, 852, L15, doi: [10.3847/2041-8213/aaa3db](https://doi.org/10.3847/2041-8213/aaa3db)
- Cunningham, T., Wheatley, P. J., Tremblay, P.-E., et al. 2022, Nature, 602, 219, doi: [10.1038/s41586-021-04300-w](https://doi.org/10.1038/s41586-021-04300-w)
- Dai, Z. G. 2020, ApJ, 897, L40, doi: [10.3847/2041-8213/aba11b](https://doi.org/10.3847/2041-8213/aba11b)
- Dai, Z. G., Wang, J. S., Wu, X. F., & Huang, Y. F. 2016, ApJ, 829, 27, doi: [10.3847/0004-637X/829/1/27](https://doi.org/10.3847/0004-637X/829/1/27)
- Danielski, C., & Tamanini, N. 2020, International Journal of Modern Physics D, 29, 2043007, doi: [10.1142/S0218271820430075](https://doi.org/10.1142/S0218271820430075)
- Davidsson, B. J. R. 2021, MNRAS, 505, 5654, doi: [10.1093/mnras/stab1593](https://doi.org/10.1093/mnras/stab1593)
- De Sanctis, M. C., Capria, M. T., & Coradini, A. 2001, AJ, 121, 2792, doi: [10.1086/320385](https://doi.org/10.1086/320385)
- Debes, J. H., & Sigurdsson, S. 2002, ApJ, 572, 556, doi: [10.1086/340291](https://doi.org/10.1086/340291)
- Debes, J. H., Walsh, K. J., & Stark, C. 2012, ApJ, 747, 148, doi: [10.1088/0004-637X/747/2/148](https://doi.org/10.1088/0004-637X/747/2/148)
- Deng, C., Huang, Y.-F., Du, C., Wang, P., & Dai, Z.-G. 2024, ApJ, 974, 215, doi: [10.3847/1538-4357/ad7256](https://doi.org/10.3847/1538-4357/ad7256)

- Do, A., Tucker, M. A., & Tonry, J. 2018, ApJ, 855, L10, doi: [10.3847/2041-8213/aaae67](https://doi.org/10.3847/2041-8213/aaae67)
- Doner, A., Horányi, M., Bagenal, F., et al. 2024, ApJ, 961, L38, doi: [10.3847/2041-8213/ad18b0](https://doi.org/10.3847/2041-8213/ad18b0)
- Dotter, A. 2016, ApJS, 222, 8, doi: [10.3847/0067-0049/222/1/8](https://doi.org/10.3847/0067-0049/222/1/8)
- Doyle, A. E., Desch, S. J., & Young, E. D. 2021, ApJ, 907, L35, doi: [10.3847/2041-8213/abd9ba](https://doi.org/10.3847/2041-8213/abd9ba)
- Doyle, A. E., Young, E. D., Klein, B., Zuckerman, B., & Schlichting, H. E. 2019, Science, 366, 356, doi: [10.1126/science.aax3901](https://doi.org/10.1126/science.aax3901)
- Duncan, M., Quinn, T., & Tremaine, S. 1987, AJ, 94, 1330, doi: [10.1086/114571](https://doi.org/10.1086/114571)
- Eckert, W. J. 1951, AJ, 56, 38, doi: [10.1086/106487](https://doi.org/10.1086/106487)
- Einstein, A. 1915, Sitzungsberichte der Königlich Preußischen Akademie der Wissenschaften, 844
- . 1916, Sitzungsberichte der Königlich Preussischen Akademie der Wissenschaften, 688
- El-Badry, K., & Rix, H.-W. 2018, MNRAS, 480, 4884, doi: [10.1093/mnras/sty2186](https://doi.org/10.1093/mnras/sty2186)
- Ellsworth, K., & Schubert, G. 1983, Icarus, 54, 490, doi: [10.1016/0019-1035\(83\)90242-7](https://doi.org/10.1016/0019-1035(83)90242-7)
- Elsila, J. E., Glavin, D. P., & Dworkin, J. P. 2009, Meteoric & Planetary Science, 44, 1323, doi: [10.1111/j.1945-5100.2009.tb01224.x](https://doi.org/10.1111/j.1945-5100.2009.tb01224.x)
- Euler, L. 1768, *Institutiones calculi integralis* (Lipsiae Et Berolini)
- Everhart, E. 1985, in Dynamics of Comets: Their Origin and Evolution, Proceedings of IAU Colloq. 83, held in Rome, Italy, June 11-15, 1984. Edited by Andrea Carusi and Giovanni B. Valsecchi. Dordrecht: Reidel, Astrophysics and Space Science Library. Volume 115, 1985, p.185, ed. A. Carusi & G. B. Valsecchi, 185
- Farago, F., & Laskar, J. 2010, MNRAS, 401, 1189, doi: [10.1111/j.1365-2966.2009.15711.x](https://doi.org/10.1111/j.1365-2966.2009.15711.x)
- Farihi, J., Gänsicke, B. T., & Koester, D. 2013, Science, 342, 218, doi: [10.1126/science.1239447](https://doi.org/10.1126/science.1239447)
- Flynn, G. J., Consolmagno, G. J., Brown, P., & Macke, R. J. 2018, Chemie der Erde / Geochemistry, 78, 269, doi: [10.1016/j.chemer.2017.04.002](https://doi.org/10.1016/j.chemer.2017.04.002)
- Forbes, J. C., & Loeb, A. 2019, ApJ, 875, L23, doi: [10.3847/2041-8213/ab158f](https://doi.org/10.3847/2041-8213/ab158f)

- Fraga, E. S., Kurkela, A., & Vuorinen, A. 2016, European Physical Journal A, 52, 49, doi: [10.1140/epja/i2016-16049-6](https://doi.org/10.1140/epja/i2016-16049-6)
- Francis, P. J. 2005, ApJ, 635, 1348, doi: [10.1086/497684](https://doi.org/10.1086/497684)
- Fraser, W. C., Bannister, M. T., Pike, R. E., et al. 2017, Nature Astronomy, 1, 0088, doi: [10.1038/s41550-017-0088](https://doi.org/10.1038/s41550-017-0088)
- Gänsicke, B. T., Schreiber, M. R., Toloza, O., et al. 2019, Nature, 576, 61, doi: [10.1038/s41586-019-1789-8](https://doi.org/10.1038/s41586-019-1789-8)
- Geng, J. J., & Huang, Y. F. 2015, ApJ, 809, 24, doi: [10.1088/0004-637X/809/1/24](https://doi.org/10.1088/0004-637X/809/1/24)
- GentileFusillo, N. P., Gänsicke, B. T., Farihi, J., et al. 2017, MNRAS, 468, 971, doi: [10.1093/mnras/stx468](https://doi.org/10.1093/mnras/stx468)
- Gkotsinas, A., Guilbert-Lepoutre, A., Raymond, S. N., & Nesvorný, D. 2022, ApJ, 928, 43, doi: [10.3847/1538-4357/ac54ac](https://doi.org/10.3847/1538-4357/ac54ac)
- Gkotsinas, A., Nesvorný, D., Guilbert-Lepoutre, A., Raymond, S. N., & Kaib, N. 2024, PSJ, 5, 243, doi: [10.3847/PSJ/ad7f4e](https://doi.org/10.3847/PSJ/ad7f4e)
- Gladman, B. J., Davis, D. R., Neese, C., et al. 2009, Icarus, 202, 104, doi: [10.1016/j.icarus.2009.02.012](https://doi.org/10.1016/j.icarus.2009.02.012)
- Gomes, R., Levison, H. F., Tsiganis, K., & Morbidelli, A. 2005, Nature, 435, 466, doi: [10.1038/nature03676](https://doi.org/10.1038/nature03676)
- Gordon, A. C., Fong, W.-f., Kilpatrick, C. D., et al. 2023, ApJ, 954, 80, doi: [10.3847/1538-4357/ace5aa](https://doi.org/10.3847/1538-4357/ace5aa)
- Greenberg, J. M., Mizutani, H., & Yamamoto, T. 1995, A&A, 295, L35
- Guilbert-Lepoutre, A. 2014, Icarus, 231, 232, doi: [10.1016/j.icarus.2013.12.014](https://doi.org/10.1016/j.icarus.2013.12.014)
- Guilbert-Lepoutre, A., Lasue, J., Federico, C., et al. 2011, A&A, 529, A71, doi: [10.1051/0004-6361/201014194](https://doi.org/10.1051/0004-6361/201014194)
- Gundlach, B., & Blum, J. 2012, Icarus, 219, 618, doi: [10.1016/j.icarus.2012.03.013](https://doi.org/10.1016/j.icarus.2012.03.013)
- Hadden, S., & Tremaine, S. 2024, MNRAS, 527, 3054, doi: [10.1093/mnras/stad3478](https://doi.org/10.1093/mnras/stad3478)
- Hahn, J. M., & Malhotra, R. 1999, AJ, 117, 3041, doi: [10.1086/300891](https://doi.org/10.1086/300891)
- Hairer, E., Lubich, C., & Wanner, G. 2006, Geometric numerical integration: structure-preserving algorithms for ordinary differential equations, Vol. 31 (Springer Science & Business Media)

- Hairer, E., & Wanner, G. 1999, Journal of Computational and Applied Mathematics, 111, 93, doi: [https://doi.org/10.1016/S0377-0427\(99\)00134-X](https://doi.org/10.1016/S0377-0427(99)00134-X)
- Halley, E. 1705, Synopsis of the Astronomy of Comets (Printed for John Senex)
- Hamilton, W. 1833, On a General Method of Expressing the Paths of Light, & of the Planets, by the Coefficients of a Characteristic Function (Printed by P.D. Hardy; Dublin)
- Harrison, J. H. D., Shorttle, O., & Bonsor, A. 2021, Earth and Planetary Science Letters, 554, 116694, doi: [10.1016/j.epsl.2020.116694](https://doi.org/10.1016/j.epsl.2020.116694)
- Hashimoto, T., Goto, T., On, A. Y. L., et al. 2020a, MNRAS, 498, 3927, doi: [10.1093/mnras/staa2490](https://doi.org/10.1093/mnras/staa2490)
- . 2020b, MNRAS, 497, 4107, doi: [10.1093/mnras/staa2238](https://doi.org/10.1093/mnras/staa2238)
- Hashimoto, T., Goto, T., Chen, B. H., et al. 2022, MNRAS, 511, 1961, doi: [10.1093/mnras/stac065](https://doi.org/10.1093/mnras/stac065)
- Heger, A., Fryer, C. L., Woosley, S. E., Langer, N., & Hartmann, D. H. 2003, ApJ, 591, 288, doi: [10.1086/375341](https://doi.org/10.1086/375341)
- Heisler, J. 1990, Icarus, 88, 104, doi: [10.1016/0019-1035\(90\)90180-H](https://doi.org/10.1016/0019-1035(90)90180-H)
- Heisler, J., & Tremaine, S. 1986, Icarus, 65, 13, doi: [10.1016/0019-1035\(86\)90060-6](https://doi.org/10.1016/0019-1035(86)90060-6)
- Higuchi, A., & Kokubo, E. 2015, AJ, 150, 26, doi: [10.1088/0004-6256/150/1/26](https://doi.org/10.1088/0004-6256/150/1/26)
- Hobbs, G., Lorimer, D. R., Lyne, A. G., & Kramer, M. 2005, MNRAS, 360, 974, doi: [10.1111/j.1365-2966.2005.09087.x](https://doi.org/10.1111/j.1365-2966.2005.09087.x)
- Holman, M. J., & Wiegert, P. A. 1999, AJ, 117, 621, doi: [10.1086/300695](https://doi.org/10.1086/300695)
- Holmberg, J., & Flynn, C. 2000, MNRAS, 313, 209, doi: [10.1046/j.1365-8711.2000.02905.x](https://doi.org/10.1046/j.1365-8711.2000.02905.x)
- Hopkins, M. J., Bannister, M. T., & Lintott, C. 2024, arXiv e-prints, arXiv:2402.04904, doi: [10.48550/arXiv.2402.04904](https://doi.org/10.48550/arXiv.2402.04904)
- Hopkins, M. J., Lintott, C., Bannister, M. T., Mackereth, J. T., & Forbes, J. C. 2023, AJ, 166, 241, doi: [10.3847/1538-3881/ad03e6](https://doi.org/10.3847/1538-3881/ad03e6)
- Hoskin, M. J., Toloza, O., Gänsicke, B. T., et al. 2020, MNRAS, 499, 171, doi: [10.1093/mnras/staa2717](https://doi.org/10.1093/mnras/staa2717)
- Huebner, W. F., Benkhoff, J., Capria, M.-T., et al., eds. 2006, Heat and Gas Diffusion in Comet Nuclei

- Hui, M.-T., Ye, Q.-Z., Föhring, D., Hung, D., & Tholen, D. J. 2020, AJ, 160, 92, doi: [10.3847/1538-3881/ab9df8](https://doi.org/10.3847/1538-3881/ab9df8)
- Inno, L., Scuderi, M., Bertini, I., et al. 2025, Icarus, 429, 116443, doi: [10.1016/j.icarus.2024.116443](https://doi.org/10.1016/j.icarus.2024.116443)
- Jeans, J. H. 1919, MNRAS, 79, 408, doi: [10.1093/mnras/79.6.408](https://doi.org/10.1093/mnras/79.6.408)
- Jenniskens, P., Fries, M. D., Yin, Q.-Z., et al. 2012, Science, 338, 1583, doi: [10.1126/science.1227163](https://doi.org/10.1126/science.1227163)
- Jewitt, D., Luu, J., & Li, J. 2025, AJ, 169, 105, doi: [10.3847/1538-3881/ada3c0](https://doi.org/10.3847/1538-3881/ada3c0)
- Jewitt, D., Luu, J., Rajagopal, J., et al. 2017, ApJ, 850, L36, doi: [10.3847/2041-8213/aa9b2f](https://doi.org/10.3847/2041-8213/aa9b2f)
- Jewitt, D., & Seligman, D. Z. 2023, ARA&A, 61, 197, doi: [10.1146/annurev-astro-071221-054221](https://doi.org/10.1146/annurev-astro-071221-054221)
- Johnson, T. M., Klein, B. L., Koester, D., et al. 2022, ApJ, 941, 113, doi: [10.3847/1538-4357/aca089](https://doi.org/10.3847/1538-4357/aca089)
- Jura, M. 2006, ApJ, 653, 613, doi: [10.1086/508738](https://doi.org/10.1086/508738)
- Jura, M., & Xu, S. 2010, AJ, 140, 1129, doi: [10.1088/0004-6256/140/5/1129](https://doi.org/10.1088/0004-6256/140/5/1129)
- . 2012, AJ, 143, 6, doi: [10.1088/0004-6256/143/1/6](https://doi.org/10.1088/0004-6256/143/1/6)
- Jura, M., & Young, E. D. 2014, Annual Review of Earth and Planetary Sciences, 42, 45, doi: [10.1146/annurev-earth-060313-054740](https://doi.org/10.1146/annurev-earth-060313-054740)
- Kahan, W. 1965, Commun. ACM, 8, 40, doi: [10.1145/363707.363723](https://doi.org/10.1145/363707.363723)
- Kaib, N. A., & Quinn, T. 2009, Science, 325, 1234, doi: [10.1126/science.1172676](https://doi.org/10.1126/science.1172676)
- Kaib, N. A., Roškar, R., & Quinn, T. 2011, Icarus, 215, 491, doi: [10.1016/j.icarus.2011.07.037](https://doi.org/10.1016/j.icarus.2011.07.037)
- Kaib, N. A., & Volk, K. 2022, arXiv e-prints, arXiv:2206.00010, doi: [10.48550/arXiv.2206.00010](https://doi.org/10.48550/arXiv.2206.00010)
- Kepler, J. 1609, Astronomia Nova (G. Voegelinus)
- Kirsten, F., Ould-Boukattine, O. S., Herrmann, W., et al. 2024, Nature Astronomy, 8, 337, doi: [10.1038/s41550-023-02153-z](https://doi.org/10.1038/s41550-023-02153-z)
- Klein, B. L., Doyle, A. E., Zuckerman, B., et al. 2021, ApJ, 914, 61, doi: [10.3847/1538-4357/abe40b](https://doi.org/10.3847/1538-4357/abe40b)

- Klinger, J. 1975, Journal of Glaciology, 14, 517, doi: [10.1017/S0022143000022000](https://doi.org/10.1017/S0022143000022000)
- . 1980, Science, 209, 271, doi: [10.1126/science.209.4453.271](https://doi.org/10.1126/science.209.4453.271)
- . 1981, Icarus, 47, 320, doi: [10.1016/0019-1035\(81\)90179-2](https://doi.org/10.1016/0019-1035(81)90179-2)
- Koester, D., Gänsicke, B. T., & Farihi, J. 2014, A&A, 566, A34, doi: [10.1051/0004-6361/201423691](https://doi.org/10.1051/0004-6361/201423691)
- Korol, V., Rossi, E. M., Groot, P. J., et al. 2017, MNRAS, 470, 1894, doi: [10.1093/mnras/stx1285](https://doi.org/10.1093/mnras/stx1285)
- Kostov, V. B., Moore, K., Tamayo, D., Jayawardhana, R., & Rinehart, S. A. 2016, ApJ, 832, 183, doi: [10.3847/0004-637X/832/2/183](https://doi.org/10.3847/0004-637X/832/2/183)
- Kozai, Y. 1962, AJ, 67, 591, doi: [10.1086/108790](https://doi.org/10.1086/108790)
- Kroupa, P. 2001, MNRAS, 322, 231, doi: [10.1046/j.1365-8711.2001.04022.x](https://doi.org/10.1046/j.1365-8711.2001.04022.x)
- Kutta, W. 1901, Zeitschrift für Angewandte Mathematik und Physik, 46, 435. [https://archive.org/details/zeitschriftfrma12runggoog/page/434\(mode/2up\)](https://archive.org/details/zeitschriftfrma12runggoog/page/434(mode/2up))
- Lattimer, J. M., & Prakash, M. 2004, Science, 304, 536, doi: [10.1126/science.1090720](https://doi.org/10.1126/science.1090720)
- Lawler, S. M., Shankman, C., Kavelaars, J. J., et al. 2018, AJ, 155, 197, doi: [10.3847/1538-3881/aab8ff](https://doi.org/10.3847/1538-3881/aab8ff)
- Le Verrier, U. J. J. 1843, Journal de mathématiques pures et appliquées, 8, 273
- . 1846, Astronomische Nachrichten, 25, 65
- Ledda, S., Danielski, C., & Turrini, D. 2023, A&A, 675, A184, doi: [10.1051/0004-6361/202245827](https://doi.org/10.1051/0004-6361/202245827)
- Levine, W. G., Taylor, A. G., Seligman, D. Z., et al. 2023, PSJ, 4, 124, doi: [10.3847/PSJ/acdf58](https://doi.org/10.3847/PSJ/acdf58)
- Levy, D. H. 1998, Space Sci. Rev., 85, 523
- Li, Y., Bonsor, A., & Shorttle, O. 2024, MNRAS, 527, 1014, doi: [10.1093/mnras/stad3131](https://doi.org/10.1093/mnras/stad3131)
- Licquia, T. C., & Newman, J. A. 2015, ApJ, 806, 96, doi: [10.1088/0004-637X/806/1/96](https://doi.org/10.1088/0004-637X/806/1/96)
- Lidov, M. L. 1962, Planet. Space Sci., 9, 719, doi: [10.1016/0032-0633\(62\)90129-0](https://doi.org/10.1016/0032-0633(62)90129-0)
- Lightman, A. P., & Shapiro, S. L. 1977, ApJ, 211, 244, doi: [10.1086/154925](https://doi.org/10.1086/154925)
- Lin, H.-N., Li, X.-Y., & Zou, R. 2024, ApJ, 969, 123, doi: [10.3847/1538-4357/ad5310](https://doi.org/10.3847/1538-4357/ad5310)
- Lin, H.-N., & Zou, R. 2024, ApJ, 962, 73, doi: [10.3847/1538-4357/ad1b4f](https://doi.org/10.3847/1538-4357/ad1b4f)

- Lintott, C. J., Schawinski, K., Slosar, A., et al. 2008, MNRAS, 389, 1179, doi: [10.1111/j.1365-2966.2008.13689.x](https://doi.org/10.1111/j.1365-2966.2008.13689.x)
- Lorimer, D. R., Bailes, M., McLaughlin, M. A., Narkevic, D. J., & Crawford, F. 2007, Science, 318, 777, doi: [10.1126/science.1147532](https://doi.org/10.1126/science.1147532)
- Luhman, K. L., Burgasser, A. J., & Bochanski, J. J. 2011, ApJ, 730, L9, doi: [10.1088/2041-8205/730/1/L9](https://doi.org/10.1088/2041-8205/730/1/L9)
- Lyne, A. G., & Lorimer, D. R. 1994, Nature, 369, 127, doi: [10.1038/369127a0](https://doi.org/10.1038/369127a0)
- Madau, P., & Dickinson, M. 2014, ARA&A, 52, 415, doi: [10.1146/annurev-astro-081811-125615](https://doi.org/10.1146/annurev-astro-081811-125615)
- Makino, J. 1991, ApJ, 369, 200, doi: [10.1086/169751](https://doi.org/10.1086/169751)
- Makino, J., & Aarseth, S. J. 1992, PASJ, 44, 141
- Malamud, U., & Perets, H. B. 2016, ApJ, 832, 160, doi: [10.3847/0004-637X/832/2/160](https://doi.org/10.3847/0004-637X/832/2/160)
- . 2017a, ApJ, 842, 67, doi: [10.3847/1538-4357/aa7055](https://doi.org/10.3847/1538-4357/aa7055)
- . 2017b, ApJ, 849, 8, doi: [10.3847/1538-4357/aa8df5](https://doi.org/10.3847/1538-4357/aa8df5)
- Maldonado, R. F., Villaver, E., Mustill, A. J., Chavez, M., & Bertone, E. 2020, MNRAS, 499, 1854, doi: [10.1093/mnras/staa2946](https://doi.org/10.1093/mnras/staa2946)
- Mannings, A. G., Fong, W.-f., Simha, S., et al. 2021, ApJ, 917, 75, doi: [10.3847/1538-4357/abff56](https://doi.org/10.3847/1538-4357/abff56)
- Margalit, B., Berger, E., & Metzger, B. D. 2019, ApJ, 886, 110, doi: [10.3847/1538-4357/ab4c31](https://doi.org/10.3847/1538-4357/ab4c31)
- Margot, J. L., Nolan, M. C., Benner, L. A. M., et al. 2002, Science, 296, 1445, doi: [10.1126/science.1072094](https://doi.org/10.1126/science.1072094)
- Mayor, M., & Queloz, D. 1995, Nature, 378, 355, doi: [10.1038/378355a0](https://doi.org/10.1038/378355a0)
- McDonald, C. H., & Veras, D. 2023, MNRAS, 520, 4009, doi: [10.1093/mnras/stad382](https://doi.org/10.1093/mnras/stad382)
- McGlynn, T. A., & Chapman, R. D. 1989, ApJ, 346, L105, doi: [10.1086/185590](https://doi.org/10.1086/185590)
- McKee, C. F., Parravano, A., & Hollenbach, D. J. 2015, ApJ, 814, 13, doi: [10.1088/0004-637X/814/1/13](https://doi.org/10.1088/0004-637X/814/1/13)
- Mekler, Y., Prialnik, D., & Podolak, M. 1990, ApJ, 356, 682, doi: [10.1086/168875](https://doi.org/10.1086/168875)
- Metzger, B. D., Margalit, B., & Sironi, L. 2019, MNRAS, 485, 4091, doi: [10.1093/mnras/stz700](https://doi.org/10.1093/mnras/stz700)

- Michilli, D., Bhardwaj, M., Brar, C., et al. 2023, ApJ, 950, 134, doi: [10.3847/1538-4357/accf89](https://doi.org/10.3847/1538-4357/accf89)
- Miller, M. C., Lamb, F. K., Dittmann, A. J., et al. 2021, ApJ, 918, L28, doi: [10.3847/2041-8213/ac089b](https://doi.org/10.3847/2041-8213/ac089b)
- Moe, M., & Di Stefano, R. 2017, ApJS, 230, 15, doi: [10.3847/1538-4365/aa6fb6](https://doi.org/10.3847/1538-4365/aa6fb6)
- Mondal, T. 2021, ApJ, 913, L12, doi: [10.3847/2041-8213/abfb75](https://doi.org/10.3847/2041-8213/abfb75)
- Morbidelli, A., Levison, H. F., Tsiganis, K., & Gomes, R. 2005, Nature, 435, 462, doi: [10.1038/nature03540](https://doi.org/10.1038/nature03540)
- Morbidelli, A., & Nesvorný, D. 2020, in The Trans-Neptunian Solar System, ed. D. Prialnik, M. A. Barucci, & L. Young, 25–59, doi: [10.1016/B978-0-12-816490-7.00002-3](https://doi.org/10.1016/B978-0-12-816490-7.00002-3)
- Mullally, S. E., Debes, J., Cracraft, M., et al. 2024, arXiv e-prints, arXiv:2401.13153, doi: [10.48550/arXiv.2401.13153](https://doi.org/10.48550/arXiv.2401.13153)
- Mustill, A. J., Veras, D., & Villaver, E. 2014, MNRAS, 437, 1404, doi: [10.1093/mnras/stt1973](https://doi.org/10.1093/mnras/stt1973)
- Nakano, S., Kobayashi, T., Meyer, E., et al. 1993, IAU Circ., 5800, 1
- Newhall, X. X., Standish, E. M., & Williams, J. G. 1983, A&A, 125, 150
- Newton, I. 1687, Philosophiae Naturalis Principia Mathematica (Societatis Regiae)
- Nimmo, K., Pleunis, Z., Beniamini, P., et al. 2025, Nature, 637, 48, doi: [10.1038/s41586-024-08297-w](https://doi.org/10.1038/s41586-024-08297-w)
- Ninio Greenberg, A., Laufer, D., & Bar-Nun, A. 2017, MNRAS, 469, S517, doi: [10.1093/mnras/stx2017](https://doi.org/10.1093/mnras/stx2017)
- Nitadori, K., & Aarseth, S. J. 2012, MNRAS, 424, 545, doi: [10.1111/j.1365-2966.2012.21227.x](https://doi.org/10.1111/j.1365-2966.2012.21227.x)
- Obertas, A., Van Laerhoven, C., & Tamayo, D. 2017, Icarus, 293, 52, doi: [10.1016/j.icarus.2017.04.010](https://doi.org/10.1016/j.icarus.2017.04.010)
- O'Connor, C. E., Lai, D., & Seligman, D. Z. 2023, MNRAS, 524, 6181, doi: [10.1093/mnras/stad2281](https://doi.org/10.1093/mnras/stad2281)
- O'Connor, C. E., Teyssandier, J., & Lai, D. 2022, MNRAS, 513, 4178, doi: [10.1093/mnras/stac1189](https://doi.org/10.1093/mnras/stac1189)
- Okuya, A., Ida, S., Hyodo, R., & Okuzumi, S. 2023, MNRAS, 519, 1657, doi: [10.1093/mnras/stac3522](https://doi.org/10.1093/mnras/stac3522)

- Orosei, R., Capaccioni, F., Capria, M. T., et al. 1999, *Planet. Space Sci.*, 47, 839, doi: [10.1016/S0032-0633\(99\)00018-5](https://doi.org/10.1016/S0032-0633(99)00018-5)
- 'Oumuamua ISSI Team, Bannister, M. T., Bhandare, A., et al. 2019, *Nature Astronomy*, 3, 594, doi: [10.1038/s41550-019-0816-x](https://doi.org/10.1038/s41550-019-0816-x)
- Palacián, J. F., & Yanguas, P. 2006, *Celestial Mechanics and Dynamical Astronomy*, 95, 81, doi: [10.1007/s10569-006-9023-z](https://doi.org/10.1007/s10569-006-9023-z)
- Parriott, J., & Alcock, C. 1998, *ApJ*, 501, 357, doi: [10.1086/305802](https://doi.org/10.1086/305802)
- Peña-Asensio, E., Visuri, J., Trigo-Rodríguez, J. M., et al. 2024, *Icarus*, 408, 115844, doi: [10.1016/j.icarus.2023.115844](https://doi.org/10.1016/j.icarus.2023.115844)
- Petzold, L. 1983, *SIAM Journal on Scientific and Statistical Computing*, 4, 136, doi: [10.1137/0904010](https://doi.org/10.1137/0904010)
- Pfalzner, S., Aizpuru Vargas, L. L., Bhandare, A., & Veras, D. 2021, *A&A*, 651, A38, doi: [10.1051/0004-6361/202140587](https://doi.org/10.1051/0004-6361/202140587)
- Pham, D., Hopkins, M. J., Lintott, C., Bannister, M. T., & Rein, H. 2024a, *ApJ*, 977, 232, doi: [10.3847/1538-4357/ad932f](https://doi.org/10.3847/1538-4357/ad932f)
- Pham, D., & Rein, H. 2024, *MNRAS*, 530, 2526, doi: [10.1093/mnras/stae986](https://doi.org/10.1093/mnras/stae986)
- Pham, D., Rein, H., & Spiegel, D. S. 2024b, *The Open Journal of Astrophysics*, 7, 1, doi: [10.21105/astro.2401.02849](https://doi.org/10.21105/astro.2401.02849)
- Platts, E., Weltman, A., Walters, A., et al. 2019, *Phys. Rep.*, 821, 1, doi: [10.1016/j.physrep.2019.06.003](https://doi.org/10.1016/j.physrep.2019.06.003)
- Pleunis, Z., Good, D. C., Kaspi, V. M., et al. 2021, *ApJ*, 923, 1, doi: [10.3847/1538-4357/ac33ac](https://doi.org/10.3847/1538-4357/ac33ac)
- Pohl, L., & Britt, D. T. 2020, *Meteoritics & Planetary Science*, 55, 962, doi: [10.1111/maps.13449](https://doi.org/10.1111/maps.13449)
- Poon, M., Rein, H., & Pham, D. 2024, *The Open Journal of Astrophysics*, 7, 109, doi: [10.33232/001c.127130](https://doi.org/10.33232/001c.127130)
- Press, W. H., & Spergel, D. N. 1988, *ApJ*, 325, 715, doi: [10.1086/166042](https://doi.org/10.1086/166042)
- Prialnik, D. 1992, *ApJ*, 388, 196, doi: [10.1086/171143](https://doi.org/10.1086/171143)
- Prialnik, D., Benkhoff, J., & Podolak, M. 2004, in *Comets II*, ed. M. C. Festou, H. U. Keller, & H. A. Weaver (University of Arizona Press), 359

- Prialnik, D., Brosch, N., & Ianovici, D. 1995, MNRAS, 276, 1148, doi: [10.1093/mnras/276.4.1148](https://doi.org/10.1093/mnras/276.4.1148)
- Prialnik, D., & Jewitt, D. 2022, arXiv e-prints, arXiv:2209.05907, doi: [10.48550/arXiv.2209.05907](https://doi.org/10.48550/arXiv.2209.05907)
- Prialnik, D., & Merk, R. 2008, Icarus, 197, 211, doi: [10.1016/j.icarus.2008.03.024](https://doi.org/10.1016/j.icarus.2008.03.024)
- Putirka, K. D., & Xu, S. 2021, Nature Communications, 12, 6168, doi: [10.1038/s41467-021-26403-8](https://doi.org/10.1038/s41467-021-26403-8)
- Quirrenbach, A. 2022, Research Notes of the American Astronomical Society, 6, 56, doi: [10.3847/2515-5172/ac5f0d](https://doi.org/10.3847/2515-5172/ac5f0d)
- Raddi, R., Gänsicke, B. T., Koester, D., et al. 2015, MNRAS, 450, 2083, doi: [10.1093/mnras/stv701](https://doi.org/10.1093/mnras/stv701)
- Rafikov, R. R. 2011, ApJ, 732, L3, doi: [10.1088/2041-8205/732/1/L3](https://doi.org/10.1088/2041-8205/732/1/L3)
- Rein, H. 2011, ArXiv e-prints. <https://arxiv.org/abs/1106.1869>
- . 2012, MNRAS, 427, L21, doi: [10.1111/j.1745-3933.2012.01337.x](https://doi.org/10.1111/j.1745-3933.2012.01337.x)
- Rein, H., & Liu, S. F. 2012, A&A, 537, A128, doi: [10.1051/0004-6361/201118085](https://doi.org/10.1051/0004-6361/201118085)
- Rein, H., & Spiegel, D. S. 2015, MNRAS, 446, 1424, doi: [10.1093/mnras/stu2164](https://doi.org/10.1093/mnras/stu2164)
- Rein, H., & Tamayo, D. 2015, MNRAS, 452, 376
- Rogers, L. K., Bonsor, A., Xu, S., et al. 2024, MNRAS, 532, 3866, doi: [10.1093/mnras/stae1520](https://doi.org/10.1093/mnras/stae1520)
- Roy, A. E., Walker, I. W., Macdonald, A. J., et al. 1988, Vistas in Astronomy, 32, 95, doi: [10.1016/0083-6656\(88\)90399-6](https://doi.org/10.1016/0083-6656(88)90399-6)
- Runge, C. 1895, Mathematische Annalen, 46, 167. <http://eudml.org/doc/157756>
- Russell, H. W. 1935, Journal of the American Ceramic Society, 18, 1, doi: <https://doi.org/10.1111/j.1151-2916.1935.tb19340.x>
- Ryder, S. D., Bannister, K. W., Bhandari, S., et al. 2023, Science, 382, 294, doi: [10.1126/science.adf2678](https://doi.org/10.1126/science.adf2678)
- Sanderson, H., Bonsor, A., & Mustill, A. 2022, MNRAS, 517, 5835, doi: [10.1093/mnras/stac2867](https://doi.org/10.1093/mnras/stac2867)
- Sasselov, D. D., & Lecar, M. 2000, ApJ, 528, 995, doi: [10.1086/308209](https://doi.org/10.1086/308209)
- Scheeres, D. J. 2007, Icarus, 189, 370, doi: [10.1016/j.icarus.2007.02.015](https://doi.org/10.1016/j.icarus.2007.02.015)

- . 2018, Icarus, 304, 183, doi: [10.1016/j.icarus.2017.05.029](https://doi.org/10.1016/j.icarus.2017.05.029)
- Schmitt, B., Espinasse, S., Grim, R. J. A., Greenberg, J. M., & Klinger, J. 1989, in ESA Special Publication, Vol. 302, Physics and Mechanics of Cometary Materials, ed. J. J. Hunt & T. D. Guyenne, 65–69
- Schorghofer, N. 2008, ApJ, 682, 697, doi: [10.1086/588633](https://doi.org/10.1086/588633)
- . 2010, Icarus, 208, 598, doi: [10.1016/j.icarus.2010.03.022](https://doi.org/10.1016/j.icarus.2010.03.022)
- . 2016, Icarus, 276, 88, doi: [10.1016/j.icarus.2016.04.037](https://doi.org/10.1016/j.icarus.2016.04.037)
- Schörghofer, N., & Hsieh, H. H. 2018, Journal of Geophysical Research (Planets), 123, 2322, doi: [10.1029/2018JE005568](https://doi.org/10.1029/2018JE005568)
- Sefilian, A. A., Rafikov, R. R., & Wyatt, M. C. 2021, ApJ, 910, 13, doi: [10.3847/1538-4357/abda46](https://doi.org/10.3847/1538-4357/abda46)
- . 2023, ApJ, 954, 100, doi: [10.3847/1538-4357/ace68e](https://doi.org/10.3847/1538-4357/ace68e)
- Shannon, A., Jackson, A. P., Veras, D., & Wyatt, M. 2015, MNRAS, 446, 2059, doi: [10.1093/mnras/stu2267](https://doi.org/10.1093/mnras/stu2267)
- Shin, K., Masui, K. W., Bhardwaj, M., et al. 2023, ApJ, 944, 105, doi: [10.3847/1538-4357/acaf06](https://doi.org/10.3847/1538-4357/acaf06)
- Shoemaker, E. M., & Wolfe, R. F. 1984, in Lunar and Planetary Science Conference, Lunar and Planetary Science Conference, 780–781
- Shoshany, Y., Prialnik, D., & Podolak, M. 2002, Icarus, 157, 219, doi: [10.1006/icar.2002.6815](https://doi.org/10.1006/icar.2002.6815)
- Simon, J. B., Armitage, P. J., Li, R., & Youdin, A. N. 2016, ApJ, 822, 55, doi: [10.3847/0004-637X/822/1/55](https://doi.org/10.3847/0004-637X/822/1/55)
- Siraj, A., & Loeb, A. 2019, Research Notes of the American Astronomical Society, 3, 130, doi: [10.3847/2515-5172/ab43de](https://doi.org/10.3847/2515-5172/ab43de)
- Smallwood, J. L., Martin, R. G., Livio, M., & Lubow, S. H. 2018, MNRAS, 480, 57, doi: [10.1093/mnras/sty1819](https://doi.org/10.1093/mnras/sty1819)
- Smallwood, J. L., Martin, R. G., & Zhang, B. 2019, MNRAS, 485, 1367, doi: [10.1093/mnras/stz483](https://doi.org/10.1093/mnras/stz483)
- Steckloff, J. K., Lisse, C. M., Safrit, T. K., et al. 2021, Icarus, 356, 113998, doi: [10.1016/j.icarus.2020.113998](https://doi.org/10.1016/j.icarus.2020.113998)

- Stephan, A. P., Naoz, S., & Zuckerman, B. 2017, ApJ, 844, L16, doi: [10.3847/2041-8213/aa7cf3](https://doi.org/10.3847/2041-8213/aa7cf3)
- Stern, S. A. 1990, PASP, 102, 793, doi: [10.1086/132704](https://doi.org/10.1086/132704)
- Stone, N., Metzger, B. D., & Loeb, A. 2015, MNRAS, 448, 188, doi: [10.1093/mnras/stu2718](https://doi.org/10.1093/mnras/stu2718)
- Sweeney, D., Tuthill, P., Sharma, S., & Hirai, R. 2022, MNRAS, 516, 4971, doi: [10.1093/mnras/stac2092](https://doi.org/10.1093/mnras/stac2092)
- Tamanini, N., & Danielski, C. 2019, Nature Astronomy, 3, 858, doi: [10.1038/s41550-019-0807-y](https://doi.org/10.1038/s41550-019-0807-y)
- Tamayo, D., Rein, H., Shi, P., & Hernandez, D. M. 2020, Monthly Notices of the Royal Astronomical Society, 491, 2885, doi: [10.1093/mnras/stz2870](https://doi.org/10.1093/mnras/stz2870)
- Tancredi, G., Rickman, H., & Greenberg, J. M. 1994, A&A, 286, 659
- Tang, L., Lin, H.-N., & Li, X. 2023, Chinese Physics C, 47, 085105, doi: [10.1088/1674-1137/acda1c](https://doi.org/10.1088/1674-1137/acda1c)
- Teboul, O., Stone, N. C., & Ostriker, J. P. 2024, MNRAS, 527, 3094, doi: [10.1093/mnras/stad3301](https://doi.org/10.1093/mnras/stad3301)
- Thompson, C., Lyutikov, M., & Kulkarni, S. R. 2002, ApJ, 574, 332, doi: [10.1086/340586](https://doi.org/10.1086/340586)
- Thompson, J. F., Weatherill, N. P., & Soni, B. K. 1999, Handbook of grid generation (Boca Raton, Fla: CRC Press)
- Touma, J. R., Tremaine, S., & Kazandjian, M. V. 2009, MNRAS, 394, 1085, doi: [10.1111/j.1365-2966.2009.14409.x](https://doi.org/10.1111/j.1365-2966.2009.14409.x)
- Tremaine, S. 2003, AJ, 125, 894, doi: [10.1086/345963](https://doi.org/10.1086/345963)
- . 2023, Dynamics of Planetary Systems (Princeton University Press)
- Trierweiler, I. L., Doyle, A. E., Melis, C., Walsh, K. J., & Young, E. D. 2022, ApJ, 936, 30, doi: [10.3847/1538-4357/ac86d5](https://doi.org/10.3847/1538-4357/ac86d5)
- Trierweiler, I. L., Doyle, A. E., & Young, E. D. 2023, The Planetary Science Journal, 4, 136, doi: [10.3847/PSJ/acdef3](https://doi.org/10.3847/PSJ/acdef3)
- Tsiganis, K., Gomes, R., Morbidelli, A., & Levison, H. F. 2005, Nature, 435, 459, doi: [10.1038/nature03539](https://doi.org/10.1038/nature03539)
- van Maanen, A. 1917, PASP, 29, 258, doi: [10.1086/122654](https://doi.org/10.1086/122654)

- Vanderburg, A., Rappaport, S. A., Xu, S., et al. 2020, *Nature*, 585, 363, doi: [10.1038/s41586-020-2713-y](https://doi.org/10.1038/s41586-020-2713-y)
- Vanderlinde, K., Liu, A., Gaensler, B., et al. 2019, in Canadian Long Range Plan for Astronomy and Astrophysics White Papers, Vol. 2020, 28, doi: [10.5281/zenodo.3765414](https://doi.org/10.5281/zenodo.3765414)
- Veras, D. 2020, *MNRAS*, 493, 4692, doi: [10.1093/mnras/staa625](https://doi.org/10.1093/mnras/staa625)
- Veras, D., & Heng, K. 2020, *MNRAS*, 496, 2292, doi: [10.1093/mnras/staa1632](https://doi.org/10.1093/mnras/staa1632)
- Veras, D., McDonald, C. H., & Makarov, V. V. 2020, *MNRAS*, 492, 5291, doi: [10.1093/mnras/staa243](https://doi.org/10.1093/mnras/staa243)
- Veras, D., Mustill, A. J., & Bonsor, A. 2024, arXiv e-prints, arXiv:2401.08767, doi: [10.48550/arXiv.2401.08767](https://doi.org/10.48550/arXiv.2401.08767)
- Veras, D., Shannon, A., & Gänsicke, B. T. 2014, *MNRAS*, 445, 4175, doi: [10.1093/mnras/stu2026](https://doi.org/10.1093/mnras/stu2026)
- Veras, D., Wyatt, M. C., Mustill, A. J., Bonsor, A., & Eldridge, J. J. 2011, *MNRAS*, 417, 2104, doi: [10.1111/j.1365-2966.2011.19393.x](https://doi.org/10.1111/j.1365-2966.2011.19393.x)
- Vida, D., Brown, P. G., Devillepoix, H. A. R., et al. 2023, *Nature Astronomy*, 7, 318, doi: [10.1038/s41550-022-01844-3](https://doi.org/10.1038/s41550-022-01844-3)
- Vinson, B. R., & Chiang, E. 2018, *MNRAS*, 474, 4855, doi: [10.1093/mnras/stx3091](https://doi.org/10.1093/mnras/stx3091)
- Virtanen, P., Gommers, R., Oliphant, T. E., et al. 2020, *Nature Methods*, 17, 261, doi: [10.1038/s41592-019-0686-2](https://doi.org/10.1038/s41592-019-0686-2)
- Vokrouhlický, D., Nesvorný, D., & Dones, L. 2019, *AJ*, 157, 181, doi: [10.3847/1538-3881/ab13aa](https://doi.org/10.3847/1538-3881/ab13aa)
- von Zeipel, H. 1910, *Astronomische Nachrichten*, 183, 345, doi: [10.1002/asna.19091832202](https://doi.org/10.1002/asna.19091832202)
- Wadiasingh, Z., & Timokhin, A. 2019, *ApJ*, 879, 4, doi: [10.3847/1538-4357/ab2240](https://doi.org/10.3847/1538-4357/ab2240)
- Walsh, K. J. 2018, *ARA&A*, 56, 593, doi: [10.1146/annurev-astro-081817-052013](https://doi.org/10.1146/annurev-astro-081817-052013)
- Walsh, K. J., & Richardson, D. C. 2006, *Icarus*, 180, 201, doi: [10.1016/j.icarus.2005.08.015](https://doi.org/10.1016/j.icarus.2005.08.015)
- Walsh, K. J., Richardson, D. C., & Michel, P. 2008, *Nature*, 454, 188, doi: [10.1038/nature07078](https://doi.org/10.1038/nature07078)
- Wang, L., Spurzem, R., Aarseth, S., et al. 2015, *MNRAS*, 450, 4070, doi: [10.1093/mnras/stv817](https://doi.org/10.1093/mnras/stv817)

- Weissman, P. R. 1983, A&A, 118, 90
- Wiegert, P., & Tremaine, S. 1999, Icarus, 137, 84, doi: [10.1006/icar.1998.6040](https://doi.org/10.1006/icar.1998.6040)
- Williams, T. G., Kreckel, K., Belfiore, F., et al. 2022, MNRAS, 509, 1303, doi: [10.1093/mnras/stab3082](https://doi.org/10.1093/mnras/stab3082)
- Wilson, T. G., Farihi, J., Gänsicke, B. T., & Swan, A. 2019, MNRAS, 487, 133, doi: [10.1093/mnras/stz1050](https://doi.org/10.1093/mnras/stz1050)
- Wisdom, J. 2015, AJ, 150, 127, doi: [10.1088/0004-6256/150/4/127](https://doi.org/10.1088/0004-6256/150/4/127)
- Wisdom, J., & Holman, M. 1991, AJ, 102, 1528, doi: [10.1086/115978](https://doi.org/10.1086/115978)
- . 1992, AJ, 104, 2022, doi: [10.1086/116378](https://doi.org/10.1086/116378)
- Wolszczan, A., & Frail, D. A. 1992, Nature, 355, 145, doi: [10.1038/355145a0](https://doi.org/10.1038/355145a0)
- Xu, S., & Bonsor, A. 2021, Elements, 17, 241, doi: [10.2138/gselements.17.4.241](https://doi.org/10.2138/gselements.17.4.241)
- Xu, S., Zuckerman, B., Dufour, P., et al. 2017, ApJ, 836, L7, doi: [10.3847/2041-8213/836/1/L7](https://doi.org/10.3847/2041-8213/836/1/L7)
- Zhang, B. 2020, Nature, 587, 45, doi: [10.1038/s41586-020-2828-1](https://doi.org/10.1038/s41586-020-2828-1)
- Zhang, K. J., Dong, X. F., Rodin, A. E., et al. 2024, arXiv e-prints, arXiv:2406.00476, doi: [10.48550/arXiv.2406.00476](https://doi.org/10.48550/arXiv.2406.00476)
- Zhang, R. C., & Zhang, B. 2022, ApJ, 924, L14, doi: [10.3847/2041-8213/ac46ad](https://doi.org/10.3847/2041-8213/ac46ad)
- Zhang, Y., & Lin, D. N. C. 2020, Nature Astronomy, 4, 852, doi: [10.1038/s41550-020-1065-8](https://doi.org/10.1038/s41550-020-1065-8)
- Zuckerman, B. 2014, ApJ, 791, L27, doi: [10.1088/2041-8205/791/2/L27](https://doi.org/10.1088/2041-8205/791/2/L27)
- Zuckerman, B., Koester, D., Reid, I. N., & Hünsch, M. 2003, ApJ, 596, 477, doi: [10.1086/377492](https://doi.org/10.1086/377492)
- Zuckerman, B., Melis, C., Klein, B., Koester, D., & Jura, M. 2010, ApJ, 722, 725, doi: [10.1088/0004-637X/722/1/725](https://doi.org/10.1088/0004-637X/722/1/725)